

DISSERTATION

CHARACTERIZATION OF INTEGRATED OPTICAL WAVEGUIDE
DEVICES

Submitted by

Guangwei Yuan

Electrical and Computer Engineering Department

In partial fulfillment of the requirements

For the Degree of Doctor of Philosophy

Colorado State University

Fort Collins, Colorado

Summer 2008

UMI Number: 3332751

Copyright 2008 by
Yuan, Guangwei

All rights reserved.

INFORMATION TO USERS

The quality of this reproduction is dependent upon the quality of the copy submitted. Broken or indistinct print, colored or poor quality illustrations and photographs, print bleed-through, substandard margins, and improper alignment can adversely affect reproduction.

In the unlikely event that the author did not send a complete manuscript and there are missing pages, these will be noted. Also, if unauthorized copyright material had to be removed, a note will indicate the deletion.

UMI[®]

UMI Microform 3332751

Copyright 2008 by ProQuest LLC.

All rights reserved. This microform edition is protected against unauthorized copying under Title 17, United States Code.

ProQuest LLC
789 E. Eisenhower Parkway
PO Box 1346
Ann Arbor, MI 48106-1346

Copyright by Guangwei Yuan 2008

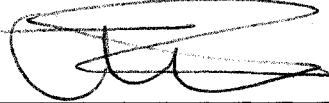
All Rights Reserved

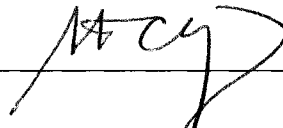
COLORADO STATE UNIVERSITY

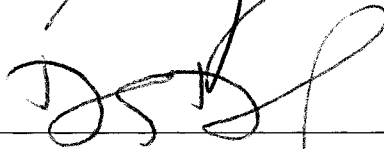
July 11, 2008

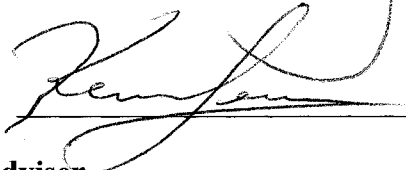
WE HEREBY RECOMMEND THAT THE DISSERTATION PREPARED UNDER OUR SUPERVISION BY GUANGWEI YUAN ENTITLED CHARACTERIZATION OF INTEGRATED OPTICAL WAVEGUIDE DEVICES BE ACCEPTED AS FULFILLING IN PART REQUIREMENTS FOR THE DEGREE OF DOCTOR OF PHILOSOPHY.

Committee on Graduate Work



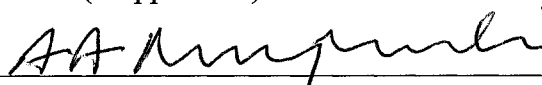






Adviser

Co-Adviser (if applicable)



Department Head/Director

ABSTRACT of DISSERTATION

CHARACTERIZATION OF INTEGRATED OPTICAL WAVEGUIDE DEVICES

The need for biosensors has dramatically increased over the last decade. A widely used medical biosensor is the blood glucose biosensor that helps to save thousands of lives each year. Integrated optical biosensors are attractive among all available biosensors for their low-cost, compactness, and portability, especially in general medical use that would save millions of dollars each year in pre-therapy examination and clinical test cost. Besides public health use, these advanced biosensors could be used in the war on terrorism by alerting troops to biological attacks. Although advantages of using integrated optical waveguide devices are obvious as addressed in following sections, the investigations are far from complete. There are many problems that need to be addressed in new device development.

At the Optoelectronics Research Lab in ECE at CSU, we explore the issues of design, modeling and measurement of integrated optical waveguide devices of interest, such as optical waveguide biosensors and on-chip optical interconnects. The measurement of this type of sensor requires the aid of either a commercial near-field scanning optical microscope (NSOM) or new proposed buried detector arrays. A novel lab-on-chip optical waveguide biosensor was designed to meet the needs for low-trace biological detection without florescent chemical agent aids. The fabrication of the

complete sensor with buried detectors was done using the 0.35 μm CMOS process at Avago Technologies, Fort Collins, Colorado. The detailed fabrication processes were designed with cooperative efforts from various research groups. Experimental results were demonstrated for using NSOM and buried detectors. Eventually, the sensor can be made so compact as to enable portable applications. By implementing the sensor array on a silicon chip, multiple analytes, such as viruses, DNA and chemical agents, can be sensed simultaneously.

The local evanescent-field array coupled (LEAC) sensor was first used to detect pseudo-adlayers on the waveguide top surface. These adlayers include SiN_x and photoresist. The field modulation that was obtained based on NSOM measurement was approximately 80% for a 17 nm SiN_x adlayer that was patterned on the waveguide using plasma reactive ion etching. Later, single and multiple regions of immunoassay complex adlayers were analyzed using NSOM. The most recent results demonstrated the capability of using this sensor to differentiate immunoassay complex regions with different surface coverage ratio. For full and zero coverage CRP immunoassay adlayer, the difference in optical intensity modulation is more than 30%. The study on buried detectors revealed a higher sensitivity of the sensor to a thin organic film on the waveguide. By detecting the optical intensity decay rate, the sensor was able to detect several nanometer thick film with 1.7 dB/mm/nm sensitivity. In bulk material analysis, this sensor demonstrated more than 15 dB/mm absorption coefficient difference between organic oil and air upper claddings. In further analysis, the optical interference phenomena were observed after the adlayer region that indicated the first order leaky waveguide mode in addition to the fundamental mode was excited by the existence of

the adlayer. These experimental results matched well with numerical simulations using the beam propagation method (BPM). In conjunction with the biosensor study, fiber-to-waveguide coupling, waveguide polishing and photolithography techniques were also investigated.

Two generations of on-chip optical interconnect chips were designed, modeled and measured. The first generation chip consists of optical waveguide test structures and leaky-mode waveguide coupled photodetectors. A 16-node H-tree waveguide was used to deliver light into photodetectors and characterized. Photodetectors at each end node of the H-tree were measured using near-field scanning microscopy. The 0.5 micrometer wide photodetector demonstrated up to 80% absorption ratio over just a 10 micrometer length. This absorption efficiency is the highest among reported leaky-mode waveguide coupled photodetectors. The responsivity and quantum efficiency of this photodetector are 0.35 A/W and 65%, respectively.

The second generation chip incorporated modifications based on results from the first generation design. The CMOS circuitry was for the first time added into the chip to recover the optical clock. The second generation chip exploits a thicker upper cladding that obeys the design rules and accommodates a second metal layer. Analysis revealed the effect of upper cladding index on attenuation coefficients. For example, some chips pulled out before deposition of upper cladding layer were experimentally studied. Due to low refractive index contrast, the absorption coefficient dropped about 70%. In contrast, the waveguide loss in the H-tree splitter region dropped dramatically. Based on the observation, a new fabrication process was proposed.

To better understand the performance of leaky-mode waveguide coupled photodetectors, a one-dimensional finite difference model is used to calculate leaky mode profiles, propagation constants and attenuation coefficients. The numerical calculation demonstrates a great match with the near field scanning optical microscopy results.

Guangwei Yuan

Electrical and Computer Engineering Department

Colorado State University

Fort Collins, CO 80523

Summer 2008

TABLE OF CONTENTS

Chapter 1 Introduction and motivation	1
1.1 Introduction	1
1.2 Background of optical waveguide	2
1.3 Motivation of optical waveguide bio-sensing	4
1.4 Motivation of on-chip optical interconnect	6
1.5 Project activities	9
1.6 Outline of the dissertation	12
References.....	13
Chapter 2 Review of dielectric waveguides and previous characterization efforts.....	16
2.1 Introduction.....	16
2.2 Optical waveguides.....	17
2.3 Waveguide modes.....	19
2.4 Mode profiles, losses, and modal projections.....	21
2.5 Characterization methodologies.....	24
2.5.1 Far-field scattering measurement.....	25
2.5.2 Near-field evanescent measurement.....	29
2.6 Evanescent field profile measurements.....	33

2.7 Discussion of tip effect on evanescent field.....	38
2.8 Summary.....	38
References.....	39
Chapter 3 Numerical simulation methods.....	43
3.1 One-dimensional mode calculation.....	43
3.1.1 Differential form of the Helmholtz equation	43
3.1.2 Absorbing boundary condition.....	45
3.1.3 Modal calculation using ABC layers.....	48
3.2 Beam propagation method.....	50
3.2.1 Finite differences representative.....	50
3.2.2 Transparent boundary condition.....	52
3.2.3 Typical BPM simulations on step changes	55
3.3 Finite difference time domain method.....	57
3.3.1 Algorithm.....	57
3.3.2 FDTD simulations on complex waveguide structures.....	59
3.4 Summary.....	61
References.....	61
Chapter 4 Novel integrated waveguide devices.....	62
4.1 Review of integrated optical waveguide sensors.....	62
4.1.1 Surface plasmon resonance.....	62
4. 1.2 Attenuated total reflection (ATR) spectroscopy.....	65
4. 1.3 Total internal reflection fluorescence (TIRF) microscopy.....	66

4.2 Local evanescent field array coupled (LEAC) waveguide sensors	67
4.2.1 Background.....	67
4.2.2 Novel sensor design.....	68
4.2.3 Advantages of LEAC sensors.....	69
4.2.4 Sensor structures.....	70
4.2.5 Preliminary sensitivity analysis.....	73
4.3 Novel on-chip optical interconnects technology.....	76
4.3.1 Monolithic on-chip interconnect.....	76
4.3.2 New on-chip optical interconnect design.....	77
4.3.3 Waveguide structure simulations.....	80
4.4 Summary.....	82
References.....	83
Chapter 5 Waveguide processing and experiment setup.....	85
5.1 Introduction.....	85
5.1.1 LEAC sensors without detector arrays.....	85
5.1.2 LEAC sensors with detector arrays.....	88
5.1.3 The on-chip optical interconnects system.....	90
5.2 Facet polishing.....	93
5.3 Light coupling.....	95
5.4 NSOM setup.....	97
5.5 Summary.....	100
References.....	100
Chapter 6 Experimental results, simulations, and discussions.....	101

6.1 Straight waveguides.....	101
6.1.1 NSOM measurement on single mode waveguides.....	102
6.1.2 NSOM measurement on multimode waveguides.....	105
6.2 Waveguide bends.....	107
6.2.1 Waveguide bend structure.....	108
6.2.2 NSOM measurement on waveguide bends.....	108
6.2.3 Numerical calculation.....	112
6.3 Local evanescent field array coupled (LEAC) waveguide biosensor.....	116
6.3.1 Pseudo-adlayer measurement and simulation.....	116
6.3.1.1 Beam Propagation Method simulation.....	117
6.3.1.2 NSOM measurement on pseudo-adlayer	119
6.3.2 Low refractive index adlayer measurement and simulation.....	125
6.3.2.1 Beam Propagation Method simulation.....	125
6.3.2.2 NSOM measurement on lower refractive index adlayer.....	127
6.3.3 Immunoassay adlayer measurement.....	129
6.4 LEAC sensor with buried detectors.....	135
6.4.1 Sensor structures.....	135
6.4.2 Photocurrent measurement	138
6.5 Leaky mode waveguide coupled photodetectors	142
6.5.1 Photodetector structure	142
6.5.2 NSOM Measurements.....	143
6.5.3 Photo-responsivity measurements	148
6.5.4 Simulations	149

6.6 Waveguide splitters and H-trees	153
6.7 Summary	160
References.....	161
Chapter 7 Achievements and conclusions	164
7.1 Achievements	164
7.1.1 LEAC sensor concept was proposed and tested	164
7.1.2 Two generations of on-chip optical interconnects characterized	167
7.2 Conclusions and suggestions	169
7.3 Complete publications and presentations	170
Appendix A: 1-D mode solver for optical waveguide.....	177
Appendix B: LASI layout of waveguide photo mask CSU_12_2004.....	187
Appendix C: Suggestions of using Rsoft.....	191

Chapter 1

INTRODUCTION AND MOTIVATION

1.1 Introduction

Conventional optical instruments transport light in the form of beams or rays that are diffracted, expanded, and focused by mirrors, lenses, prisms, or non-linear optics. Although such beams are easily obstructed or scattered by various objects, this form of free-space transmission of light is the basis of most optical systems [1].

There is an alternative means to transport light with the use of optical waveguides. It has been developed to provide long or short distance optical wave transmission without the use of lenses. Optical waveguides have important applications in flexibly directing light to receivers, and in the fabrication of miniaturized optical and optoelectronic devices. Over the last few decades, integrated optical waveguides have become a well-established technology. They have been found useful for versatile applications of many industrial sectors, such as optical, biological and optoelectronic manufacturing [1].

The integrated optical waveguide technology enjoys many advantages over conventional optical instruments, such as mirrors and lenses, etc. For example: As deep sub-micron CMOS technology advances, the interconnect delay due to inter-metal and metal ground capacitance has become a dominating factor that significantly reduces overall performance of a microprocessor. Integrated optical interconnect is predicted as an alternative technique for on-chip communication. Here, optical waveguides provide the connections between transiting and receiving components. Optical interconnects enjoy

high data rates and are immune to parasitic capacitive effects that affect the metal interconnect performance. Hence, there is an increasing need to develop an optical clock distribution system for high-end processors implemented in commercial CMOS technology as a platform for on-chip optical interconnect. CMOS chips containing functioning optical waveguide H-trees and polysilicon photodiodes need to be fabricated. The result is a monolithic, planar, on-chip interconnect technology that can be positioned at various levels in the backend metal stack [2-5].

Additionally, lab-on-chip optical waveguide biosensors continue to stimulate many research activities. Future waveguide sensors are required to be capable of simultaneous, reagentless immunoassay sensing of multiple pathogens or other protein based species in point-of-care clinical diagnostics, food safety, environmental monitoring, and biosecurity applications. Thin optical waveguides provide platforms for high sensitive, non-destructive optical sensing. In addition, potential compatibility with well-established silicon and silicon-on-insulator CMOS technology allows for low cost manufacturing and integrated signal processing electronics [6-10].

1.2 Background of Optical Waveguides

The fundamental concept of an optical waveguide is that an optical material of higher refractive index surrounded in an optical material of lower refractive index acts as a light channel. Light is trapped inside the channel and propagates via multiple total internal reflections. An optical waveguide can be made a slab, strip, or cylinder. Presently, the most widely used waveguides are optical fibers, which are made of concentric cylinders of low-loss optical material such as silica-glass. Figure 1.1 below illustrates conventional

optical waveguide configurations.

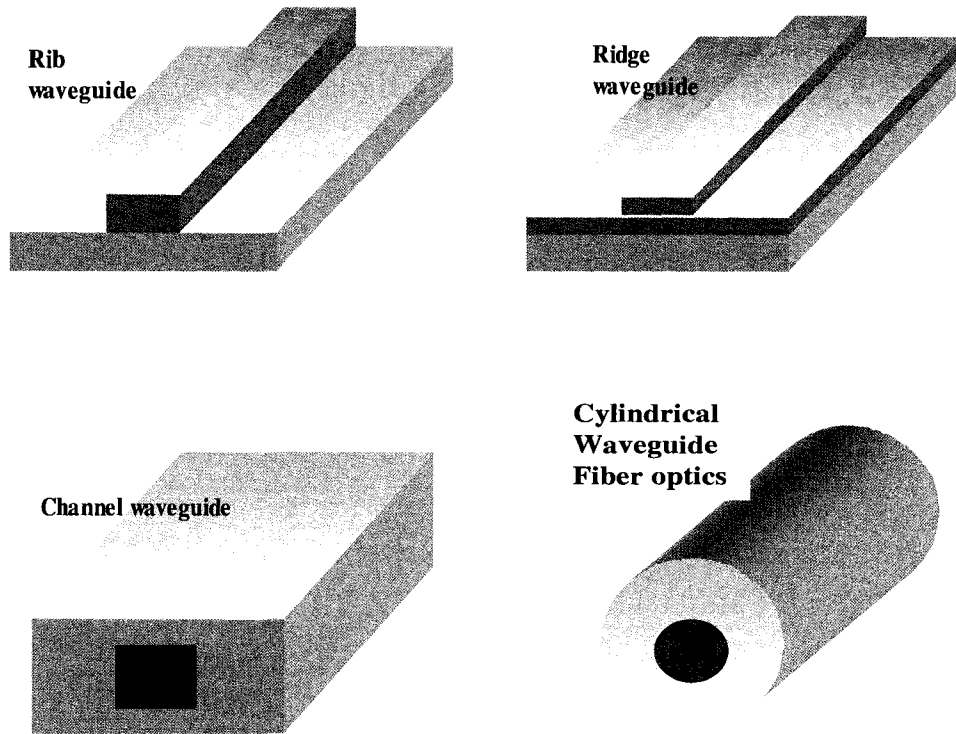


Figure 1.1: Rib, ridge, channel and cylindrical waveguides.

The most investigated waveguide devices are passive elements. Light needs to be excited into the waveguides via external sources such as laser diodes and LEDs. These optical waveguide devices and components are integrated for the generation, focusing, splitting, combining, isolation, polarization, coupling, switching, modulation and detection of light, in some cases all on a single chip. Investigation activities on laser diodes, which exploit waveguide channels as optical resonant cavities.

At present, the most useful characterization method for integrated optical waveguide is near-field scanning optical microscopy (NSOM). The NSOM technique, which has been

developed for more than 20 years, presents advantages over its predecessor, the far field scanning method, of higher optical resolution and local detection of the evanescent field. This technique has been frequently used for optical waveguide characterization in light propagation properties, spatial modes profile, and guided modes interference [11-14]. In our studies, we mainly rely on NSOM to characterize a couple of novel waveguide devices: optical waveguide sensor and on-chip optical interconnect.

1.3 Motivation of Optical Waveguide Bio-sensing

Integrated optical bio-sensing is an innovative field that is extremely important to the United States and to the rest of the world especially to the bio-sensing research community. The research area has increasingly been a worldwide attractive research area of highly technical and fundamental importance.

The integrated optical waveguide biosensor is regarded as a potential key to societal progress throughout the world, driving economic properties and national public health and improves the quality of life, especially in the general medical use. Due to high compatibility of current CMOS technology, it would save millions of dollars each year in pre-therapy examination cost. Besides public health use, the biosensor would be used in homeland security [15]. How to effectively and quickly respond to biological threats is a remaining problem all biosensor investigators encounter. Because many biological agents are contagious, and during the lag time of detection, infected persons could continue to spread the disease, further increasing its reach. The advanced biosensors would be a novel technology becoming available that permits identification of biological agents within minutes, when concentrations are low but often still dangerous.

The integrated optical waveguide biosensor devices, also call lab-on-chip devices, can be made so compact and in an array sensing format to merit portable applications [16-18]. Figure 1.2 shows a lab-on-chip SU8 waveguide sensor that is multianalyte sensing capable [19]. The unusual cross-sectional area of the fluidic channel was created to limit the analyte exposure to the waveguide surfaces, allowing only 1-dimensional analyte diffusion to the multiple immobilized dye/enzyme region. The success of advanced optical biosensors would also alleviate the cost in pre-therapy medical examination, clinic test in a more reliable and fast means. The results would benefit nation wide; improve health care and working environment, and can be transferred to homeland security applications. Therefore, integration is important factor to obtain the advantages the novel biosensor would bring to us. Through full integration of biological, optical, and electronic components, especially current silicon CMOS technology, a compact, fast, real time and comprehensive bio-information detection, acquisition and data analysis system would be possible.

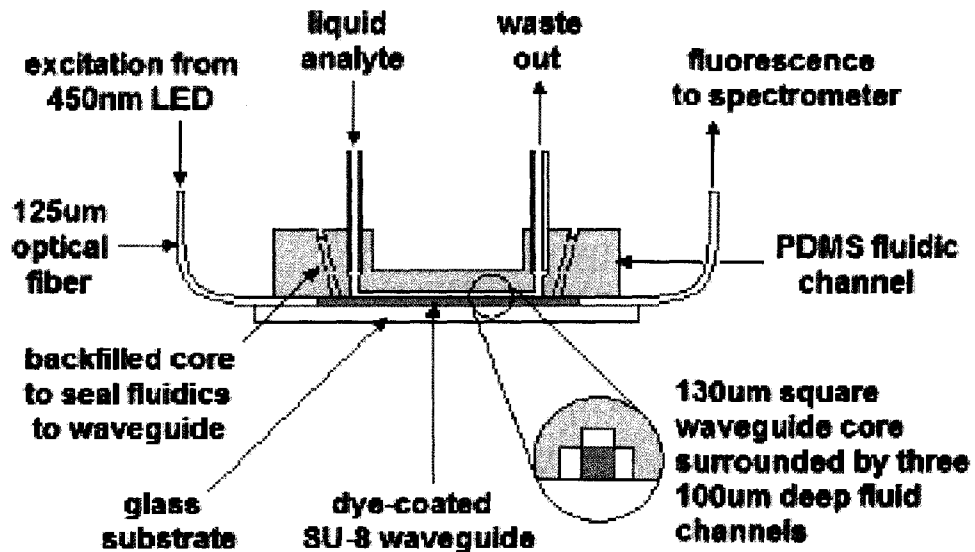


Figure 1.2: A multianalyte-capable integrated optical waveguide biosensor. (reproduced from Reference 19)

The integrated optical waveguide biosensor under investigation at Colorado State University would potentially detect low-trace bioagents, often in complex milieu containing hundreds of other proteins. Those agents optical biosensor are seeking to detect can be Clinical Pathogens (viruses, bacteria), Biowarfare Agents, Drugs and Drug Metabolites, Proteins (antibodies, enzymes), Toxicity or Disease indicators, Fermentation Products and Environmental Agents (small molecules, proteins, ions). Materials can also be detected and identified are DNA, RNA, and other small biological molecules.

1.4 Motivation of On-Chip Optical Interconnect

Over the last four decades, the need for increase in the level of functional integration on-chip, circuit density, and performance has fueled improvements in integrated circuit manufacturing technology. The enhancements in performance achieved until now have been consistent with Gordon Moore's prediction of an exponential growth in transistor density on-chip, as can be seen from Moore's Law comparison with microprocessor generations and predicted by the international technology roadmap for semiconductors (ITRS) [20]. However, the increase in circuit density, the global interconnect clock skew, timing delay, and signal jitter due to increased global interconnect length on each microprocessor generation is significantly increasing with every microprocessor generation. As we move into deep sub-micron CMOS technology the limitations due to wire scaling may significantly reduce overall processor performance, as well as factors such as power consumption and area, are driving the investigation of optical interconnect

technologies for on-chip use [5].

The ITRS has predicted that new technologies need to be implemented as early as the year 2009 in order to achieve interconnect and processor performance goals to overcome signal latency effects in conventional metal connections. The on-chip optical interconnect provides necessary impetus for technology advances along the Moore's Law well beyond the path that is projected by using conventional metal connections. The research on on-chip optical interconnect is significant. The research explores a novel data communication aspect by the use of on-chip optical interconnect and photodetectors that offer advantages of increased bandwidth, reduced size and weight, and reduced cost over competitive electronic interconnect. Figure 1.3 illustrates diagrams of the metal interconnect and optical interconnect. Avoiding parasitic capacitive effects, optical waveguides provide direct connections between transmitting and receiving components. The delay and latency of optical signals are greatly reduced. On the other hand, optical interconnect provides designers more flexibility in power budget. Figure 1.4 shows the optical interconnect offers better power delay product over metal interconnect at the 45 nm CMOS technology node. The research result has a number of applications to the entire electronic and information industry, such as high-speed serial data transportation in computer network. Benefited by the well-established silicon CMOS foundry in United States, the research results can be disseminated faster and more conveniently through industrial sections nation wide. In general, optical interconnect offer the advantage that they can handle high data rates and are not affected by parasitic resistive and capacitive effects. The research results would increase the information technology to a higher level.

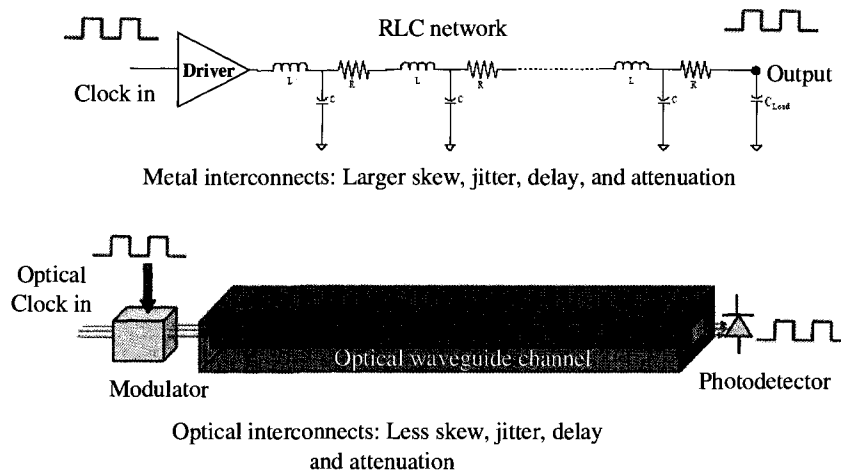


Figure 1.3 Metal interconnect and optical interconnect (reproduced from Reference 21).

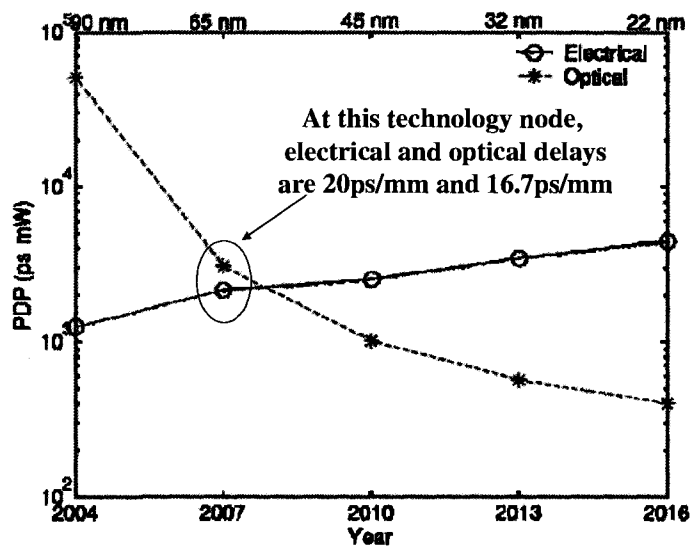


Figure 1.4 Power delay product of metal interconnect and optical interconnect (reproduced from Reference 21).

The disadvantages of optical interconnect technology in the initial development stage can not be neglected. First, fabrication of optical chips is costly when sub-micron feature size is desired. Second, integration of light source and light coupling are difficult problems encountering all the investigators. Lastly, but not least, optical loss reduction is every

investigator's pursuit, but not effectively achieved.

1.5 Project Activities

In research projects to develop novel integrated optical waveguide devices, such as the waveguide biosensor and on-chip optical interconnect, we exploited design, modeling, and measurements research activities.

Design

In our study, we proposed several novel integrated optical waveguide devices and configurations. We are the first research group to propose the local evanescent-field array coupled (LEAC) optical waveguide sensor that relies on specific binding of analytes to one of several localized regions of immobilized biological molecule probes, to modify the waveguide cross section and, thus, the local evanescent field. An array of detector elements along the length of the waveguide, each opposite a region of specific antibody type, can sense the modification in the evanescent field due to local adlayers of bound antigens. Additionally, in conjunction with development of LEAC sensors, we proposed an evanescent field coupled photodetector array. Similar to NSOM that detect the evanescent field on the upper surface of the waveguide, the detector elements in the lower cladding region can detect the power in the evanescent field tail as well. The integrated biosensor devices can be made in CMOS technology so compact to merit portable applications. By implementing sensor array on a silicon chip, such as virus, DNA and chemical agents, can be sensed simultaneously. In the on-chip optical project, we designed a CMOS compatible waveguide and waveguide coupled photodetector,

thereby demonstrating a monolithic optical interconnect system. We designed and simulated a novel metal-semiconductor-metal photodetector array for the sensor using a CMOS compatible process. This photodetector is twenty times smaller than the size of typical photodetectors in similar applications and becomes a leading candidate of next generation on-chip photodetectors for CMOS compatible optical interconnect.

Modeling

Numerical modeling of the optical field allows us to predict integrated optical waveguide devices' performance. In our studies, we extensively exploit numerical methodologies, such like, 1-D mode calculation, beam-propagation method, and finite difference time domain simulation. We significantly improved the integrated optical waveguide device performance through optical modeling. For example, a false alarm in a biological sensing system would be high cost. In the biosensor project, simulation revealed that the optical field disturbance from one sensor element needs to be minimized or at least controlled before light is incident on the next one, which was later, proved via near-field scanning measurements [6]. Thus, a successful LEAC sensor design requires minimal space between adjunct sensor elements. In further study, a great amount of efforts would be aiming to improve the sensitivity while retaining system stability, since the sensor was well engineered to isolate the signals due to biological targets from environment noises as well interference from other sensed targets. In conjunction with leaky mode waveguide coupled photodetector study, we investigated a modal overlap calculation method based on 1-D numerical mode solutions in the effective index approximation that provided good predictions of the photodetector performance. The simulation results indicated that

relatively short photodetectors also have relatively good absorption coefficients that allow a compact device design.

Measurements

A challenge in characterization of waveguide devices and systems is in the tools. Until now, most reported measurements on waveguide devices were done using either far field or near field scanning techniques. In our studies, near field scanning optical microscopy (NSOM) technique, numerical methods and a novel buried detector array method, are exploited. The advantage of NSOM over far-field fiber scanning and typical scatter imaging implementations is the resolution it provides. This resolution can be important, for example, to verify the transverse mode profile or to observe mode beating phenomena as discussed below, as well as high attenuation over a short distance. For example, a leaky mode waveguide coupled photodetector would have a $0.67 \text{ dB}/\mu\text{m}$ effective absorption coefficient allowing a relatively short $10 \mu\text{m}$ -long photodetector to absorb 83% of the incident power as determined via near-field scanning optical microscopy (NSOM). To measure a photodetector of this size, the far-field scanning method is proven far from sufficient. Through NSOM experiments, we successfully proved the LEAC biosensing concept, analyzed leaky mode waveguide coupled photodetectors, and other waveguide components. Waveguide preparation techniques, such as the fiber-to-waveguide coupling and waveguide facet polishing, are critical steps and essential in our measurement. In characterization of photodetectors, we also conducted photocurrent Vs bias voltage measurement. NSOM was also used to determine the effective absorption coefficient of a waveguide-coupled leaky-mode polysilicon photodetector.

1.6 Outline of the Dissertation

Chapter 2 summarizes the background information of the integrated optical waveguides. The basic theory for optical waveguides is presented. We also review previous waveguide characterization methods, such as scattering and near-field measurements. The previous work on waveguide characterization will be discussed.

Chapter 3 describes numerical methods for design and modeling optical waveguides. Three different numerical methods will be discussed, including one-dimensional mode calculation method, two-dimensional beam propagation method, and finite difference time domain method. Their applications to the waveguide components and devices are discussed.

Chapter 4 describes two novel waveguide devices and systems: the local evanescent-field array coupled waveguide sensors and on-chip optical interconnect. The fundament of concepts for both devices will be presented. The design considerations are included.

Chapter 5 discusses waveguide processing and experimental setup for our studies.

Chapter 6 presents the simulations and measurements different waveguide components, devices and systems. In part one and two, the experimental results for single-mode and multimode straight waveguides and waveguide bends are covered. In part three, we evaluate the performance of the LEAC sensors to different type adlayers. In the last part, we describe the characterization work for components of an on-chip optical interconnect system.

Chapter 7 summarizes conclusions and suggestions for future work.

References:

- [1] B. E. A. Saleh, M. C. Teich, "Fundamentals of Photonics," Wiley Series in Pure and Applied Optics, John Wiley & Sons, Inc, 1991.
- [2] N. M. Jokerst, T. K. Gaylord, E. Glytsis, M. A. Brooke, S. Cho, T. Nonaka, T. Suzuki, D. L. Geddis, J. Shin, R. Villalaz, J. Hall, A. Chellapa, and M. Vrazel, "Planar Lightwave Integrated Circuits With Embedded Actives for Board and Substrate Level Optical Signal Distribution," IEEE Transactions on Advanced Packaging, vol. 27, pp. 376-385, May. 2004.
- [3] G. Yuan, R. Pownall, P. Nikkel, C. Thangaraj, T. Chen and K.L. Lear, "Characterization of CMOS compatible waveguide coupled leaky-mode photodetectors," IEEE Photonics Tech. Letters, vol. 18, pp.1657-1659, August, 2006.
- [4] R. Pownall, G. Yuan, P. Nikkel, T. Chen, K. L. Lear, "Geometry Dependence of CMOS-compatible, Polysilicon, Leaky-Mode Photodetectors," IEEE Photonics Technology Letters, vol 19, pp. 513- 515, April, 2007.
- [5] A. M. Raza, "A truly CMOS compatible waveguide coupled photodiode for on-chip optical interconnect," M.S. Thesis, Colorado State University, Fort Collins, CO, 2005.
- [6] G. Yuan, M. D. Stephens, D. S. Dandy, and K. L. Lear, "Initial demonstration of a local, evanescent, array coupled biosensor concept," B4P-G, IEEE Sensor Conference Proc., Oct. 2005.
- [7] G. Yuan, M. D. Stephens, D. S. Dandy, K. L. Lear, "Novel local evanescent field detection waveguide multianalyte biosensor," SPIE Proceedings, Volume 5557, pp. 140-146, Oct. 2004.

- [8] G. Yuan, M. D. Stephens, D. S. Dandy, and K. L. Lear, "Direct imaging of transient interference in a single mode waveguide using near-field scanning optical microscopy," *IEEE Photonics Technology Letters*, vol 17, pp. 2382-2384, Nov. 2005.
- [9] G. Yuan, M. D. Stephens, D.S. Dandy, J. Gerding, A. Van Orden, K.L. Lear, "Evanescent field response to small features on a planar waveguide biosensor", *Proceedings of the IEEE LEOS 19th Annual Meeting*, paper TuQ3, pp. 304-305, Montreal, Canada, Oct. 30, 2006.
- [10] G. Yuan, M. D. Stephens, D.S. Dandy, J. Gerding, A. Van Orden, K.L. Lear, "Local evanescent, array coupled (LEAC) biosensor response to low index adlayers," *Conference on Lasers and Electro-Optics 2006, CThL7*, Long Beach, California, May25, 2006.
- [11] G. H. Vander Rhodes, B. B. Goldberg, M. S. Ünlü, S. T. Chu, W. Pan, T. Kaneko, Y. Kokobun, and B. E. Little, "Measurement of internal spatial modes and local propagation properties in optical waveguides," *Applied Physics Letters*, Vol. 75, No. 16, pp. 2368-2370, Oct. 1999.
- [12] S. Bourzeix, J. M. Moison, F. Mignard, F. Barthe, A. C. Borccara, C. Licoppe, B. Mersali, M. Allovon, and A. Bruno, "Near-field optical imaging of light propagation in semiconductor waveguide structures," *Appl. Phys. Lett.*, vol. 73, No. 8, pp. 1035-1037, 1998.
- [13] W. Ji, D. Kim, H. J. Kim, Beom-Hoan O, S. Park, E. Lee, and S. G. Lee, "NSOM-Based Characterization Method Applicable to Optical Channel Waveguide With a Solid-State Cladding," *IEEE Photonic Technology Letters*, Vol. 17, No. 4, pp. 846-848, April, 2005.

- [14] A. L. Campillo, J. W. P. Hsu, K. R. Parameswaran, M. M. Fejer, "Direct imaging of multimode interference in a channel waveguide," *Optics Letters*, Vol. 28, No 6, pp. 399-401, Mar. 2003.
- [15] F. Ligler, "Biosensors for identification of biological warfare agents," *Biosens. Bioelectron.* 14, pp. 749, 2000.
- [16] C.A. Rowe-Taitt, J. W. Hazzard, K. E. Hoffman, J.J. Cras, J.P. Golden, F.S. Ligler, "Simultaneous detection of six biohazardous agents using a planar waveguide array biosensor", *Biosens. Bioelectron.* 15, pp. 579, 2000.
- [17] C.A. Rowe, S.B. Scruggs, M.J. Feldstein, J.P. Golden, and F.S. Ligler, "An array immunosensor for simultaneous detection of clinical analytes," *Analytical Chemistry*, 71, pp 433-439, 1999.
- [18] D. A. Chang-Yen, B. K. Gale, "Design, fabrication, and packaging of a practical multianalyte-capable optical biosensor," *Journal of Microlithography Microfabrication and Microsystems*, Vol 5, Iss 2, pp. 8, 2006.
- [19] D. A. Chang-Yen, B. K. Gale, "Design and Fabrication of a Multianalyte-Capable Optical Biosensor Using a Multiphysics Approach," *Proc. of IEEE Microtechnologies in Medicine and Biology*, Oahu , Hawaii , May, 2005.
- [20] Gordon E. Moore, "Cramming More Components Onto Integrated Circuits," *Electronics Magazine*, Vol. 38, no. 8, pp. 114-117, April 19, 1965,
- [21] *Intel Technology Journal*, "Optical Technologies and Applications", Vol. 8, Issue 2, May, 2004.

Chapter 2

OPTICAL WAVEGUIDES AND PRESENT CHARACTERIZATION TECHNIQUES

2.1 Introduction

To develop more understanding of integrated optical waveguides, it is necessary for us to review fundamentals of guided-wave devices and conventional waveguide characterization methodologies. Our work greatly benefits from many researchers' previous work on optical waveguides. For example, a series of technical articles addressing optical waveguide issues firstly appeared on the Bell System Technical Journal and Journal of Vacuum Science and Technology. These articles addressed an important waveguide characterization method that exploited a scatter light scanning technique on sputtered glass waveguides [1-2]. The measurement method focuses on the loss property of glass waveguides and provides both industry and research institutes means to analyze waveguides, and helped make optical fiber networks possible [3-8]. As metal waveguides found great use in conventional radar communications, optical waveguides such as silica glass fiber developed at a very fast pace in early 70s, and were vital in global optical communication networks. Much improved from this precedent, near-field scanning optical microscopy caught much attention from the middle of the 1990s. It has been well adapted to characterization of integrated photonic waveguides world-wide since then [9-15]. Milestones were made in 1999, which were instructional to our work at Colorado State

University, when a group of researchers at Boston University demonstrated the application of NSOM tip to measure the local evanescent field [16]. Other experimentalists at the University of Virginia for the first time observed modal interference in a channel waveguide by measuring the evanescent fields [17]. In recent years, the use of NSOM is well extended as an auxiliary measurement tool for analysis of optical waveguide biosensors, photonics crystals, active waveguide devices, such as lasers and LED, etc [18,19]. With the characterization method improving, various optical waveguide devices were invented and exploited. Most recently, significant progresses has been recently achieved in the development of high-speed short-length inter- and intra- chip optical interconnects using integrated optical waveguides.

In this chapter, the background theory of optical waveguides is presented in Section 2.1. Where the method to solve waveguide modes, losses, and evanescent fields are extensively discussed. In Section 2.2, we will review the background of optical waveguides and waveguide characterization efforts. The advantages and disadvantages of current characterization techniques will be discussed. Waveguide characterization methods are discussed, such as far field scanning and near field scanning optical microscopy (NSOM) methods. At last, previous work on characterization of optical waveguides using NSOM is reviewed in Section 2.3.

2.2 Optical waveguides

Optical waveguides have many forms as introduced in Chapter 1. To obtain a straightforward understanding of how that guided wave devices work, a simple slab waveguide model is used. Assume a slab of optical material of refractive index n_1 is

surrounded by claddings of lower refractive indices n_2 . To travel without loss, the light must be trapped and guided inside the slab governed by rules of total internal reflection as shown in Figure 2.1. Light is incident into the slab and propagates along the length of the waveguide which is taken to be parallel to the z-axis. Light is reflected at the slab boundaries with an angles θ to the z-axis and goes through multiple total internal reflections. The angle θ is required to be smaller than the critical angle $\theta_c = \pi/2 - \sin^{-1}(n_2/n_1)$ at the slab boundaries to ensure no loss in reflections [20]. Otherwise, light would diminish along the length of the waveguide by losing a fraction of power at each reflection. However, in reality, light diminishes at the slab boundaries due to scattering loss even guided wave condition is met, but only by a relatively small amount in typical waveguides.

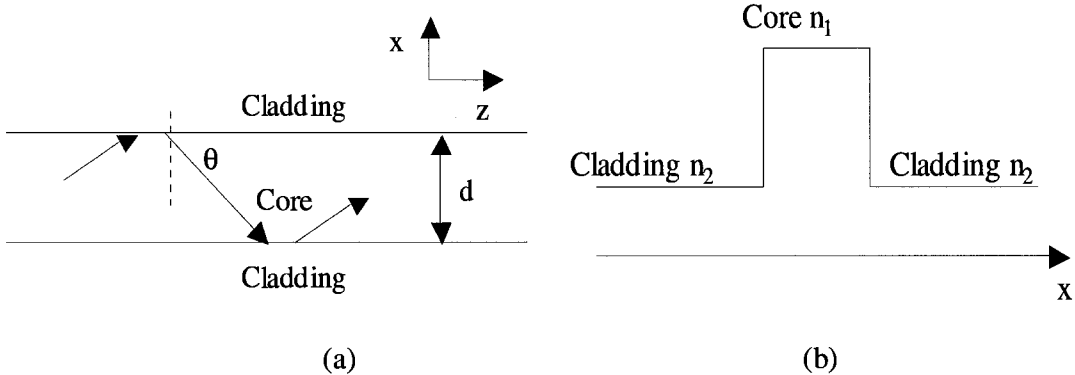


Figure 2.1: a) Light incident in a slab waveguide with angles $\theta < \theta_c$ are confined due to total internal reflection, b) corresponding refractive index profile of this slab waveguide.

Although the simplicity of the slab waveguide is attractive from a modeling perspective, not many devices are made in slab waveguide form. Some level of approximations would be needed in order to simplify a complex waveguide structure to a slab form. In practice, waveguides are in three-dimensional. However, in the slab model, only x and z -axis or the

x-z plane is considered. For, waveguides with large width-to-thickness ratio, this approximation would be regarded as appropriate. When the width-to-thickness ratio is smaller than 10, the effect of width should be considered.

2.3 Waveguide modes

When a refractive index profile of a slab waveguide is known, we are able to calculate the mode profiles of the guided wave. To determine the slab waveguide modes, the Helmholtz equation for a given waveguide structure and refractive index profile is set for solved. Certain boundary conditions need to be applied when in solving the Helmholtz equation. To begin, we assume that light rays bouncing between the boundaries of the slab due to total international reflection. Self-consistency condition requires that the total phase shift in the x-axis must be zero or a multiple of 2π when light completes a round trip in this direction. The total phase shift is contributed from both propagation phase shift and phase shift due to reflection, as illustrated in Figure 2.2.

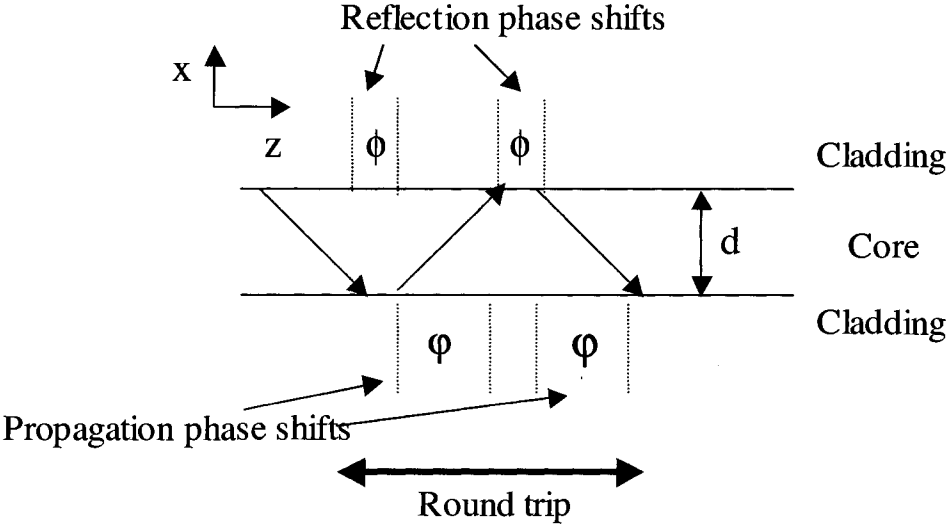


Figure 2.2: Phase shifts in a slab waveguide.

Assuming only a TE (transverse electric) mode in a slab waveguide, we look into the electric field (E-field) of the mode in the x-axis. Light propagating along the waveguide is of a monochromatic wavelength λ . In free space, the wavevector of the incident light is denoted as $\beta_0=2\pi/\lambda$. This wavevector can be separated into x and z-components, $k_x = \beta_0 \sin\theta$ and $k_z = \beta_0 \cos\theta$, respectively. The first part of the phase shift, propagation phase shift ($2\phi=2k_x d$), is denoted as the phase delay between the twice-reflected wave to the original wave in term of the thickness of the slab d , which is expressed in Equation 2.1. The reflection phase shifts, on the other hand, 2ϕ , are introduced by internal reflections at the slab boundaries and are expressed in Equation 2.2. Following the self-consistency rule, the sum of propagation phase shift and reflection phase shift must be equal to a multiple of 2π for a complete round trip as expressed in Equation 2.3.

$$2\phi = 2k_x d \quad (\text{Eq. 2.1})$$

$$2\phi = -4 \tan^{-1} \left(\left(\frac{\sin^2 \theta_c}{\sin^2 \theta} - 1 \right)^{-1/2} \right) \quad (\text{Eq. 2.2})$$

$$2(\phi + \varphi) = 2m\pi, m = 0, 1, \dots \quad (\text{Eq. 2.3})$$

When substituting (Eq. 2.1) and (Eq. 2.2) into (Eq. 2.3), we obtain a transcendental equation (Eq. 2.4), where m is an integral number.

$$\tan\left(\frac{\pi d}{\lambda} \sin \theta - \frac{m\pi}{2}\right) = \left(\frac{\sin^2 \theta_c}{\sin^2 \theta} - 1\right)^{-1/2}, m = 0, 1, \dots \quad (\text{Eq. 2.4})$$

Although a numerical method, which will be discussed in the next Chapter, is ready and available to find nearly-precise solutions using extensive computer-aided computation power, we benefit from a graphical plot that is informative and easier for us to look up waveguide modes. To begin, both the right hand side and the left hand side of Equation 2.4 are plotted versus $\sin\theta$. Every intersection point indicates a guided mode that can exist in the waveguide, as illustrated in Fig 2.3.

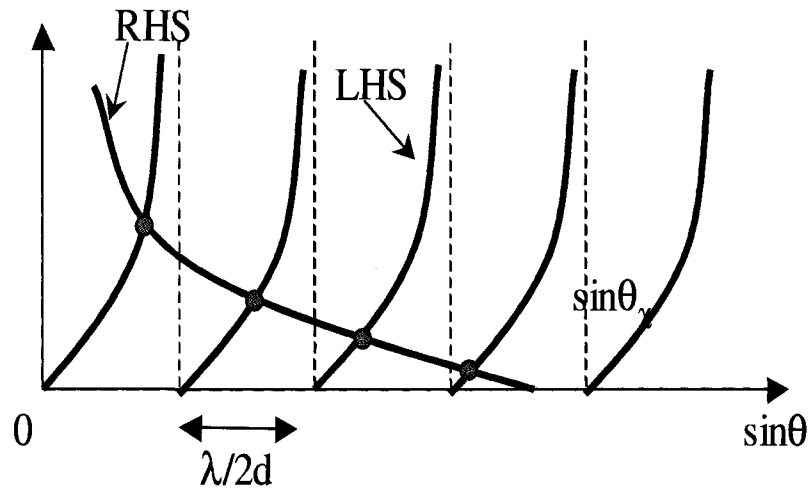


Figure 2.3: Graphic solutions to Equation 2.4.

2.4 Mode profiles, losses, and modal projections

We might be wondering how the waveguide modes look and how the E-field profiles are distributed. The graphic solutions of Figure 2.3 provide the incident angles of each mode, θ_m ($m=0,1,\dots$) of the guided modes. Recall the propagation constants in the z-axis for each mode are defined as $\beta_m = n_1 \sin\theta_m k_0$, which are all the same for all three different waveguide regions: upper cladding, core and lower cladding. Notably, the propagation constants in the x-direction are different in the three regions. As derivation reflects, the

constant is denoted as $k_{xm}=(\beta_0^2 n_1^2 - \beta_m^2)^{1/2}$ in the core and $p_m=(\beta_m^2 - \beta_0^2 n_2^2)^{1/2}$ in the claddings, assuming a symmetric waveguide which has same upper and lower cladding refractive indices is used. That is the field distribution is sinusoidal in the core and exponentially decaying in both claddings. Thus, we are able to write the E-field distributions in Eq. (2.5), where A_m is the constant of input E-field strength.

$$E_m(x) = \begin{cases} A_m \cos(k_{xm} d / 2) \exp(-p_m(x - d / 2)) & -d / 2 \geq x \\ A_m \cos(k_{xm} x) & -d / 2 \leq x \leq d / 2 \\ A_m \cos(k_{xm} d / 2) \exp(p_m(x + d / 2)) & x \geq d / 2 \end{cases} \quad (\text{Eq. 2.5})$$

One interesting point is, unlike the free space Gaussian beam, the guided waveguide mode does not spread into the transverse x direction as it propagates. This property allows a no-loss transmission of light. The guided wave inside the core is confined by evanescent wave field in the claddings. The extent of the evanescent field can be quantified by penetration depth, $1/p_m$. The larger the penetration depth, the more fraction of power is confined in the evanescent field. Higher order modes penetrate deeper into claddings than lower order modes. The penetration depth of the fundamental mode is smallest of all the waveguide modes. Figure 2.4 illustrates the field profiles of the 0th, 1st and 2nd order modes. Figure 2.5 shows the end view image (far field image) of a real ridge waveguide mode. The mode profile in the figure is Gaussian-like indicating a fundamental mode guided in the waveguide.

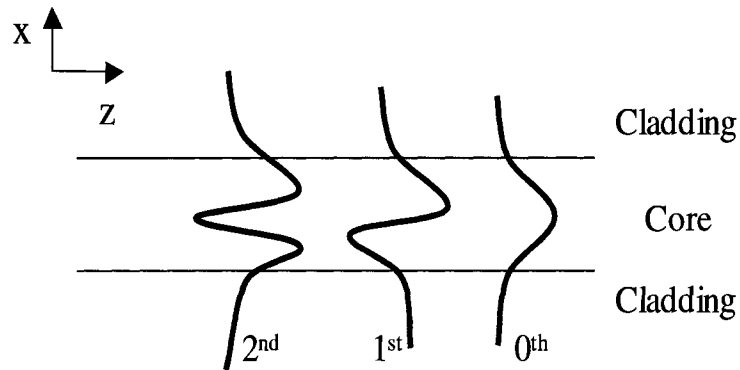


Figure 2.4: Field profiles of the first three order E-field modes of a slab waveguide.

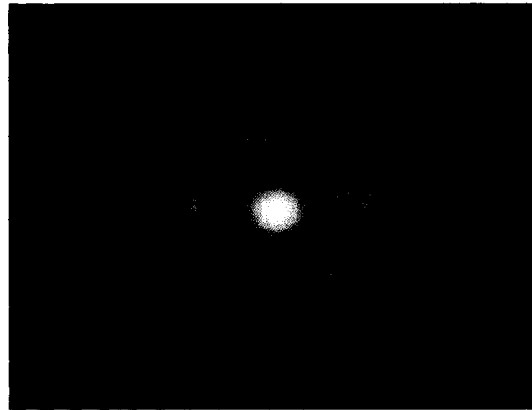


Figure 2.5: End view image of a ridge waveguide (reproduced from Reference 21).

There are three loss mechanisms in a straight optical waveguide: absorptive loss, leaky mode loss and scattering loss. The absorptive and leaky mode loss can be minimized by choosing appropriate waveguide materials and structures. The scattering loss is mostly due the roughness of interfaces introduced in the fabrication process. Because of loss, the waveguide modes attenuate in the light propagation direction. The propagation constants now have both real and imaginary part as $\beta_m = \beta_{mr} + i\beta_{mi}$. The imaginary part of the propagation constant determines the attenuation rates, $\alpha_m = 10 \log_{10}(e)\beta_{mi}$, where the

$10\log_{10}(e)$ factor allows the loss to be expressed in dB.

Modal projections are widely used in optical devices such as interferometers and multiplexers. Understanding the concept of modal projection helps us in analysis of both local evanescent field detection and leaky mode coupling. A mode can be coupled back and forth in a dual waveguide system, like an interferometer, as illustrated in Figure 2.6 (a). The light power is shared by the two waveguides at different ratios. This is an example of evanescent field coupling. An extreme example is shown in Figure 2.6 (b), where the two waveguides are placed together and the top waveguide is terminated at half-length. This is an example of leaky mode coupling. Light coupled in the bottom waveguide is determined by the modal profile at half-length position. The mode projection calculation will be visited in Chapter 6.

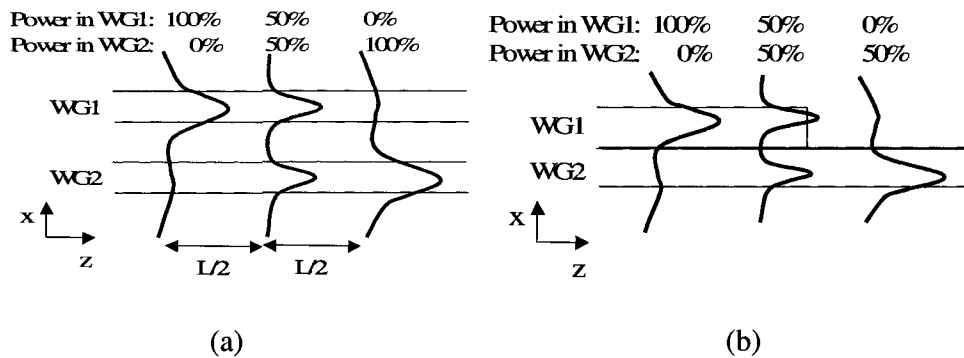


Figure 2.6: Schematics of (a) evanescent field coupling and (b) leaky mode coupling.

2.5 Characterization methodologies

The need for quick development of integrated waveguide devices motivates characterizations done by a fast and accurate means. Properties such as propagation losses, modal interferences and local evanescent field perturbations are of greatest interested. For

decades, there were a couple of experimental methodologies most frequently used in optical waveguide characterizations, including far-field scattering measurement and near-field evanescent measurement.

2.5.1 Far-field scattering measurement

The light attenuation rate is an important parameter to evaluate an optical waveguide. Long before near-field optical scanning microscopy (NSOM) became an available technique to characterize waveguide losses, researchers solely relied on far-field scattering measurement that quantifies the attenuation rate of light propagation by measuring scattered light from a relatively large distance from the waveguide core [22-25].

The far-field scattering measurement is based on the assumption that the attenuation rate is a constant over a certain waveguide length. Thus the scattered light in the far field remains a fixed ratio to the light power still confined in the waveguide core. By fitting the far-field intensity, it is a simple process to obtain an exponential decay constant that can be taken as the attenuation rate. Being a non-contact characterization technique, far-field scattering measurement has been well developed as a relatively accurate, easy to use, nondestructive, and inexpensive means to obtain waveguide losses.

Early far-field scattering measurements employed a glass fiber that was scanned along the waveguide channel [7-8]. The experimental setup is illustrated in Figure 2.7. The light is coupled into the waveguide via a right-angle prism. During the measurement, the glass fiber with one open end is mounted on a mechanical translation stage at a constant distance from the waveguide. Then, the fiber is scanned in one dimensional along the waveguide length. Scattered light is coupled into the open end and fed into a high sensitive photodetector located at the other open end of the fiber. One-dimensional measurement is

conducted at different longitudinal positions above the waveguide. However, this method has an obvious disadvantage. It is difficult to maintain the fiber tip over the top of the waveguide, for example, while maintaining the alignment to the waveguide and constant distance from the tip to the waveguide.

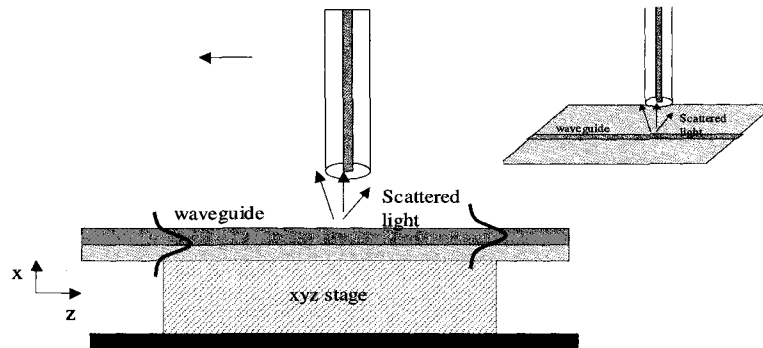
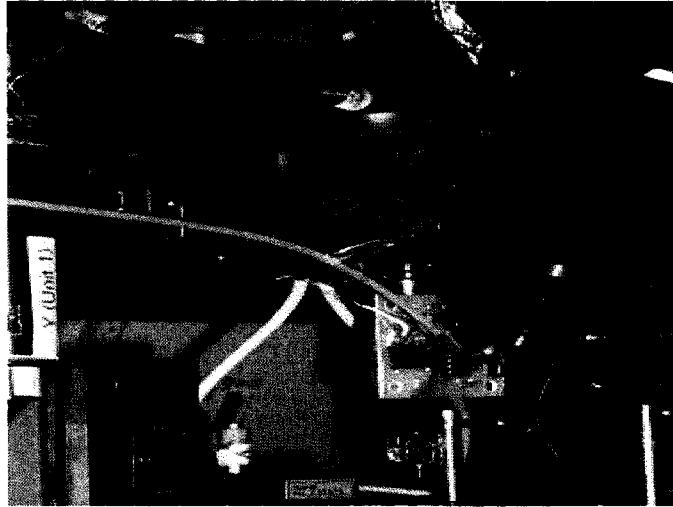


Figure 2.7, Side view of a far field scanning setup. (Inset) Angle view.

Figure 2.8 (a) shows a far field scanning system that has been currently being developed by the Optoelectronics Research Group at Colorado State University [26]. Here the scanning tip uses a cleaved multimode fiber with $125\ \mu\text{m}$ cladding diameter and $50\ \mu\text{m}$ core diameter. The cleaved fiber tip was mounted on a tuning fork shown in Figure 2.8 (b). A motorized translation stage controls the height of the tip and position in the X-Y plane. Figure 2.9 (a) shows far field intensity image of a $4\ \mu\text{m}$ wide straight waveguide. Unlike conventional one-dimensional scanning, far field intensity was measured in the Y-Z plane in an area of $80\ \mu\text{m} \times 90\ \mu\text{m}$. The red dashed line denotes the centerline of the waveguide. The far-field intensity image shows a Gaussian-like profile. The far field light intensity along the centerline of the waveguide was plotted with the solid line in Figure 2.9 (b). The

fit curve (dashed line) shows a 13.5 dB/mm intensity decay rate along the waveguide propagation direction.

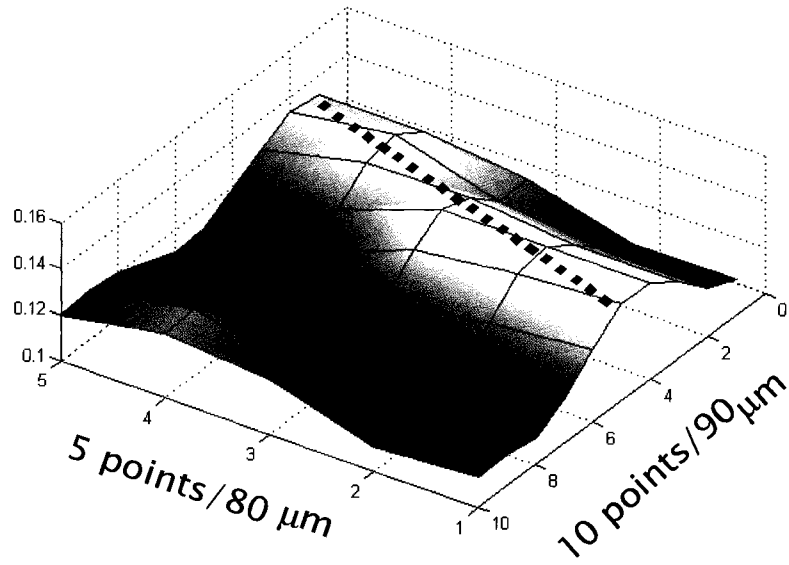


(a)

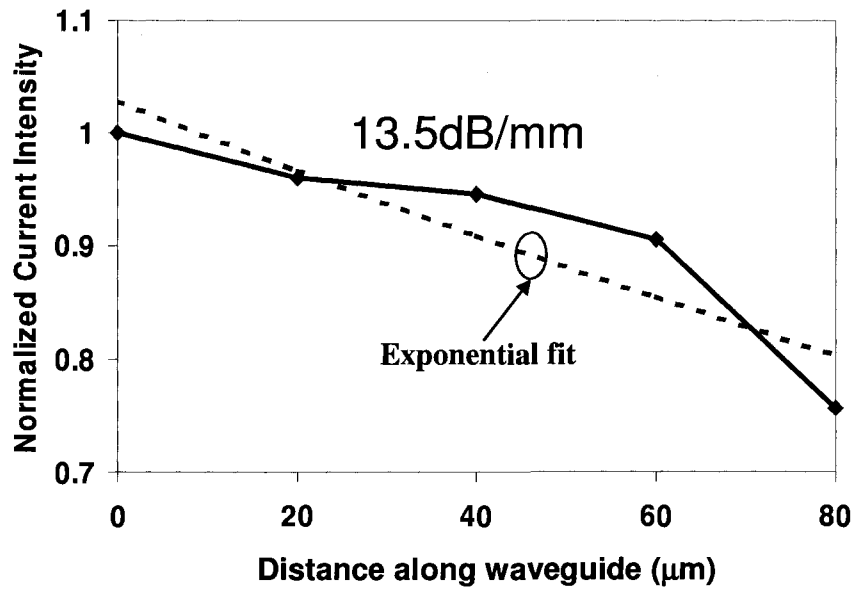


(b)

Figure 2.8: a) A far field scanning system developed by the Optoelectronics Research Group, Colorado State University b) The cleaved fiber tip mounted on a tuning fork. (Courtesy of Rongjin Yan)



(a)



(b)

Figure 2.9: a) Far field intensity image of a 4 μm wide straight waveguide. The red dashed line denotes the centerline of the waveguide. b) The far field light intensity along the centerline of the waveguide (Solid). (Courtesy of Rongjin Yan)

2.5.2 Near-field evanescent measurement

In contrast to the far-field scanning method, near-field evanescent measurement techniques provide a means not only of tracking waveguide losses but also obtaining higher resolution information, such as mode profiles. Most importantly, local field perturbations at a sub-wavelength scale which could be introduced by small defects, abrupt interfaces, or real time refractive index profile changes, can be determined as well. Correspondingly, near-field evanescent measurement requires a much more complicated system.

Early NSOM system development dates back in the 1980s when two groups of researchers at IBM Zurich (Pohl et al) and Cornell (Lewis et al) almost independently demonstrated transmission mode near-field scanning optical microscopy (NSOM) [27]. Both groups adapted a sub-wavelength metal-coated optical tip as the scanning probe and exploited feedback system to control and maintain the probe distance to the targeted sample. Resolution was claimed as 25nm which was as low as one twentieth of the wavelength of the incident light. Not until mid-90s did researchers start to utilize NSOM to analyze integrated photonic structures. In an early experiment [25], the NSOM tip was placed above a straight waveguide performing one-dimensional scans at multiple points along a pair of straight waveguides. NSOM with a tapered fiber tip was used to observe multiple TM modes in a small section of SiN_x on SiO_2 waveguide [28]. The fiber tips used in the experiments were tapered to sub-100nm diameter and coated with metal and were placed into an evanescent field generated by total internal reflection. The light captured and guided in the fiber was measured at other fiber end using high sensitivity optical detectors. Most recently, interferometric NSOM was reported with the capability to

recover the phase information of optical fields in nominally symmetric waveguide splitters.

The major components of a NSOM system are the feedback and control mechanisms, scanning probe, light source and detectors, and sample stages as illustrated in Figure 2.10. The off-the-shelf NSOM systems are far more complicated such as the Olympic NSOM system illustrated in Figure 2.11. NSOM makes use of evanescent or non-propagating fields that exist only near the surface of the object. These fields carry the high frequency spatial information about the object and have field intensities that decay exponentially with distance from the object. The penetration depth can be as small as a few tens of nanometers. Because of this, feedback and control mechanisms are required to accurately detect the distance between the scanning probe and the sample surface. The operation modes, which are either contact or tapping (intermittent contact) modes, are very similar to the feedback mechanisms in atomic force microscopy (AFM). Consequently, near-field optical microscopy offers a reliable and accurate topographic scanning capability. The spatial resolution of NSOM can be as small as a few nanometers in lateral scans. The scanning can be done either at a constant height or with regulated height by using a feedback mechanism [29]. The light source and detector are separated from the feedback and control mechanisms. Depending on the light collection modes, the light source can be reflected, scattered, or evanescent field from sample surface. A high sensitivity optical detector, such as an avalanche photo diode (APD) or a photomultiplier tube (PMT), are desired for detectors due to the weak optical signal.

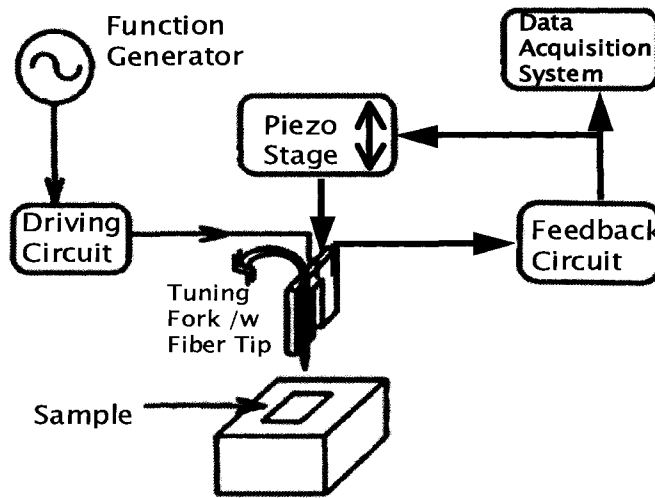


Figure 2.10: Schematic of a typical NSOM system (reproduced from Reference 30).

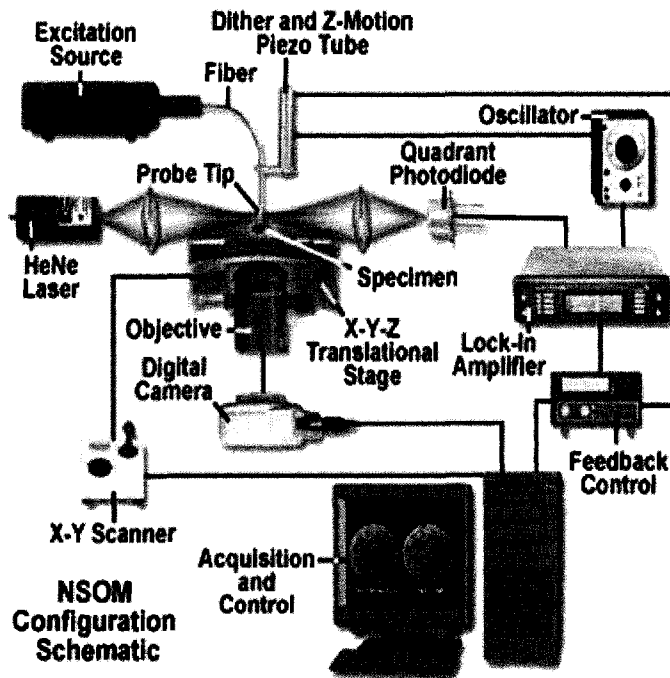


Figure 2.11: A NSOM system (reproduced from Reference 30).

The scanning tip is usually a pulled or etched optical fiber coated with metal except at the tip in straight or bent form, or micro-etched probe with a pinhole in the center of the pyramidal tip, as illustrated in Figure 2.11 (a) and (b). Although scanning tips without pinholes are relatively complex to set up and operate, their contrast and sensitivity are better than others are.

There are two categories of position feedback control. Shear Force Feedback was originally proposed by Karrai and R.D.Grober in 1995 and is currently most used technique, as shown in Figure 2.11 (a). In this case, the NSOM tip is mounted on the side of a tuning fork which oscillates at its resonance frequency. The tuning fork can be regarded as a RLC network with high Q factor. When operating at a resonant frequency, the tuning fork has very high sensitivity to the shear force introduced by the interaction between the fiber tip and sample surface. The shear-force feedback method laterally dithers the probe tip at a mechanical resonance frequency in proximity to the specimen surface. The change in the sample topology would reflect the amplitude or phase change of the tuning fork. The higher sensitivity of the tuning fork, the higher resolution of topology can be obtained. The other feedback mechanism is shown in Figure 2.11(b). Where a reference laser beam is focused on the back plane of bent NSOM tip and reflected to an optical detector array. The interaction between the tip and sample surface will change the bend curvature of the back plane, thus the reflected beam direction into the optical detector array.

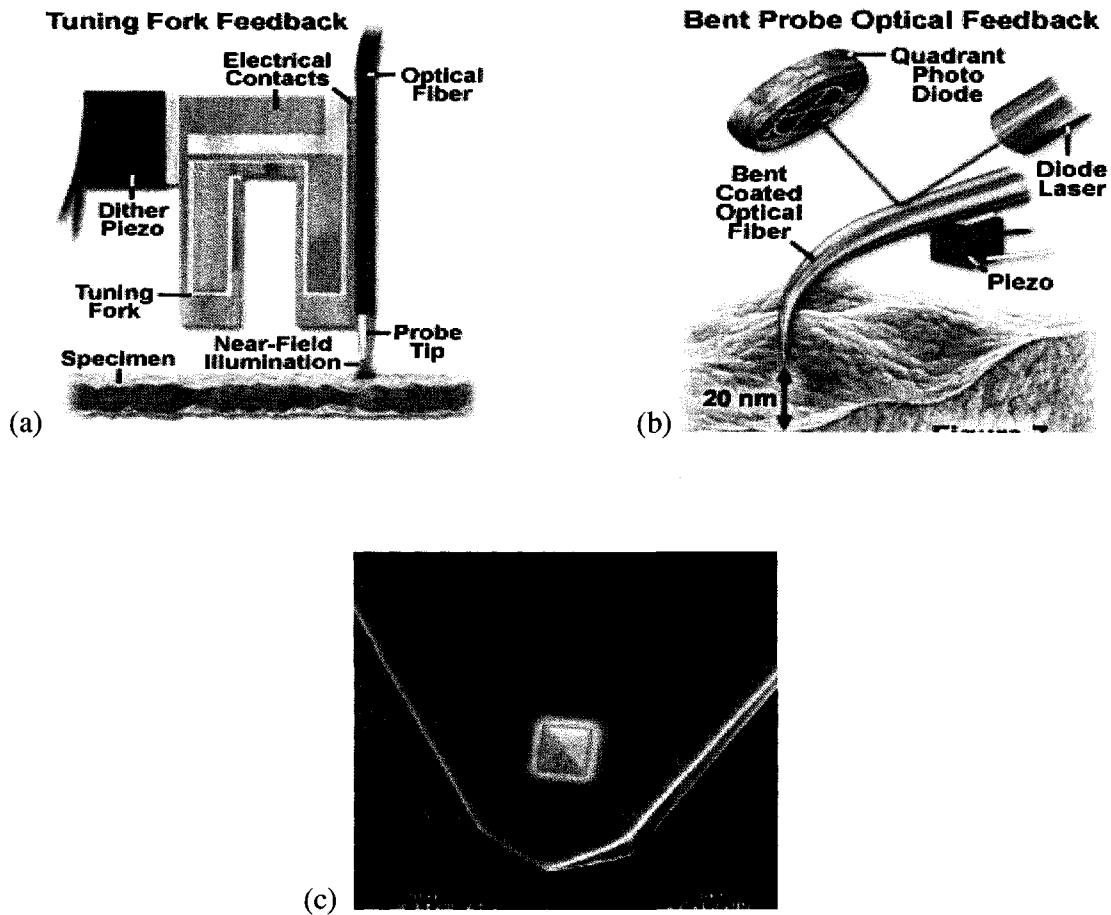


Figure 2.11: (a) Shear-force feedback technique using an aperture tip, (b) back-plane reflection technique using an aperture-less tip (reproduced from Reference 30), (c) a Alpha-SNOM tip (reproduced from Reference 31).

2.6 Evanescent field profile measurements

In this section, we primarily discuss previous work in measuring optical waveguide mode profiles by use of NSOM. A standard scanning tip setup is shown in Figure 2.12. Light from an external cavity laser was coupled into the waveguide via a pigtailed fiber

[10-11]. During scanning, the NSOM tip was placed on the top surface of the waveguide, measuring both surface height and light intensities. This model work was to study the evanescent field above the cladding of a channel waveguide. The waveguide core is composed of a doped glass of index of $n=1.65$ surrounded by the claddings (SiO_2) of index of $n=1.44$. The tip collected optical power in the evanescent tail of the guided modes. Evanescent field was captured by the fiber tip in the plane perpendicular to the direction of light propagation. The collected light was transmitted along the fiber and detected with an InGaAs photodiode. The light intensity profile is plotted in Figure 2.13 (a) superimposed on waveguide schematic. As shown in the plot, the intensity decayed exponentially as a function of tip to waveguide core distance. This result demonstrated an excellent agreement with the mode calculation, also shown in Figure 2.13 (a). A vertical line data scan at $y=0$ is shown in Figure 2.13 (b), presented as an exponentially decaying behavior in agreement with theoretical predictions.

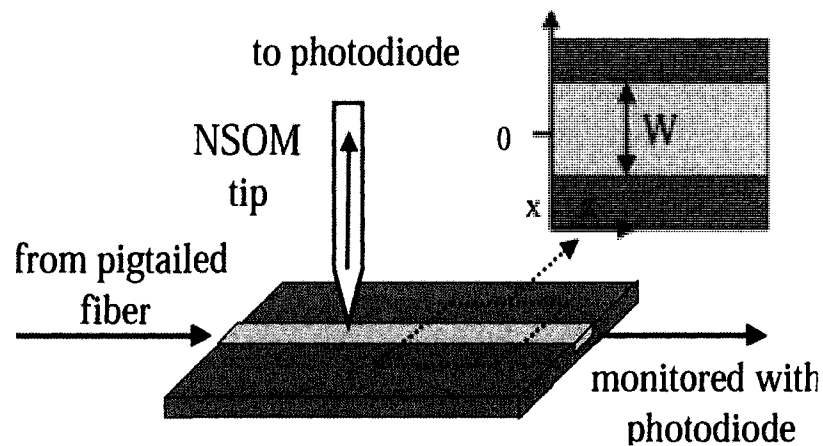
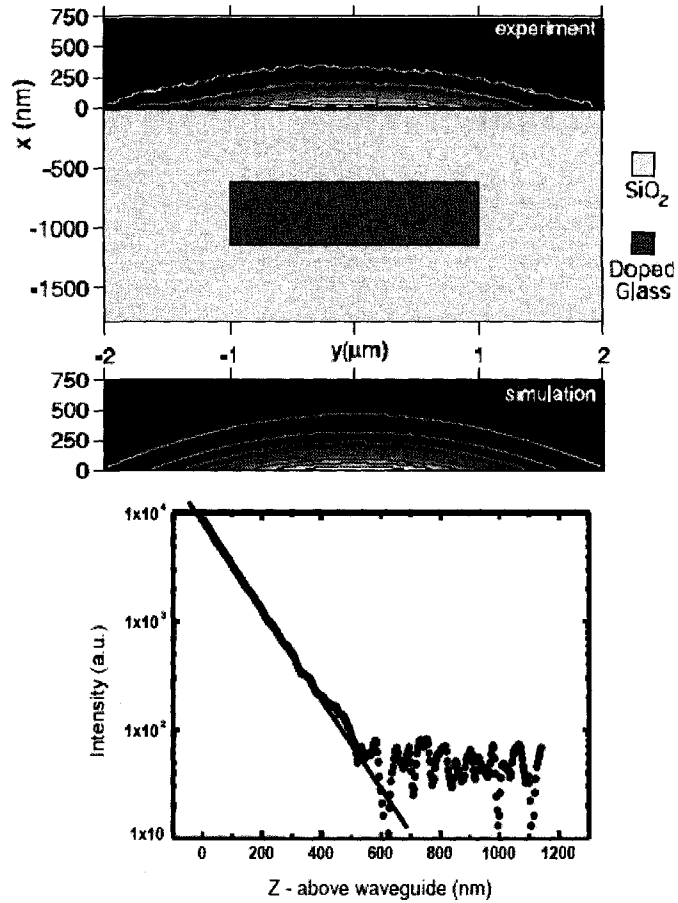


Figure 2.12: Experimental setup (reproduced from Reference 17).



(a)

(b)

Figure 2.13: (a) Measured and simulated evanescent field intensity of a channel waveguide, (b) line scan of at $y=0$, with exponential fit with intensity decay rate. (reproduced from Reference 17).

Direct measurement of multimode interference in a channel waveguide was demonstrated [17]. The observation revealed periodic transitions from a single-peak Gaussian-like optical intensity profile to a double-peak intensity profile. The sample

studied in the experiment was a 10 μm wide waveguide in a LiNbO_3 crystal. A tunable infrared diode laser was used to couple light into the waveguide. The experiment exploited a sharpened single-mode optical fiber as the NSOM probe, which was held 10 nm constantly above the waveguide surface using shear force feedback. Interestingly, fiber tips were not coated with metal in order to maximize the captured light by the NSOM tip. It was calculated that the waveguide studied supported only TM modes. NSOM imaged light intensity at various positions on the waveguide. Two 30 μm x 30 μm NSOM images were acquired at nearby positions along the waveguide, as plotted in Figure 2.14 (a) and (b). The intensity images present transitions between a Gaussian-like mode distribution with a single peak and a symmetric double-peaked mode distribution. It indicates that the mode-beating phenomenon resulted from two-mode interference in the waveguide. Considering the mismatch between optical intensity profiles of waveguide and the input fiber which couples light into the waveguide, there are probably two modes initially coupled into the waveguide. Further, the mode of the fiber has a mean field radius of 3.2 μm . This radius does not match that of the fundamental waveguide mode, whose mean field radius is calculated to be 3.5 μm . One dimensional mode calculation agrees well with the measured field intensity profiles. Figure 2.15 (a) and (b) illustrate cross sections of the both the measured and calculated light intensity profiles, each normalized to its respective maximum intensity. As the first published modal interference study, this experiment inspired the investigation of transient phenomena in an optical waveguides and established NSOM as a real time detection tool for waveguide sensing. Our following studies focused on guided mode and leaky mode interference which proved essential in optical interconnect characterization as well.

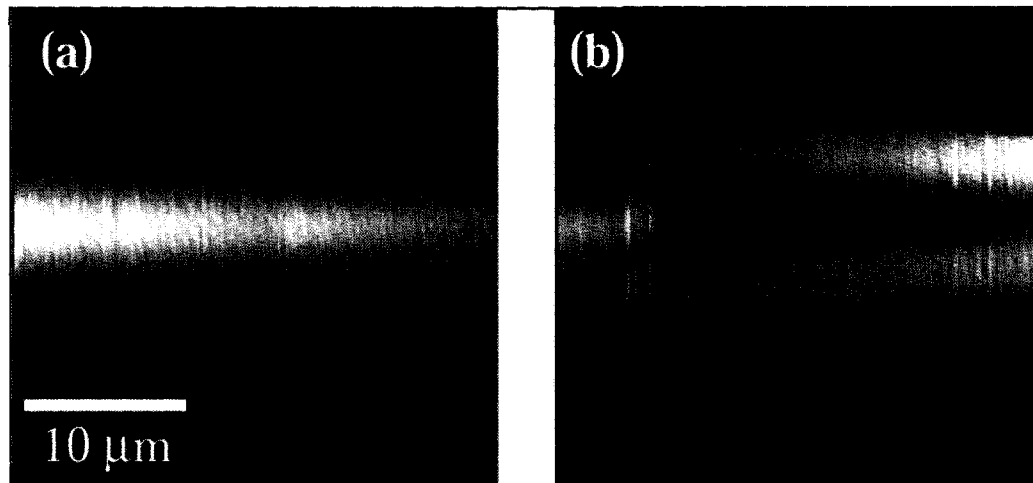


Figure 14: (a) Gaussian-like intensity profile with a single peak, (b) transition from single-peak to double-peaked distribution. (reproduced from Reference 16).

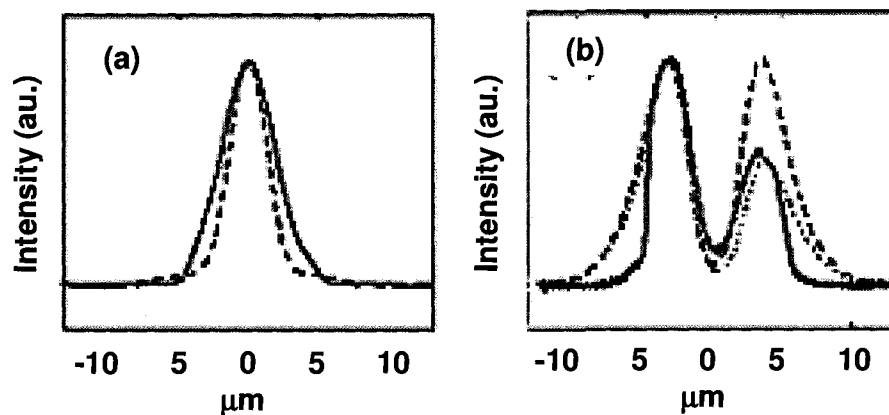


Figure 15: Normalized line scans of the light intensities, (a) single-peaked distribution, (b) double-peaked distribution. (Measured NSOM in solid curves and calculated dashed curves. Reproduced from Reference 16).

2.7 Discussion of tip effect on evanescent field

In performing a NSOM experiment, we want to know how much the effect of a NSOM tip on the evanescent field is. The researchers from Boston University experimentally demonstrated only a weak perturbation of evanescent field was observed when a NSOM tip was placed close to the waveguide core [16]. The presence of a NSOM tip in the evanescent field of the waveguide will scatter optical power from the guided modes, causing a reduction in overall transmission through the waveguide. The experimental setup utilized a photodiode to monitor the reduction in total output power at the waveguide end facet during NSOM scanning. Two different types of tips were used: uncoated tips and tips coated with ~ 100 nm of Al. In both the coated and uncoated cases, a small reduction in output power was observed. The amount of reduction was between about 0.5% and 1.2%. The metal-coated tip was observed to cause more scattering than the uncoated tip. The same research group performed multiple simulations to estimate the effect of an NSOM tip on the local field. In these simulations, the tip-to-sample spacing was varied. It was found that the penetration depths were roughly the same: $8.981 \mu\text{m}$ for the uncoated case, and $9.001 \mu\text{m}$ for the coated case. Both decay constants are close to the theoretical result when no NSOM tip is present. From the experimental and theoretical analysis, the evanescent field perturbation due to a NSOM tip is proved insignificant to comprise mode profile analysis.

2.8 Summary

In this chapter, we summarized background of integrated optical waveguides and waveguide characterization methods. Previous characterization efforts conducted by a few

research groups provide us an experimental foundation for using NSOM to analyze waveguide components, devices and systems.

References:

- [1] S. E. Miller, "Integrated Optics: An Introduction," Bell System Technical Journal, vol. 48 pp. 2059-2069, 1969.
- [2] E. G. Spencer et al., "Ion-Beam Techniques for Device Fabrication," Journal of Vacuum Science and Technology, vol. 8, pp. 52-70 1972.
- [3] K. C. Kao, R. B. Dyott, and A. W. Snyder, "Design and analysis of an optical fiber waveguide for communication," in Trunk Telecommunications by Guided Waves, Proceedings of IEEE, pp. 211-217, Sept. 1970.
- [4] D. B. Keck, P. C. Schultz, and F. Zimar, "Attenuation of multimode glass optical waveguides," Appl. Phys. Lett., vol. 21, pp. 215-217, Sept. 1972.
- [5] T. C. Rich and D. A. Pinnow, "Total optical attenuation in bulk fused silica," Appl. Phys. Lett., vol. 20, pp. 264-266, Apr. 1, 1972.
- [6] A. R. Tynes, A. D. Pearson, and D. L. Bisbee, "Loss mechanisms and measurements in clad glass fibers and bulk glass," J. Opt. Soc. Amer., vol. 61, pp. 143-153, Feb. 1971.
- [7] A. Jacobsen, N. Neuroth, and F. Reitmayer, "Absorption and scattering losses in glasses and fibers for light guidance," J. AmCeramic Soc., vol. 54, pp. 186-187, Apr. 1971.
- [8] D. Marcuse, "Higher-order loss processes and the loss penalty of multimode operation," Bell Syst. Tech. J., vol. 51, pp. 1819-1836 Oct. 1972.

- [9] D. W. Pohl, W. Denk, and M. Lanz, "Optical stethoscopy: Image recording with resolution," *Appl. Phys. Lett.*, vol. 44, no. 7, pp.651–653, 1984.
- [10] M. L. M. Balistreri, A. Driessen, J. P. Korterik, L. Kuipers, and N. F. van Hulst, "Quasi interference of perpendicularly polarized guided modes observed with a photon scanning tunneling microscope," *Opt. Lett.*, vol. 25, no. 9, pp. 637–639, 2000.
- [11] S. Bourzeix, J. M. Moison, F. Mignard, and F. Barthe, "Near-field optical imaging of light propagation in semiconductor waveguide structures," *Appl. Phys. Lett.*, vol. 73, no. 8, pp. 1035–1037, 1998.
- [12] X. Borrise, D. Jimenez, N. Barniol, F. Perez-Murano, and X. Aymerich, "Scanning near-field optical microscope for the characterization of optical integrated waveguides," *J. Lightw. Technol.*, vol. 18, no. 3, pp. 370–374, Mar. 2000.
- [13] H. E. Jackson, S. M. Lindsay, C. D. Poweleit, D. H. Naghski, G. N. De Brabander, and J. T. Boyd, "Near field measurements of optical channel waveguide structures," *Ultramicroscopy*, vol. 61, pp. 295–298, 1995.
- [14] K. Karrai and R. D. Grober, "Piezoelectric tip-sample distance control for near field optical microscopes," *Appl. Phys. Lett.*, vol. 66, no. 14, pp. 1842–1844, 1995.
- [15] S.-R. Park, J. Jeong, B.-H. O, S.-G. Lee, and E.-H. Lee, "Polarizationinsensitive design and fabrication of hybrid sol-gel arrayed waveguide gratings," *Opt. Lett.*, vol. 28, no. 6, pp. 381–383, 2003.
- [16] G. H. Vander Rhodes, B. B. Goldberg, M. S. Ünlü, S. T. Chu, W. Pan, T. Kaneko, Y. Kokobun, and B. E. Little, "Measurement of internal spatial modes and local propagation properties in optical waveguides," *Applied Physics Letters*, vol 75, pp. 2368-2370, October 1999.

- [17] Campillo, AL; Hsu, JWP; Parameswaran, KR; Fejer, MM.. "Direct imaging of multimode interference in a channel waveguide," Optics Letters, vol 28, pp. 399-401, June 2003.
- [18] <http://ultra.bu.edu/papers/lfw-97-LD-NSOM.pdf>
- [19] K. Okamoto, M. Lončar, T. Yoshie, A. Scherer, Y. Qiu and P. Gogna, "Near-field scanning optical microscopy of photonic crystal nanocavities", Applied Physics Letters, vol. 2, no. 11, pp. 1676-1678, Mar 2003.
- [20] Bahaa, et al. "Fundamentals of Photonics," Wiley Interscience, 1991
- [21] <http://www.ieee.org/organizations/pubs/newsletters/leos/feb04>
- [22] Ikuo Awai, Hidetoshi Jun-ichi kenoue Onodera, Young-kyu Choi, Masamitsu Nakajima, and Jun-ichi kenoue "Improved method of loss measurement for optical waveguides by use of a rectangular glass probe," Applied Optics, Vol(31), Apr. 1992.
- [23] Yasuyuki Okamura, Shinji Yoshinaka, and Sadahiko Yamamoto, "Measuring mode propagation losses of integrated optical waveguides: a simple method," Applied Optics, vol 22, Dec. 1983.
- [24] A. W. Snyder, "Power loss in optical fibers," Proceedings of IEEE, vol. 60, pp. 757-758, June 1972.
- [25] D. Pohl, W. Denk, and M. Lanz, "Optical stethoscopy: Image recording with optical resolution $\lambda/20$," Applied Physics Letters, Vol (44), pp. 651-653, 1984.
- [26] R. Yan, G. Yuan, R. Pownall, and K.L. Lear, "Waveguide characterization using shear force scanning optical microscopy," American Physical Society March Meeting 2007, Denver, March 5-9, 2007.

- [27] A. Lewis, M. Isaacson, A. Harootunian, and A. Muray, "Development of a 500 angstrom resolution microscope. I. Light is efficiently transmitted through $\lambda/16$ diameter apertures," Ultramicroscopy, vol 13, pp. 227-231,1984.
- [28] S. Bourzeix, J. M. Moison, F. Mignard, and F. Barthe, "Near-field optical imaging of light propagation in semiconductor waveguide structures," Applied Physics Letter, Vol(73), No. 8, pp. 1035-1037, Aug. 1998.
- [29] G. Yuan, M.D. Stephens, D.S. Dandy, K. L. Lear, "Direct imaging of transient interference in a single-mode waveguide using near-field scanning optical microscopy," IEEE Photonics Technology Letters, Volume 17(11), pp.2382 – 2384, Nov. 2005.
- [30] <http://www.olympusmicro.com/primer/techniques/nearfield/nearfieldhome.html>
- [31] www.witec.de

Chapter 3

NUMERICAL SIMULATION METHODS

In this chapter, we describe numerical methods for determining waveguide mode profiles and simulating light propagation in optical waveguide devices. In Section 3.1, we will discuss a one-dimensional mode calculation method and absorbing boundary condition. In Section 3.2, we will discuss a two-dimensional beam propagation method and transparent boundary condition. In Section 3.3, finite difference time domain (FDTD) method by directly solving the Maxwell's equations is discussed.

3.1 One-dimensional mode calculation

One-dimensional (1-D), effective-index mode calculations provide insight into the operation of waveguide devices [1]. This method is a simple and effective tool for solving waveguide mode profiles and propagation constants. In our study, this method has been exploited in determining absorption coefficients of leaky mode coupled waveguide photodetectors and effects of adlayers on evanescent-fields in a waveguide sensor.

3.1.1 Differential form of the Helmholtz equation

As a simple example, we analyze the fundamental mode of a three-layer slab waveguide illustrated in Figure 3.1. Refractive indexes of the waveguide core and upper/lower claddings are n_1 and n_2 , respectively. The requirement for a total internal reflection, $n_1 > n_2$, needs to be met. In our simulation, only TE modes are considered. The E field profiles are

governed by the Helmholtz equation.

$$\frac{d^2 E}{dx^2} + k_0^2 (n^2(x) - n_{eff}^2) E = 0 \quad (\text{Eq. 3.1})$$

The simulation window is on the x-axis and is divided into a uniform grid. The grid size is ΔX , and the total number of grid points is M . The lateral axis can be expressed as:

$$x = j\Delta X, \quad j=1,2,\dots,M \quad (\text{Eq. 3.2})$$

where ΔX is the grid point spacing.

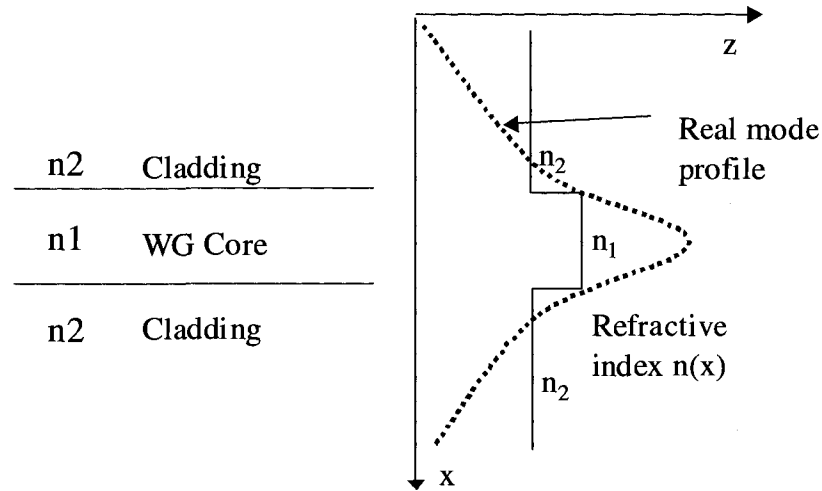


Figure 3.1: A slab waveguide's fundamental TE mode field profile.

The Helmholtz equation, (Eq.3.1), can be approximated in a finite difference form. The derivative term in this equation is expanded using the Taylor series expansion method. Higher-order terms in the expansion are neglected, since they are usually insignificant

when the grid size is chosen small enough. Then the second-order derivative can be expressed as (Eq.3.3):

$$\frac{d^2 E_j}{dx^2} \cong \frac{E_{j+1} - 2E_j + E_{j-1}}{\Delta X^2} \quad (\text{Eq. 3.3})$$

When substituting (Eq.3.3) into the (Eq.3.1), we are able to write the Helmholtz equation as:

$$\frac{E_{j+1}}{\Delta X^2} - \left(\frac{2}{\Delta X^2} - (n_j)^2\right)E_j + \frac{E_{j-1}}{\Delta X^2} = (n_{eff})^2 E_j \quad (\text{Eq. 3.4})$$

3.1.2 Absorbing boundary condition

It is obvious from (Eq.3.4) that E field strengths can be iteratively solved if we know the boundary condition for E_1 and E_M . For a confined mode, one could assume that E_1 and E_M placed at infinity and should be equal to zero, but in this case, an infinite simulation region would not be practical for simulation. However, for a finite simulation region, E_1 and E_M are unknown nonzero values although they are most likely insignificantly small. Therefore, certain assumptions and approximations are needed in order to proceed in solving Eq. 3.4 and obtaining a waveguide mode profile.

An absorbing boundary condition (ABC) is a commonly used method for waveguide simulations [2-3]. Here, an artificial, finite, absorbing layer or so-called ABC layer is placed at the two boundaries of the simulation region. In practice, the artificial layer's refractive index consists of a real part and an imaginary part. The real part of the ABC's

refractive index is assumed to be the same as that of the closest cladding layer's [1]. The imaginary part of refractive index is made position dependent and gradually, in linear or parabolic form, increased from zero at the inner boundary to a chosen value at the outer boundary, as illustrated in Figure 3.2. The value needed be chosen to ensure that the field intensity drops to an insignificant quantity, for example, 10^{-3} of peak intensity. The value also depends on the ABC layer thickness and the grid size. It is acceptable to assume that E_1 and E_M are zeros at the outer boundary. The addition of ABC layers and assigned zero value of E_1 and E_M do not considerably affect the field profile in the simulation region which is between the ABC regions.

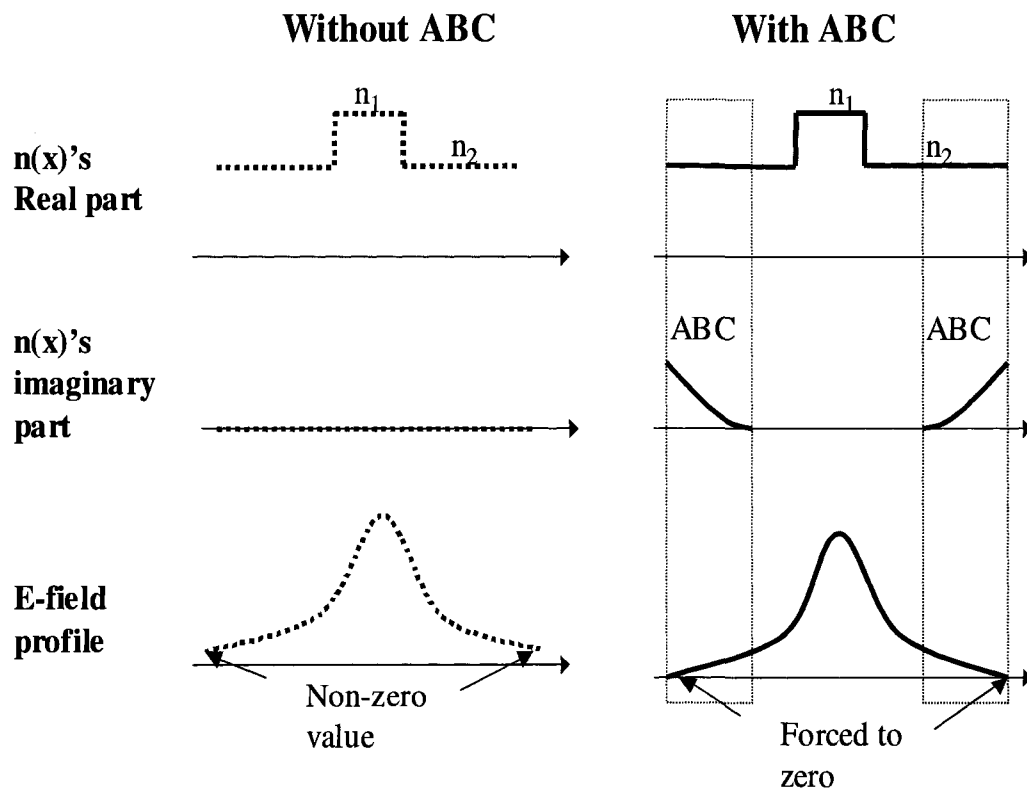


Figure 3.2: Implementation of an ABC layer

With ABC layers and zero valued field intensities at boundaries, one is able to iteratively solve the field profile using (Eq.3.4). Figure 3.3 illustrates the simulation region with ABC layers. The method is to write (Eq.3.4) in a matrix formation as (Eq. 3.5). E field intensity profiles of waveguide modes are eigen-modes of this matrix equation. Eigen-values of this equation are equal to the squares of the effective indexes.

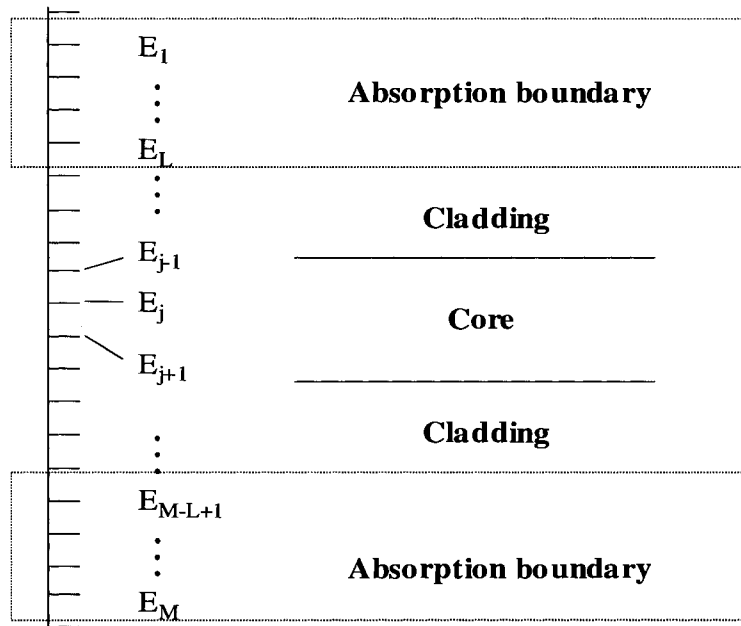


Figure 3.3: Simulation window and ABC layers.

$$\begin{array}{c}
 \left[\begin{array}{ccc}
 n_1^2 - \frac{2}{\Delta X^2} & \frac{1}{\Delta X^2} & \\
 \dots & \dots & \\
 \frac{1}{\Delta X^2} & n_L^2 - \frac{2}{\Delta X^2} & \frac{1}{\Delta X^2} \\
 \frac{1}{\Delta X^2} & n_{L+1}^2 - \frac{2}{\Delta X^2} & \frac{1}{\Delta X^2} \\
 \dots & \dots & \dots \\
 \dots & \dots & \dots \\
 \frac{1}{\Delta X^2} & n_{M-L}^2 - \frac{2}{\Delta X^2} & \frac{1}{\Delta X^2} \\
 \frac{1}{\Delta X^2} & n_{M-L+1}^2 - \frac{2}{\Delta X^2} & \frac{1}{\Delta X^2} \\
 \dots & \dots & \dots \\
 \frac{1}{\Delta X^2} & n_M^2 - \frac{2}{\Delta X^2} & \\
 \dots & \dots &
 \end{array} \right]
 \end{array}$$

$$\begin{array}{c}
 \left[\begin{array}{c}
 E_1 \\
 E_2 \\
 \vdots \\
 E_j \\
 \vdots \\
 E_M
 \end{array} \right] = n_{eff}^2 \left[\begin{array}{c}
 E_1 \\
 E_2 \\
 \vdots \\
 E_j \\
 \vdots \\
 E_M
 \end{array} \right]
 \end{array}$$

(Eq. 3.5)

3.1.3 Modal calculation using ABC layers

1-D modal calculation is used as a fast and reliable means to simulate intensity profiles. For example, this method can reveal the field difference due to a small change in the refractive index, as illustrated in Figure 3.4. In Waveguide 1, the core is made of 100 nm SiN_x (n=1.8) with a 900 nm upper cladding of air layer (n=1) and a 2000 nm lower cladding of SiO₂ layer (n=1.45). The simulation region is 4 μm thick along plus two additional 500 nm ABC layers placed at the two boundaries. Waveguide 2 preserves all the layers in Waveguide 1 and has an additional minimal 100 nm thick biological adlayer (n=1.45) on the upper surface of the core. The simulation grid size is chosen to be 0.01 μm and 401 grid points are chosen for the entire simulation region corresponding to a ΔX=10nm. The imaginary refractive index linearly increases from zero to 0.1 in the ABC layers.

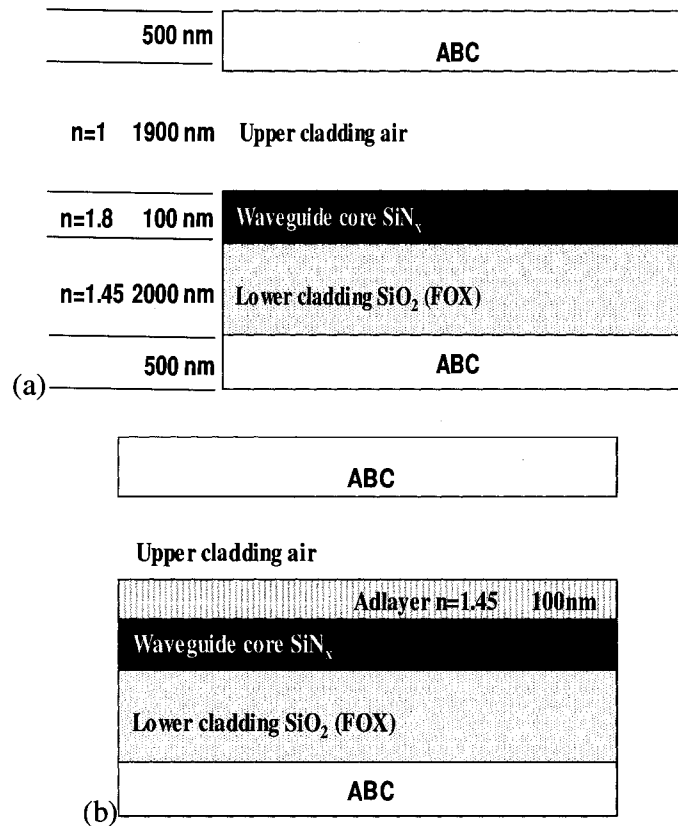


Figure 3.4: Waveguide structures: (a) Without adlayer and (b) With adlayer.

Figure 3.5 plots the fundamental mode profiles for Waveguide 1 (red) and Waveguide 2 (blue). In Waveguide 1, the evanescent field tails out of the core deep into the lower cladding region. The penetration depth is approximately 500 nm. That indicates that most of the optical power is confined in the claddings due to a thin waveguide core. In comparison, adding the 100 nm high refractive index layer changes the intensity profile significantly. The new penetration depth is approximately 200 nm, which is less than half of the previous case. Light power is mostly confined in the core region. This observation shows promise for thin film sensing, since that the evanescent field profile depends on the presence of the adlayer on waveguide surface. Thus local change in the refractive index is manifested in the evanescent field intensity modulation in the lower cladding. There is a

notable effect of the ABC on the evanescent field tail in the lower cladding without the adlayer that the field strength falls on a non-exponential curve. This is due to the non-zero imaginary part of the refractive index in the ABC regions.

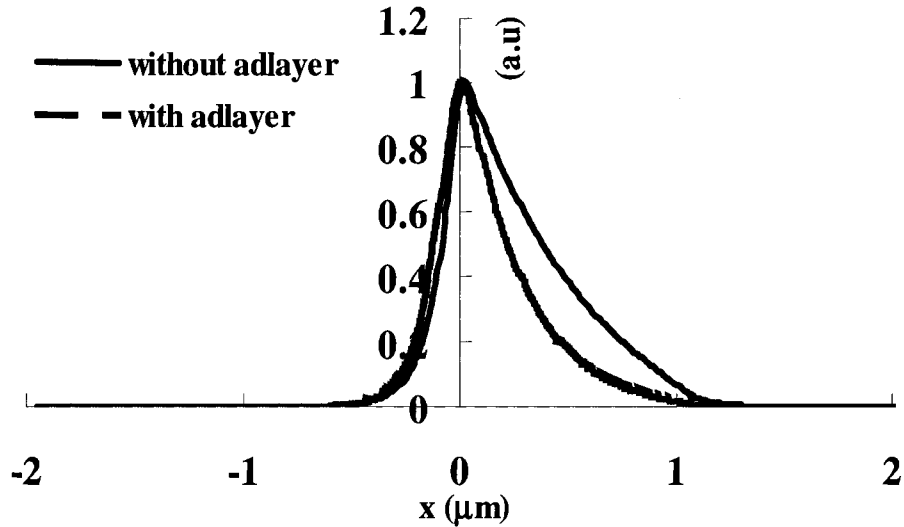


Figure 3.5: Field profiles for the waveguide with adlayer (red) and without adlayer (blue).

3.2 Beam propagation method

Besides the one dimensional modal calculation method, the beam propagation method (BPM) is a powerful modeling tool to simulate light propagation along an optical waveguide. Different types of BPM have been developed using scalar, semi-vectorial or full-vector models. For a slab waveguide, the scalar BPM that assumes a slowly varying field profile envelope, is sufficient for modeling [3].

3.2.1 Finite difference representation

We start with the Helmholtz equation in the second order derivative form for both x and

z components, as expressed in (Eq. 3.6).

$$\frac{d^2 E(x, z)}{dx^2} + \frac{d^2 E(x, z)}{dz^2} + k_0^2 n^2(x, z) E(x, z) = 0 \quad (\text{Eq. 3.6})$$

A slowly varying E field profile can be expressed as in (Eq.3.7), where the varying part is in the exponential form:

$$E(x, z) = E(x) \times e^{(-jn_{\text{eff}}k_0z)} \quad (\text{Eq. 3.7})$$

Substituting (Eq. 3.7) into (Eq. 3.6), we are able to rewrite the Helmholtz equations as:

$$2jn_{\text{eff}}k_0 \frac{\partial E}{\partial z} - \frac{\partial^2 E}{\partial z^2} = \frac{\partial^2 E}{\partial x^2} + k_0^2 (n^2(x) - n_{\text{eff}}^2) E \quad (\text{Eq. 3.8})$$

The second order term for the z components $\frac{\partial^2 E}{\partial z^2}$ is small enough to neglect. The first order terms in (Eq. 3.7) can be written as:

$$\frac{\partial E}{\partial z} = \frac{E_j^{i+1} - E_j^i}{\Delta Z} \quad (\text{Eq. 3.9})$$

The second order term for the x components is rewritten as:

$$\frac{\partial^2 E}{\partial x^2} = \frac{E_{j+1}^i - 2E_j^i + E_{j-1}^i}{(\Delta X)^2} \quad (\text{Eq. 3.10})$$

When putting together (Eq. 3.9) and (Eq. 3.10) with (Eq. 3.8), we get the Helmholtz equation in a difference form where uniform grid sizes in both x and z components,

$\alpha=1/(\Delta Z)^2=1/(\Delta X)^2$, are used.

$$2jn_{eff}k_0 \frac{E_j^{i+1} - E_j^i}{\Delta Z} = (E_j^{i+1} - 2E_j^i + E_j^{i-1})\alpha + (E_{j+1}^i - 2E_j^i + E_{j-1}^i)\alpha + k_0^2(n^2(x) - n_{eff}^2)E_j^i$$

(Eq. 3.11)

3.2.2 Transparent boundary condition

Similar to the 1-D modal calculation method, we need to apply a certain boundary condition when using the beam propagation method (BPM). The most commonly used boundary condition for BPM is the transparent boundary condition (TBC) [5]. TBC layers effectively reduce the reflections at the outer boundaries.

The method is based on the assumption that any traveling light waves incident on the boundaries will leave the simulation region and never bounce back. Fig 3.6 shows the simulation region implemented with TBC. At the two boundaries of the simulation region, the field intensities of E_0 (at $0\Delta X$) and E_{M+1} (at $(M+1)\Delta X$) at all slices along the z-axis can be approximated in terms of E_1 (at $1\Delta X$) and E_M (at $M\Delta X$). The left-traveling wave's field intensity at $1\Delta X$ is $E_1 = E \exp(jk_x x_1)$, so E_0 should be $E_1 \exp(-jk_x \Delta X)$. Here, k_x is the x component of the wavevector. Similarly, E_{M+1} should be $E_M \exp(-jk_x \Delta X)$.

Assume field profiles E^{i-1} at $(i-1)\Delta Z$ and E^i at $i\Delta Z$ are known. The field profile at $z=(i+1)\Delta Z$, E^{i+1} , can be mapped from E^{i-1} and E^i using (Eq. 3.11).

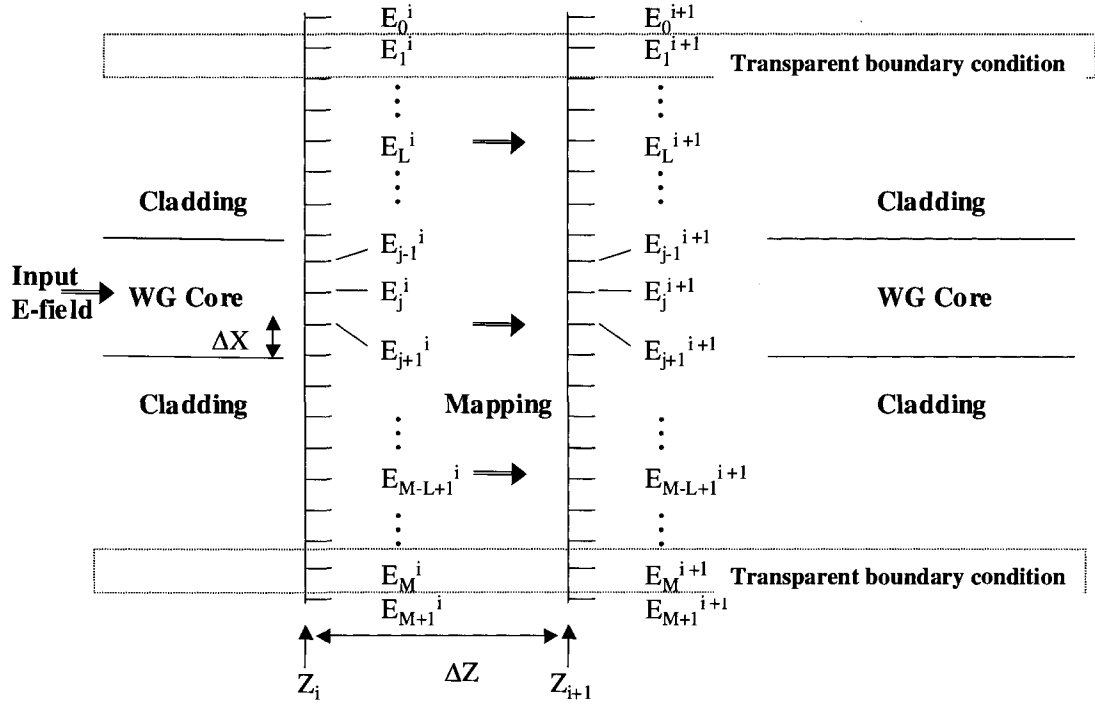


Figure 3.6: Simulation region implemented with TBC.

Following the steps in [5], we denote the matrix elements in the simulation region except for the rows in the TBC layers.

$$A_j^{i+1} = -\alpha$$

$$B_j^{i+1} = 2\alpha + \frac{4j\beta}{\Delta Z} - k_0^2 [(n_j^{i+1})^2 - n_{eff}^2]$$

$$C_j^{i+1} = -\alpha$$

$$D_j^i = \alpha E_{j-1}^i + [-2\alpha + \frac{4j\beta}{\Delta Z} + k_0^2 [(n_j^i)^2 - n_{eff}^2]] E_j^i + \alpha E_{j+1}^i \quad (\text{Eq. 3.12})$$

The rows in the TBC layers can be written as:

$$\begin{aligned}
B_1^{j+1} &= \alpha(2-r) + \frac{4j\beta}{\Delta Z} - k_0^2[(n_1^{i+1})^2 - n_{eff}^2] \\
B_M^{j+1} &= \alpha(2-r) + \frac{4j\beta}{\Delta Z} - k_0^2[(n_M^{i+1})^2 - n_{eff}^2] \\
D_1^i &= \alpha r E_1^i + [-2\alpha + \frac{4j\beta}{\Delta Z} + k_0^2[(n_1^i)^2 - n_{eff}^2]] E_1^i + \alpha E_2^i \\
D_M^i &= \alpha E_M^i + [-\alpha r + \frac{4j\beta}{\Delta Z} + k_0^2[(n_M^i)^2 - n_{eff}^2]] E_M^i \\
\gamma &= \exp(-jk_x \Delta X)
\end{aligned} \tag{Eq. 3.13}$$

At last, substituting (Eq. 3.12) and (Eq. 3.13) into (Eq. 3.11), one writes an eigen-mode matrix form as (Eq. 3.14). Field intensity profiles at all slices along z axis can be iteratively solved.

$$\begin{array}{c}
\boxed{B_1^{l+1} \quad C_1^{l+1}} \leftarrow \text{TBC} \\
A_2^{l+1} \quad B_2^{l+1} \quad C_2^{l+1} \\
\quad \dots \quad \dots \quad \dots \\
\quad \quad \quad \dots \quad \dots \quad \dots \\
\quad \quad \quad \quad \quad A_{j-1}^{l+1} \quad B_{j-1}^{l+1} \quad C_{j-1}^{l+1} \\
\quad \quad \quad \quad \quad A_j^{l+1} \quad B_j^{l+1} \quad C_j^{l+1} \\
\quad \quad \quad \quad \quad \quad \dots \quad \dots \quad \dots \\
\quad \quad \quad \quad \quad \quad \quad \dots \quad \dots \quad \dots \\
\quad \quad \quad \quad \quad \quad \quad \quad \dots \quad \dots \quad \dots \\
\quad A_{M-1}^{l+1} \quad B_{M-1}^{l+1} \quad C_{M-1}^{l+1} \\
\quad A_M^{l+1} \quad B_M^{l+1} \rightarrow \text{TBC}
\end{array}
\begin{array}{c}
\left[\begin{array}{c} E_1^{l+1} \\ E_2^{l+1} \\ \cdot \\ \cdot \\ E_j^{l+1} \\ \cdot \\ \cdot \\ E_M^{l+1} \end{array} \right] = \left[\begin{array}{c} D_1^l \\ D_2^l \\ \cdot \\ \cdot \\ D_j^l \\ \cdot \\ \cdot \\ D_M^l \end{array} \right]
\end{array}$$

(Eq. 3.14)

3.2.3 Typical BPM simulations on step changes

As an example, we use the commercial BPM code (BEAMPROP/FULLWAVE v4.6) from RSoft Inc. to simulate light propagation along a waveguide structure with a step change of an adlayer or multiple adlayers as shown in Figure 3.7. The simulation region's thickness is 4 μm . The waveguide core is made of 100 nm SiN_x ($n=1.8$) with 1900 nm air upper cladding ($n=1$) and 2000 nm SiO_2 lower cladding ($n=1.45$). A transparent boundary condition layer was appended to each boundary of the simulation region. A 50 nm thick SiN_x adlayer ($n=1.8$) is placed on the upper surface of the waveguide core starting from $z=40 \mu\text{m}$, thus to form a step change in the refractive index profile and to cause the field perturbations. The total simulation length is 100 μm .

Light is input into the simulation region from left to right. The incident modal profile is assumed to be the fundamental TE mode. Figure 3.8 shows the E field response to the adlayer as a result of BPM simulation. Here, the field profile is relatively stable along the waveguide before the adlayer region. Strong perturbations are found in the adlayer region.

This observation is vital because that it reveals the existence of a transient leaky waveguide mode superimposed on a guided mode. The field oscillation is due to the mode interference between a guided mode and a leaky mode. However, the leaky mode attenuates along the light propagation direction at a fast decay rate. When the leaky mode intensity drops to an insignificant level, we assert that all the power is confined in the guided mode. Usually the leaky mode drops to half over a 30 to 100 μm distance.

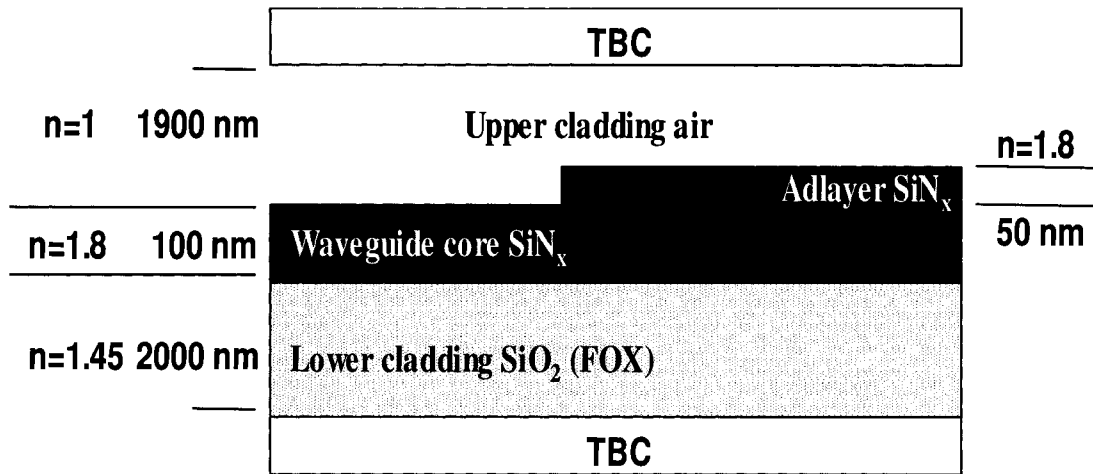


Figure 3.7: A waveguide with step adlayer.

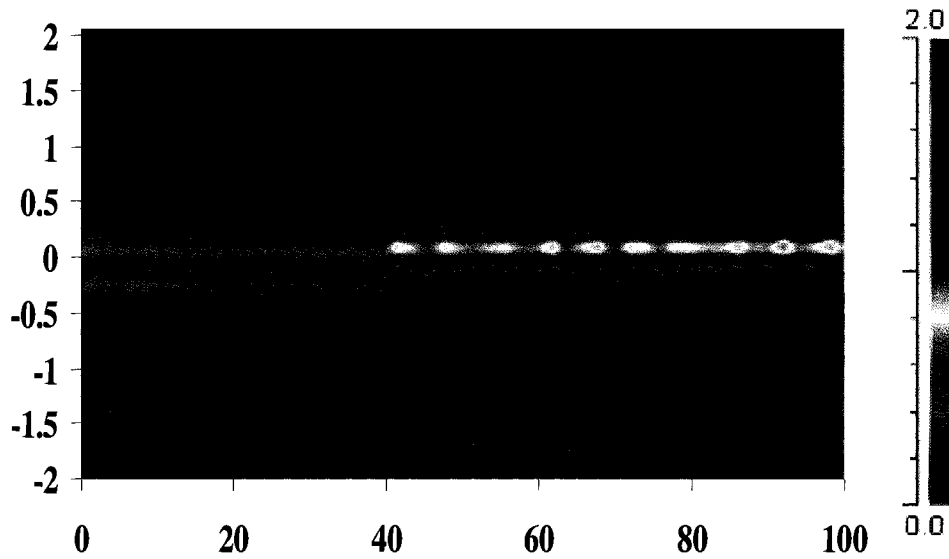


Figure 3.8: False color plot of the field response to an adlayer.

3.3 Finite difference time domain method

The finite difference time domain (FDTD) method is a numerical simulation method that was originally used to simulate microwave propagation in a radar system [5]. The advantage of this method is that it yields very rigorous solutions, not restricted to simplified or approximated conditions, to Maxwell's equation [3]. The FDTD algorithm iteratively solves the E and H fields at discrete time steps. Similar to BPM, the H and E fields at different time frame are interactively solved in a two-dimensional matrix form.

3.3.1 Algorithm

We start with the normalized Maxwell's equations:

$$\begin{aligned}\frac{\partial \mathbf{D}}{\partial t} &= \nabla \times \mathbf{H}, & \mathbf{D} &= \epsilon_r \mathbf{E} \\ \frac{\partial \mathbf{H}}{\partial t} &= -\frac{1}{\mu_r} \nabla \times \mathbf{E}\end{aligned}\tag{Eq. 3.14}$$

The Maxwell's equations can be rewritten as following:

$$\begin{aligned}\frac{H_z^{n+1}(i, j) - H_z^n(i, j)}{\Delta t} &= c \frac{E_y^{n+1}(i, j) - E_y^n(i-1, j)}{\Delta x} - c \frac{E_x^{n+1}(i, j+1) - E_x^n(i, j)}{\Delta y} \\ \frac{D_x^{n+1}(i, j+1) - D_x^n(i, j+1)}{\Delta t} &= -c \frac{H_x^{n+1}(i, j+1) - H_x^{n+1}(i, j)}{\Delta y} \\ \frac{D_y^{n+1}(i+1, j) - D_y^n(i+1, j)}{\Delta t} &= c \frac{H_y^{n+1}(i+1, j) - H_y^{n+1}(i, j)}{\Delta x}\end{aligned}\tag{Eq. 3.15}$$

Assume that the initial H field distribution at time $t=0.\Delta T$ is known. The H fields surrounding the position (i, j) are $H_z^n(i, j-1)$, $H_z^n(i, j+1)$, $H_z^n(i-1, j)$, and $H_z^n(i+1, j)$. The E field at position (i, j) , $E_z^n(i, j)$, can be derived using (Eq. 3.15), as well as E fields at general positions other than $(i.\Delta X, j.\Delta T)$, only if they are at the same time frame $t=n.\Delta T$ illustrated

in Figure 3.9. Reciprocally, the calculated E fields are used to solve the H field at the next time frame, $t=(n+1).\Delta T$.

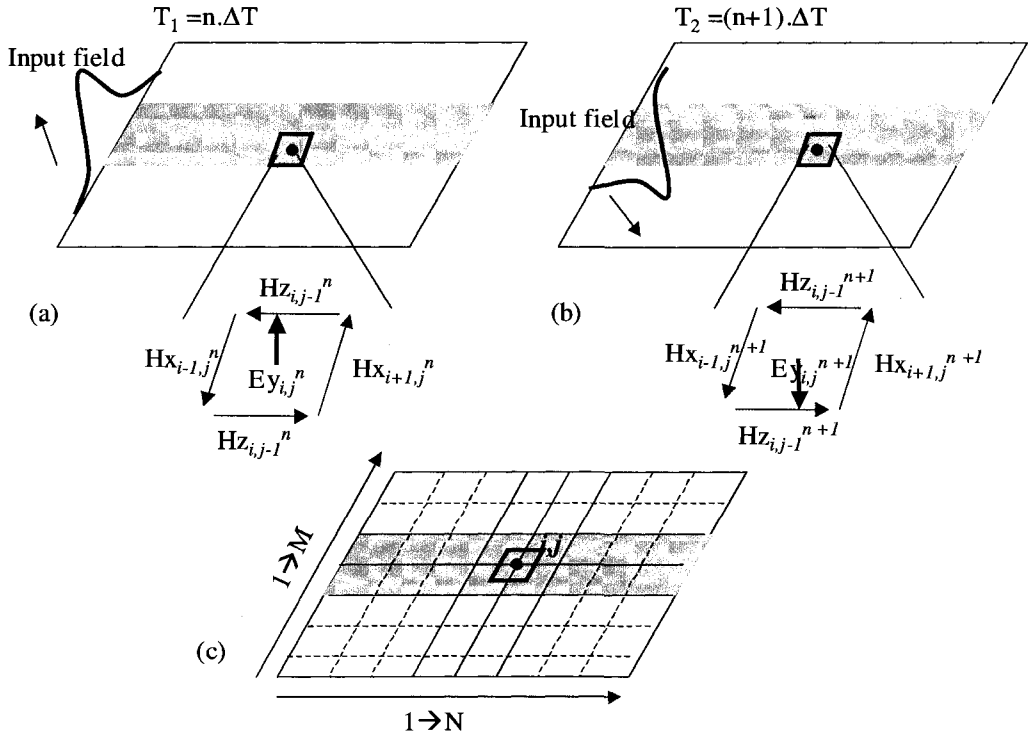


Figure 3.9: Schematic of the FDTD algorithm.

The most used boundary condition for FDTD simulations is called the perfectly matched layer (PML) method. This provides a reflectionless interface between the region of interest and the PML layers at all incident angles. The layers themselves are lossy, so that for a small distance into the layers the wave is significantly attenuated. For conciseness, we will not discuss this method in this dissertation. Interested readers can find relevant discussion in reference [3].

3.3.2 FDTD simulations on complex waveguide structures

Without applying any restrictions or approximations, FDTD method is widely used in simulation of much more complex waveguide structures other than straight waveguides, such as waveguide bends. In our study, we use waveguide bends to guide light into a desired direction. The simulations are done using both commercial FDTD code from Rsoft and a customized program written in MATLAB. A sample study of a waveguide bend is shown in Figure 3.10. Here, the waveguide core is made of $0.5 \mu\text{m}$ wide SiN_x with an effective refractive index ranging from 1.5 to 1.7 with SiO_2 ($n=1.45$) serving as claddings. The bending radius is $25 \mu\text{m}$, as shown in Figure 3.10. Two cases are simulated with the refractive index of the waveguide core chosen to be $n=1.7$ and $n=1.5$ for case a and case b respectively.

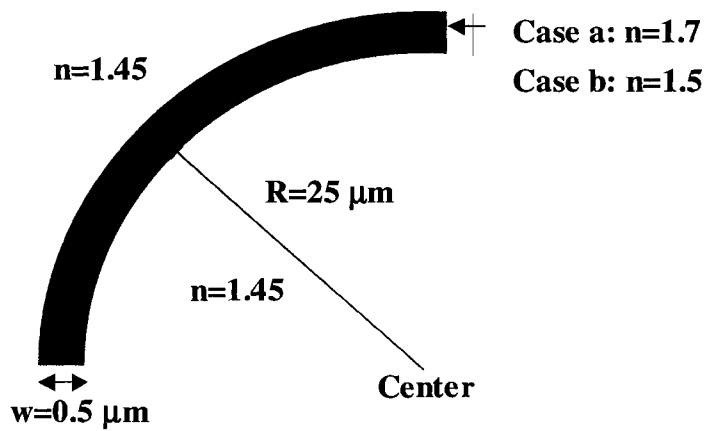


Figure 3.10: Waveguide bend with $25 \mu\text{m}$ radius.

Figure 3.11 shows the simulation results for both cases. A slight optical loss is found for the waveguide bend with high refractive index of waveguide core, which indicates a tight light confinement. In contrast, due to a lower optical confinement, the second waveguide bend suffers higher optical loss.

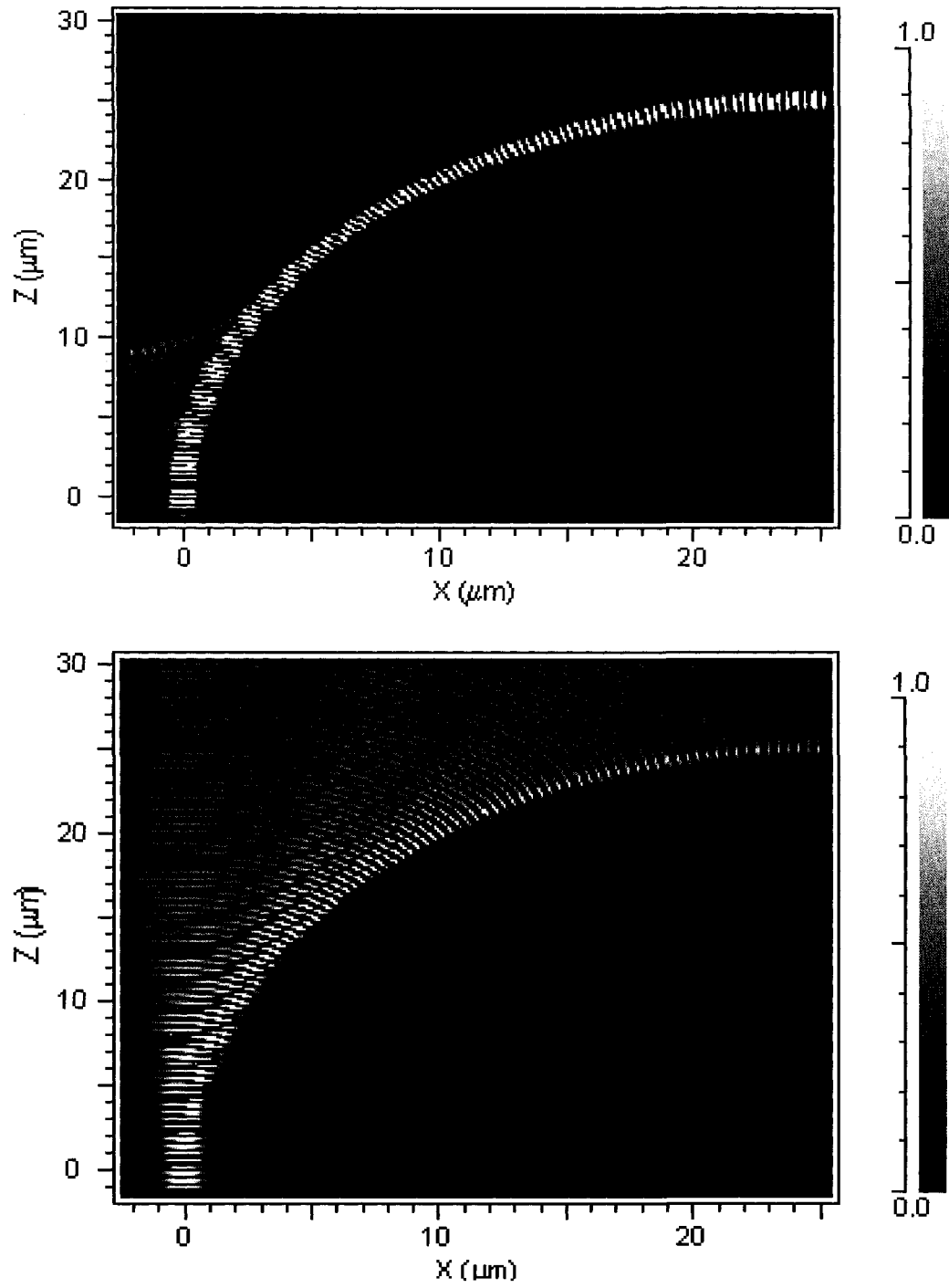


Figure 3.11: Gray scale intensity plot of the E field in a waveguide bend with (a) high optical confinement ($n_{\text{core}}=1.7$), (b) low optical confinement ($n_{\text{core}}=1.5$).

3.4 Summary

In this chapter, we have discussed three different numerical simulation methods. All methods are proven useful in the aspects of their applications. We also discussed boundary conditions associated to the above simulation methods. The better understanding of numerical simulation methods enable us optimize waveguide design and fabrications and interpret experimental observations, which will be address in following chapters.

Reference:

- [1] L. A. Coldren and S. W. Corzine, "Diode Lasers and Photonic Integrated Circuits". John Willey & Sons, Inc, 1995. Vukovic, "Fourier Transformation Analysis of Optoelectronic Components and Circuits", PhD thesis, Nottingham University, April 1999.
- [2] P. E. Lagasse, R. Baets, "Application of propagating beam methods to electromagnetic and acoustic wave propagation problems: a review", *RadioSci.*, 22, pp.1225-1233, 1987.
- [3] Kenji Kawano and Tsutomu Kitoh, "Introduction to Optical Waveguide Analysis: Solving Maxwell's Equation and the Schrodinger Equation". Wiley-IEEE, 2001.
- [4] G. R. Hadley, "Transparent boundary condition for beam propagation methods", *Opt. Lett.*, 16, pp.624-626, 1991.
- [5] Dennis M. Sullivan, "Electromagnetic Simulation Using the FDTD Method". Wiley-IEEE Press, 2000. J.-P. Berrenger, "A perfectly matched layer for the absorption of electromagnetic waves", *J. Comput. Phys.*, vol. 114, pp. 185-200, 1994

Chapter 4

NOVEL INTEGRATED OPTICAL WAVEGUIDE DEVICES

In previous chapters, we have reviewed the fundamentals of optical waveguides, and related experimental and numerical methods. In this chapter, we will discuss two new integrated optical waveguide devices, a local evanescent-field array coupled (LEAC) sensor and an on-chip optical interconnect system. For both devices, we describe novel leaky-mode waveguide coupled and evanescent field coupled photodetectors. Before that, we review some previous optical waveguide devices, such as SPR and ATR sensors, etc.

4.1 Review of integrated optical waveguide sensors

4.1.1 Surface plasmon resonance

Surface plasmon resonance (SPR) is currently a widely used method to detect ultra thin biological films on a metal or dielectric surface. SPR was first discovered in 1902 by R.M Wood [1]. However, its first practical applications dated as late as in 1980s when several groups of researcher found SPR's high sensitivity in detecting thin films. B. Liedberg's research on surface-plasmon resonance for gas detection and biosensing was proven a milestone in SPR sensing [2]. UK researchers, P.B.Daniels et al., first reported immunochemical sensing using surface plasmon resonance in 1988 [3]. They experimentally tested the avidin-biotin binding pair and α -feto protein antibody-antigen thin films. Results demonstrated a concentration-dependent response at around a

nanomolar with a response time of a few minutes. In following years, a layer thickness of about 5 nm was detected by Piehler, et al [4]; four-channel SPR multiple sensing was reported by Berger, et al. [5]; an acoustic wave modulating the input wavelength was reported by Caruso [6]; and phase imaging was reported by Notcovich, et al[7].

As reported in the above articles, SPR can be used to monitor the local refractive index change during adsorption of cells and proteins onto the metal surface. From the shift of resonant angle, parameters such as mass or thickness of adsorbed layers can be determined based on knowledge of the refractive index and mass density of the target. The surface-plasmon is a coupled, localized transverse magnetic (TM) electromagnetic field/charge-density oscillation, which may propagate along an interface between two media only at a specific resonant condition. SPR is currently regarded as a promising optical system and technique for detection, imaging, and visualization of minimal changes, of the order of 10^{-6} in refractive index, in the near field. Figure 4.1 shows the schematic of a SPR setup where the metal film is regarded as a waveguide component in an SPR system. The core sensing part includes the glass prism, metal coating and bio-adalyer as illustrated in Figure 4.2. When sensing biotin-avidin binding, SPR responds to the binding concentration increase as the avidin solution exposure time goes on, as illustrated in Fig. 4.3.

The disadvantages of SPR technology arise from its bulky setup that utilizes a metal-coated prism as the sensing platform. With a few exceptions, one setup is limited to detect one type of immunoassay interaction at a time. This technology exploits optical-electrical phenomenon arising from the interaction of light with a thin metal film.

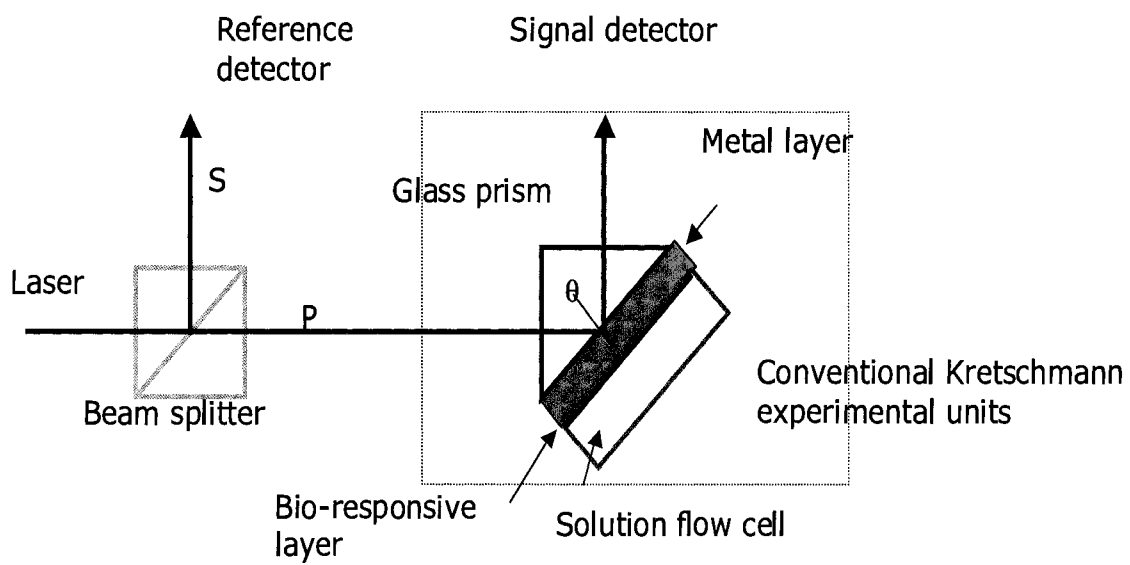


Figure 4.1: Surface plasmon resonance (SPR) setup.

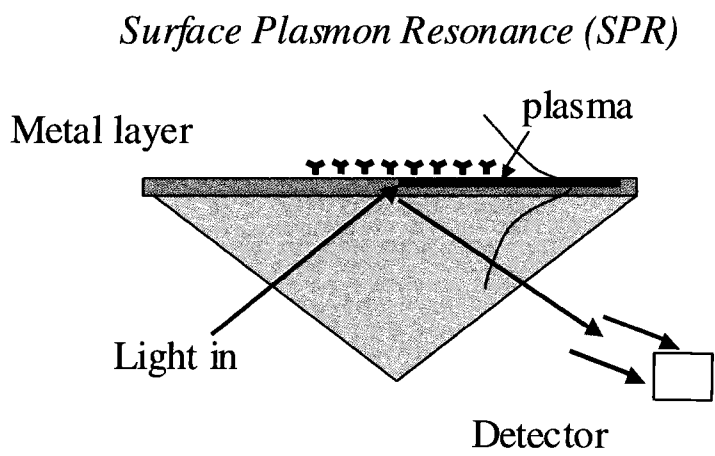


Figure 4.2: The sensing part of a SPR setup.

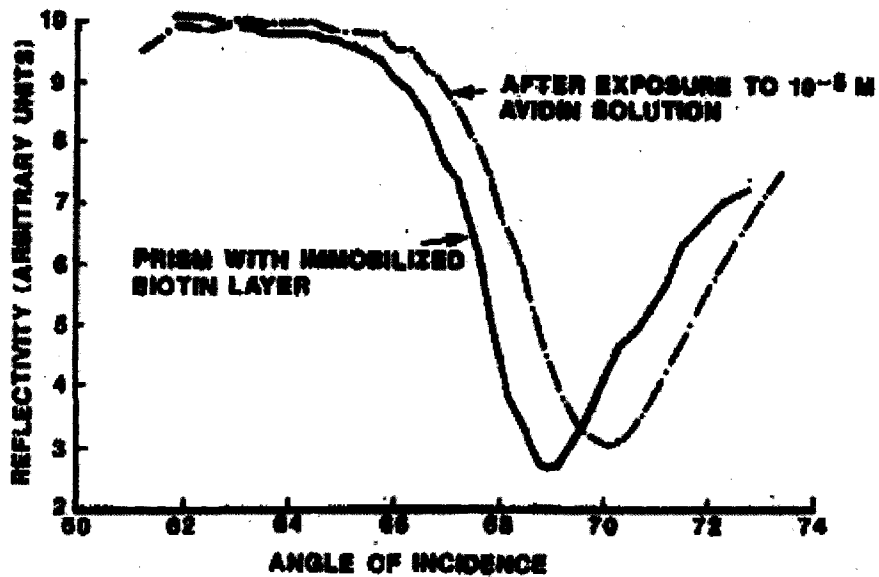


Figure 4.3: Resonant angle shifts as the exposure time of an avidin solution increases. (reproduced from Reference 2)

4. 1.2 Attenuated total reflection (ATR) spectroscopy

Attenuated total reflection (ATR) spectroscopy is used for characterization of bulk materials or thick films [8]. Figure 4.4 shows the schematic of an ATR setup. The sample to be sensed is attached to the upper surface of the waveguide in the sensing region. Light is guided into this region via total internal reflections. This internal reflectance creates an evanescent wave that extends beyond the surface of the waveguide into the sample. The sample absorbs light power, thus the evanescent wave will be attenuated. The attenuated light can be monitored at the end facet of the waveguide by visible or infrared photodiodes.

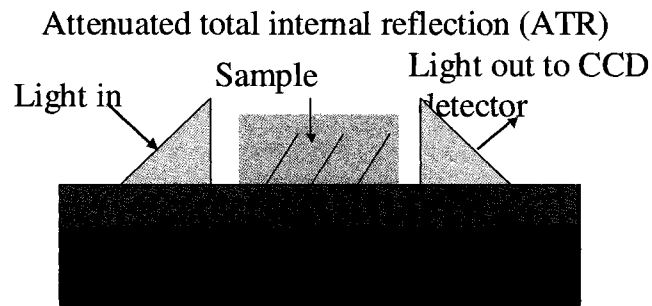


Figure 4.4: Attenuated total reflection (ATR) setup.

The disadvantages of ATR technology include the following issues: First, the setup is relatively bulky due to non-local sensing mechanism. Second, in most cases, only one sample can be measured at a time.

4. 1.3 Total internal reflection fluorescence (TIRF) microscopy

The operation of a TIRF system is similar to that of ATR technology. TIRF is used to measure a thin region of sample, usually less than 200 nm [9]. Figure 4.5 shows the schematic of a TIRF setup.

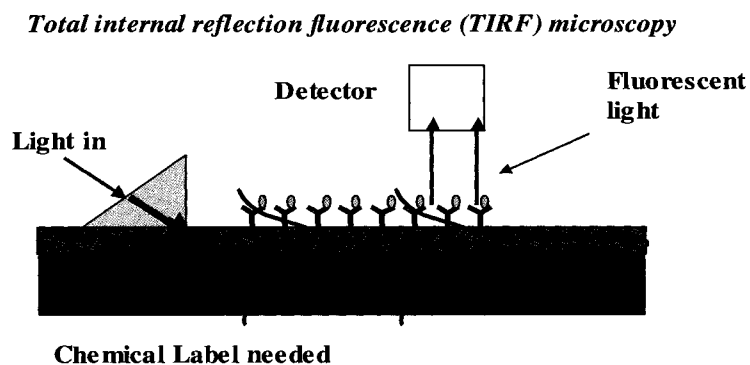


Figure 4.5: Total internal reflection fluorescence (TIRF) setup.

In TIRF measurements, a dielectric waveguide is used to generate an evanescent wave that selectively illuminates and excites fluorescent-labeled samples in contact with the waveguide's upper surface. A fluorescent detector is placed above the sensing region that collects the light emanating from the fluorescent-labeled samples. The fluorescent labels absorb the energy from the evanescent field that decreases the total transmission of the waveguide. Therefore, the decrease in transmitted light can be detected at the end facet of the waveguide by visible or infrared photodiodes.

4.2 Local evanescent field array coupled (LEAC) waveguide sensors

4.2.1 Background

As stated in Chapter 1, point-of-care clinical diagnostics, food safety, environmental monitoring, and biosecurity applications continue motivating simultaneous, reagentless immunobiosensing of multiple pathogens or other protein based species using a compact sensor [10,11]. High-density sensing arrays enhance redundancy, miniaturization, and multiplexing.

Conventional optical waveguide sensor techniques such as attenuated total reflection, Raman scattering, and fluorescence spectrometry, have been well investigated and employed for biosensor applications. While these techniques have the advantages such as low optical loss and high sensitivity, the limited number of analytes that can be simultaneously detected using a single waveguide, as well as large inaccuracy when sensing ultra-small quantities, restricts their applications. The LEAC sensor is being developed for the purpose of sensing quantities from 10^{-10} to 10^{-12} mol [10]. This novel

sensor is also designed for needs of detecting small volumes of multiple analytes while possessing comparable sensitivity to conventional techniques for various medical, biological and environmental situations.

4.2.2 Novel sensor design

A concept for a local evanescent array coupled waveguide biosensor has been proposed. The sensor mechanism relies on formation of a protein based adlayer via specific binding of an analyte target to one of several localized patches of immobilized biological molecule probes to modify the waveguide cross-section and thus the optical field under the patch. A buried array of evanescently coupled photodetector elements along the length of the waveguide, each opposite a region of specific antibody type, locally sense the modification in the evanescent field due to adlayers of bound analytes. The local, evanescent, array coupled (LEAC) biosensor concept allows tens to thousands of separate molecular probes to be monitored along a single waveguide due to the local detection mechanism. For example, to get a thousand sensors on a 1 cm long waveguide, sensing regions need to be 10 μm including spacing between distinct sensors. 9.5 μm long photodetectors with 0.5 μm long spacings were patterned for this specific design. Sensing of biomolecules such as proteins, pathogenic viruses, and bacteria is possible with this device. High-density detector arrays also allow for differential signal detection, redundancy, and miniaturization. Additionally, potential compatibility with well-established silicon and silicon-on-insulator CMOS technology allows for low cost manufacturing and integrated signal processing electronics.

Figure 4.6 illustrates the schematic of a LEAC sensor. Bio-adlayers binding on a single-mode optical waveguide effectively increase the thickness of the core layer, thus decreasing the evanescent field tail absorbed by the underlying detector. The solid curves illustrate the waveguide mode profiles at different positions along the light propagation direction. An array of detector elements along the length of the waveguide, each opposite a region of specific antibody type, can sense modulations of evanescent field.

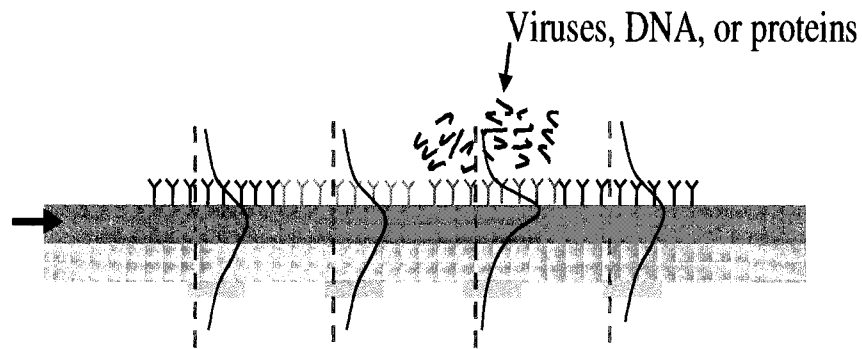


Figure 4.6: Concept of a LEAC sensor

4.2.3 Advantages of LEAC sensors

The LEAC sensors have advantages over current optical waveguide sensor technologies in several aspects. Although both LEAC sensors and SPR sensors rely on refractive index changes, LEAC sensors could be implemented much more compactly than SPR sensors. ATR sensors rely on either optical absorption in the adlayers. Absorption detectors compare input and output power, which requires very accurate measurements on the input power. Without knowledge of the absolute quantity of input light power, approximations cannot be avoided and therefore increase uncertainty level. Raman or fluorescence sensors operate in photon emission modes and produce weak optical signals from adlayer-localized binding events. Similar to absorption mode, a lack

of accurate knowledge of emission efficiencies unavoidably introduces errors in the system and weaken detection sensitivity.

Fortunately, the LEAC sensor approach relies on neither absorption nor indirect optical emission processes. In the LEAC sensor, only changes in the distribution of the local optical field are used for detection. Accurate knowledge of exact input power level in the waveguide is not required. Therefore, this detection mode is insensitive to variation in coupling efficiency. Only relative changes in evanescent field intensity are to be quantified. On the other hand, the LEAC design avoids the use of fluorescent tags or reagents. This new type of sensor preserves the advantages of optical immunoassay biosensing specificity without the need to physically or chemically modify the analyte, e.g. by adding fluorescent tags or other reagents. As a plus, it provides detection thresholds so small that only a few thousand antigen-antibody binding events are required, enabling multianalyte detection using tens of microns long and a few nanometer thick arrays of different analyte probes.

In general, the proposed novel sensor is expected to have significant advantages over previous optical waveguide approaches, which also is proved with the evidence from sensitivity calculations discussed in Section 4.2.6.

4.2.4 Sensor structures

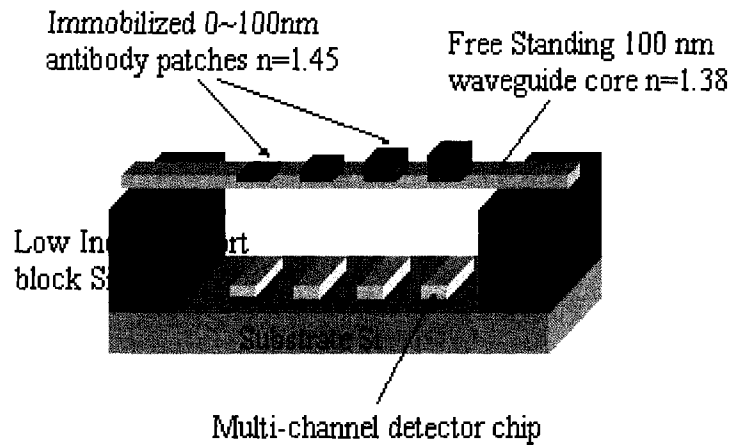
Waveguide cores of the LEAC sensor are constructed from SiN_x , which is a material commonly used for interconnect metal encapsulation. SiO_2 used between metal layers serves as the cladding. Isolated polysilicon regions typically used for resistors or gates are adapted as photodetectors. The thickness of the waveguide core is an essential parameter

that affects the modulation of the evanescent fields in the claddings. It was shown in numerical analysis that an ultra-thin waveguide core provides greater sensitivity to the adlayers due to a larger evanescent field tailing into the cladding regions [11]. The LEAC sensor exploits SiN_x waveguide films of 80–110 nm thickness, almost two orders of magnitude thinner than that of waveguide films for conventional integrated optical waveguide (IOW) sensors. Based on the detection mechanism for the LEAC sensor, optimal sensitivity can be obtained by designing waveguide structures with large evanescent field tails in the lower cladding.

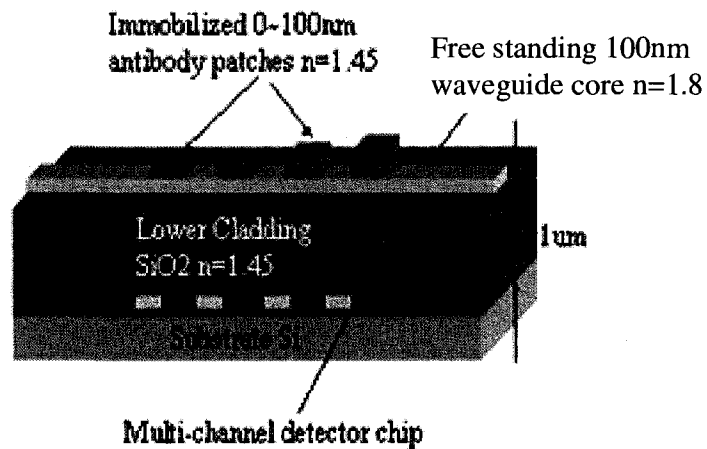
The originally proposed sensor structure was a symmetric configuration, where a freestanding waveguide core was formed to bridge between two supporting SiO_2 blocks, illustrated in Figure 4.7(a). The fabrication process of this configuration needed is relatively complicated. An alternative method exploits an asymmetric waveguide structure, shown in Figure 4.7(b), avoiding etching a cavity below the waveguide core. Furthermore, SiN_x film deposited directly on the SiO_2 presents less mechanical stress than that of freestanding configuration. Due to the asymmetric refractive index profile, the sensor in Figure 4.7 (b) provides more sensitivity for the same core thickness.

Sensing with use of the LEAC sensor can be conducted by a buried detector array, shown in Figure 4.7 (a) and (b). The isolated polysilicon regions and metal vias form metal-semiconductor-metal (MSM) photodetectors. Multianalyte-sensing can be achieved on a single chip using an array of photodetectors in submicron scale spatial resolution. The modification in the evanescent field due to adlayers of bound analytes is locally sensed by an element of a photodetector array along the length of the waveguide, each element being opposite to a region of a specific type of antibody. The optical signal is

first transformed into electrical current or voltage signals. Then integrated solid-state analog or digital circuitry, similar in theory to CCD and CMOS circuitry, reads out the electrical signals. Implemented with multiple photodetector arrays, the sensor is ready to detect and analyze arrays of different immobilized antibodies on the waveguide surface, as illustrated in Figure 4.8.



(a)



(b)

Figure 4.7: a) Symmetric and b) asymmetric sensor configurations.

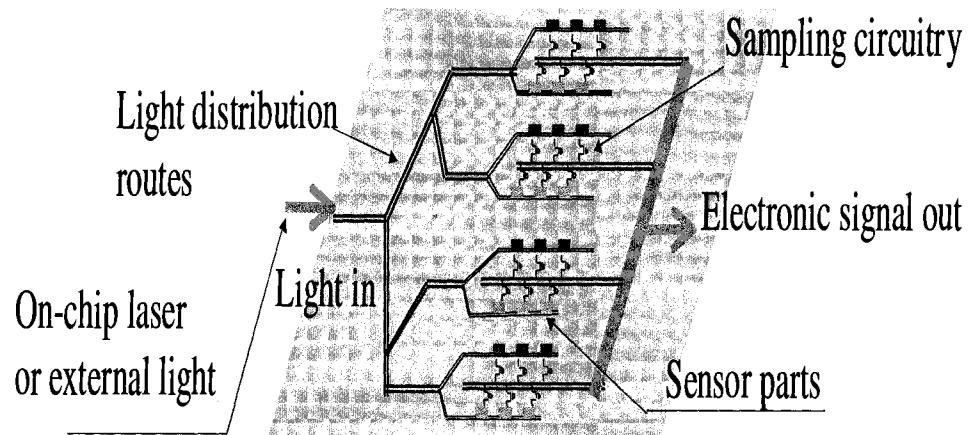


Figure 4.8, multiple sensing scheme of a LEAC sensor

An alternative detection method is using a near-field scanning optical microscope (NSOM) tip to interrogate the evanescent field strength on the upper surface of the waveguide. As discussed in Chapter 2, this method is widely used to analyze internal optical properties in generic waveguides or other waveguide structures. The NSOM tip captures optical power in the upper evanescent field with and without the binding analyte adlayer followed by a post-measurement analysis to determine the change in the adlayer thickness. In the following chapters, we mainly focus on NSOM measurements to verify the functionality of LEAC sensors.

4.2.5 Preliminary sensitivity analysis

The sensitivity of the waveguide system in response to a biological adlayer can be modeled by calculating the modulation in optical intensity captured by a photodetector element. In our modeling, we have the detector to core distance S . The core thickness before binding is d_1 , and after binding is d_2 . For convenience, we denote the bare waveguide core thickness as d , and any adlayer thickness as d_a . The other parameters are

fixed, such as refractive index of antigen and or antibody films. It is denoted as index $n_a=1.45$, since most antigens and antibodies are proteins. The evanescent field modulation due to the binding on the waveguide top surface is shown in Fig. 4.9.

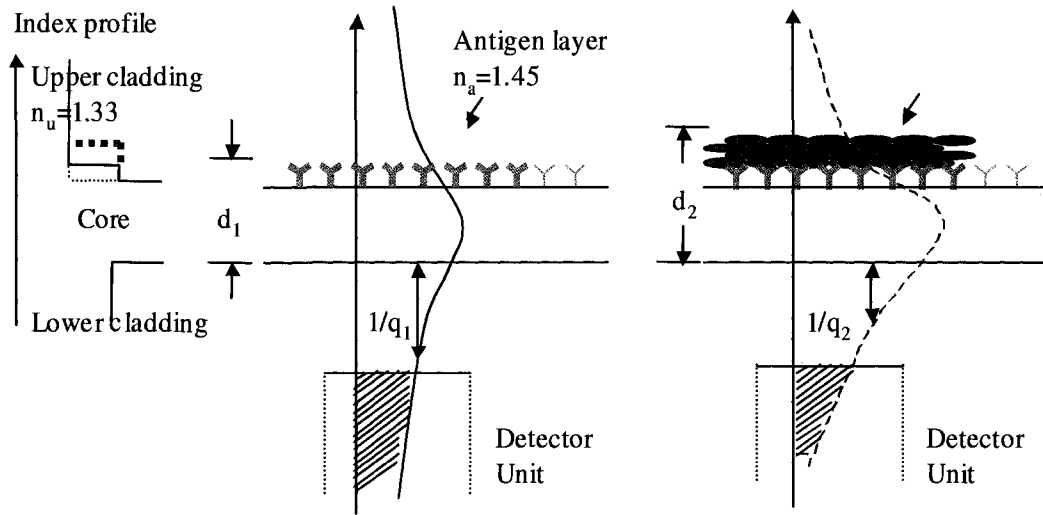


Figure 4.9: modeling of LEAC sensor detection. Refractive index profile (Left) and optical intensity profile before antigen-antibody binding (Middle) and after antigen-antibody binding (Right).

Neglecting y-axis, we can analytically write the solution for the fundamental TE_{00} mode as following:

$$E'(x) = \begin{cases} Ae^{qx} = ae^{qx}, & x < 0 \\ Bf(x) \cong a + bx + cx^2, & 0 \leq x \leq d \\ Ce^{-g(x-d)} = (a + bd + cd^2)e^{-g(x-d)}, & d < x \end{cases} \quad (\text{Eq. 4.1})$$

where β is the propagation constant, g and p are decay constants in the upper and lower claddings. The $f(x, \beta)$ is a sinusoidal function representing the mode profile in the

waveguide core which can be approximated using Taylor expansion to the second order as $a+bx+cx^2$. The penetration depths are $1/g = 1/\sqrt{\beta^2 - k^2 n_u^2}$ and $1/q = 1/\sqrt{\beta^2 - k^2 n_l^2}$ in the upper and lower cladding regions. As discussed in previous chapters, a larger penetration depth means evanescent field tails further in to the cladding region. The field normalization factor is A , which can be expressed as:

$$\begin{aligned}
 A^2 &= \int_{-\infty}^{\infty} E'(x)^2 dx \\
 &= \frac{a^2}{2q} + \frac{(a + bd + cd^2)^2}{2g} + (a^2d + abd^2 + \frac{2acd^3}{3} + \frac{b^2d^3}{3} + \frac{bcd^4}{2} + \frac{c^2d^5}{5}) \\
 &\cong \frac{a^2}{2q} + \frac{a^2 + 2abd}{2g} + a^2d
 \end{aligned}
 \tag{Eq. 4.2}$$

The field projection ratio between $E_1^l(x)$ and $E_0^l(x)$ is η , which can be expressed as:

$$\begin{aligned}
 \eta &= \frac{\int_{-\infty}^{\infty} E_1^l(x) E_0^l(x) dx}{A_1 A_0} \\
 &\cong \frac{\frac{a_1 a_0}{q_1 + q_0} + \frac{a_0 a_1 + a_0 b_1 d_0 + a_1 b_0 d_0^2}{g_1 + g_0} (1 - g_1 \Delta d) + a_1 a_0 d_0 + d_1 \Delta d + b_1 d_0 \Delta d}{\left(\frac{a_1^2}{2q_1} + \frac{a_1^2 + 2a_1 b_1 d_1}{2g_1} + a_1^2 d_1 \right)^{\frac{1}{2}} \left(\frac{a_0^2}{2q_0} + \frac{a_0^2 + 2a_0 b_0 d_0}{2g_0} + a_0^2 d_0 \right)^{\frac{1}{2}}}
 \end{aligned}
 \tag{Eq. 4.3}$$

Where $\Delta d = d_1 - d_0$ is the thickness difference. P_0 and P_1 denotes the optical intensity captured by the detector before and after the antigen-antibody binding, respectively. In order to calculate intensity difference, we use some approximations. Assume that this system is an asymmetric waveguide operating near the fundamental mode cut off region. The penetration depth in the lower cladding is much larger than that in the upper cladding region and the waveguide core thickness, $1/q \gg 1/g \gg d, \Delta d$. This means that optical

power is mainly confined in the evanescent field in the lower cladding.

So the normalized detected power difference can be expressed as:

$$\begin{aligned} \Delta P / P_0 &= \frac{P_0 - P_1}{P_0} \\ &= \frac{\int_{-\infty}^S E_0'(x)^2 dx - \eta^2 \frac{A_0^2}{A_1^2} \int_{-\infty}^S E_1'(x)^2 dx}{\int_{-\infty}^S E_0'(x)^2 dx} \cong 1 - \frac{4q_1q_0}{(q_1 + q_0)^2} e^{-2(q_1 - q_0)S} \end{aligned} \quad (\text{Eq. 4.4})$$

In the Equation 4.4, S is core to detector distance. In calculation, η , which is approximately equal to $\frac{2\sqrt{q_1q_0}}{q_1 + q_0}$, is a value less than unity. In general, analytical calculation reveals the modulation in optical intensity is a function of adlayer thickness and detector to core distance. The larger adlayer thickness and detector to core distance the larger the normalized modulation of the sensor, and vice versa.

4.3 Novel on-chip optical interconnect technology

4.3.1 Monolithic on-chip interconnect

Monolithic on-chip interconnects are designed to demonstrate a purely on-chip, multi-GHz, optical interconnect system implemented in deep submicron CMOS technology from commercial silicon foundries. A group of researchers from Colorado State University and Avago Technology, Inc, Ford Collins, Colorado has been investigating a novel monolithic on-chip interconnect technology that purely exploits materials already used in commercial CMOS technology over years. Portions of the following section are taken from co-authored publications with this group[12].

The International Technology Roadmap for Semiconductors (ITRS) has predicted that

new technologies need to be implemented as early as the year 2009 in order to achieve interconnect and processor performance goals. The relatively high speed, low power consumption, low transmission loss, and decreased sensitivity to process variations of optical interconnects make them an attractive alternative to electrical interconnects for on-chip global signals.

Monolithic optical sources and detectors are highly desirable for CMOS interconnects. While direct bandgap materials may be added to CMOS ICs by heteroepitaxy or other heterogeneous integration techniques, silicon based components are particularly attractive for CMOS ICs. While there is currently substantial interest in silicon based sources, there is also a need for readily integrated photodiodes with adequate responsivity and speed for future high performance processor clock rates.

The low absorption coefficient of silicon at infrared wavelengths complicates the fabrication of efficient normal incidence photodiodes using the thin depletion regions available in conventional CMOS technology without relying on slowly diffusing carriers. Thus, researchers have investigated alternative detector structures. One option is to enhance the absorption of thin silicon layers by placing them in resonant cavities. Other approaches use structures with orthogonal directions for light propagation and carrier transport.

4.3.2 New on-chip optical interconnect design

The work presented here also uses perpendicular optical and carrier transport axes but oriented for use in planar, waveguide based optical interconnects. Planar optical interconnect technologies maintain form factors of conventional IC technology and

minimize or eliminate the need for optical alignment to external or hybrid optical assemblies. The waveguide based photodiode structure is motivated by the goals of producing monolithic, planar, on-chip optical interconnects using only commercial CMOS technology for optical transport and detection. This approach should enhance the insertion of optical interconnect technologies in CMOS. Hilleringman and Gosser previously demonstrated coupling of silicon oxynitride waveguides to silicon p-n detectors using butt and leaky mode coupling as well as angled mirrors .

In order to achieve high speed, the use of a thin silicon layer as detector is essential to ensure that only carriers generated in the high field region contribute to the photocurrent. However, a thin silicon layer results in low responsivity for normal incidence devices. Thus there is a trade off, and a device that meets both the photoresponse and high-speed requirements needs to be designed. The device bandwidth depends on the contact spacing and the thickness of the semiconductor device. It is evident from previous literature that the use of a thin layer of polysilicon and comparable contact spacing has resulted in an improvement in the time response of photodiodes because carriers are generated in the high field regions only. The use of waveguide coupling and lateral incidence would result in improved responsivity as the thin polysilicon layer would ensure that only carriers generated in the high field region contribute to photocurrent, and the lateral incidence would result in an increase in the effective absorption length along the direction of light incidence. Thus the use of lateral waveguide incidence would result in high responsivity and the use of polysilicon would result in an increase in the bandwidth of the photodiode, as shown in Figure 4.10.

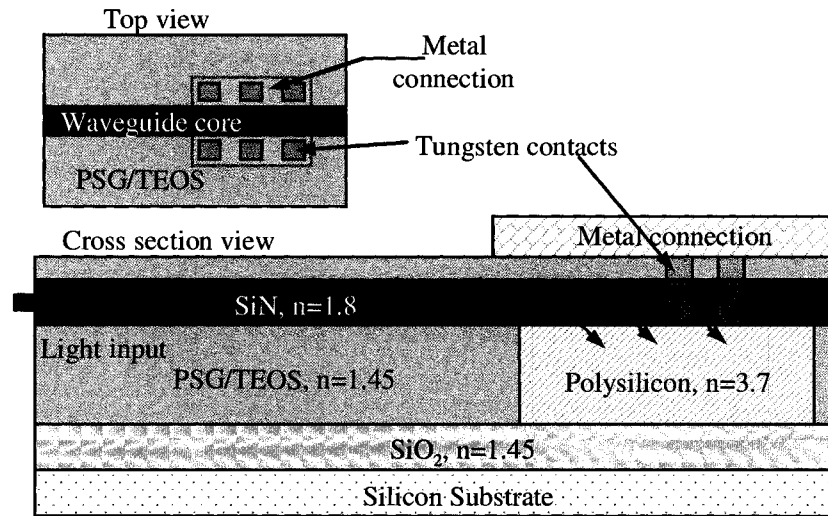


Figure 4.10: Cross-section of the waveguide and photodetector (the inset shows the top view of the detector).

In order to enhance the CMOS compatibility of planar optical interconnects, only materials already present in commercial CMOS processes are used for the waveguide and photodiode presented here. Thus the waveguide core is silicon nitride typically used for copper encapsulation; the waveguide cladding is composed of the intermetal low-k dielectric layers; and the photodetector is fabricated from undoped polysilicon used for gates and resistors. The initial application envisioned is on-chip, low skew, optical clock distribution via a waveguide H-tree. While CMOS compatible optical sources are still under development, an off-chip, low-jitter, mode locked laser diode could be edge coupled via fiber to the input of the H-tree. Figure 4.9 shows the cross section of a prototype interconnect system. However, by using amorphous or low temperature polysilicon, the detector and associated waveguide can be placed anywhere in a typical multilevel metal stack. A MSM (metal-semiconductor-metal) type structure is formed

using tungsten vias as Schottky contacts to the undoped polysilicon island running alongside the silicon nitride waveguide core with each side connected by first level metal. With bias, the carriers are transported laterally between the Schottky contacts across a gap with a dimension of approximately three times the critical dimension for that CMOS generation. The use of a thin polysilicon MSM photodiode not only allows freedom to place the waveguides and detectors at various levels in the backend layers but also isolates the detector from the noisy substrate environment and prevents slow diffusion currents.

In fabrication, we need consider the compatibility of the system to the CMOS process. Here the lower cladding, which is composed of the lower PSG layer and the field oxide, has a thickness of $0.7\mu\text{m}$. In addition, the combined thickness of the core and upper cladding is restricted to be $0.6\mu\text{m}$ thick to allow contact window etches to reach the polysilicon layer.

4.3.3 Waveguide structure simulations

The propagation loss dependence on the waveguide core thickness was calculated using Rsoft's beam propagation method program. In the simulation, it was initially assumed that only the TE_{00} mode was launched into the waveguide. Figure 4.10 shows decreasing losses for the waveguide structure as core thickness is increased. The structure was modeled with air directly above the thin top cladding, as would be the case for a prototype structure with only one metal layer, making the overall waveguide structure asymmetric. A more complete process with multiple metal layers would allow thicker lower and upper claddings. The simulations assumed a root mean square (RMS) surface

roughness of 1nm. Figure 4.10 shows that the loss decreases with increasing core thickness due to the reduction in evanescent field coupling to the substrate. Losses on the order of 1dB/cm are tolerable for on-chip interconnect lengths of a few centimeters. For thicknesses greater than approximately 0.45 μm , a second TE mode becomes bound, and its loss is shown in Figure 4.10. The measured propagation loss is approximately 8 dB/cm for a 0.5 μm wide, 0.35 μm thick waveguide which indicates higher RMS surface roughness.

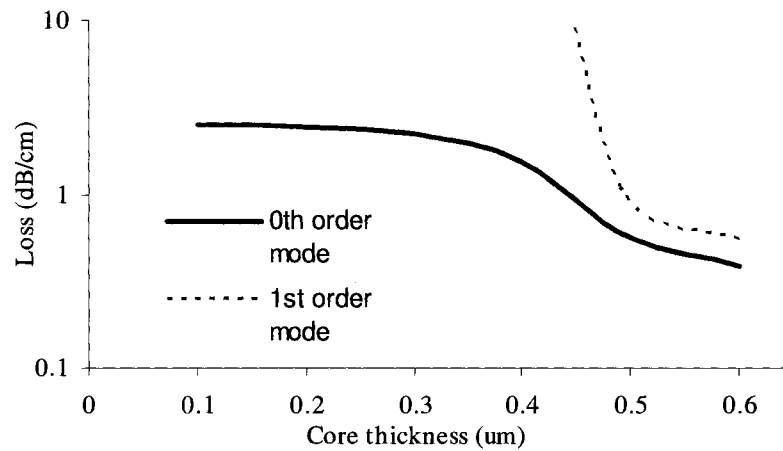


Figure 4.10: Propagation loss vs. the waveguide core thickness for the 0th and 1st order modes at 780nm wavelength

Simulations were performed using 2-dimensional (2D) finite-difference time domain (FDTD) code to determine bending loss for the critical bending radius of the waveguide. A plot of the loss in dB for a 90° bend as a function of center radius for a 0.5 μm wide waveguide at $\lambda=780\text{nm}$ appears in Figure 4.11. The large 1.8/1.45 index step offers strong light confinement and permits tight bending radii, thereby reducing the overall

silicon area used as compared to previous work in this area. As an example, a bending radius of $10\mu\text{m}$ gives a loss of $0.1\text{dB}/90^\circ$ bend. An H-tree with 2^n nodes requires a sequence of n such bends for each path so that a 16 node H-tree would introduce a bending loss of only 0.4 dB. The measured loss is approximately 3 dB for a $25\mu\text{m}$ radius, $0.5\mu\text{m}$ wide waveguide splitter.

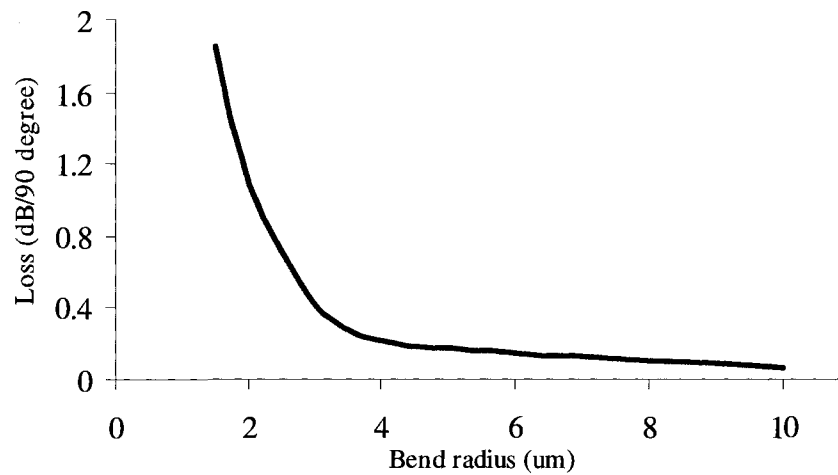


Figure 4.11 Bend loss vs. bending radius at 780 nm for 90 degree bends for a $0.5\mu\text{m}$ wide waveguide.

4.4 Summary

In this chapter, we reviewed previous optical waveguide devices, such as SPR and ATR sensors, etc. We presented the concepts of two new integrated optical waveguide devices, a local evanescent-field array coupled (LEAC) sensor and an on-chip optical interconnect system. In the initial analysis, both analytical and numerical simulations were conducted to provide an inspiration for sensor design.

Reference

- [1] R. W. Wood, "On a remarkable case of uneven distribution of light in a diffraction grating spectrum," *Philosophical Magazine*, 4, pp. 396-402, 1902.
- [2] B. Liedberg et al "Surface plasmon resonance for gas detection and biosensing," *Lab.Sensors Actuat.* 4, pp. 299-30, 1983..
- [3] P. B. Daniels, J. K. Deacon, M. J. Eddowes and D. G. Pedley, "Surface plasmon resonance applied to immunosensing," *Sens. & Actuat.* 15, pp. 11-18,1988.
- [4] A. Brecht, J. Piehler, G. Lang, G. Gauglitz, "A direct optical immunosensor for atrazine detection. *Analytica Chimica Acta.*, 311, pp. 289-299,1995.
- [5] Charles E. H. Berger, Tom A. M. Beumer, Rob P. H. Kooyman, and Jan Greve "Surface Plasmon Resonance Multisensing," *Anal. Chem.*, 70 (4), pp. 703 -706, 1998.
- [6] Frank Caruso, Kenichi Niikura, D. Neil Furlong, and Yoshio Okahata "Ultrathin Multilayer Polyelectrolyte Films on Gold: Construction and Thickness Determination", *Langmuir*, 13 (13), pp. 3422 -3426, 1997.
- [7] Ariel G. Notcovich, V. Zhuk, and S. G. Lipson, "Surface plasmon resonance phase imaging", *Applied Physics Letters*, Vol. 76, pp. 1665-1667, 2000.
- [8] <http://www.eng.uah.edu/~kchittur/bmreview/node2.html>
- [9] <http://www.feinberg.northwestern.edu/cif/tirf.htm>
- [10] D.S. Dandy, K. L. Lear, et al. "Proposal of a multianalyte physiological optical waveguide sensor, " sponsored by NIH, 2002-2007.

- [11] G. Yuan, M. Stephens, D. Dandy, and K.L. Lear, "Novel local evanescent field detection waveguide multianalyte biosensor", Optical Information Systems II in series Proceedings of SPIE, vol. 5557, pp. 140-146, Oct. 2004.
- [12] A. M. Raza, "A truly CMOS compatible waveguide coupled photodiode for on-chip optical interconnects," M.S. Thesis, Colorado State Univ., Fort Collins, CO, 2005.
- [13] G. Yuan, R. Pownall, P. Nikkel, C. Thangaraj, T. W. Chen, and K. L. Lear, "Characterization of CMOS compatible, waveguide coupled leaky-mode photodetectors," IEEE Photonics Technology Letters, Vol. 18, pp. 1657-1659, 2006.

Chapter 5

WAVEGUIDE FABRICATION AND EXPERIMENTAL SETUP

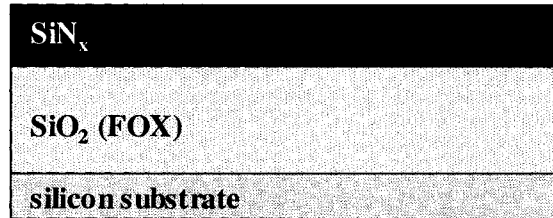
5.1 Introduction

In this chapter, we will discuss fabrication processes for the LEAC sensor and the on-chip optical interconnect system. The fabrication steps will be described in Section 5.1. We will also discuss other waveguide processing steps such as polishing and coupling in Section 5.2. Finally, the NSOM system used in characterization studies is described in Section 5.3.

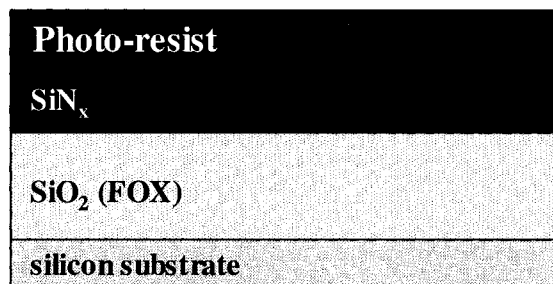
5.1.1 LEAC sensors without detector arrays

LEAC sensor fabrication exploits traditional thin film growth, photolithography, and dry etch technologies. In the initial studies, sensors without the buried detectors are fabricated in the CSU cleanroom facility. To begin, a 105 nm thick SiN_x film was deposited on a SiO_2/Si wafer using NH_3/argon sputtering, where the SiO_2 lower cladding thickness is about 2 μm . A 2 μm wide ridge waveguide core was defined by partially dry etching the surrounding SiN_x layer in CF_4/O_2 plasma. The etch depth and thus ridge height is approximately 21 nm. The fabrication process is illustrated in Figure 5.1. A longitudinal cross section of the resulting waveguide is illustrated in Figure 5.2. The top surface of the SiN_x film is left exposed to the air that serves as the upper cladding, allowing the NSOM to examine the evanescent field there. Refractive indices of the core and lower cladding are

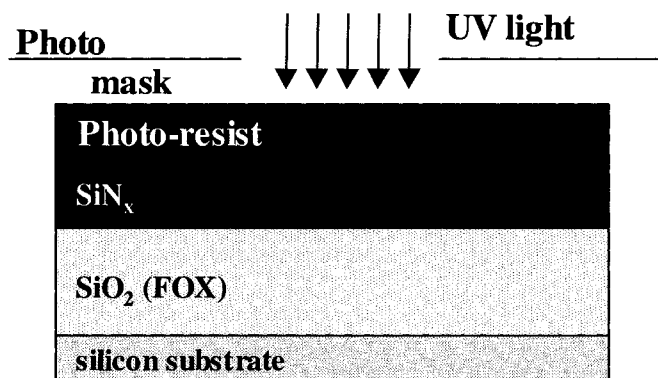
1.8 and 1.45, respectively [1]. Figure 5.3 shows a microscopic image of waveguide channels.



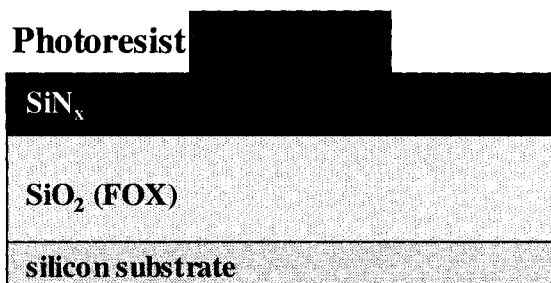
(a) SiN_x on SiO_2/Si wafer



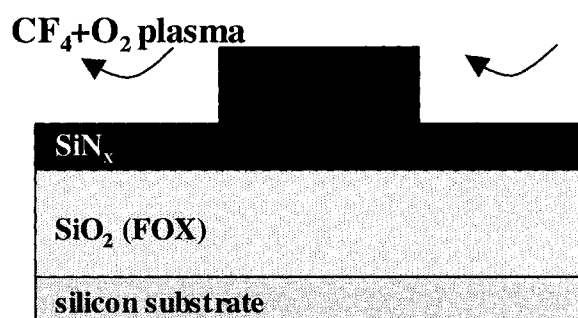
(b) Spinning photoresist



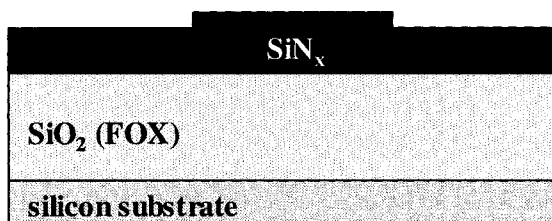
(c) Masking



(d) Developing



(e) Plasma etch



(f) Cleaning

Figure 5.1: LEAC sensor (without photodetectors) fabrication process.

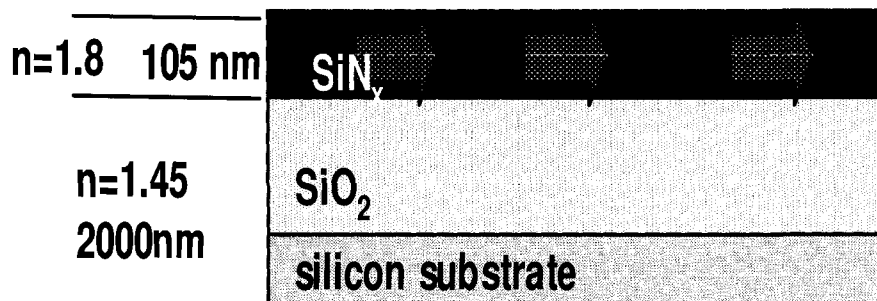


Figure 5.2: longitudinal cross section of the sensor structure.

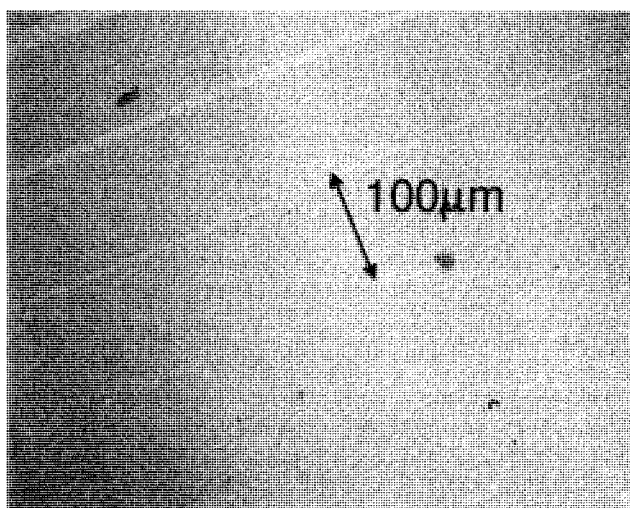
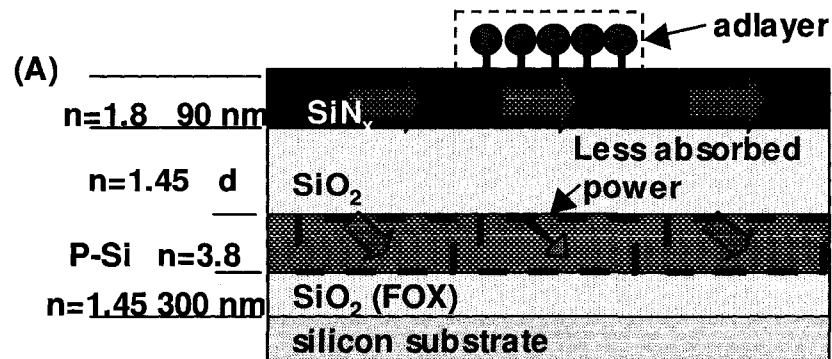


Figure 5.3: Microscopic image of waveguide channels.

5.1.2 LEAC sensors with detector arrays

The fabrication sequence of LEAC sensors with buried detector arrays were designed with assistance of Matt Stephens and laid-out by Ahmad from Colorado State University using the above techniques as well [2]. The evanescently coupled photodiodes and waveguide, shown in Figure 5.4(a), are obtained by following a sequence of steps. To begin, a silicon-on-insulator (SOI) wafer is used with a top layer of 250nm to 400nm of undoped silicon or polysilicon that is to be later patterned to form the detector array. A

d=1000nm layer of SiO₂ is deposited on top of the polysilicon to serve as the lower cladding. The thickness of this layer is chosen to balance the waveguide loss and detector sensitivity. Next, a 90 to 100 nm layer of SiN_x (n=1.8) is either PECVD or sputter deposited over the SiO₂ and partially etched to form a 2 to 3 μm wide, single mode waveguide ridge as illustrated in Figure 5.4(b). The top surface of the SiN_x film is left exposed allowing analyte attachment with the air or fluid above it serving as the upper cladding. After the ridge definition, a deep CF₄/O₂ plasma etch through the remaining SiN_x and SiO₂ exposes the surface of the polysilicon layer. A CF₄/O₂ plasma etch isolates a continuous 40 μm wide polysilicon strip under the waveguide. A series of metal fingers as seen in Figure 5.4(b) are deposited to form contacts and probe pads along each side of the waveguide. An end view of the device layout geometry is illustrated in Figure 5.4(c). The width of metal fingers is chosen to determine the effective length of each detector array element. A common ground single metal pad connects all of the fingers/detectors on one side of the waveguide and a series of metal pads connect the fingers/detectors one-to-one on the other side of the waveguide. Voltage bias between each these pads and the common ground pad creates an electric field oriented perpendicular to the direction of light propagation.



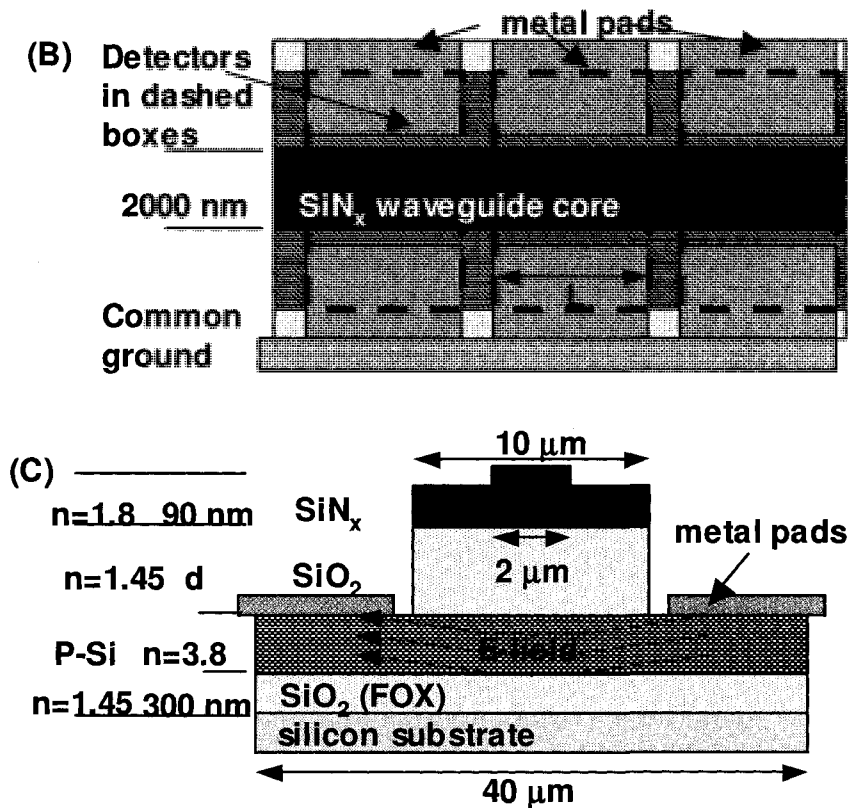
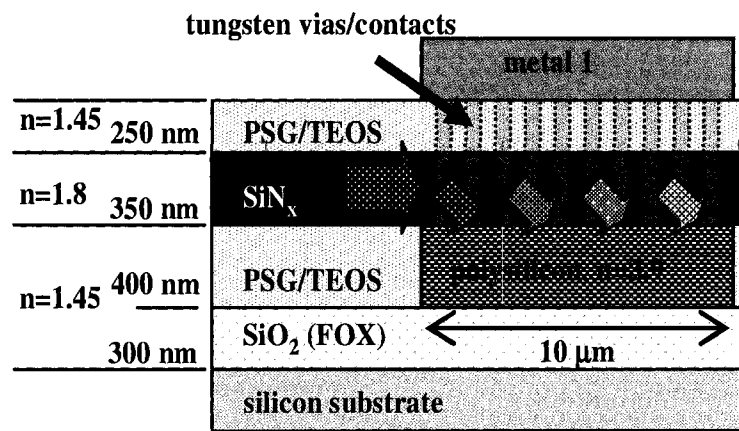


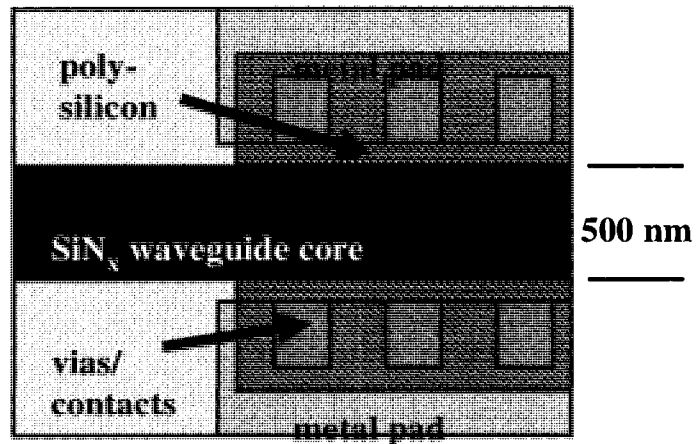
Figure 5.4: (a) Side view of the waveguide and evanescently coupled, buried detector array. Less optical power is absorbed by the middle detector element due to the attachment of an adlayer on the upper surface of the waveguide, (b) top view, (c) end view.

5.1.3 The on-chip optical interconnect system

For the on-chip optical interconnect system, waveguides and photodetectors were fabricated with a commercial 0.35 μm CMOS technology at the Avago Technologies (formerly a part of Agilent Technologies) facility in Fort Collins, Colorado [3]. The MSM photodiode and waveguide structures, shown in cross-section in Fig 5.5, are obtained by following a sequence of steps similar to those employed in conventional CMOS gate, dielectric, contact, and first layer metal processes.



Longitudinal cross-section



Top view

Figure 5.5: Cross-sectional (Top) and top view (Bottom) diagrams of the waveguide and photodetector. (reproduced from Reference 3).

The first steps are the deposition of 255 nm thick polysilicon on 300 nm of thermal field oxide (FOX) on a silicon substrate, masking, and etching to form isolated polysilicon

mesas. The polysilicon differs from that used for gate and resistor layers only in the fact that it is not doped with a subsequent implant process. The complex refractive index of the polysilicon was determined to be $n = 3.9 + i0.038$ at 650 nm based on thin film reflectivity measurements [4]. The attenuation corresponds to an absorption coefficient of 1.6 dB/ μm . Next, a 500 nm or thicker layer of phosphosilicate glass (PSG, $n=1.45$), is deposited over the exposed field oxide and polysilicon and subsequently chemical-mechanically polished (CMP) until it is planar and the top surface of the polysilicon layer is exposed. A 0.35 μm thick SiN_x ($n=1.8$) layer is then deposited and etched to a 0.5 μm width to form the waveguide core which passes over the polysilicon region. Additional PSG is deposited to clad the sides and top of the waveguide core. The second PSG layer is also planarized by CMP until the upper cladding thickness is approximately 0.25 μm . This relatively thin upper cladding allows a NSOM to measure the optical intensity distribution along waveguides.

The combined thickness of this PSG layer and the SiN_x core must also be kept thin enough to allow etching of a contact via to the polysilicon. In a more complete implementation, the deposition of additional PSG for higher metal interlayer dielectrics would add to the upper cladding thickness. Either using thicker field oxide, or placing a low temperature polysilicon or amorphous silicon detector and waveguide core above the first layer metal can increase the lower cladding thickness. After via etching, tungsten contacts to the polysilicon are deposited and first layer metal is patterned for interconnects and probe pads. The top view in Figure 5.5 schematically illustrates the device layout geometry. A row of square, 0.3 μm x 0.3 μm tungsten filled vias are placed along each side of the waveguide. The length of the polysilicon region along the waveguide is chosen to be 10 μm

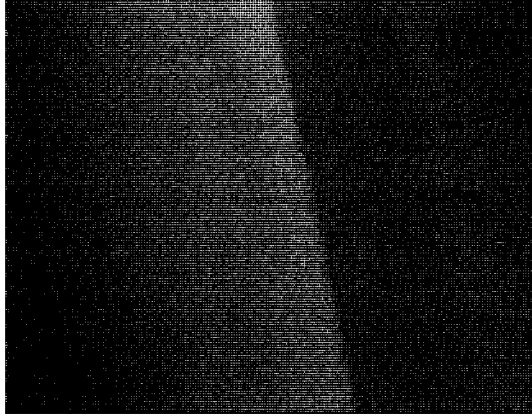
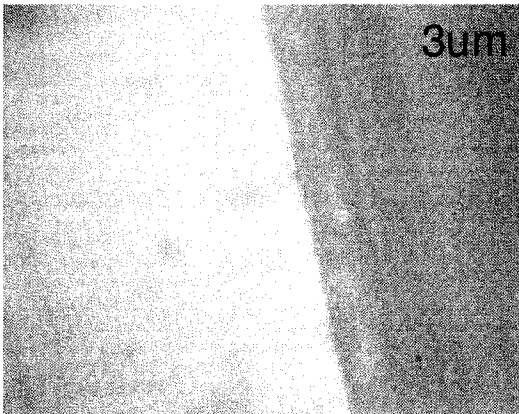
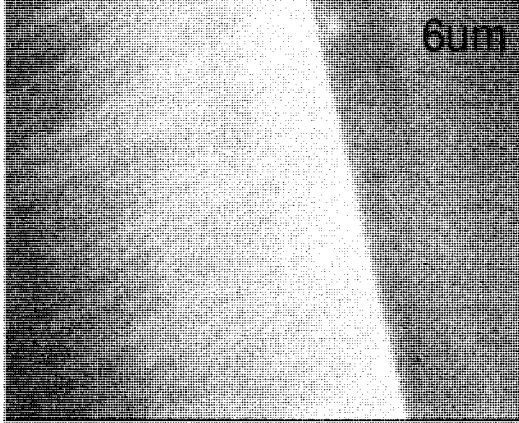
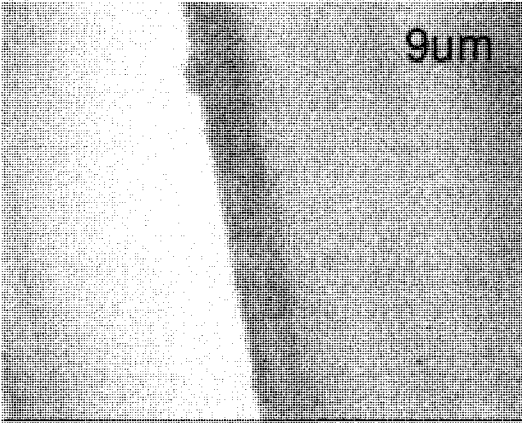
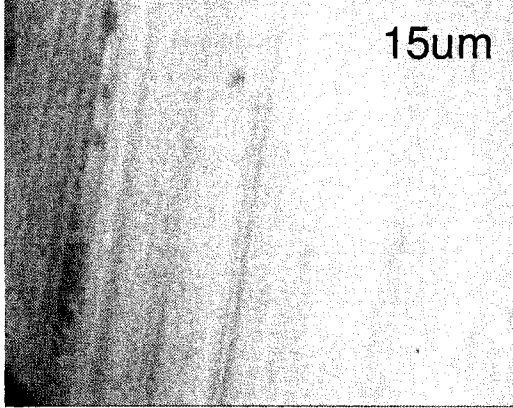
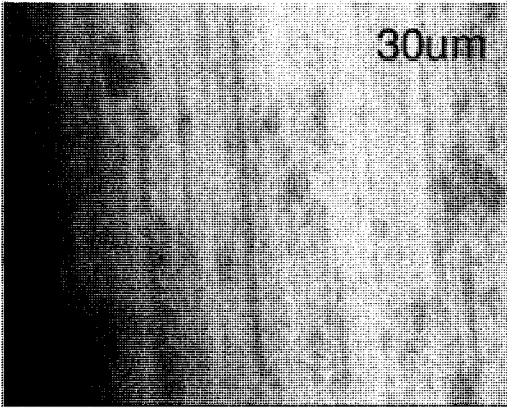
to allow adequate absorption as discussed below. A row of squares rather than a single elongated tungsten contact is used to conform to the CMOS process design rules. A single metal pad connects all of the contacts on one side of the waveguide and a second metal pad similarly connects the contacts on the other side of the waveguide. Voltage bias between these two pads creates an electric field oriented perpendicular to the direction of light propagation. The distance between the inner edges of the rows of contacts is restricted to a minimum of approximately $1.1\ \mu\text{m}$ for the $0.35\ \mu\text{m}$ design rules used here, or about three times the technology critical dimension in general depending on the minimum waveguide width and via to waveguide alignment tolerances. The separation of the contact rows has the same impact as the finger spacing parameter would in a conventional MSM detector. The scaling of the contact spacing with the CMOS technology generation will allow lower bias voltages in future devices.

5.2 Facet polishing

Polishing is an important part in the process of waveguide fabrication. The optoelectronic research group at Colorado State University has been working on a simple method for polishing waveguide facets [4].

During the polishing, protection of the waveguide surface is vital. This was achieved by bonding the sample's upper surface to a glass plate with crystal bond. A plastic module is then used to hold the bonded sample. Polishing papers with various grit sizes are used to polish the facet, going from $30\ \mu\text{m}$, $15\ \mu\text{m}$, $9\ \mu\text{m}$, $6\ \mu\text{m}$, $3\ \mu\text{m}$, $1\ \mu\text{m}$, $0.5\ \mu\text{m}$, $0.1\ \mu\text{m}$ to $0.05\ \mu\text{m}$. Figure 5.6 shows microscopic images of the resulting facet after each polishing step. These images are approximately of $300\ \mu\text{m} \times 240\ \mu\text{m}$ in area. The sample is then

washed with acetone and de-ionized water. In order to completely clean the sample of crystal bond, the sample can be treated in oxygen plasma in the CSU cleanroom.



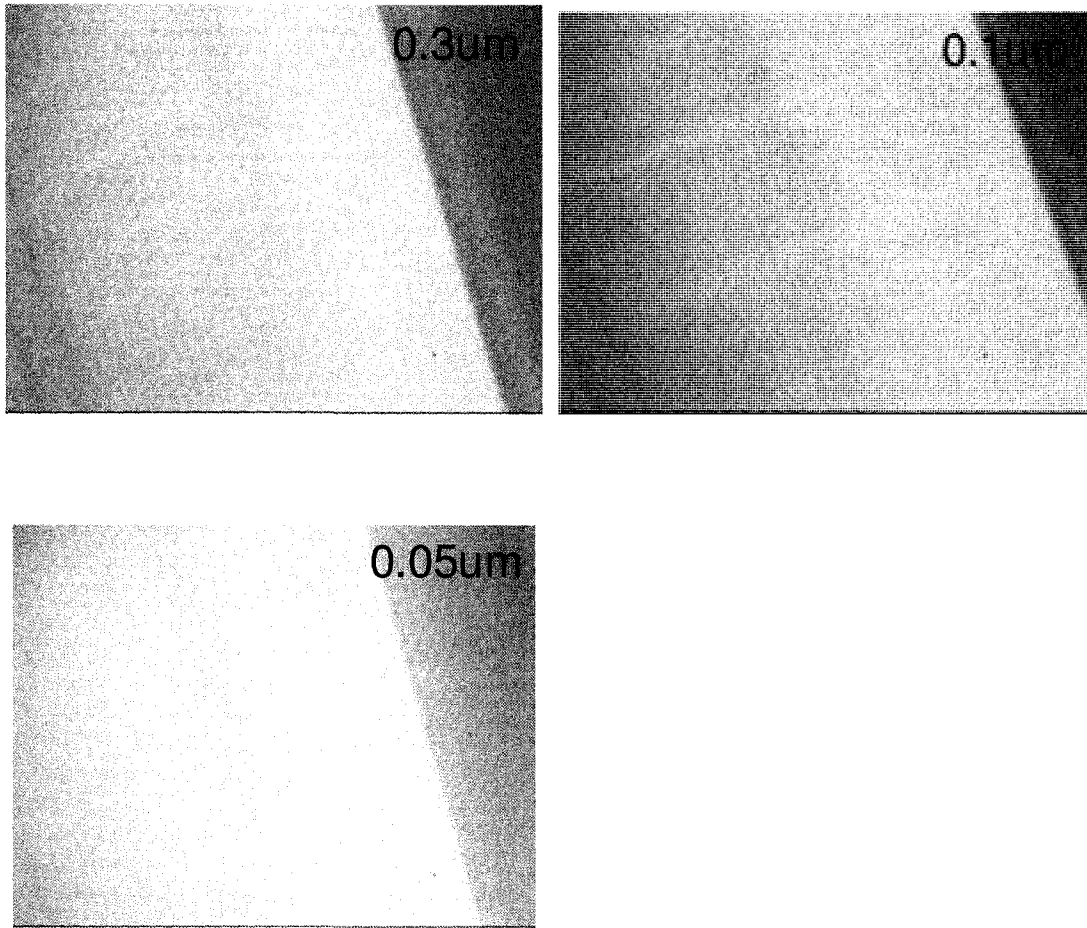


Figure 5.6: Microscopic image of the waveguide facet after each polishing step.

5.3 Light coupling

In our studies, we exploit the end-fire method to couple light into the waveguide simply by aligning the end of the optical fiber against the waveguide facet as illustrated in Figure 5.7. A 3-axis piezoelectric translation stage from Thorlabs was used to align the fiber to the edge of the chip [4]. The resolution of the piezoelectric translator was 10 nm in all 3 axis. A laser diode to fiber coupler was used to deliver light into the 4 μm core signal mode fiber. A 654 nm laser diode was powered by a laser diode current driver. Fiber was clamped on the fiber holder which was mounted on the non-movable part of the translation stage. The

waveguide under test was mounted on a height adaptor and aligned using the translation stage. The typical beam diameter of visible single mode fibers used for the studies is approximately $4\ \mu\text{m}$. The mode field diameter of a $0.5\ \mu\text{m}$ wide, $0.35\ \mu\text{m}$ thick waveguide for the optical interconnect system is about $1\ \mu\text{m}$. The coupling efficiency is about 14% [3]. The mode calculation code can be found in Appendix A. Figure 5.8 shows light coupling images of waveguides on two different chips. Figure 5.8 shows light coupling images of waveguides on two different chips.

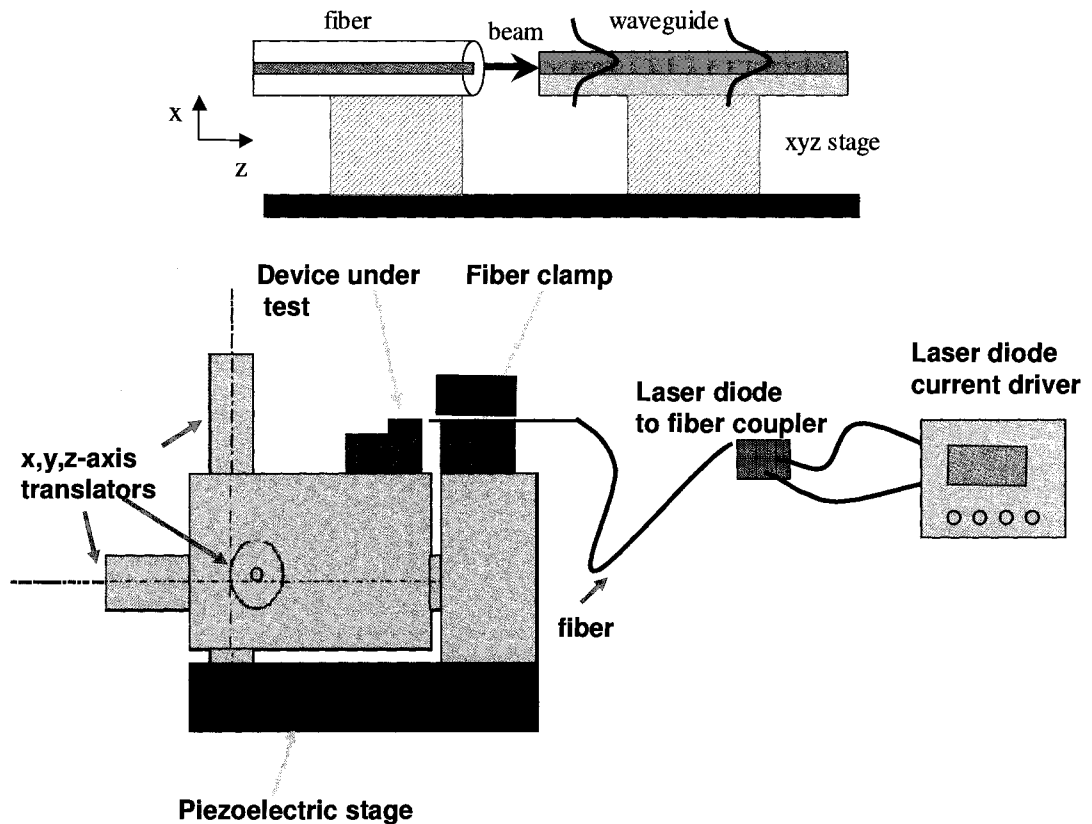


Fig 5.7: Schematic of the end-fire coupling configuration (reproduced from Reference 4).

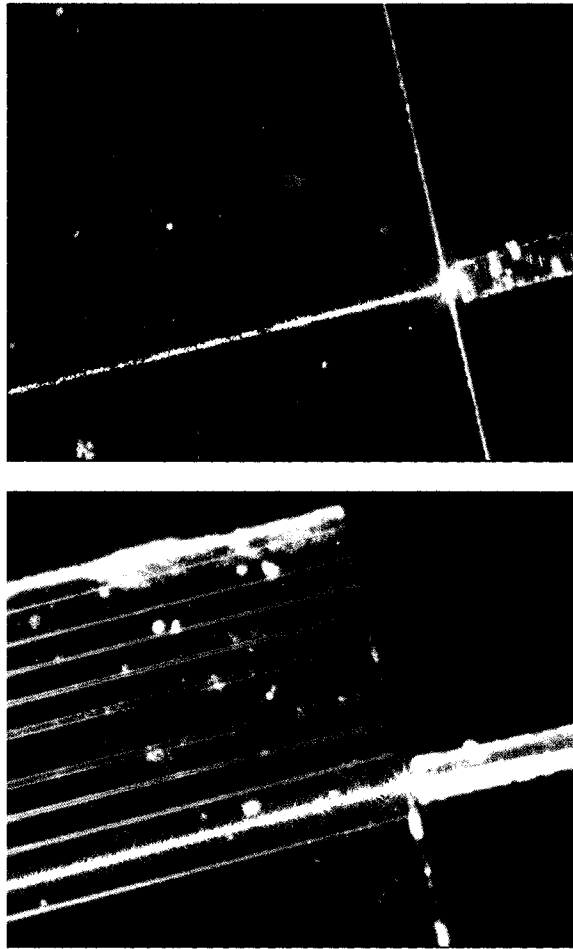


Figure 5.8: Light coupling images.

5.4 NSOM setup

NSOM measurements reported in the following chapters employed an Alpha-SNOM system from WiTec is shown in Figure 5.9 along with details of the optical detection part [5]. This system has simultaneous optical and topographical profiling capability.

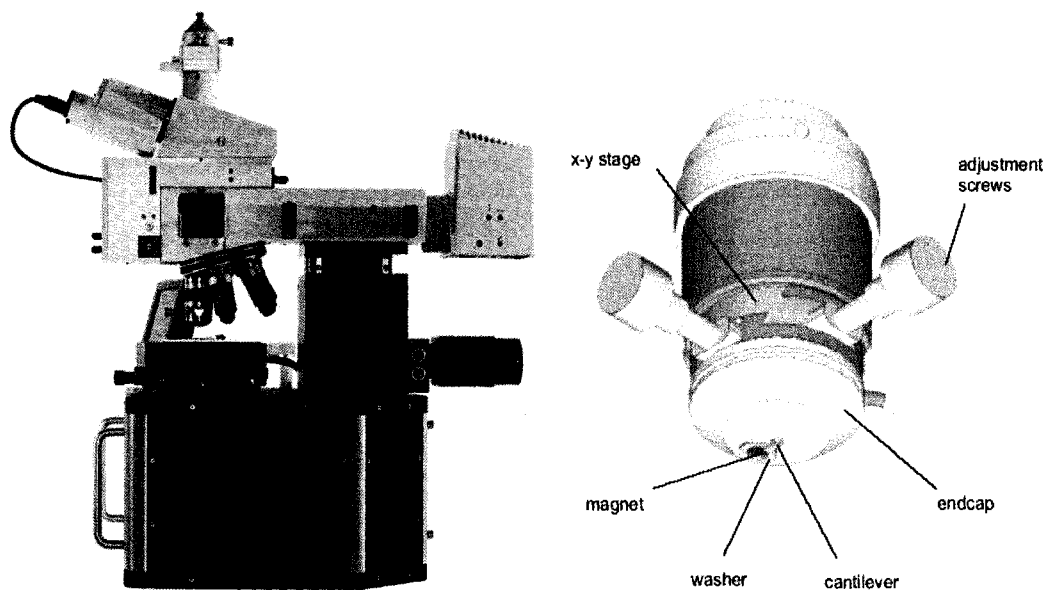


Figure 5.9: Witec Alpha-SNOM system (left). Optical detection part (right). (reproduced from Reference 6).

The experimental setup is shown in Figure 5.10(a). The combination of atomic force microscopy (AFM) and NSOM tip is a hollow aluminum pyramid integrated onto a Si cantilever that converts the evanescent field to a propagating wave by locally frustrated total internal reflection. The tip is shown in Figure 5.10 (b). A photomultiplier tube is aligned to a subwavelength diameter pinhole centered in the tip to detect the wave emanating from the tip that is proportional to the evanescent field. A reference laser beam reflecting off the cantilever is directed to a quadrant detector by a dichroic beam splitter and is used to sense tip deflection in AFM mode. As the tip is moved toward the top surface of the waveguide studied here, an exponentially increasing optical field is observed in addition to a constant signal due to reference beam scattering, verifying that the evanescent field can be distinguished from scattered reference beam light, illustrated in Figure 5.10(c).

During in-plane optical profiling, the NSOM was operated in contact mode so that the field at the top surface of the waveguide was measured.

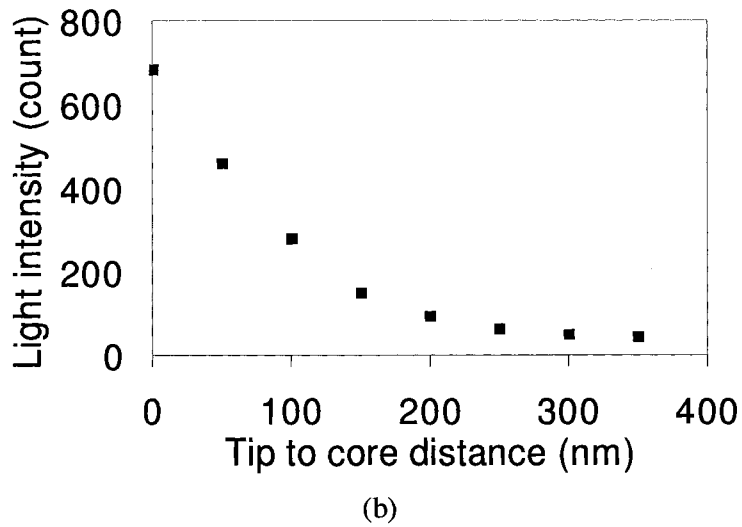
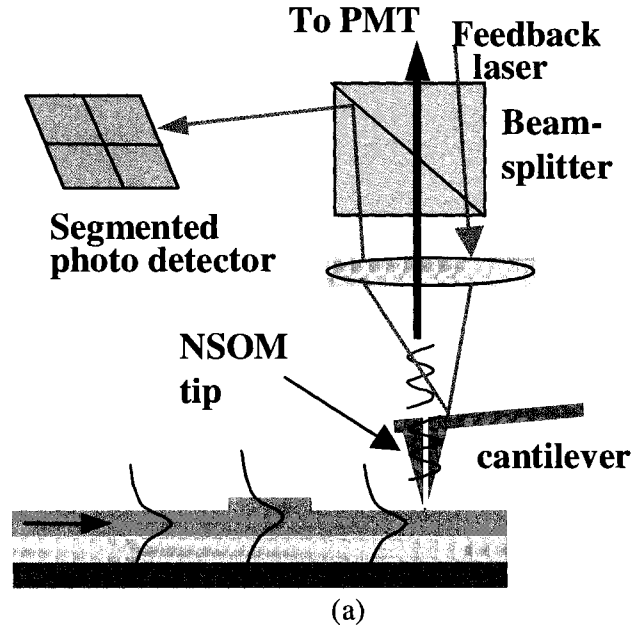


Figure 5.10: (a) Schematic illustration of Witec Alpha-SNOM using optical detection of cantilever deflection,,(b) an exponentially decreasing optical field as the tip moves away from the top surface of the waveguide,

5.5 Summary

We described the fabrication procedure for the prototype LEAC waveguide sensors and on-chip optical interconnect systems. We also presented the methods for waveguide facet polishing and light coupling. Finally, we presented the NSOM setup used for following waveguide characterization. Initial studies demonstrated the capability of the NSOM tip to measure the evanescent field of an optical waveguide.

Reference:

- [1] Guangwei Yuan M.D. Stephens, D.S. Dandy, K. L. Lear, “Direct imaging of transient interference in a single-mode waveguide using near-field scanning optical microscopy,” *IEEE Photon. Tech. Letters*, Vol. 17(11), pp. 2382 – 2384, Nov. 2005.
- [2] Guangwei Yuan, Ahmad Al Omari, Matthew D. Stephens, David S. Dandy, and Kevin L. Lear, “Implementation of buried detector arrays for waveguide sensors”, *Proceedings of LEOS 19th Annual Meeting*, paper, TuW5, **pp. 358–359**, October 2006
- [3] Guangwei Yuan, R. Pownall, P. Nikkel, C. Thangaraj, T. W. Chen, and K. L. Lear, “Characterization of CMOS compatible, waveguide coupled leaky-mode photodetectors,” *IEEE Photonics Technology Letters*, Vol. 18, pp. 1657-1659, 2006.
- [4] A. M. Raza, “A truly CMOS compatible waveguide coupled photodiode for on-chip optical interconnects,” M.S. Thesis, Colorado State Univ., Fort Collins, CO, 2005.
- [5] Guangwei Yuan and K.L. Lear, “Metrology of integrated waveguide devices and systems using near-field scanning optical microscopy”, *Technical Digest, A NIST Symposium for Photonic and Fiber Measurements (SOFM)*, pp. 24-27, Sept. 2006.
- [6] www.witec.de

Chapter 6

EXPERIMENTAL RESULTS, SIMULATIONS, AND DISCUSSIONS

This chapter will discuss experimental results and simulations of waveguide devices, such as straight waveguides, waveguide bends, waveguide sensors, and on-chip optical interconnects.

6.1 Straight waveguides

Straight waveguides are fundamental elements in integrated optical waveguide devices or systems. Principally, straight waveguides are used to carry optical power or signals from sources to receivers. Propagation loss is one of the important factors to determine the performance of a straight waveguide and is parameterized by the light attenuation coefficient. In recent years, multimode interferometer (MMI) devices, which mainly consists of multiple segments of, either single mode or multimode straight waveguides [1], have been given attention for potential applications in optical signal coupling and multiplexing. Therefore, determining the modal behavior in straight waveguides was vital in order to understand complex waveguide devices.

In this section, we are going to describe the characterization work of different straight waveguides. These waveguides were in three categories, single mode waveguide, lateral multimode waveguide, and longitudinal multimode waveguide.

6.1.1 NSOM measurement on single mode waveguides

The following context reports the experimental results as well as numerical simulation results in the investigation of straight waveguides conducted by Dr. Kevin Lear and Dr. Dandy's groups at Colorado State University and has been published with co-authors in Reference [3] and is partial incorporated below.

The single mode waveguides might be the simplest form in all waveguides devices. Fabrication of a single mode waveguide was straightforward. We will briefly describe the structure of the single mode waveguide studied that was fabricated using the traditional photolithography techniques described in Chapter 5.

The waveguide core consists of an 88-nm-thick SiN_x film deposited onto a $\sim 2 \mu\text{m}$ thick SiO_2 lower cladding supported on a Si substrate. No solid upper cladding was deposited above the SiN_x .

This approach also provides the NSOM ready access to the evanescent field in the air above the core, which serves as the upper cladding. Dry etching of 21 nm of the SiN_x outside a $\sim 2 \mu\text{m}$ -wide ridge defined the lateral extent of the core.

Waveguide mode profiles can be solved using the 1-D modal solver code discussed in Appendix A. The solver solves the E-field and effective index in the vertical direction. The calculated effective index of the waveguide core in the lateral direction was $n_{\text{eff}}=1.4529$.

Alternatively, to solve the effective index of the nonguiding cladding regions of the waveguide, we used the method reported by N. Jaeger and W. Lai in 1992 [2]. The effective index of the waveguide claddings in the lateral direction can be calculated as

$$n_{eff_claddings} = n_{eff} + \int_{-\infty}^{+\infty} n(y)\Delta n(y)E(y)^2 dy / n_{eff} .$$

Where the $n(y)$ was the vertical index profile of the lateral waveguide claddings. $\Delta n(y)$ was the index difference between the core and claddings. $E(y)$ was the vertical electrical field distribution in the waveguide core. The calculated effective index of the waveguide claddings was $n_{eff_claddings}=1.4510$. Therefore, the vertical and horizontal V-parameters were 0.45 and 0.735, respectively.

To analyze the straight waveguide, NSOM was used to directly measure the evanescent field on the upper surface of the waveguide. The NSOM instrument used was a α -SNOM system from WiTec described in Chapter 5.

During in-plane optical profiling, the NSOM was operated in contact mode so that the field at the top surface of the waveguide was measured. NSOM experiments yielded light intensity and topography maps simultaneously. The surface topology of the ridge waveguide, shown in Figure 6.1(a), and the lateral intensity distribution of the evanescent field immediately above the core, illustrated in Figure 6.1 (b), were simultaneously acquired with the NSOM.

The ridge appears 1 μm wider than the nominal waveguide width due to the blunt nature of the probe tip around the optical aperture. The optical intensity pattern reveals a smooth, fundamental mode distribution without oscillations associated with mode beating.

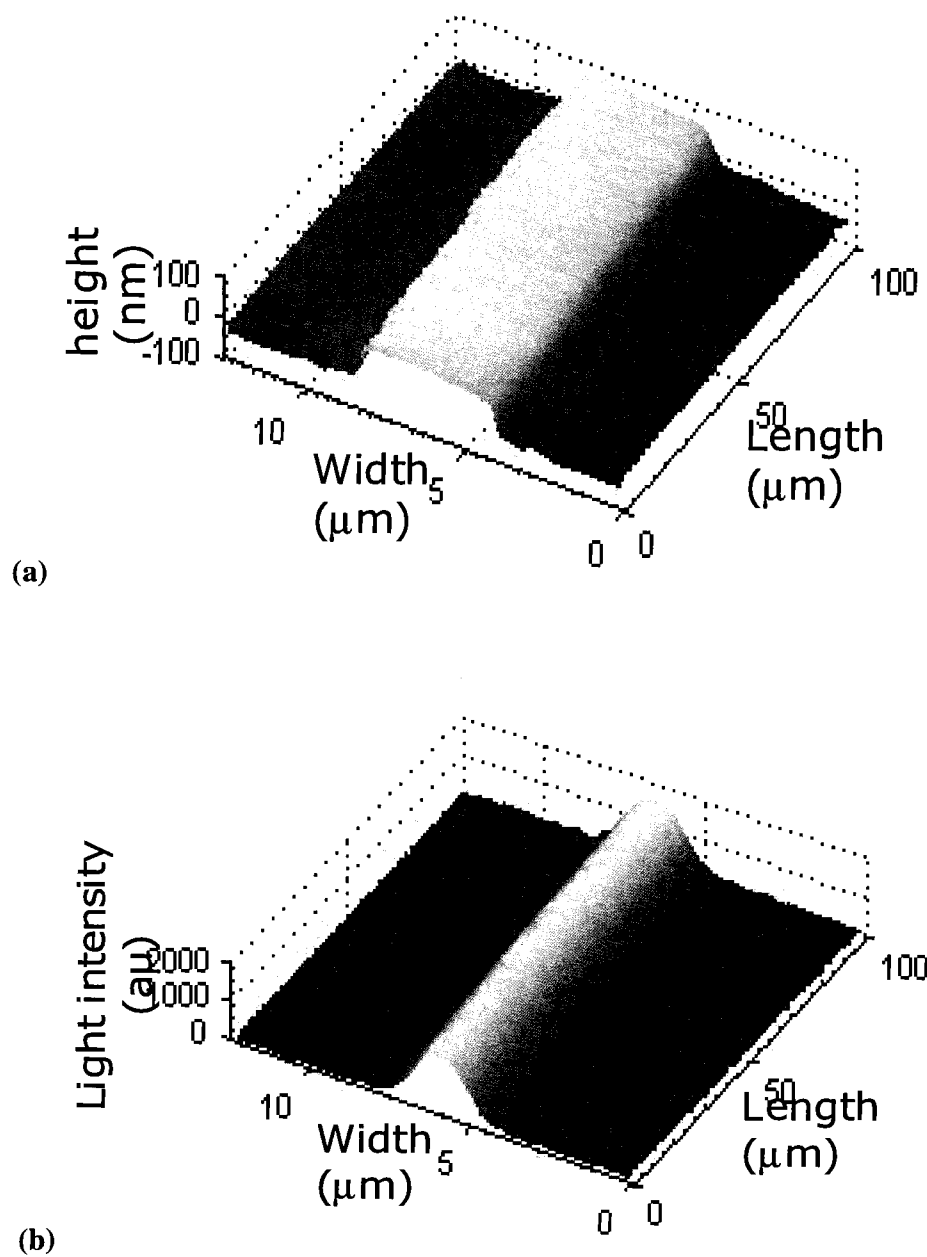


Figure 6.1: NSOM measurements of (a) surface topography and (b) optical intensity of a single mode straight waveguide.

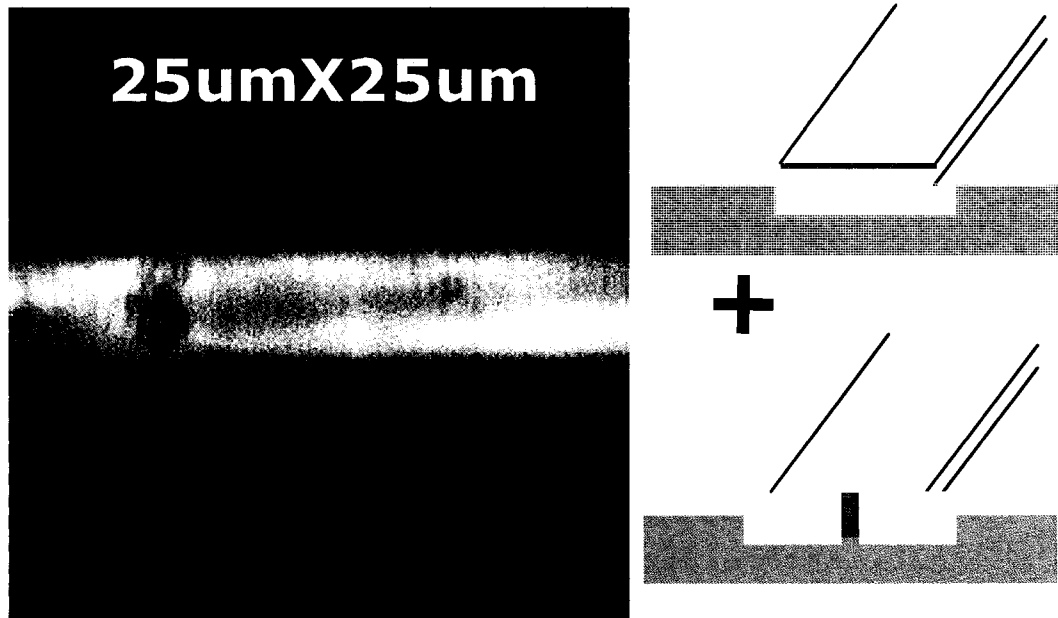
6.1.2 NSOM measurement on multimode waveguides

As opposed to a single mode waveguide, a multimode waveguide simply enlarges either core width or core thickness. The first multimode waveguide studied consists of a 105 nm thick SiN_x film deposited onto a ~2 μm thick SiO₂ lower cladding supported on a Si substrate. Air above the core serves as the upper cladding. A complete dry etching 105 nm of the SiN_x outside a 4 μm-wide ridge defined the lateral extent of the core. The calculated effective index of the waveguide was $n_{\text{eff}}=1.4718$ and effective index of the waveguide claddings was $n_{\text{eff_claddings}}=1.2633$. Therefore, the vertical and horizontal V-parameters were 0.54 and 14.5, respectively.

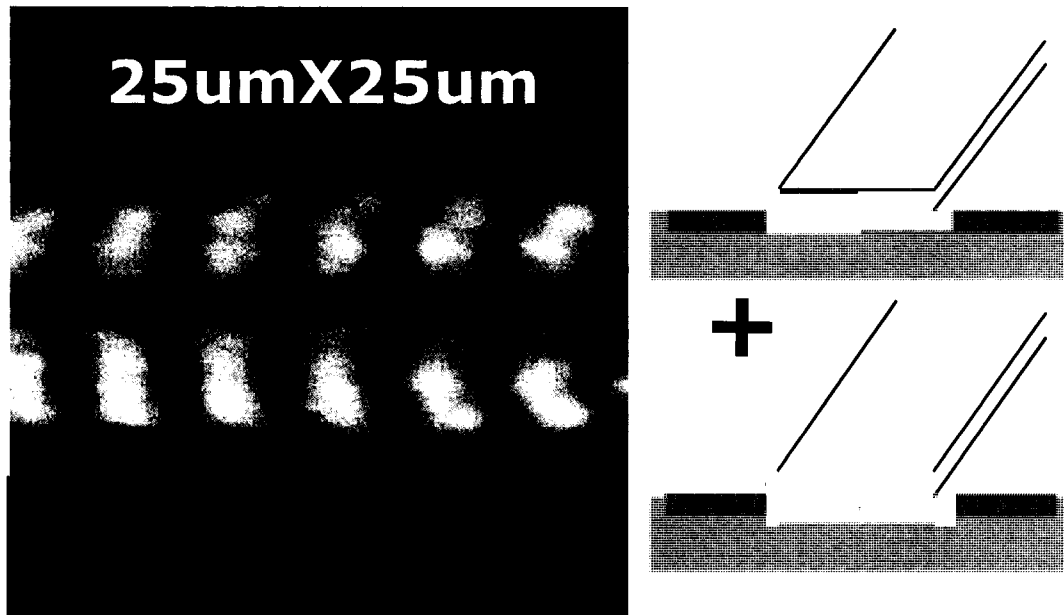
NSOM characterization revealed modal interference in this waveguide. The optical intensity pattern resulted in multiple horizontally transverse modes seen in Figure 6.2. From reading the pattern, we assert that the waveguide supports at least two waveguide modes, which were TE₀₀ and TE₁₀, confirmed by modal calculations which were discussed in Chapter 3 and Appendix A. Due to modal interference, the NSOM data in Figure 6.2 shows the maximal intensity shifting back and forth laterally as the modes travel down the waveguide with different propagation constants. The interference period was more than 25 μm which was the upper limit of the scan region of this measurement.

A second waveguide consists of a 500 nm thick of a SiN_x film on the same lower cladding and substrate. A partially dry etching of 250 nm of the SiN_x outside a 10 μm-wide ridge defined the lateral extent of the core. The calculated effective index of the waveguide was $n_{\text{eff}}=1.7330$ for the fundamental mode and effective index of the waveguide claddings was $n_{\text{eff_claddings}}=1.7020$. Therefore, the vertical and horizontal V-parameters were 2.57 and 157, respectively. The NSOM light intensity scan showed

interference between multiple vertical transverse modes as seen in Figure 6.3, where a periodic extinction of the surface intensity when the modes were out of phase at the top of the waveguide. The beat distance was much smaller than that of in Figure 6.2, indicating a larger difference in effective indices for the two modes. The effective index for the first mode was $n_{\text{eff}} = 1.5350$. The beating period was approximately $4 \mu\text{m}$, corresponding to $\Delta n_{\text{eff}} = 0.17$ which was close to the estimated difference 0.20. An interesting phenomena was that the lowest order mode in the waveguide was TE_{01} , while not the fundamental mode TE_{00} . This was probably due to a scratched waveguide facet.



(a)



(b)

Figure 6.2: Surface optical intensity shows modal interference between the schematically illustrated modes for a) a 105 nm thick and 4 μm wide waveguide, and b) a 500 nm thick and 10 μm wide waveguide.

6.2 Waveguide bends

The following section reports the experimental results from waveguide bend study as well as numerical simulation results as published in Reference [4]. Waveguide bends were frequently used in integrated optical waveguide circuits, photonic devices, and optical sensors for delivering light into specific receivers [5,6]. Several theoretical models have been used to investigate modes in waveguide bends. Among them, the conformal index transformation method was regarded as a simple and effective method to solve for the mode profile. However, experimental observations have not previously been reported on the evolution of modes in waveguide bends. Here, we will for the first time

demonstrate characterization of a 90° waveguide bend and bending waveguide mode interference.

6.2.1 Waveguide bend structure

The 90° waveguide bend studied here was fabricated using traditional sputtering, optical lithography, and etching processes that resulted in a 110 nm thick rib waveguide core of SiN_x with refractive index 1.8 on top of a 2 μm-thick SiO₂ lower cladding of index 1.45 deposited on a Si wafer. A 4 μm wide rib waveguide core was defined by partially dry etching the surrounding SiN_x layer in a CF₄/O₂ gas. Air serves as the upper cladding allowing NSOM measurements of the evanescent field above the core. The waveguide had a centerline bending radius of R_c = 400 μm. Although this was a 3-D waveguide structure, 2-D effective index conformal mapping was sufficient to determine the lateral mode profiles. Before mapping, the waveguide core region has an effective index of 1.468 surrounded by a region with an effective index of 1.45, as illustrated in Figure 6.3. The inner radius of the core was R₁ = 398 μm and the outer radius was R₂ = 402 μm. The angle between the interface where the straight waveguide enters the bend and the position being studied was θ. The waveguide sample was facet polished and coupled with a visible, 654 nm, laser diode using single mode (4/125 μm diameter) fiber.

6.2.2 NSOM measurement on waveguide bends

NSOM measurements simultaneously yielded light intensity and topography images, allowing the lateral mode position in the waveguide to be determined. Figure 6.4 illustrates a three-dimensional (3-D) NSOM surface height plot of a waveguide bend. Figure 6.5 illustrates the intensity distribution in the bending waveguide segments

centered at $\theta = 20^\circ, 40^\circ, 60^\circ,$ and 80° , with dotted lines showing the measured topographic edge of the ridge. Each scanned area was $25 \mu\text{m} \times 25 \mu\text{m}$. Strong mode interference was observed at 20° , but diminishes further along the bend. Although the bent waveguide supports a fundamental mode ($m = 0$) as well as a higher order mode ($m = 1$), the latter attenuates much faster than the fundamental. At larger angles ($\theta = 60^\circ$ and 80°), mode profiles become smooth, as the fundamental mode dominates the beam profiles.

To extract the attenuation coefficients for the two modes, α_0 and α_1 , in the presence of interference, the total magnetic field due to the interfering modes was expressed as $H(\theta, r) = A_0 H_0(r) \exp(i\beta_0 R_c \theta - \alpha_0 R_c \theta) + A_1 H_1(r) \exp(i\beta_1 R_c \theta + i\phi - \alpha_1 R_c \theta)$, where $A_0 = 0.96$ and $A_1 = 3.4$ were the relative amplitudes of the two modes, $H_m(r)$ was the transverse field distribution of the m^{th} mode, and $\phi = 0.74\pi$ was the relative phase difference in the modes at the start of the bend. Relative amplitudes of these modes were obtained by fitting the measured NSOM intensity profiles. Similarly, by fitting the evolution of the profile as well as the combined intensity, it was estimated that the attenuation loss of the fundamental and the first order mode were $0.46 \text{ dB}/90^\circ$ and $15.1 \text{ dB}/90^\circ$, respectively. The extracted coefficients produce transverse intensity profiles in good agreement with the NSOM measurements. Similar to the use of tightly coiled fibers to strip higher order modes, the greater than 14 dB difference in attenuation of the first higher order mode demonstrates that planar waveguide bends can be used as practical mode filters.

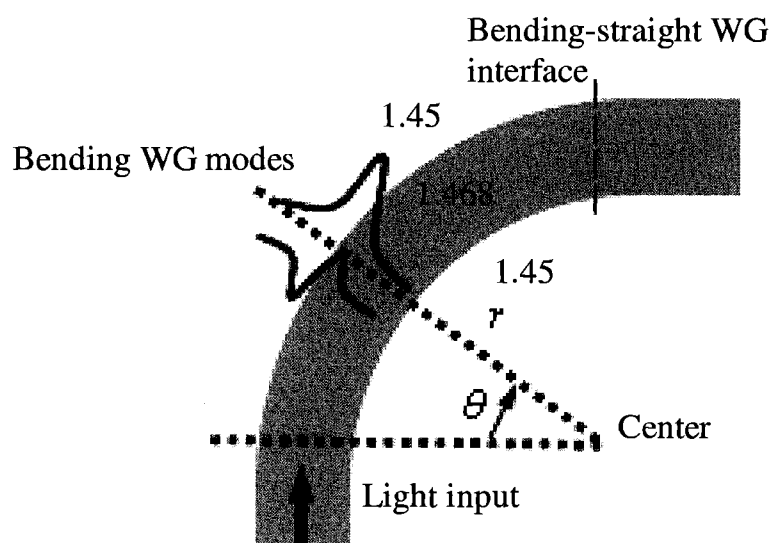


Figure 6.3: Schematic diagram (not to scale) of a 90° waveguide bend connected to straight sections. The effective indexes of the waveguide core and cladding regions were 1.468 and 1.45 respectively. The waveguide bend supports two guided modes.

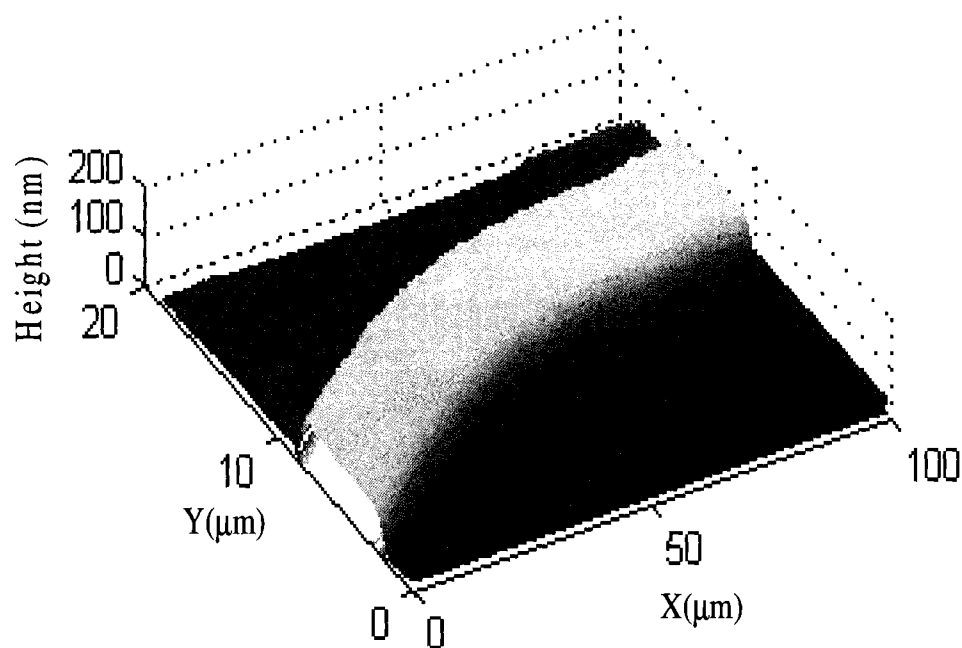


Figure 6.4: 3-dimensional NSOM surface height plot.

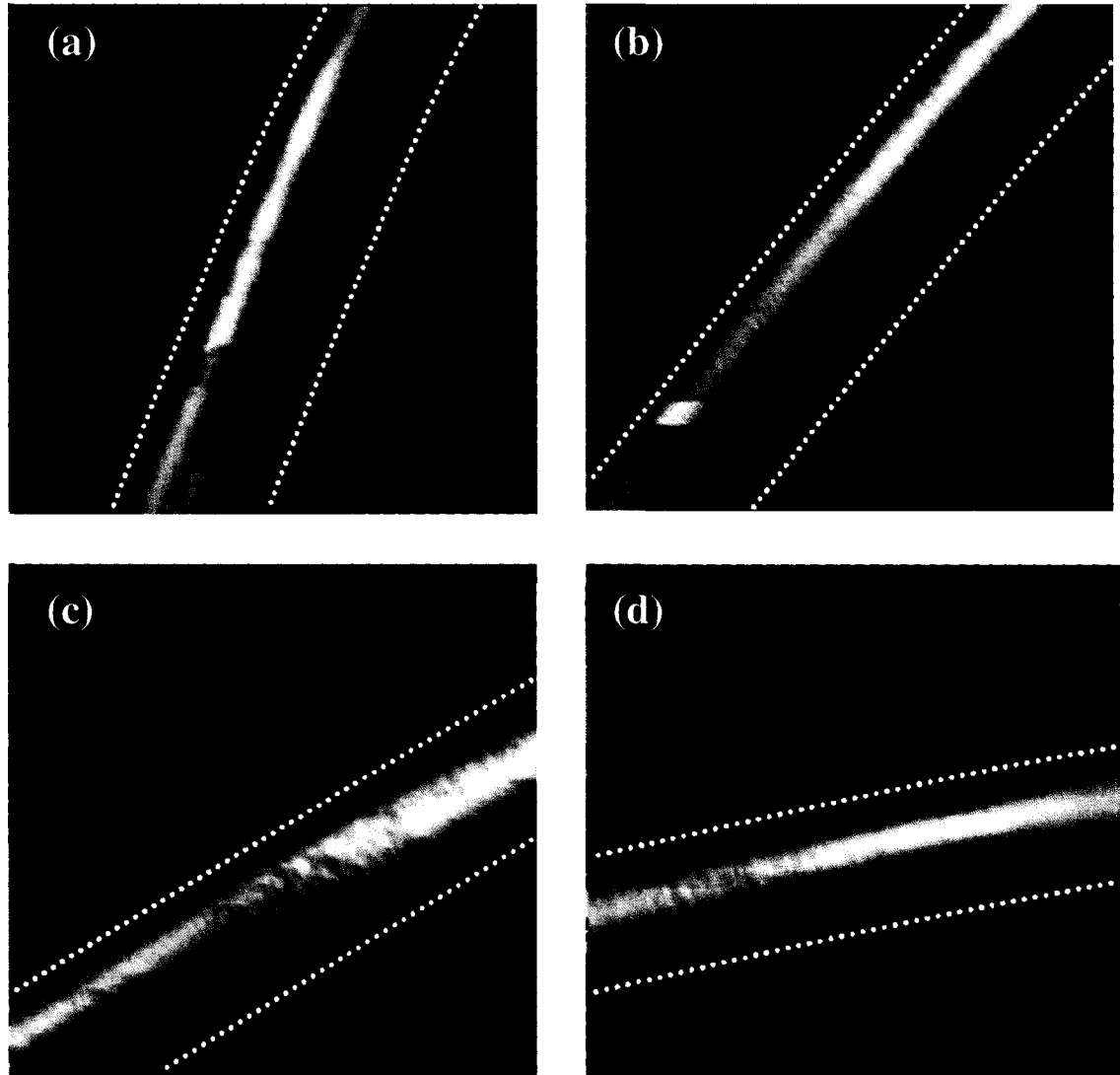
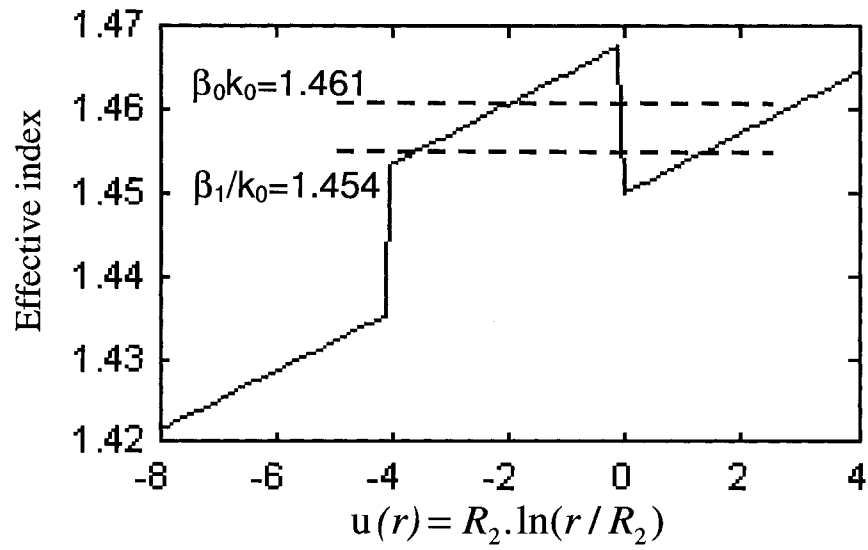


Figure 6.5: NSOM images of optical intensity at (a) 20°, (b) 40°, (c) 60°, and (d) 80°, from the start of the waveguide bend. Dotted lines denote the waveguide core boundaries. As determined from simultaneous topographical scans.

6.2.3 Numerical calculation

A conformal index transformation based on new coordinate parameters $u(r) = R_2 \ln(r/R_2)$ and $n(u) = n(r)e^{u/R_2}$ were used to solve for the waveguide mode profiles, $H_0(r)$ and $H_1(r)$, in the bend. As a result, a tilted effective index profile was shown in Figure 6.6(a) with arrows corresponding to the outer (I) and inner (II) core boundaries. The one-dimensional (1-D) mode calculation found only two lateral TE modes ($m = 0$ and 1) can be supported in this waveguide bend. Detailed description of the 1D mode calculation was discussed in Chapter 3. Effective indexes for both modes were illustrated in Figure 6.6 (a) by two dashed lines, which were $\beta_0/k_0 = 1.461$ and $\beta_1/k_0 = 1.454$ where β_m was the propagation constant for the m^{th} mode and k_0 was the free space wave-vector. H-field profiles of the two modes in the waveguide bend were plotted in Figure 6.6 (b). Dashed lines indicate the waveguide core boundaries. These modes were similar in shape to those for the straight waveguide but were shifted off center toward the outer boundary.

The evolution of the transverse mode profiles were illustrated in Figure 6.7. The measured values at different angles were shown as points, and theoretical fitting curves were shown as solid lines. The intensity profiles clearly show the presence of multimode interference which decays along the length of the bend. In particular, at 80° the mode profile was dominated by the fundamental mode.



(a)

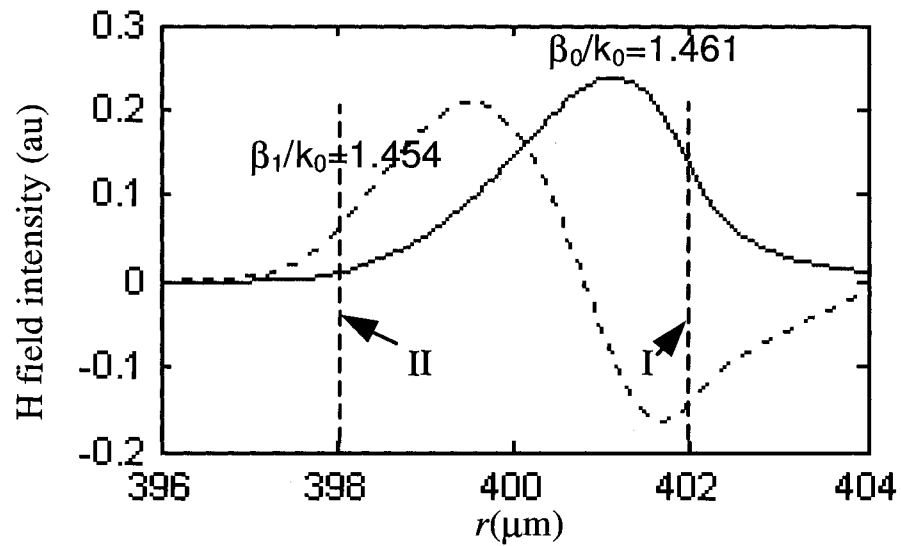


Figure 6.6: (a) Effective refractive index profile in the waveguide bend. Dashed lines mark the effective indexes of the guided modes, (b) H-field profiles of the guided modes in the bend.

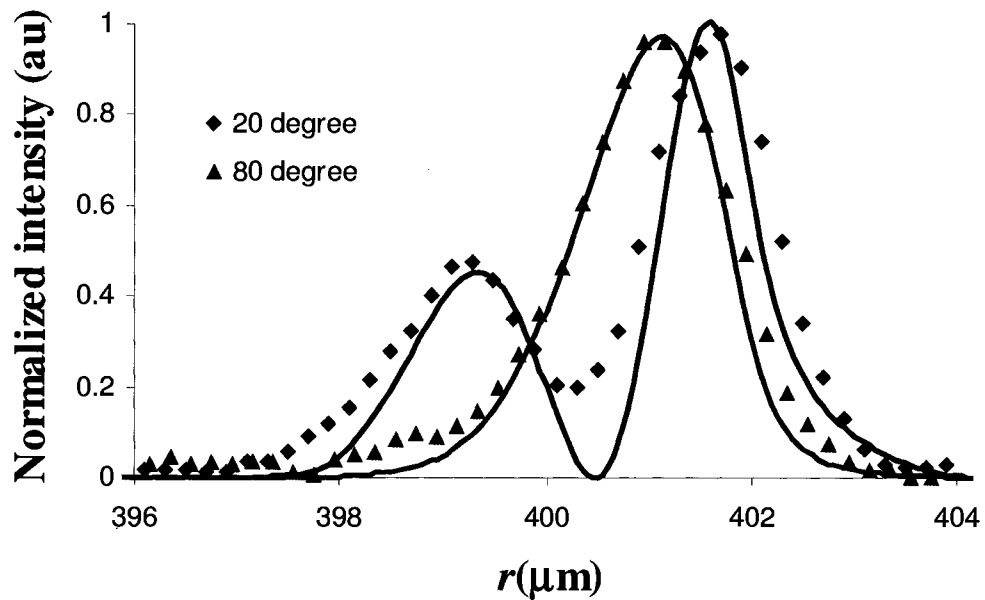
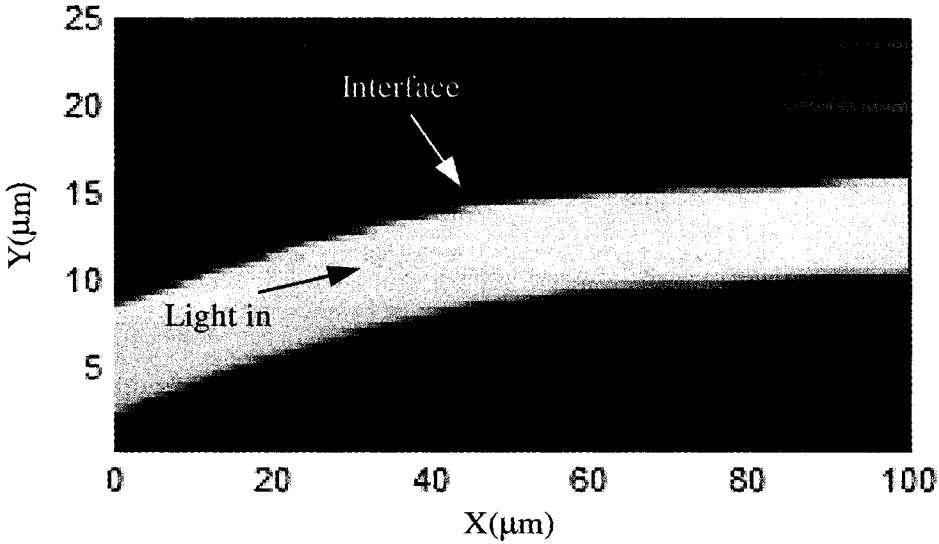


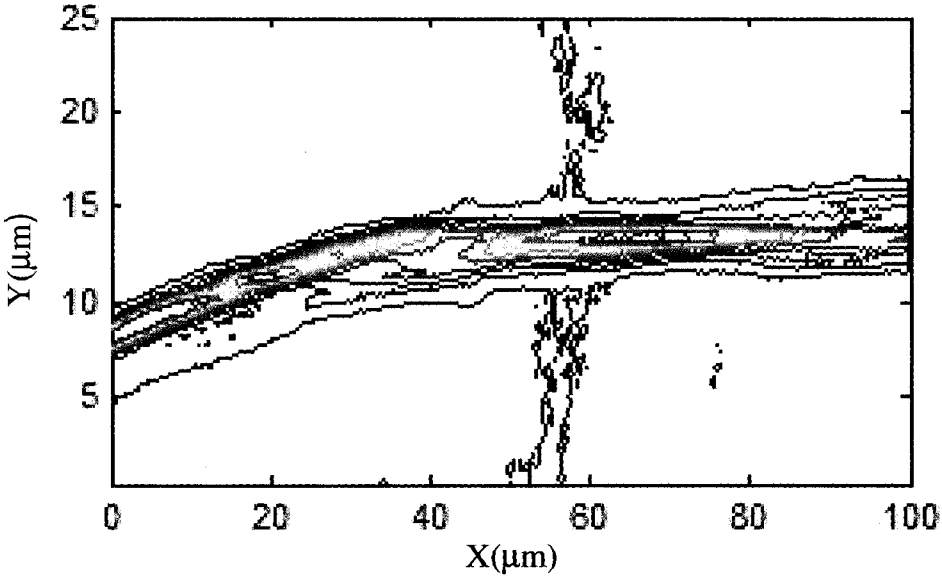
Figure 6.7: Optical intensity distributions at different positions. Points were NSOM experimental data and solid curves were the theoretical fit.

Additional insertion loss due to scatter was found at the exit interface from the bending waveguide to the straight waveguide. Figure 6.8(a) shows a NSOM intensity scan of this region. At the end of the bend, 92% of the power was in the fundamental mode, which was strongly shifted toward the outer boundary. However, in the straight waveguide, the power distribution was symmetrically centered for all modes. Therefore, at the interface, scattered light as well as guided modes of the straight waveguide was excited, as clearly seen in Figure 6.8(b). The scattering field was observed to be directed perpendicular to the straight waveguide. Further study was needed to understand this observation. However, it was evident that it may be useful to engineer the exit waveguide to match the modes of the bend or otherwise gradually shift the mode toward the center

of the straight waveguide to reduce this insertion loss. Possible solutions to reduce the insertion loss include implementation of a width-varying bends or adaptation of an offset between the straight waveguide and waveguide bend.



(a)



(b)

Figure 6.8: (a) False intensity image of waveguide topology around the bend-to-straight waveguide interface. (b) Contour plot of optical intensity in the same area.

6.3 Local evanescent field array coupled (LEAC) waveguide biosensor

In proof of concept experiments, near-field scanning optical microscopy (NSOM) studies have been conducted to investigate the field modulation prior to fabrication of buried photodetectors. The following sections represent research work on local evanescent field array coupled (LEAC) waveguide biosensors by Dr. Kevin Lear, Dr. David Dandy and Dr. Charles Henry's groups at Colorado State University. Portions of the following section are taken from co-authored publications with these groups. Adlayers of different materials were studied, including SiN_x , photoresist and immunoassay complexes. Continuing work has been done towards characterization of a complete sensor with buried detectors.

6.3.1 Pseudo-adlayer measurement and simulation

The following section reports the experimental results as well as numerical simulation results published in Reference [7]. To mimic an adlayer on the waveguide top surface, a 105 nm thick SiN_x film was first deposited on a SiO_2/Si wafer using NH_3/argon sputtering, where the SiO_2 lower cladding thickness was about 2 μm . A 2 μm wide ridge waveguide core was defined by partially dry etching the surrounding SiN_x layer in CF_4/O_2 plasma. The etch depth and thus ridge height was determined to be 21 nm. An artificial adlayer was created by masking 10 μm wide bars oriented perpendicular to the waveguide, and etching the exposed SiN_x an additional 17 nm. The waveguide core thickness after the adlayer etch was 88 nm, and the ridge depth was 21 nm. A longitudinal cross section of the resulting waveguide and adlayer structure was illustrated in Figure 6.9 (a). The top surface of the SiN_x film was left exposed to the air that serves

as the upper cladding, allowing the NSOM to examine the evanescent field there. Refractive indices of the core and lower cladding were 1.8 and 1.45, respectively.

6.3.1.1 Beam Propagation Method simulation

Optical propagation through the waveguide with the adlayer structure was simulated by two-dimensional bidirectional beam propagation method (BPM) using commercial software from RSoft. The BPM simulation method was introduced in Chapter 3.

The incident beam was assumed to be the TE_{00} mode at a wavelength of 654 nm. The three regions of the waveguide before, coincident with, and after the adlayer were referred to as Regions I, II, and III, respectively. The image of electric field magnitude in Figure 6.9 (b) clearly shows an interference effect in Region III. The interference was due to the excitation of a leaky mode in addition to the guided mode.

Since the two modes have different propagation constants, the phase difference between them accumulates as they propagate, causing a sinusoidal intensity evolution due to mode beating. The effective indexes of the guided and dominant leaky mode in Region III were 1.459 and 1.441, respectively. Since the effective refractive index of the leaky mode was less than 1.45, which was the refractive index of the lower cladding. The leaky mode propagates into the lower SiO_2 (1.45 refractive index) cladding and gradually dissipates. The light intensity in the waveguide core of the adlayer region, as shown in Figure 6.9 was stronger than other simulation regions. This was because an adlayer on the waveguide surface effectively changes the refractive index profile. As we discussed in Chapter 2, this results a less evanescent field in the lower cladding region and high

optical confinement of the waveguide core. The effective indexes of the guided and dominant leaky mode in Region II were 1.472 and 1.444, respectively.

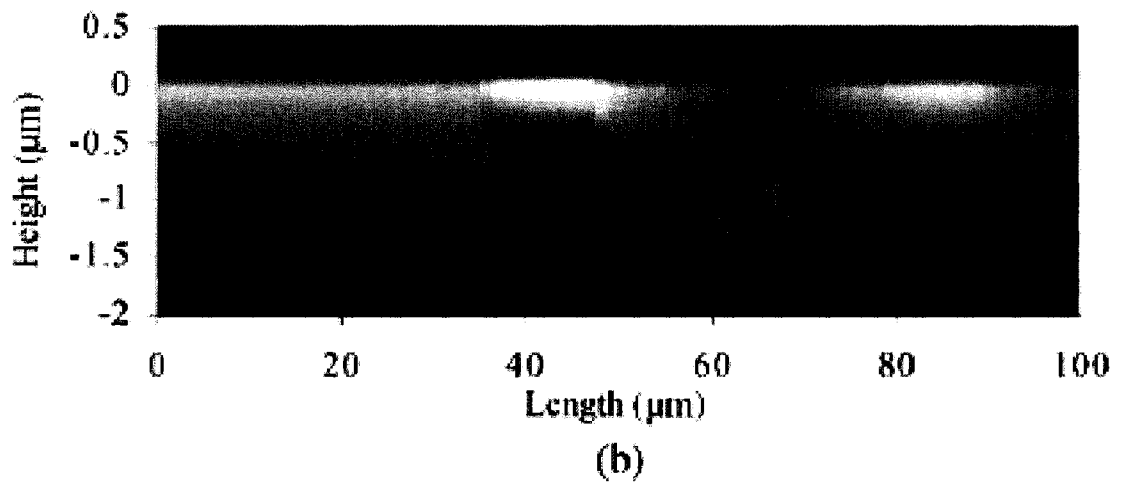
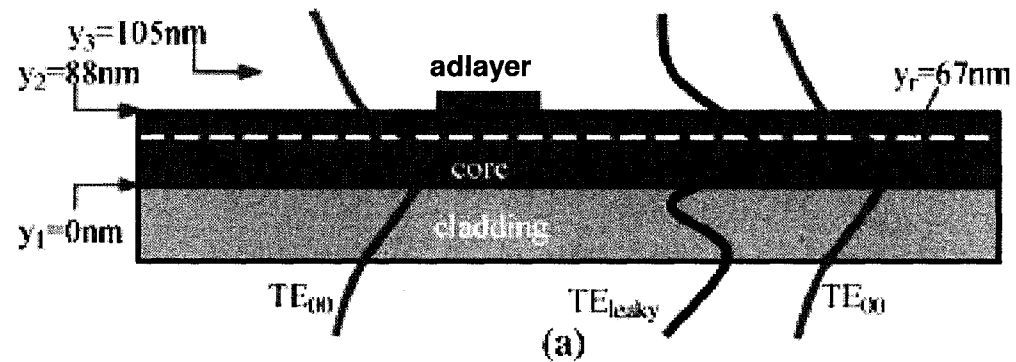


Figure 6.9: (a) Cross section of waveguide and adlayer and (b) BPM simulation of transverse electric field magnitude.

6.3.1.2 NSOM measurement on pseudo-adlayer

NSOM was used to measure the evanescent field changes due to intentional SiN_x adlayer formed on top surface of the waveguide core. NSOM experiments yielded light intensity and topography maps simultaneously. Figure 6.10(a) shows a topography image over a $10 \mu\text{m} \times 100 \mu\text{m}$ scanned area based on surface height information. The waveguide width appears larger than $2 \mu\text{m}$ because of the NSOM tip size. Light was coupled into the waveguide approximately 4mm to the left of the area shown. Figure 6.10(b) illustrates a simultaneously obtained contour plot of the measured light intensity from the same scanned area. The image clearly shows a strong change in the optical evanescent field when the wave encounters the adlayer region. Modal calculations determined that the waveguide supports only one guided mode, TE_{00} , in all three regions. The 4 mm distance from the input facet assures a stable mode in Region I. As a result, a Gaussian shaped optical field profile was found corresponding to the guided TE_{00} mode in Region I in agreement with the modal calculation.

Lateral optical field profiles were plotted in Figure 6.11 positions (a) before the adlayer, (b) at minimal light intensity after adlayer and (c) at maximal light intensity after adlayer. The background intensity level was due to the scattered light from the reference laser and was constant at different positions. In position (a), before the adlayer, a Gaussian-shaped optical field profile corresponds to the guided TE mode in the waveguide. At positions (b) and (c) after the adlayer, the optical profiles represent destructive and constructive interference, respectively, between the guided mode and the leaky mode. Although the transverse profiles in Region III remain symmetric, their

distributions were narrowed and broadened 20% at points of destructive and constructive interference, respectively.

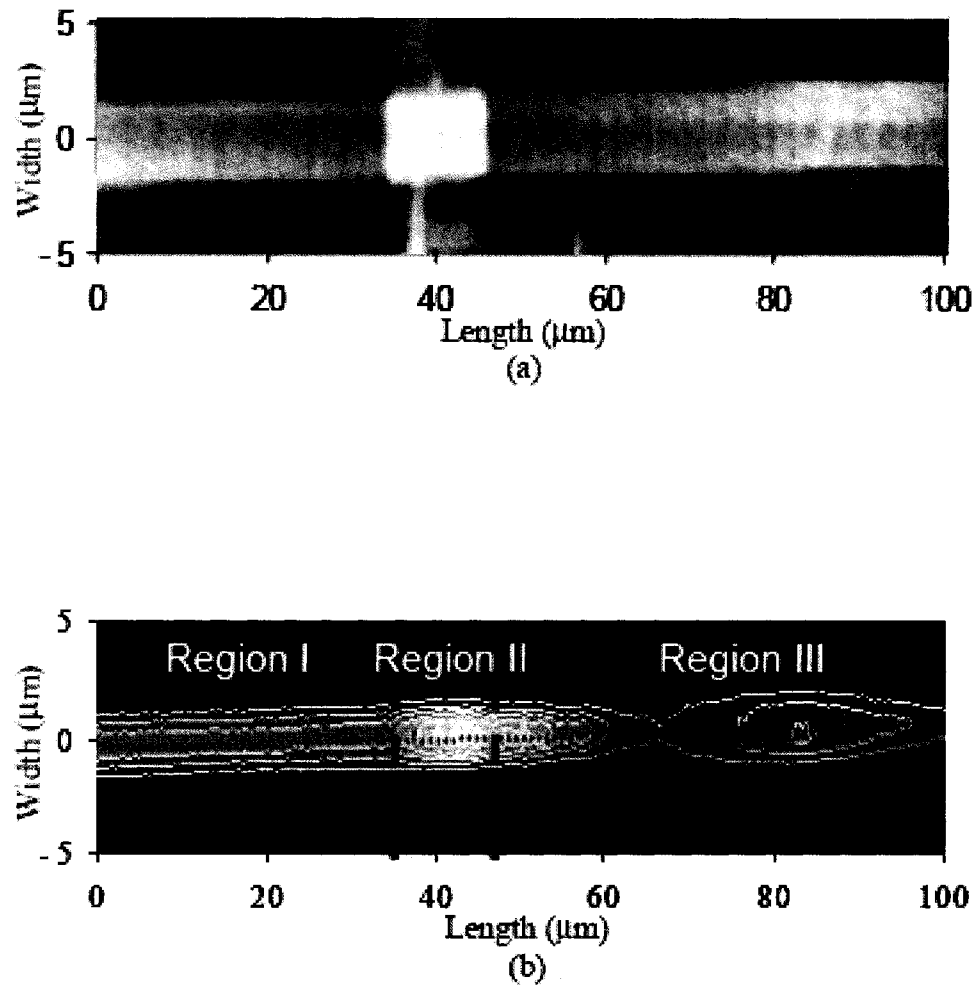


Figure 6.10: (a) Grayscale plot of the topography along the waveguide and (b) grayscale and contour plot of measured light intensity for the same region. The horizontal dotted line shows the centerline used for the longitudinal intensity plot. The three regions of the waveguide before, coincident with, and after the adlayer were referred to as Regions I, II, and III, respectively.

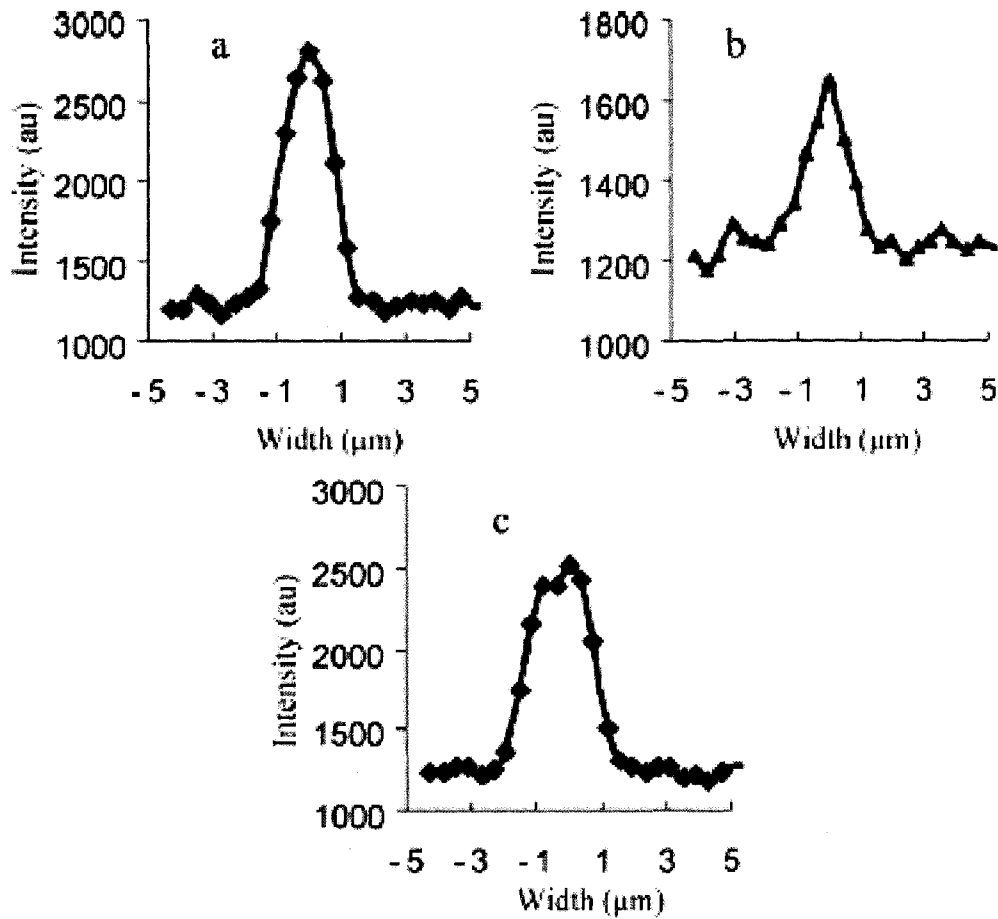


Figure 6.11: Measured optical intensity distributions as a function of transverse position in the waveguide at positions (a) before the adlayer, (b) at minimum light intensity after adlayer and (c) at maximum light intensity after adlayer.

The intensity distribution along the centerline of the waveguide from both NSOM measurements and BPM simulations were presented in Figure 6.11, along with the surface height. The BPM simulation results, which include no adjustable parameters, agree very well with the measured results. The input power level when subtracted off the

background ($P_{bg}=1000$ counts) was $P=1760$ counts and the maximum intensity change, in Figure 6.11, was $\Delta P=1420$ counts. Thus optical intensity modulation capability of the adlayer was about $\Delta P/P=81\%$.

Noise in the measured intensity originates from the scattered light due to the surface roughness. The average noise level was approximately $P_n=26$ counts and therefore the estimated optical SNR was 55:1. This result supports the potential of this waveguide sensor configuration to analyze nanoscale adlayers, such as molecular monolayers.

In Region III, a large, damped oscillation of the evanescent field was observed as well as predicted by BPM calculations. The effective index of the guided mode was 1.459. In addition to the guided mode, a strong leaky mode of effective index 1.441 was also excited by the field perturbation in the adlayer region, which gradually dissipates in Region III by leaking into the lower cladding (SiO_2 , $n=1.45$). The 1-D modal calculation uses absorption boundary condition as described in Chapter 3. Fitting the measured data with an exponential decay curve produces an estimated attenuation coefficient of 152 dB/cm for the leaky mode while the guided mode attenuation was 8 dB/cm. The average interference period was measured to be 36 μm , again in good agreement with the 38 μm period predicted by BPM simulations and corresponding to a difference of in effective index for the guided and leaky mode.

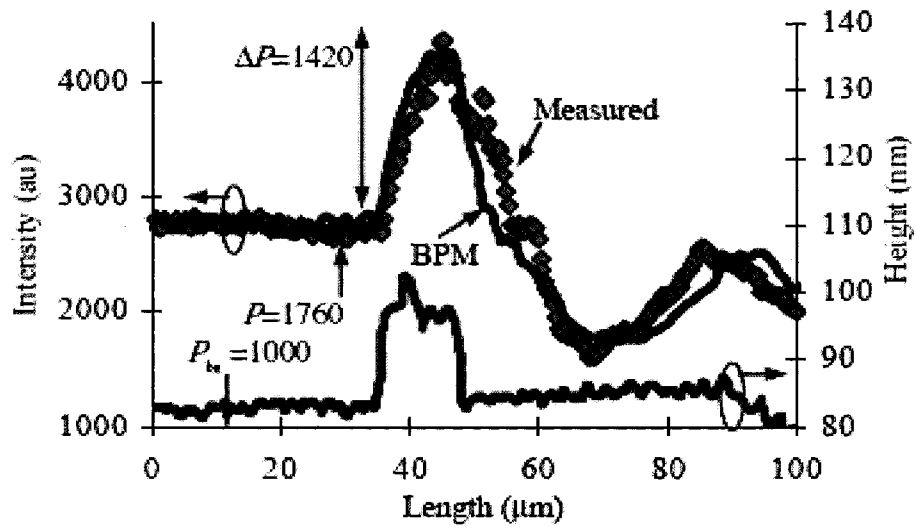


Figure 6.12: Longitudinal dependence of the optical field (top) based on BPM simulation (solid) and NSOM measured data (diamonds) and surface height (bottom).

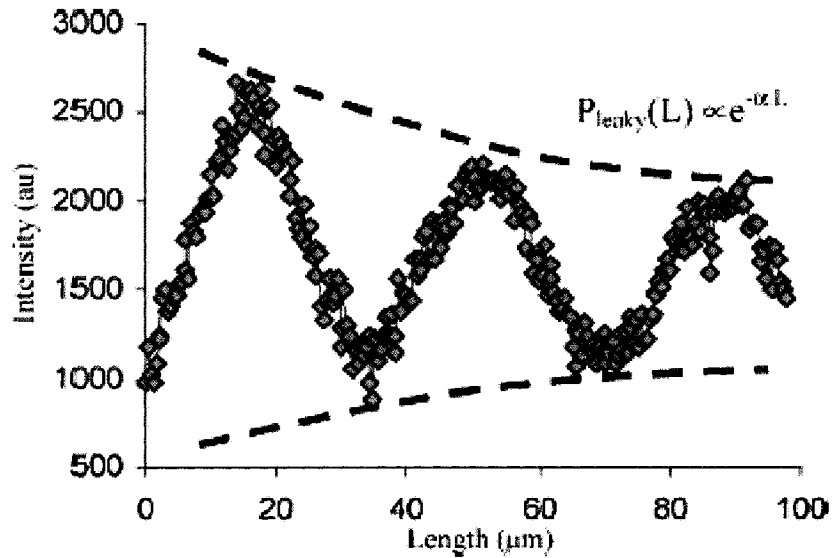


Figure 6.13: Measured optical intensity oscillation after adlayer (diamonds) and exponential decay fit to envelope amplitude (dashed line).

Another measurement was done on 8nm-thick, 5 μm -long adlayers spaced by 35 μm . The region outside the 3 μm wide ridge waveguide was etched by 31 nm. The optical field, seen in Figure 6.14, appears noisy due to multimode interference. Despite this noise, the signal to noise ratio was approximately 40:1 [8].

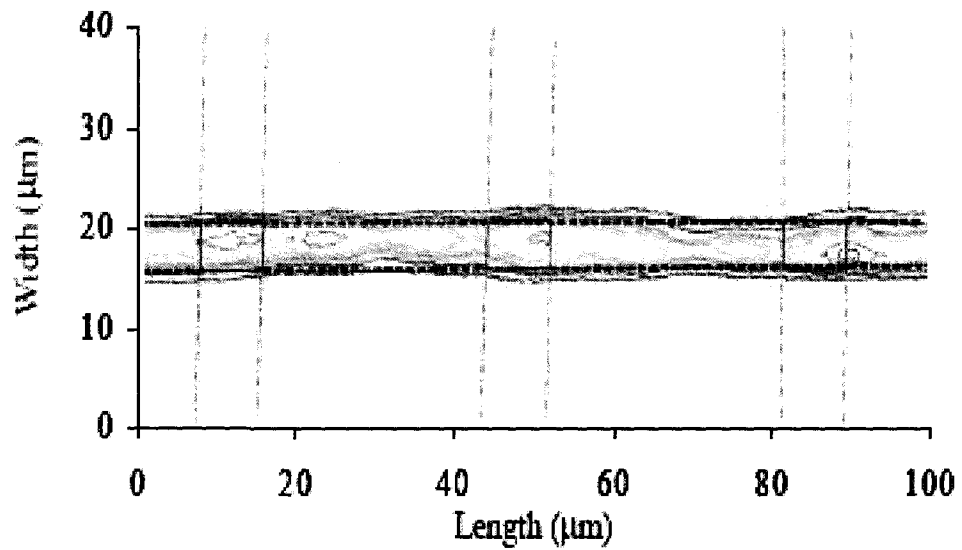


Figure 6.14: Contour plot of measured light intensity along the waveguide. Light propagates from left to right. The vertical dashed lines show the locations of the adlayers and the horizontal dashed lines indicate the edges of the waveguide.

6.3.2 Low refractive index adlayer measurement and simulation

Although strong evanescent field modulations were observed with intentional step changes of the waveguide core, the adlayers' refractive indices were too high to represent that of real biological materials. Here we report field response of the LEAC sensor to a lower refractive index material that provides better mimic to the refractive index of proteins [9]. So, we chose to investigate adlayers made of photoresist (Shipley 1818) which has a refractive index $n=1.56$ close to an average $n=1.43$ for most biological materials.

6.3.2.1 Beam Propagation Method simulation

For the waveguides, a 105 nm thick SiN_x film was deposited on a SiO_2/Si wafer using NH_3/argon sputtering, where the SiO_2 cladding thickness was about 2 μm . A 2 μm wide ridge waveguide core was defined by dry etching 16 nm of the surrounding SiN_x layer in a CF_4/O_2 plasma. An artificial adlayer of photoresist (Shipley 1818, $n=1.56$) was patterned by photolithography to create a 10 μm wide bar oriented perpendicular to the waveguide. The photoresist thickness ranged from 90 to 120 nm as determined by the topographic profiling capability of the α -SNOM system from WiTec. Figure 6.15 shows a longitudinal cross-sectional view of the waveguide and the photoresist adlayer. The three regions of the waveguide before, coincident with, and after the adlayer were referred to as Region I, II and III, respectively.

Optical propagation through the waveguide with the photoresist adlayer structure was simulated by two-dimensional bidirectional beam propagation method (BPM) using commercial software by RSoft, shown in Figure 6.16. The incident beam was assumed to

be the TE_{00} mode at a wavelength of 654 nm and the adlayer thickness was taken as 100 nm. Modal calculations determined that the waveguide supports only one guided mode, TE_{00} , in all three regions.

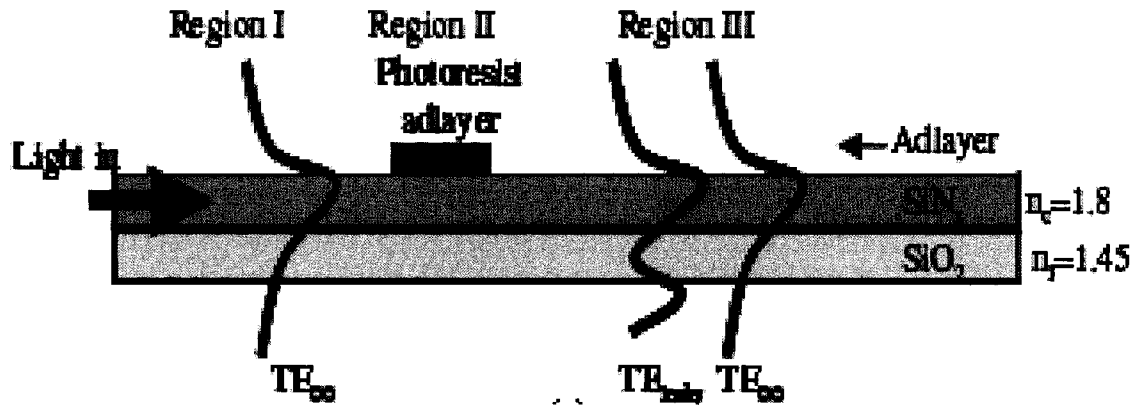


Figure 6.15: Longitudinal cross-sectional view of the waveguide and photoresist adlayer configuration.

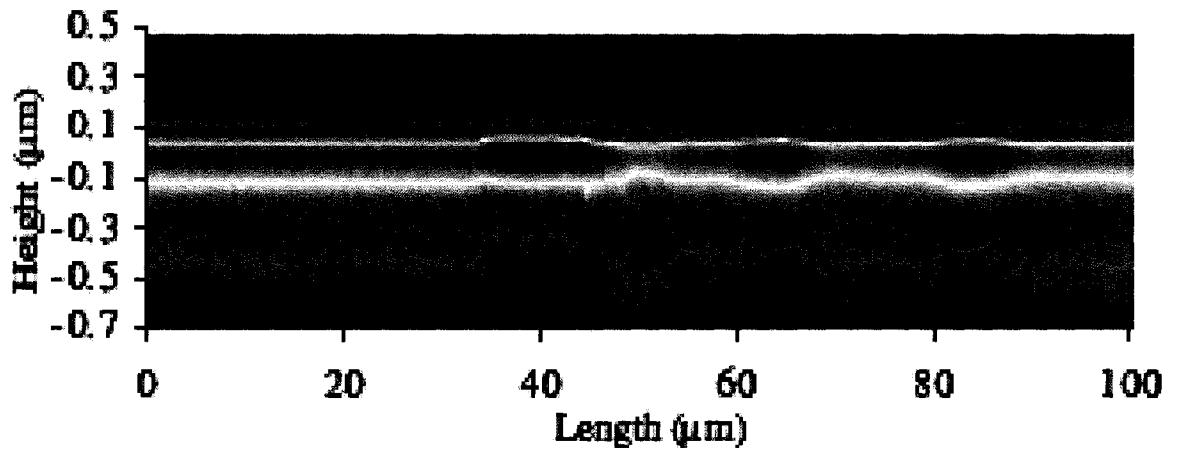
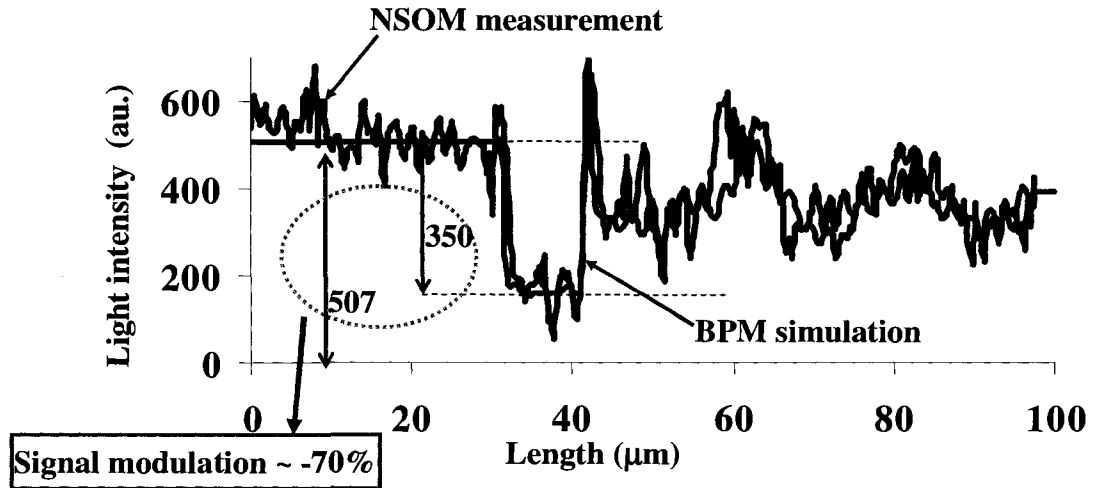


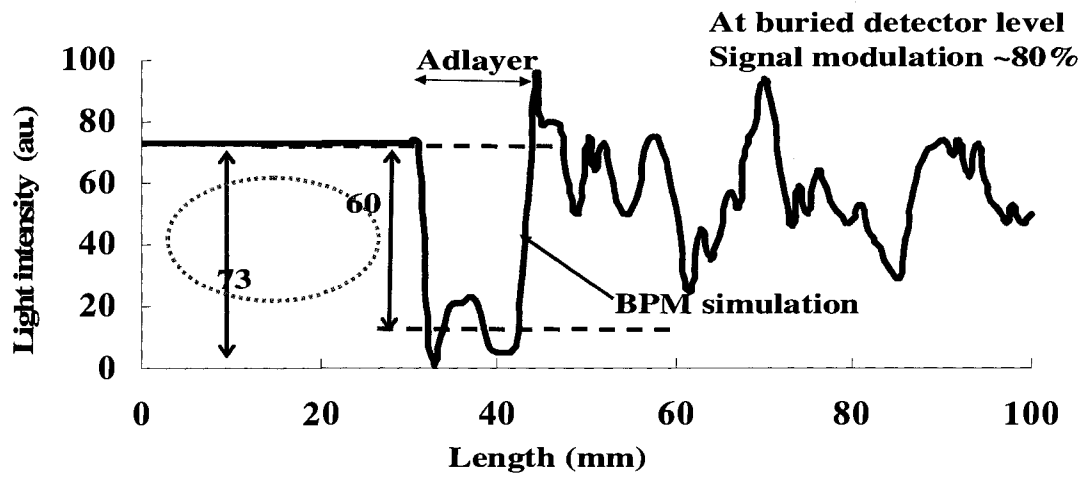
Figure 6.16: False color plot shows the BPM simulated electrical field distribution.

6.3.2.2 NSOM measurement on lower refractive index adlayer

Similar to our previous observations, NSOM measurement revealed a transient modal interference originating from the mode beating between the bound mode and the leaky mode in Region III. The strength of the oscillation was taken as an important indicator of the adlayer's optical properties because the optical intensity modulation depth was directly related to the thickness of the adlayer and the adlayer's refractive index. The modulation depth in this case was defined as the difference between the input intensity in Region I and Region II in the adlayer region. The thin blue curve in Figure 6.17(a) represents the corresponding plot of the measured light intensity along the top surface of the waveguide in Region I and III, and along the top surface of the photoresist in Region II. The plot clearly shows a strong change in the optical evanescent field when the wave encounters the adlayer region and, in Region III, a large damped oscillation of the evanescent field was observed as expected. The modulation depth in Region III was unique to the height of the photoresist adlayer for a given refractive index. The BPM simulation results, which contain no adjustable parameters, agree very well with the measured results as shown as by the thick red curve in the same plot in Region I and III. The difference in the Region II was because the experimental data was obtained on the top of the photoresist while the BPM data was obtained still on the top surface of the waveguide core. The input intensity in Region I was 507 counts and the difference between input intensity and the minimum intensity in Region III immediately after the adlayer was 350 counts. Thus estimated modulation depth was approximately -70. Figure 6.16(b) shows the simulated optical field intensity response to the adlayer at the photodetectors level. A positive signal modulation was obtained and approximately 80%.



(a)



(b)

Figure 6.17: (a) the corresponding plots of the NSOM measured (thin blue) and BPM simulated (thick red) light intensity along the top surface of the waveguide in Region I and III and the photoresist in Region II, (b) BPM simulated field modulation at the photodetectors level.

6.3.3 Immunoassay adlayer measurement

Recall the mechanism of the LEAC sensor relies on specific binding of analytes or targets to one of several localized regions of immobilized biological molecular probes, such as antibodies or ssDNA, to modify the waveguide cross-section and thus shift the local evanescent field. An array of photodetector elements along the length of the waveguide can sense the modification in the evanescent field due to local adlayers of bound analytes or targets, such as antigens.

Besides inorganic and photoresist adlayers, NSOM measurements were conducted by the LEAC sensor investigators on immunoassay complex adlayers. The adlayer consists of biotinylated BSA, strept-avidin, anti-CRP and CRP layers. The total thickness of the immunoassay adlayer ranges from 12nm without CRP to 15nm with 95% CRP coverage [10,11]. The multiple layer immunoassay complex was uniformly patterned on the waveguide surface via microfluidic channels.

For the first experiment, we demonstrate the optical field response of the sensor to a 18 nm thick immunoassay complex. The multiple layer immunoassay complex was patterned on to waveguide surface via a single microfluidic channel. The channel length is 75 μm . The adlayer consists of BSA, biotin, Anti-CRP, and FITC labeled CRP layers as illustrated in Figure 6.18(a). Figure 6.18(b) and (c) show the NSOM topologic and light intensity scans over a 20 μm by 100 μm region. The adalyer measured approximately 75 μm long, and the 2 μm wide ridge waveguide only supports one waveguide mode, the fundamental TE mode. The total SiN_x thickness is 90 nm and the waveguide ridge height is 10nm. The calculated effective index of the waveguide before the adlayer is $n_{\text{eff}}=1.4570$ and $n_{\text{eff_claddings}}=1.4504$ for the claddings. Therefore, the vertical

and horizontal V-parameters are 0.5 and 1.3, respectively. The calculated effective index of the adlayer region is $n_{\text{eff}}=1.4640$ and $n_{\text{eff_claddings}}=1.4563$ for the claddings, which has a horizontal V-parameter 1.4.

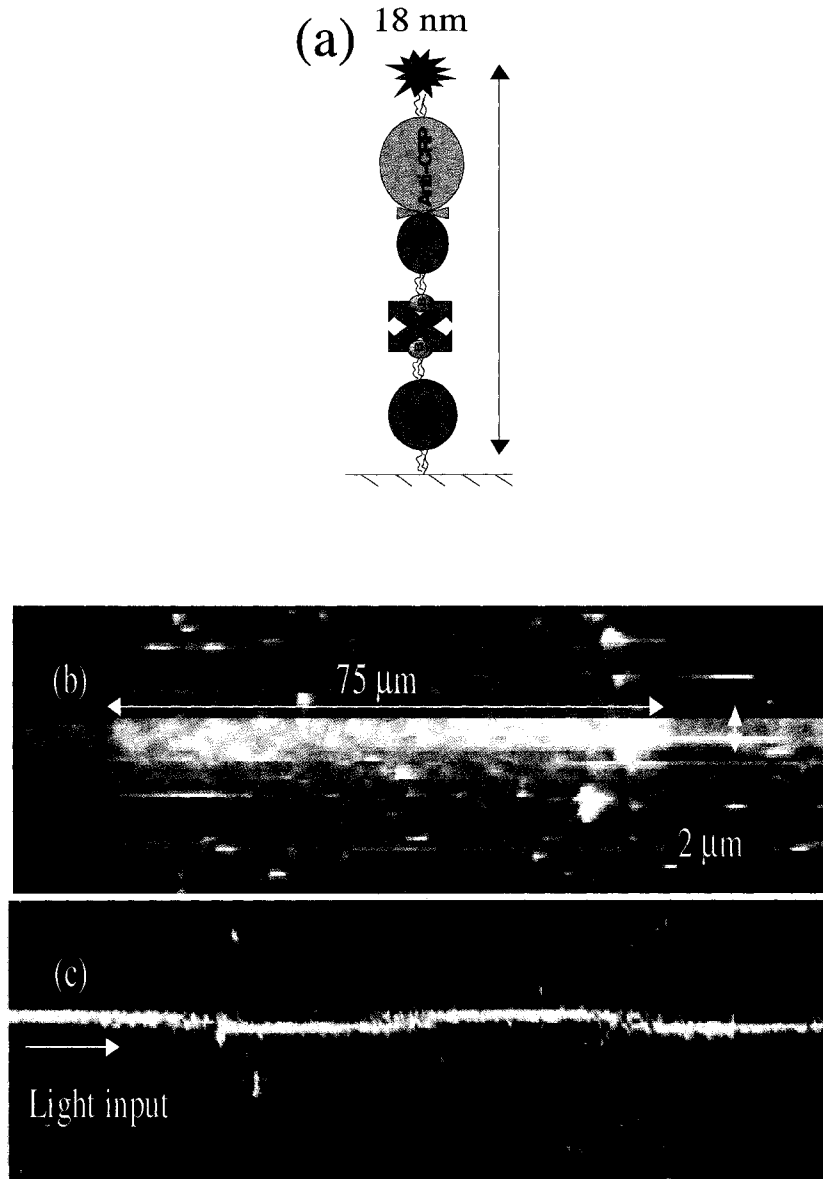


Figure 6.18: (a) Schematic of adlayer, (b) topologic, (c) light intensity,

When the light is incident on the adlayers, a periodic interference in the light intensity is observed. Since the local refractive index of the adlayer region is increased that enables the waveguide to guide more than the fundamental mode. The line scans of the height and light intensity are plotted in Figure 6.19, both along the center line of the waveguide. The optical interference in the adlayers region is resulted from the modal beating from the guided and leaky modes which will be discussed in following text. The beating period is approximately $60 \mu\text{m}$ which gives $\Delta n_{\text{eff}}=0.011$, while the calculated $\Delta n_{\text{eff}}=0.007$ for the fundamental and leaky mode.

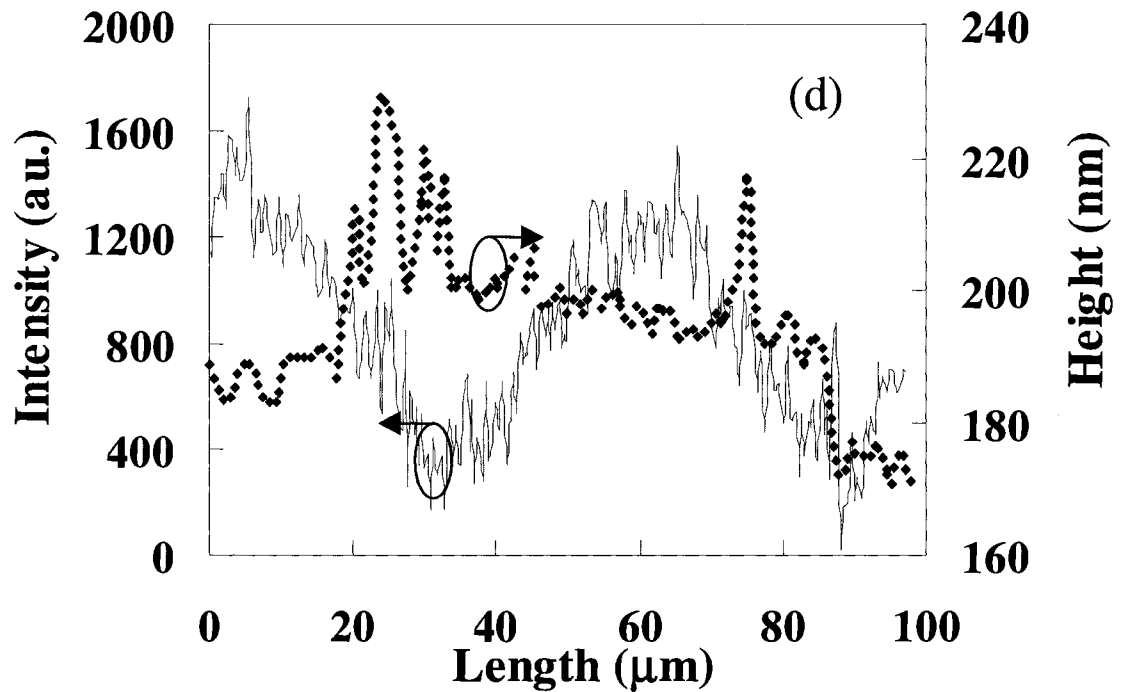


Figure 6.19: Height scan and light intensity scans along the center line of waveguide.

In the second experiment, we studied the response of the optical field to an immunoassay adlayer with 95% CRP coverage, shown in Figure 6.20(a). The concentration of the CRP solution is 1 mg/ml. The waveguide is approximately 2 μm wide and has a ridge height of 10 nm. Figure 6.20(b) shows the NSOM topographic images over 20 μm by 200 μm region along the waveguide that confirms the adlayers extend approximately 75 μm along it. Light propagating from left to right has a Gaussian distribution with the intensity profile before entering the region that confirms a single mode waveguide configuration. Analysis of the longitudinal intensity along the waveguide is plotted in Figure 6.20(c), which indicates the adlayer increases the average intensity. The input light intensity is 787 counts and the average light intensity increase due to the existence of the adlayer is 796 counts. Therefore the light intensity of the waveguide sensor is about 101% for only a 15nm (measured) high adlayer. Strong intensity oscillations are observed after the immunoassay complex that match our previous experimental results.

The third experiment was done with multiple adlayers on the waveguide. The waveguide's ridge height is 16.5 nm. Three 50 μm long features, as shown in Figure 6.21(a), are patterned on the waveguide, each with different CRP layer coverage. The CRP solution concentrations in the three channels are 1) 0mg/ml, 2)0.6 μg /ml, and 3)0.6mg/ml. As a result, the surface coverage are 0%, 1% and 90% respectively. The analysis shows that light intensity modulations are 12.8%, 15.7% and 30.2% correspondingly, shown in Figure 6.21(b). The CRP adlayer's thickness is 3 nm, therefore the differential signal is 0.26dB/nm. For a 90% CRP coverage, the light

modulation is much lower than the 95% CRP experiment. The reason may be due to light confinement that is sensitive to the waveguide's ridge heights [11,12].

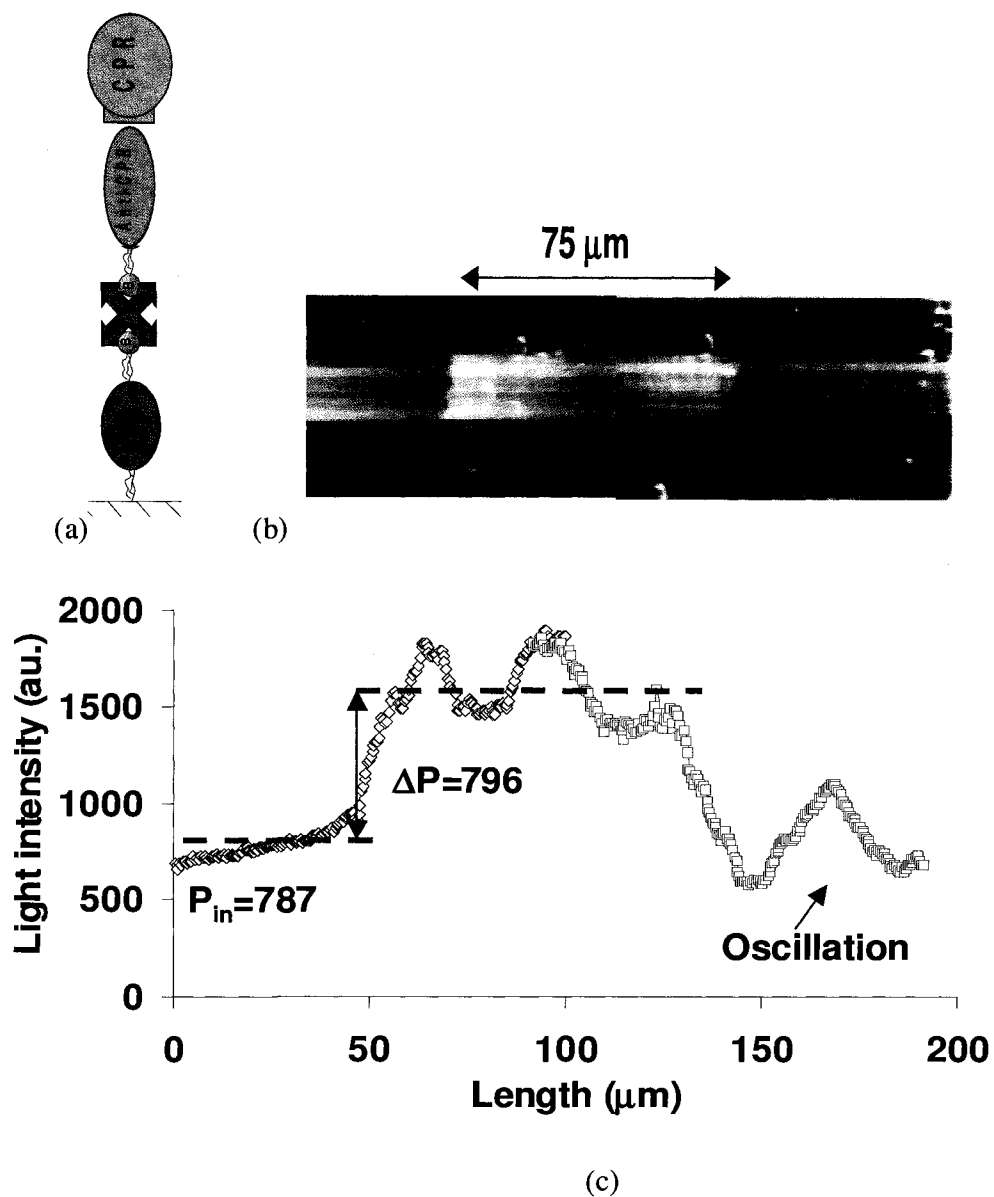
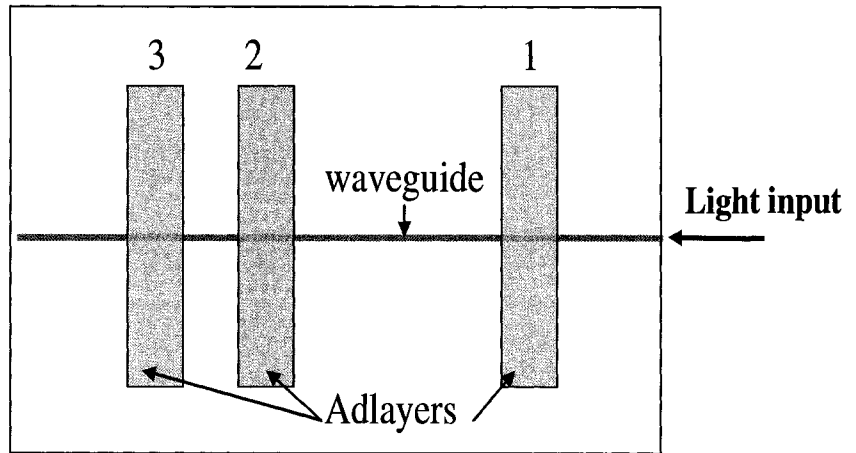


Figure 6.20: (a) An immunoassay complex consists of biotinylated BSA, Strept-Avidin, Anti-CRP and CRP. (b) NSOM topology image of a 95% coverage CRP layer on the waveguide. (c) Light intensities along the waveguide.

Patterned features:

- 1: No CRP
- 2: Dilute CRP
- 3: Saturated CRP



(a)

	Surface Coverage	Intensity Modulation
0.6mg/ml	90%	30.2%
0.6ng/ml	1%	15.7%
0ng/ml	0%	12.8%

(b)

Figure 6.21: (a) Schematic of multiple-immunoassay adalyer with different CRP coverage and, (b) table of the CRP coverage vs. intensity modulations.

6.4 LEAC sensor with buried detectors

Buried detector arrays for the optical waveguide biosensor were also designed, fabricated in commercial CMOS technology and tested [21-26]. In following section, we will discuss the experimental results from buried detector studies for the LEAC sensor, which were originally published in Reference [13]. The buried photodetectors offer an evanescent detection system integrated on the same chip as the waveguide, eliminating the need for NSOM to study the field distribution modification due to adlayers. Initial results demonstrate high sensitivity to both bulk refractive index changes and an 8 nm thick BSA biological film.

6.4.1 Sensor structures

The completed LEAC sensors were fabricated using commercial 0.35 μm CMOS technology where optical waveguides, photodetectors, vias, and two-metal interconnect layers were integrated on silicon wafers, shown in Figure 6.21. The LEAC sensors were obtained by following a sequence of steps similar to those employed in conventional CMOS gate, dielectric, contact, and first layer metal processes. The complete sensor structure is shown in Figure 6.22. A sensor structure has been designed that integrates an optical waveguide above an array of polysilicon metal-semiconductor-metal (MSM) photodetectors. In the sensor configuration, the photodetectors are placed 1.4 μm from the waveguide core into the lower cladding, shown in Figure 6.23, to enhance the fractional signal modulation and reduce the effective absorption coefficient. Due to challenges in molecular probe immobilization, the sensors were initially tested with thin, bulk adlayers on the waveguide.

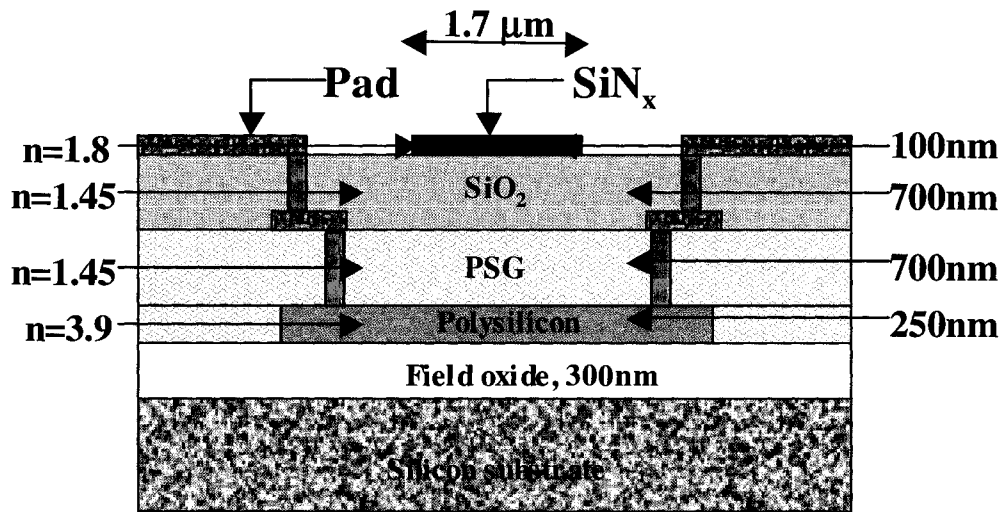


Figure 6.21: (a) Schematic of the cross-sectional end view of the waveguide and photodetectors

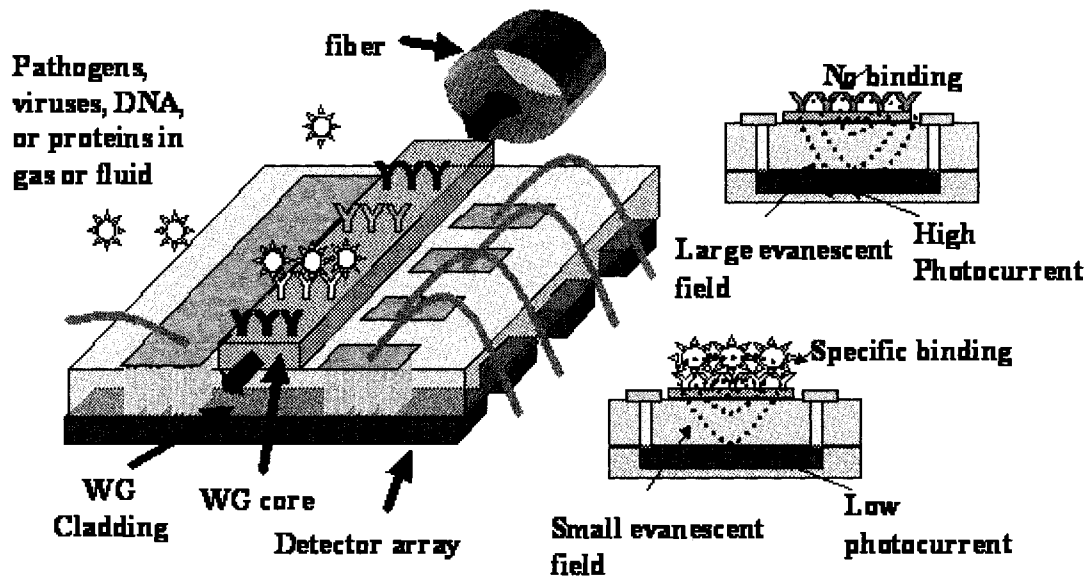


Figure 6.22: Schematic of the waveguide sensor. Specific binding of pathogens or other analytes shifts the local mode profile that can be detected either via near-field scanning optical microscopy or buried detector arrays.

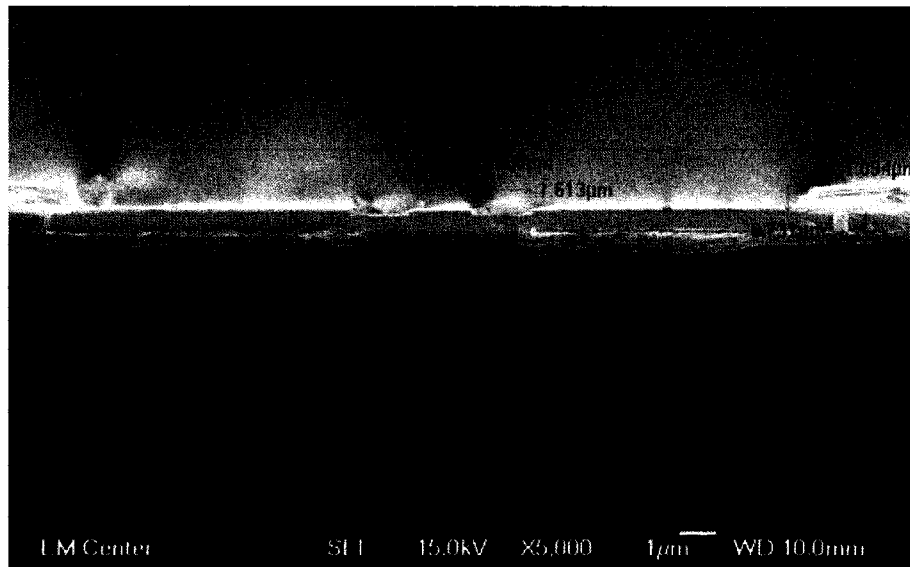
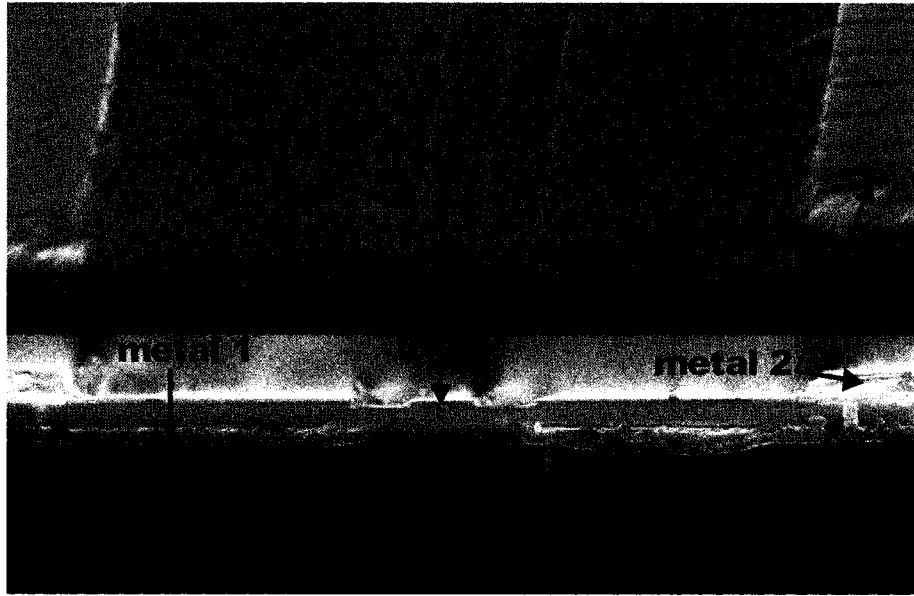


Figure 6.23: SEM images showing the top surface of the sensor superimposed over the cross-sectional end view

6.4.2 Photocurrent measurement

The integrated sensor chips are fiber coupled and tested with different sensing region materials to establish their response. First, the waveguide end facets at the edges of individual die are polished for end-fire coupling of a 654 nm laser diode via visible single mode fiber (4/125 μm core/cladding diameter). A pair of probe needles applies voltage bias between each of the individual detector pads and the common ground pad that creates an electric field oriented perpendicular to the direction of light propagation. The photocurrents are measured using either an HP 4145 semiconductor parametric analyzer or a Keithley 2400 SourceMeter. Figure 6.24 shows the test configuration. Due to mode mismatch between the output of the 4 μm diameter fiber and the 1 μm mode field diameter of the waveguide, coupling efficiency is low, and only approximately 10 μW is coupled into the waveguide. When biased, the photodetectors operated as expected. The DC photocurrent and dark current of a 98 μm long photodetector with 5 μm contact spacing across a 1.7 μm wide waveguide is shown as a function of bias in Figure 6.25. The mean photocurrent-to-dark-current ratio is approximately 1:1 for the bias range. This ratio can readily be improved by coupling more light into the waveguide.

Figure 6.26 shows the photocurrent measurements of large-pitch (100 μm) array detectors with air and oil as the waveguide upper cladding. Due to the high refractive index contrast between the waveguide core and air, the waveguide mode intensity tails out into the lower cladding and into the highly absorbing photodetectors. Photocurrents are proportional to the light in the guided mode and decrease along the waveguide as the power in the waveguide is attenuated. The measured photocurrent decay rate was 15.6 dB/mm or $\alpha_{\text{air}}=35.9 \text{ cm}^{-1}$ with air as the upper cladding. When oil ($n = 1.45$) was placed

on the waveguide top surface to reduce the index contrast, the photocurrent decay rate dropped to 4.3 dB/mm or $\alpha_{oil}=9.9 \text{ cm}^{-1}$. The signal modulation for an individual detector is estimated based on the assumption that the input power P_{in} is the same with air or oil. Therefore the absorbed optical powers are $P_{air}=P_{in}(1-e^{-\alpha_{air}L})$ and $P_{oil}=P_{in}(1-e^{-\alpha_{oil}L})$, where L is the length of the detector. The signal modulation strength, $\Delta = (P_{air} - P_{oil})/P_{air} \cong (\alpha_{air} - \alpha_{oil})/\alpha_{air}$, when the detector length L is small. Based on the measured absorption coefficients, the signal modulation is $\Delta_{oil/air}=72\%$.

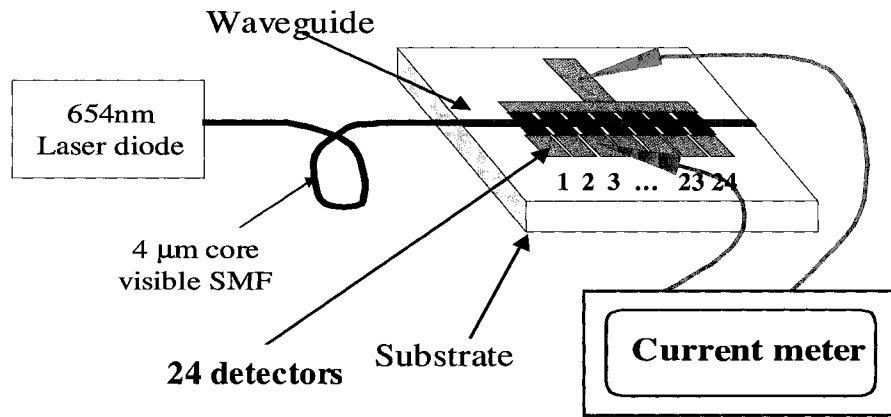


Figure 6.24: Apparatus for testing integrated waveguide sensors.

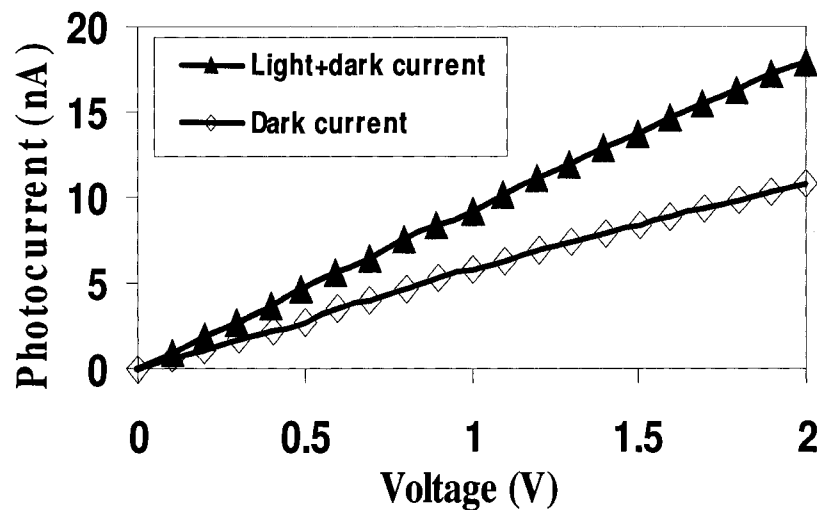


Figure 6.25: Dark current and photocurrent of a 98 μm long photodetector.

Two potential mechanisms may contribute to the reduced decay rate in the presence of higher index fluids. The intended operation relies on the increased upper cladding index to shift the evanescent field away from the photodetectors, lowering both the absolute photocurrent at the beginning of the waveguide and the optical, and thus photocurrent, decay rate along the waveguide. However, the lower index contrast between the cladding and core also reduces scatter due to sidewall roughness. The ratio of scattering loss for oil and air is $(n_{\text{core}}^2 - n_{\text{oil}}^2)/(n_{\text{core}}^2 - n_{\text{air}}^2) = 0.51$. Even if all scattering is attributed to sidewall roughness, the expected decrease in attenuation of 49% is notably less than the observed decrease in attenuation of 72%, indicating that a measurable amount of the attenuation change is due to the desired sensing mechanism. The change in photocurrent decay rate due to evanescent field shift will be more dominant in lower loss samples employing partially etched ridge waveguides.

In addition to bulk index changes, a film on the surface of the waveguide can also modulate the power received by the underlying detectors. Another experiment was carried out to measure the detector response to a monolayer of biotinylated bovine-serum-albumin (Bio-BSA) film adsorbed onto the waveguide surface. A 1% BSA solution is commonly used to block non-specific adsorption of proteins and other molecules on surfaces, and its thickness is typical of biological adlayers created via immunoassay and hybridization. The waveguide sample was first cleaned using de-ionized water. Then the sample was incubated with Bio-BSA solution for 30 minutes, and the excess solution was dried in a nitrogen stream. The decay rates of the photocurrents measured using a medium pitch (10 μm) photodetector array with and without the BSA layer were 17 dB/mm and 31 dB/mm, respectively, as shown in Figure 6.27. The 14

dB/mm difference resulting from the 8 nm thick film corresponds to 1.75 dB/mm/nm.

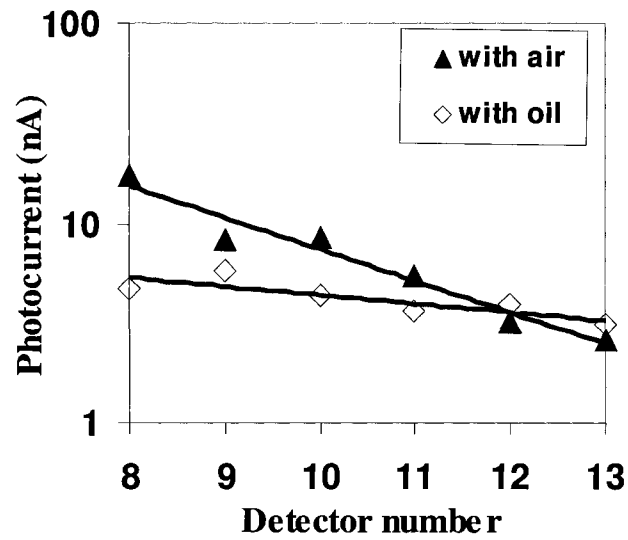


Figure 6.26: Photocurrent measurements with air (filled triangles) and oil (open diamonds) as upper claddings.

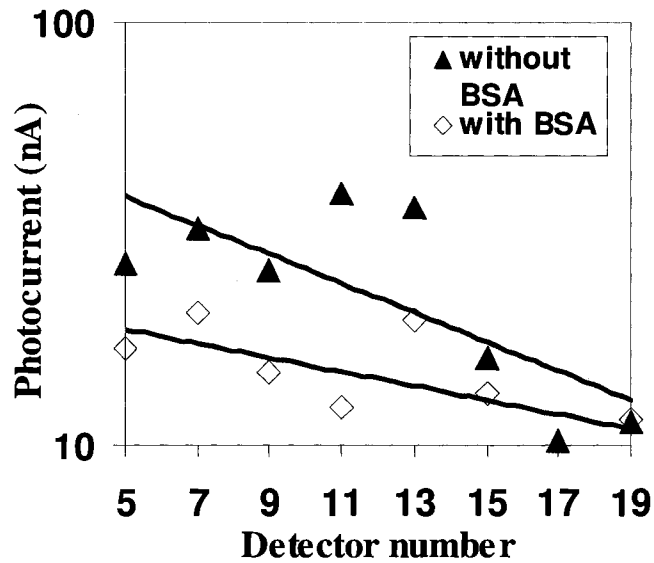


Figure 6.27: Photocurrent response to an 8 nm BSA layer covering the waveguide's top surface. The anomalously high photocurrents for detectors in the center of the array, such as detector 11 and 13, are attributed to uncoupled light scattering from probes.

6.5 Leaky mode waveguide coupled photodetectors

This section reports work that was part of a project to investigate an optical clock distribution system for high-end processors implemented in commercial CMOS technology as a platform for on-chip optical interconnect studies that were published with co-authors[14,15].

6.5.1 Photodetector structure

Progresses has been made in developing high efficient waveguide coupled photodetectors. Nathan et al [16] reported photodetectors relying on coupling light from 12 μm thick, 20 μm wide SU8 multimode waveguides into silicon pn photodiodes which demonstrated effective absorption coefficients ranged from a minimum of 2.2×10^{-3} dB/ μm to a maximum of 3.05×10^{-3} dB/ μm , somewhat exceeding all of the precedent results except for those of Baba and Kokobun [17]. The latter authors coupled an optical waveguide with a SiO₂ core to a silicon p-n photodiode, achieving effective absorption coefficients of up to 0.027 dB/ μm with an anti-reflection coating and 0.001 dB/ μm without an anti-reflection coating.

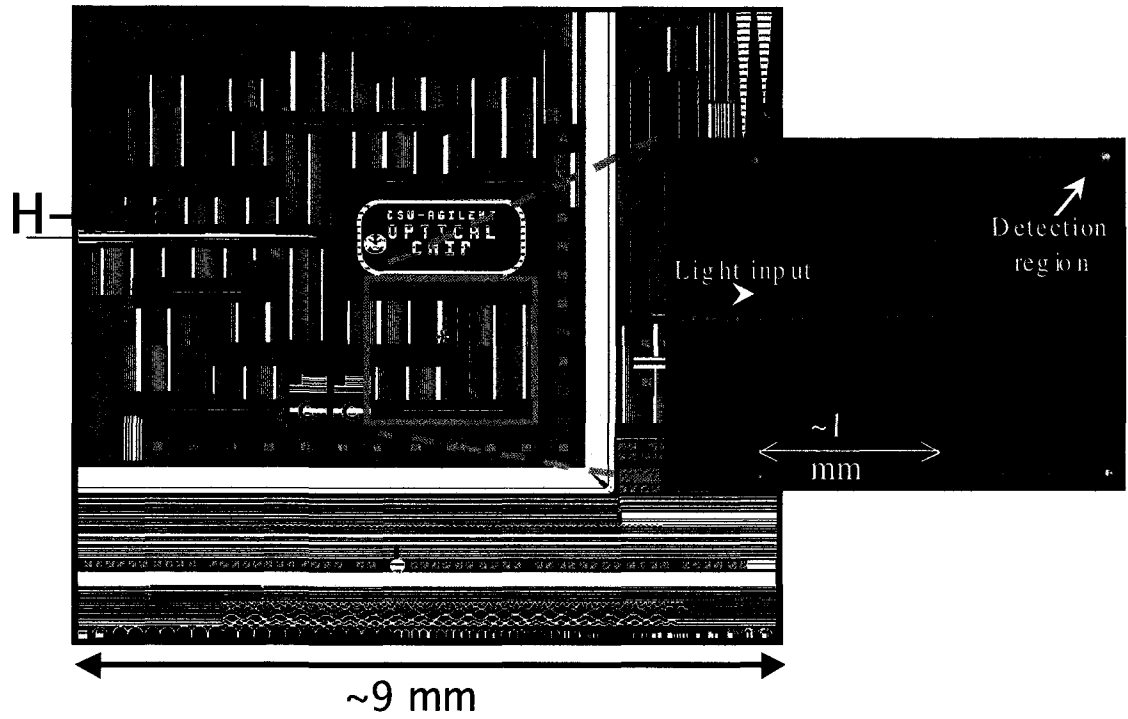
Our leaky-mode waveguide coupled photodetectors, as a continuing work to and, in contrast to and, use only materials and processing, which exist in standard commercial CMOS technologies. These detectors can be placed at any point in the backend of the process and do not occupy substrate area, although a low temperature polysilicon or amorphous silicon deposition was required if the detectors were positioned after the first level of metal. The on-chip optical interconnects chips were fabricated using commercial 0.35 μm CMOS technology on 6-inch wafers at the Avago Technologies facility in Fort

Collins, Colorado. Figure 6.28 (a) illustrates the completed 16-node H-tree waveguide interconnects with T-shape splitters and leaky mode coupled photodetectors. The inset shows a microscopic image of the lit H-tree. The SiN_x waveguides and polysilicon metal-semiconductor-metal (MSM) photodiode structures, shown in cross-section in Figure 6.28 (b), were obtained by following a sequence of steps described in reference [14,15]. All thicknesses and refractive indices shown in Figure 6.28 (b) were nominal values, where air serves as the upper cladding of the waveguide.

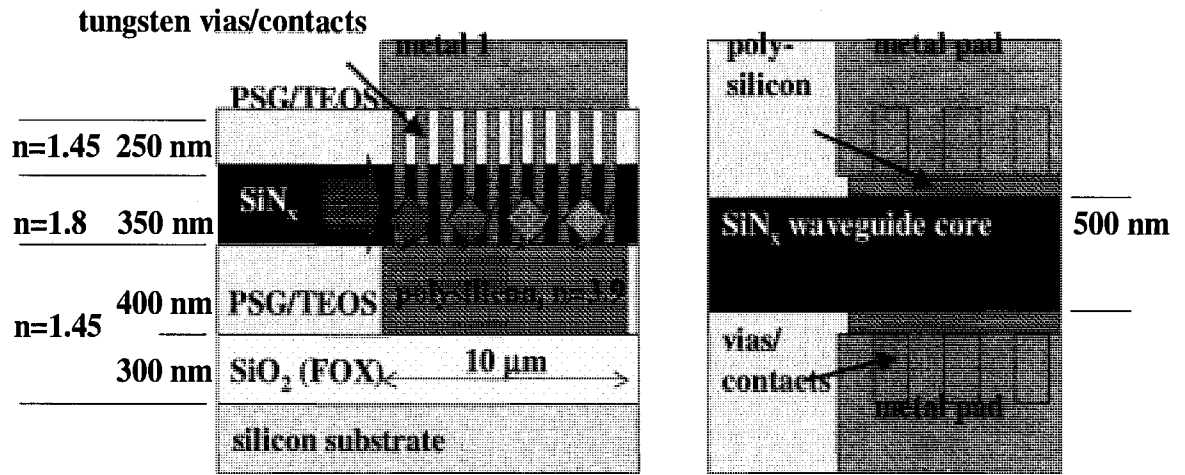
To minimize barriers to adoption of this technology, only materials already present in CMOS chips were being used to implement the necessary components. CMOS chips containing functioning optical waveguide H-trees and polysilicon photodiodes have been fabricated. In practice, we characterized waveguides and photodetectors with 250nm or 950nm thick phosphosilicate glass (PSG) or tetraethyl ortho-silicate (TEOS) layers as upper claddings. Due the nature of the evanescent field at the surface dropping exponentially as the cladding thickness increases, only the case with 250 nm thick PSG/TEOS layer has been characterized.

6.5.2 NSOM Measurements

NSOM operated in contact mode measured the optical intensity at the upper PSG/TEOS to air interface along the waveguide immediately before and above the detector. The same light coupling method has been used here that was described earlier in Chapter 5, where the edge of the chip was polished to allow end-fire coupling of a 654 nm laser diode via visible single mode fiber.



(a)

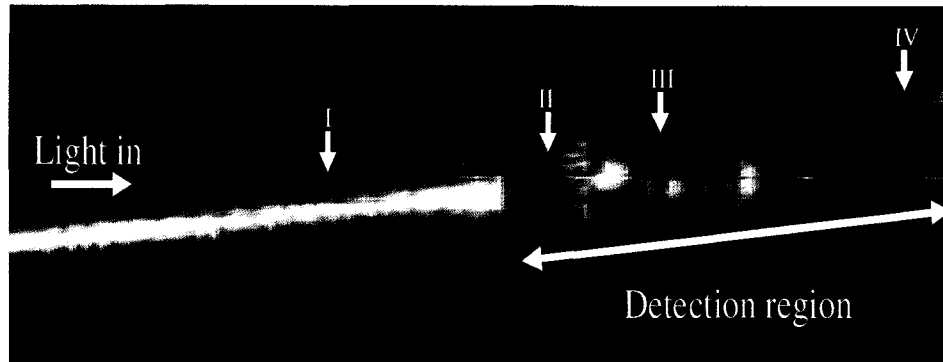


(b)

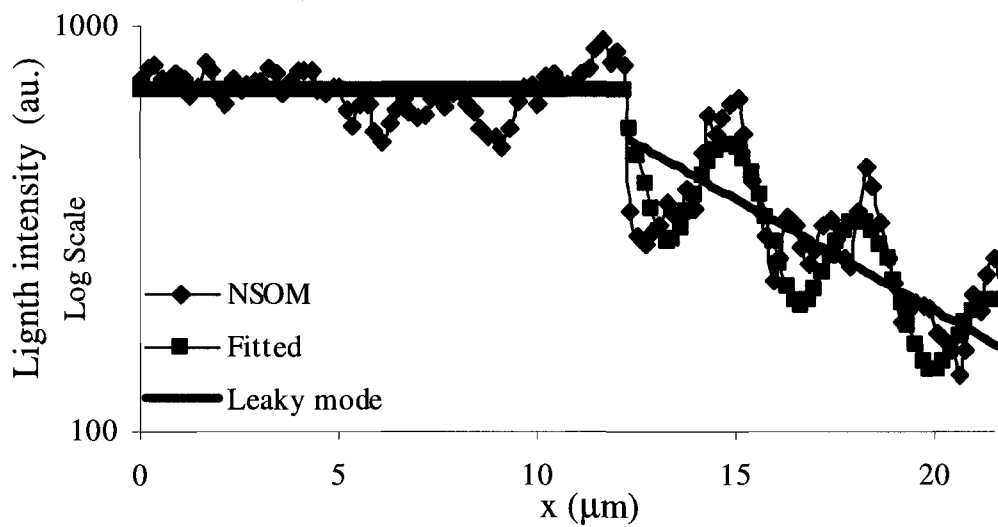
Figure 6.28: (a) Schematic of a first generation optical interconnect chip with a 16 node H-tree . Inset: microscopic image of the lit H-tree. (b) Waveguide and photodetector cross-section views.

Figure 6.29(a) illustrates a false color plot of the measured light intensity over a $10\ \mu\text{m} \times 21.5\ \mu\text{m}$ scanned area on the sample surface. The image clearly shows a strong intensity decrease in the detector region where the light was either absorbed or scattered due to the polysilicon layer. Before the detector, a Gaussian shaped optical field profile was observed, which corresponds to the guided fundamental TE mode. The measured intensity distribution along the centerline of the waveguide was plotted on a log scale in Figure 6.29 (b) clearly showing oscillations about an average exponential decay. Least squares fitting to the centerline intensity and its average in the detector region provide measured values for α_{eff} and the beat length of the oscillations. The slope of the average intensity gives a measured $\alpha_{\text{eff}} = 0.67\ \text{dB}/\mu\text{m}$ in excellent agreement with the predicted value of $0.68\ \text{dB}/\mu\text{m}$ by 1-D modal calculation.

However, the measured beat length was $3.4\ \mu\text{m}$ while the predicted one was $\lambda/(1.54 - 1.24) = 2.2\ \mu\text{m}$, where 1.54 was the effective index for the bound photodetector mode and 1.24 for the radiation mode. and the initial average surface intensity above the detector was observed to drop relative to the waveguide region while the 1-D modal calculations predict an increase by 2.25. Further investigation was required to understand the impact of the 3-D nature of the modes and NSOM coupling dependence on modal properties to resolve these discrepancies. The measured $\alpha_{\text{eff}} = 0.67\ \text{dB}/\mu\text{m}$ was the largest value published to date for a silicon detector and corresponds to 79% power transfer from the leaky mode to the $10\ \mu\text{m}$ long detector. Including the effect of overlap projection and the modes bound to the p-Si indicates that 83% of the incident power was absorbed by the $10\ \mu\text{m}$ long poly-Si detector. Similar calculations at $\lambda = 850\ \text{nm}$ predict that 70% of the power would be absorbed at that longer wavelength.



(a)



(b)

Figure 6.29: (a) Near-field image of the measured light intensity over a $10 \mu\text{m} \times 21.5 \mu\text{m}$ scanned area on the sample surface. Note that the horizontal and vertical scales were different. (b) Intensity distribution on the waveguide and detector centerline from measurements (diamonds), fit to leaky and radiation modes (dashed), and fit to only the leaky mode (solid).

A second chip without deposition of upper cladding was measured using NSOM to determine the effective absorption efficiency of a 30 μm long photodetector. The measured intensity distribution along the centerline of the waveguide was presented on a log scale in Figure 6.30 clearly showing an exponential decay in the detector region. Least squares fitting to the centerline intensity and its average in the detector region provide a slope of the average intensity that gives a measured $\alpha_{\text{eff}} = 0.32 \text{ dB}/\mu\text{m}$, in contrast to our previous work that demonstrated $0.67 \text{ dB}/\mu\text{m}$ for a detector region with 1.45 refractive upper/lateral cladding.

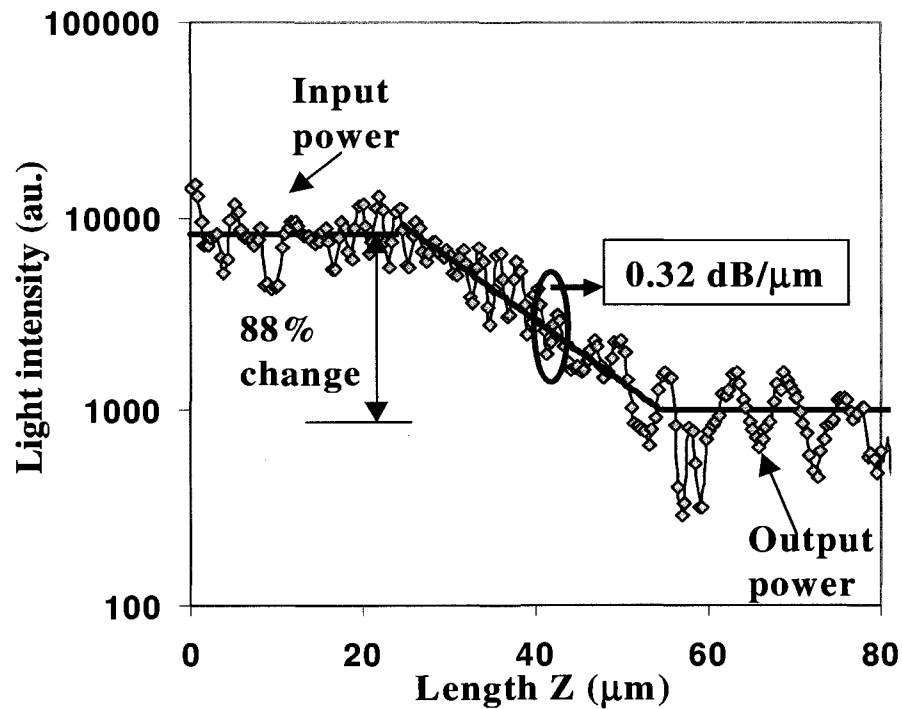


Figure 6.30: Intensity distribution on the waveguide and detector centerline from measurement (diamonds), and least square fit to average intensity (solid line).

When the scattering loss was neglected, the measured $\alpha_{\text{eff}} = 0.32 \text{ dB}/\mu\text{m}$ corresponds to 88% power transfer from the leaky mode to the 30 μm long detector but would correspond to only 79% power transfer to a 10 μm long detector. Removal of the upper and lateral claddings caused a tighter optical confinement in the waveguide region that reduced the absorption coefficient in the photodetector region.

6.5.3 Photo-responsivity measurements

When biased, the photodetectors operated as expected and demonstrated an excellent on/off ratio across a broad bias voltage range. The measured DC photocurrent and dark current of a 10 μm long photodetector with 1.14 μm contact spacing across a 0.5 μm wide waveguide was shown as a function of bias in Figure 6.31. The mean photocurrent-to-dark-current ratio exceeds 500 for biases above 2 V. In the next section, we determined that 1.2 mW of laser power from the fiber output delivers approximately 1.75 μW incident on the photodetector at each output node of the 16 node H-tree. The 0.6 μA photocurrent at 10 V bias voltages corresponds to a responsivity of 0.35 A/W and quantum efficiency of 67%. The difference between the actual quantum efficiency and the 83% power absorption in the p-Si can be attributed to recombination at grain boundaries.

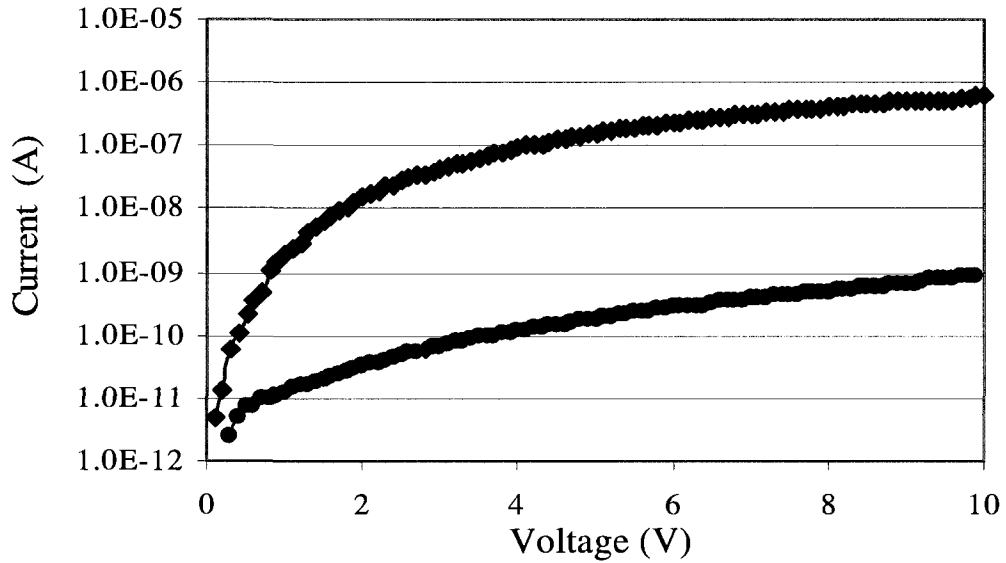


Figure 6.31: Dark current (filled diamonds) and photocurrent (filled circles) of a leaky-mode poly-Si metal-semiconductor-metal (MSM) photodiode due to an estimated $1.7 \mu\text{W}$ of incident power at 654 nm. (Courtesy of Bob Pownall, Colorado State University)

6.5.4 Simulations

For the leaky mode waveguide coupled photodetector structure described in Chapter 4, we used one-dimensional (1-D), effective-index mode calculations to do the simulations. The simulations provide us insight into the operation of the device and NSOM observations. To begin, the effective indices of both the $0.5 \mu\text{m}$ wide SiN_x ($n=1.80$) waveguide core and the $2.3 \mu\text{m}$ wide poly-Si ($n=3.85+i0.038$) detector, both clad by SiO_2 ($n=1.45$, equivalent to phosphosilicate glass, PSG), were calculated for $\lambda=654 \text{ nm}$ considering only the transverse index variation parallel to the substrate. The extinction coefficient for poly-Si was obtained from thin film measurements [19]. Outside the detector region, there is one transverse electric (TE) and one transverse magnetic (TM)

mode bound to the SiN_x core. The TM mode's lower confinement factor in the waveguide region results in high relative loss due to substrate absorption and surface scattering in the H-tree leading to the detectors so that only TE modes were considered near the detector. Figure 6.32 shows the end view of the leaky mode waveguide coupled photodetector. In the lateral direction, we consider the fundamental magnetic mode for the waveguide core. Here, a slab waveguide structure was used for calculation. The waveguide core was $0.5 \mu\text{m}$ wide and has a refractive index 1.8, surrounded by a medium of SiO_2 of refractive index 1.45. The resulting effective indices for the laterally confined SiN_x ($n_{\text{eff}}=1.71$) and poly-Si ($n_{\text{eff}}=3.809+i0.0384$) were then used for vertical solutions of the modes using a one-dimensional numerical solution with absorbing boundary conditions positioned $1.0 \mu\text{m}$ into the air and substrate. The 1-D modal calculation code can be found in Appendix A.

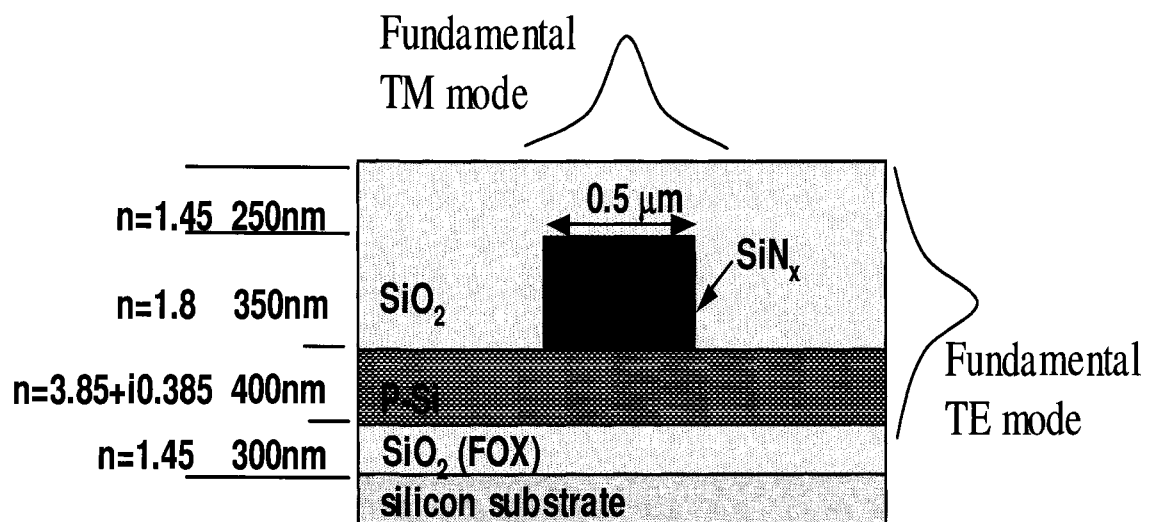
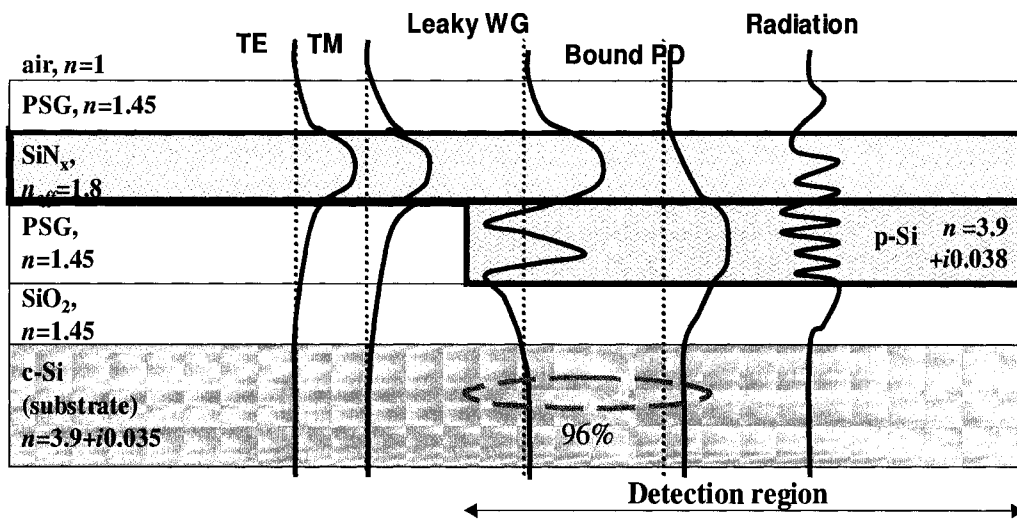
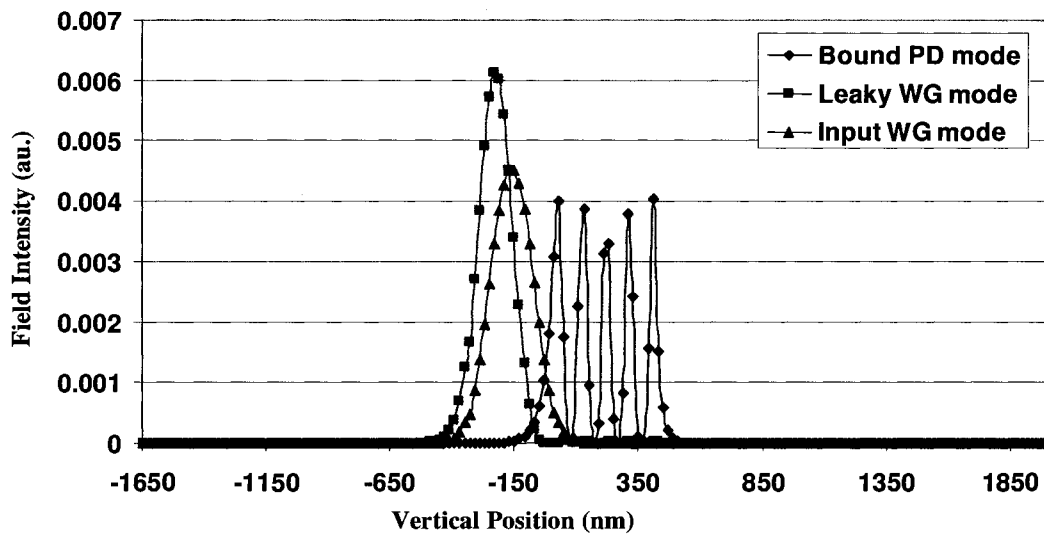


Figure 6.32: End view of the leaky mode waveguide coupled photodetector.



(a)



(b)

Figure 6.33: (a) Modes types in waveguide and photodetectors,. Observed interference between bound WG and radiation modes as bound PD mode has little surface intensity. The percentage of leaky waveguide modes and bound photodetector modes was 96% of the total power. (b) Calculated mode profiles for the bound photodetector mode, leaky waveguide mode and input waveguide mode.

Mode parameters determined from the effective index calculations reveal the factors responsible for the detector's strong optical absorption. The incident TE mode in the waveguide before the poly-Si was projected onto a variety of TE modes bound to the poly-Si, leaking from the SiN_x core into the poly-Si, and radiating into the SiO₂, shown in Figure 6.33 (a) and (b).

The effective indices, n_{eff} , and associated effective absorption coefficients, α_{eff} , of all of these modes were listed in Table 6.1. The distribution of the incident power into each mode was given in terms of the field overlap, a , with the incident mode. The majority, 60%, of the incident power was projected into a mode primarily confined to the SiN_x but leaking into the poly-Si at a rate that gives an effective absorption coefficient of 0.68 dB/ μm , a value equal to 21% of the bulk poly-Si absorption coefficient. 35.5%, of the incident was directly coupled into five modes bound to the high index poly-Si detector and therefore rapidly absorbed. The other 4.5% of the incident power was transferred to radiation modes free to propagate in the SiO₂. The table also lists normalized E-field strengths at the SiO₂/air surface probed by the NSOM, including the mode overlap factor. The surface was 250nm above the SiN_x core. Only the leaky waveguide mode and first radiation mode have significant surface strength.

TABLE I
MODE PARAMETERS

Mode	a^2 , overlap	n_{eff} of mode	α_{eff} (dB/ μm)	E_{surf} (norm.)
Incident mode without p-Si	1	1.62	$<10^{-3}$	1
Bound detector modes ($n_{\text{eff}} > 1.71$)	0.048	$3.74 + i 0.039$	3.3	7.1×10^{-9}
	0.031	$3.54 + i 0.040$	3.4	1.4×10^{-8}
	0.028	$3.17 + i 0.043$	3.6	2.1×10^{-7}
	0.030	$2.60 + i 0.049$	4.1	1.4×10^{-5}
	0.218	$1.76 + i 0.048$	4.0	6.1×10^{-2}
Leaky wave- guide mode ($1.71 > n_{\text{eff}} > 1.45$)	0.60	$1.54 +$ $i 0.0081$	0.68	1.5
Radiation modes ($n_{\text{eff}} < 1.45$)	0.021	$1.24 +$ $i 0.0062$	0.52	1.3

Table 6.1: Modes obtained as solutions to photodetector structure. Only the primary radiation mode was listed.

6.6 Waveguide splitters and H-trees

In addition to leaky-mode waveguide coupled photodetectors discussed above, other vital components in an on-chip optical interconnect system were waveguide splitters. The splitters were parts of a waveguide H-tree to deliver an optical clock signal to 16 nodes where leaky mode waveguide coupled photodetectors convert the optical signal to photocurrent, as shown in Figure 6.3. Optical intensity recorded with NSOM measurement along the H-tree was used to examine the performance of the splitters by extracting the loss and branching ratios.

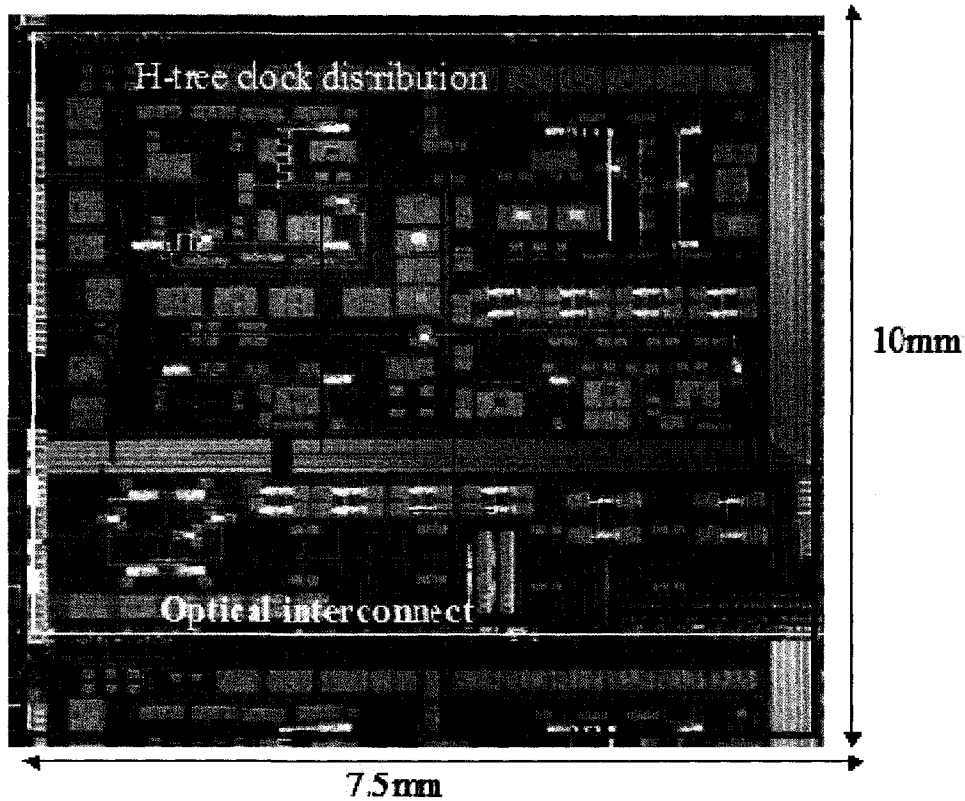


Figure 6.34: Microphotograph of a second generation H-tree with 16 nodes.

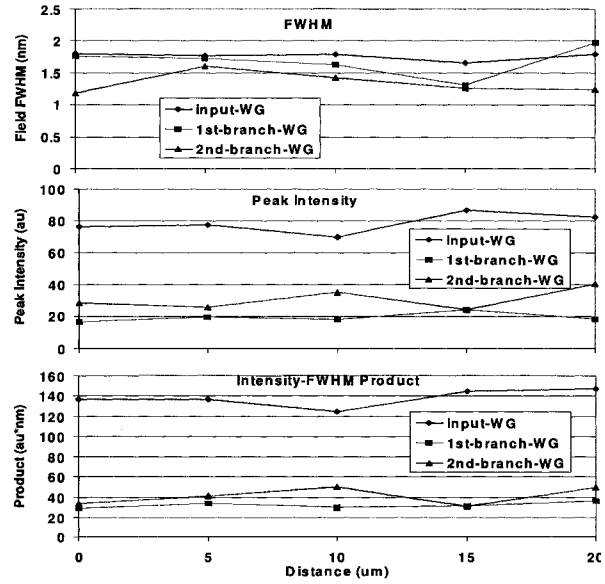
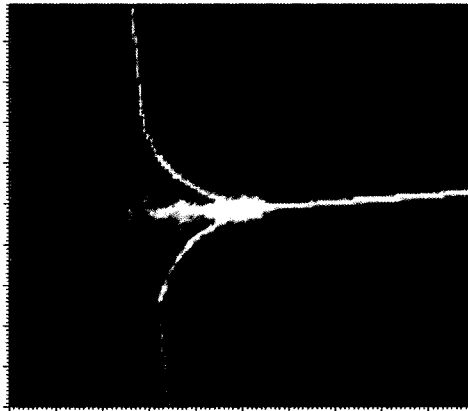
Waveguides were fabricated with vertical dimensions described in Chapter 4 and four T-splitters were used between the input and each output. The entrance branch of the first generation chip was designed as a taper with width varying from $200\ \mu\text{m}$ to $8\ \mu\text{m}$ and the widths of the waveguide were halved at each T-splitter, making the waveguide widths 4, 2, 1, $0.5\ \mu\text{m}$. Each T-splitter was designed with two waveguide bends of $25\ \mu\text{m}$ radius. The wafer was cut so that only one small H-tree beginning with the $2\ \mu\text{m}$ wide waveguide consists of three waveguide splitters. The total waveguide length from input to output of the quarter H-tree was approximately 2 mm for the quadrant of the 16-node

H-tree (a 4 node small H-tree). The global loss, consisting of T-splitter loss, light coupling loss and straight waveguide propagation loss, was measured to be approximately 16.1 dB using the NSOM method. About 7.9 dB loss comes from three (one 2 μm -to-1 μm and two 1 μm -to-0.5 μm) T-splitters. To quantify the loss for each splitter, three scans were done over 10 μm straight waveguide distance in the regions before and after the splitter. The average full width half maximum (FWHM) of the intensity profiles were measured along with average peak intensity, shown in Figure 6.35. The product of average peak intensity and average FWHM, were P_0 before the splitter, and P_1 and P_2 for the two branches after the splitter. Therefore the excess loss was simply calculated as $10\log_{10}[(P_1 + P_2)/ P_0]\text{dB}$. The excess losses for the three splitters were then determined to be 2.7dB for the 2 μm -to-1 μm splitter, 2.1dB for the 1st 1 μm -to-0.5 μm splitter and 0.5 dB for the 2nd 1 μm -to-0.5 μm splitter. The split loss was believed due to an abrupt change in the splitter area, as shown in Figure 6.36. The variation in the measured excess loss for different splitters is due to two possible reasons, the variation in the process and the input mode profiles. The later was studied in Reference [18], which also addressed the relation between mode profiles and branching ratios. Evidently, the lower loss was found for the 2nd 1 μm -to-0.5 μm splitter than the 1st one. The 2nd splitter had a signal-mode like input mode profile while the other one had a mode interference.

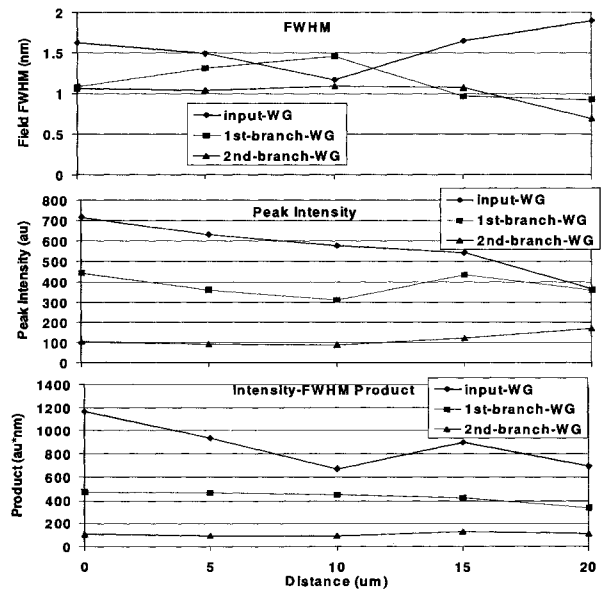
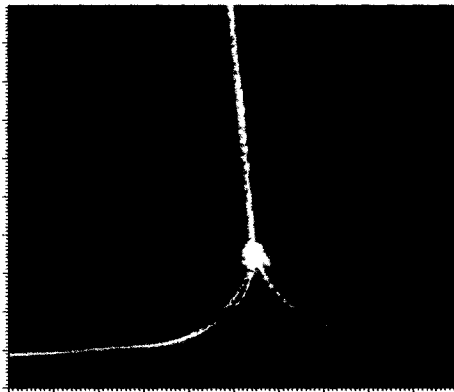
The second contribution of the global loss was the light coupling loss from fiber to the 2 μm wide 0.35 μm thick waveguide where approximately 85 % of the optical power from a single mode fiber was estimated lost, thus increasing the global loss by 8.2 dB. The on-chip portion of the global loss, not including the high fiber coupling loss, was 4.8 dB for the branch through 1st 1 μm -to-0.5 μm splitter and 3.2 dB for the branch through 2nd

1 μ m-to-0.5 μ m splitter using the measured excess losses in previous paragraph. The third source of the global loss was propagation loss, which was measured 2.6 dB over the 2 mm waveguide at 1.3 dB/mm rate.

A



B



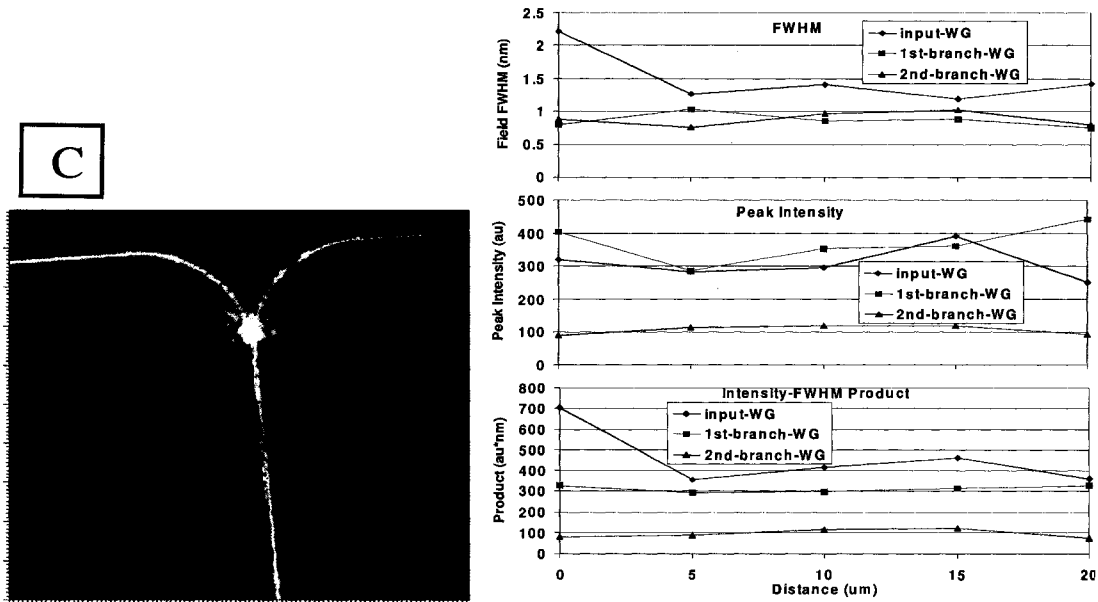


Figure 6.35: NSOM measurements on (a) 2 μ m-to-1 μ m splitter, (b) first 1 μ m-to-0.5 μ m splitter and (c) second 1 μ m-to-0.5 μ m splitter.

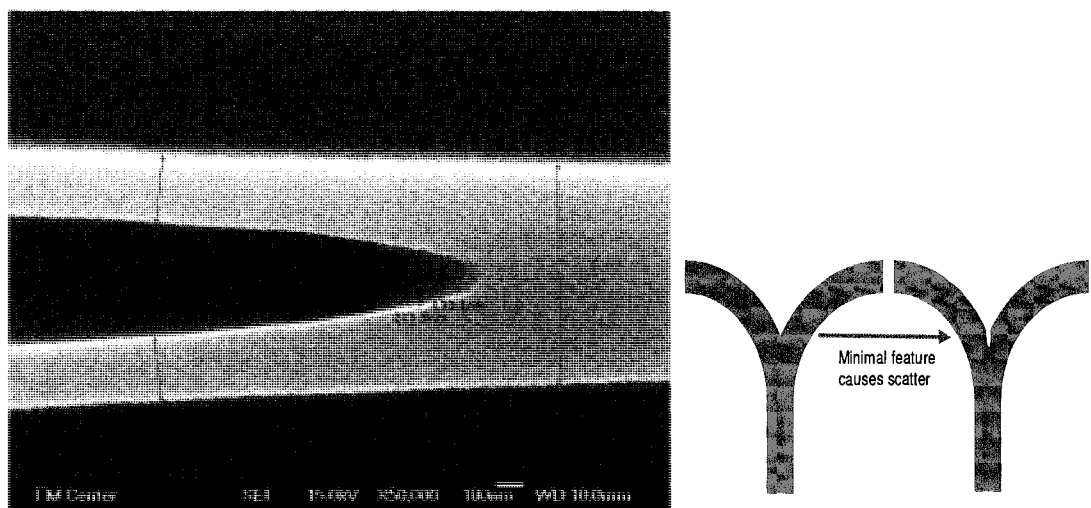


Figure 6.36: SEM image shows the minimal feature at a splitter that might causes unusual loss. Courtesy of Bob Pownall.

In the following experiment, we demonstrated that a splitter with a higher refractive index contrast presented lower loss. In this study, a waveguide splitter with the same 25 μm output bend radius but with no upper or side cladding was analyzed. Figure 6.37 (a) illustrates a false color plot of the measured light intensity over a 70 μm \times 100 μm scanned area on the waveguide splitter surface. The input waveguide width was same as the width of the right- and left- hand branches. The side cladding refractive index was the dominant effect for the large reduction in excess loss. The average light intensities in the input waveguide and two branch waveguides were studied. The observed excess loss of the splitter was less than 0.1 dB. The light intensity distribution in a 25 μm bending radius splitter with 250 nm TEOS as upper and lateral cladding was plotted for comparison. This splitter is a 1 μm -to-0.5 μm splitter.

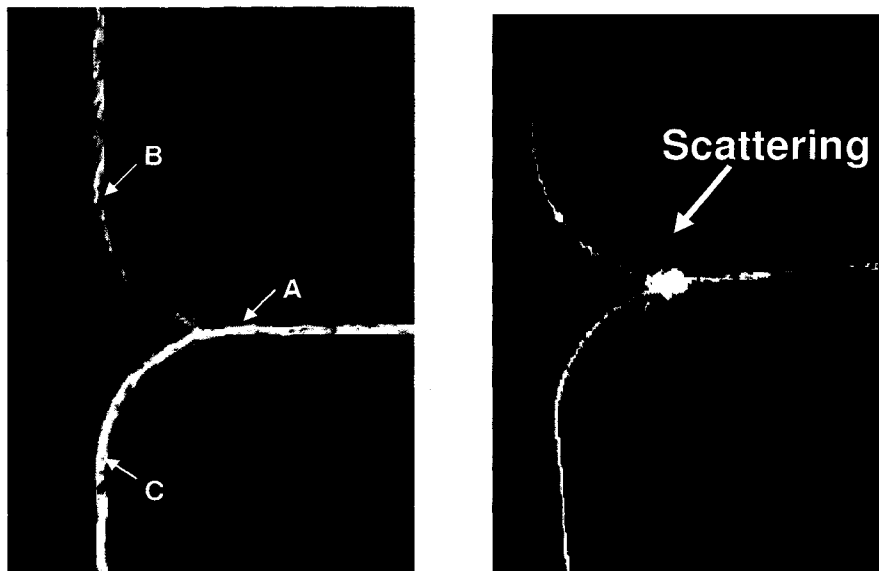


Figure 6.37. Near-field images of the measured light intensity on 25 μm radius splitters on (a) a 1 μm -to-1 μm splitter with air as upper/lateral cladding , (b) a 1 μm -to-0.5 μm splitter with PSG as upper/lateral cladding.

A significant scattering loss was found at the input waveguide to splitter interface, as illustrated in Figure 6.37 (b), which was estimated to result in approximately 3 dB light excess loss. The low optical loss through the first splitter was due to higher refractive index contrast between the waveguide core and waveguide lateral cladding. Lateral optical field profiles were plotted in Figure 6.38 at position A on the input waveguide and positions B on the right hand branch and C on the left hand branch, as marked by arrows in Figure 6.37. In the input waveguide, there were one TE and one TM mode bound to the SiN_x core. The TM mode's lower confinement factor in the waveguide region results in high relative loss due to substrate absorption and surface scattering in the H-tree leading to the detectors so that only TE modes were considered near the detector.

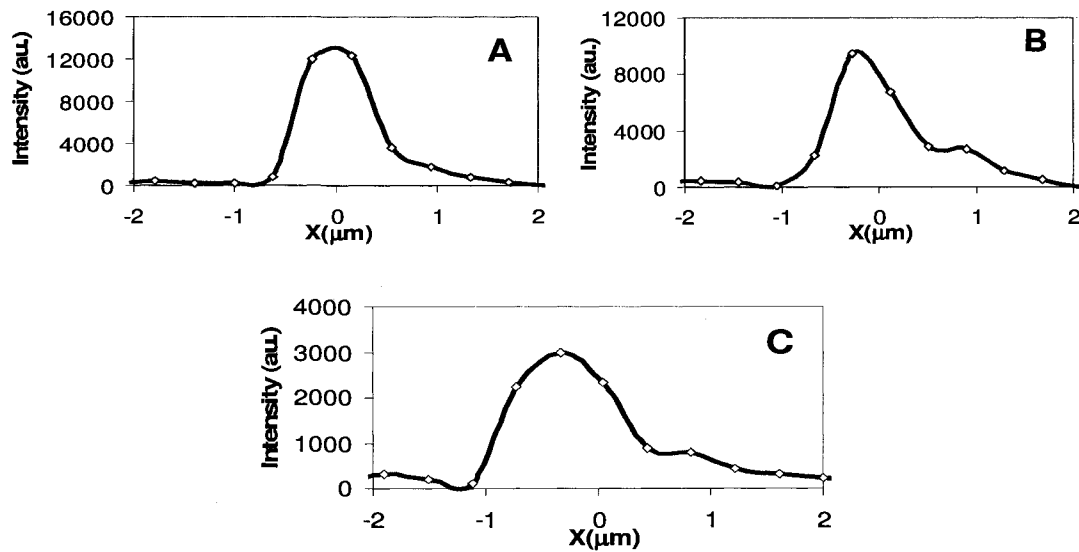


Figure 6.38: Measured optical intensity distributions as a function of transverse position in the waveguide at positions along the waveguide indicated by the arrows in Figure 6.37(a).

The calculation shows there were three waveguide modes in the horizontal direction for this 1 μm wide input waveguide, with effective refractive indices of 1.6661, 1.5931, and 1.4660. However, the NSOM result showed the dominant mode is the fundamental mode. For a 0.5 mm wide waveguide, there was one mode with effective refractive index 1.6152. These optical field profiles at the exits (positions B and C) of two branches were similar in shape to those for the straight waveguide but were shifted off center toward the outer boundary. The phenomena has been reported on our previous study of 90° waveguide bend in Chapter 6, Section 2 and Reference [4]. The modal profiles denote there were two lateral TE modes ($m = 0$ and 1) supported in the waveguide bend. Consequently, at the exit interface from the bending waveguide to the straight waveguide, both of TE modes in the waveguide bends were guided in to the straight waveguide. For example, the light intensity along the light propagation direction in the right hand branch presents a periodic interference between fundamental mode and higher order mode. However the higher mode suffers a much larger propagation loss in the straight waveguide than the fundamental mode and diminishes within a few hundred microns. As a result, only the fundamental mode was found prior to the photodetector region. As opposed to Reference [4], the modal mismatching losses from the waveguide bends and straight waveguide were small enough to be neglected seen from the NSOM results. This is probably due the high refractive index contrast between claddings and waveguide core.

6.7 Summary

This chapter reports NSOM results on straight waveguides, waveguide bends, waveguide biosensors, leaky mode coupled photodetectors and waveguide splitters. First-hand

observations were made in the discovery of leaky mode interference in a straight waveguide, modal evolution in a waveguide bend, evanescent field modulation in a biosensor and refractive index profile dependent photodetector absorption and waveguide splitter loss. Numerical simulations, such as 1-D modal calculation and conformal index transformation, were widely adapted to understand the experimental observations. Photocurrent measurements were conducted to prove the concept of a buried photodetector array for the biosensor and leaky mode waveguide coupled photodetectors in an on-chip optical interconnect system.

Reference:

- [1] A. V. Mule, R. Villalaz, T. K. Gaylord, and J. D. Meindl, "Photopolymer-Based Diffractive and MMI Waveguide Couplers," *IEEE Photonics Technology Letters*, Volume 16, No. 11, Nov. 2004.
- [2] N. Jaeger and W. Lai, "Calculation of the effective index for nonguiding regions," *Appl. Opt.* 31, pp. 7183-7190, 1992.
- [3] Guangwei Yuan and Kevin L. Lear "Metrology of Integrated Waveguide Devices and Systems Using Near-Field Scanning Optical Microscopy," *Symposium on Optical Fiber Measurements (SOFM)*, Boulder, CO, Sept. 18-19, 2006.
- [4] G. W. Yuan, M.D. Stephens, D.S. Dandy, K. L. Lear, "Characterization of a 90 degrees waveguide bend using near-field scanning optical microscopy," *Applied Physics Letters*, 87 (19), Art. No. 191107, Oct. 2005.
- [5] A. Nesterov and U. Troppenz, "A Plane-Wave Boundary Method for Analysis of Bent Optical Waveguides," *J. Lightwave Technol.* 21, pp. 1-3, Oct. 2003.

- [6] W. Berglund and A. Gopinath, "WKB Analysis of Bend Losses in Optical Waveguides," *J. Lightwave Technol.* 18, 1161-1166, 2000.
- [7] G. W. Yuan, M.D. Stephens, D.S. Dandy, K. L. Lear, "Direct imaging of transient interference in a single-mode waveguide using near-field scanning optical microscopy," *IEEE Photon. Tech. Letters*, Vol. 17(11), pp.2382 – 2384, Nov. 2005.
- [8] G. Yuan, M. Stephens, D. Dandy, and K.L. Lear, "Initial demonstration of a local, evanescent, array coupled biosensor", *Proceedings of 4th IEEE International Conference on Sensors 2005*, paper B4P-G, pp. 908-911, October 2005.
- [9] G. Yuan, M. Stephens, D. Dandy, J. Gerding, A. Van Orden, and K. Lear, "Local Evanescent, Array Coupled (LEAC) Biosensor Response to Low Index Adlayers", *Proceedings of Conference on Lasers and Electro-Optics, CLEO 2006*, paper CThL7, May 2006.
- [10] K. L. Lear, G. Yuan, M. Stephens, X. He, R. Pownall, R. Yan, P. Nikeel, C. Henry, T. Chen, D. Dandy. "A Waveguide Biosensor's Local Evanescent Field Response to an Immunoassay Complex," *Digest of the IEEE LEOS Summer Topical Meetings*, pp. 97-98, July 2007.
- [11] K. L. Lear, G. Yuan, M. Stephens, X. He, R. Pownall, R. Yan, C. S. Henry, and D. Dandy, "Response of Local Evanescent Field to Varying Immunoassay Complex Coverage," *Proceedings of LEOS 20th Annual Meeting*, pp. 302-303, Oct. 2007
- [12] Rongjin Yan, G. Yuan, Kevin L. Lear, Matthew D. Stephens, Xinya He, Robert Pownall, Charles S. Henry, and David S. Dandy. "Characterization of evanescent field response to varying immunoassay layer thickness on planar waveguides." Submitted to *IEEE Photonics Technology Letters*

- [13] G. Yuan, R. Pownall, P. Nikkel, M. Stephens, X. He, C. Henry, T. Chen, D. Dandy and K.L. Lear, "Characterization of integrated waveguide sensors with buried photodetectors," in preparation
- [14] A. Raza, G. Yuan, C. Thangaraj, T. Chen, and K.L. Lear, "Waveguide coupled CMOS photodetector for on-chip optical interconnects", Photonic Devices and Algorithms for Computing VI in series Proceedings of SPIE, vol. 5556, pp. 27-33, October 2004
- [15] G. Yuan, R. Pownall, P. Nikkel, C. Thangaraj, T. Chen and K.L. Lear, "Characterization of CMOS compatible waveguide coupled leaky-mode photodetectors," IEEE Photon. Tech. Letters, vol. 18, pp.1657-1659, August 2006.
- [16] M. Nathan, O. Levy, I. Goldfarb, A. Ruzin, "Monolithic coupling of a SU8 waveguide to a silicon photodiode," Journal of Applied Physics, vol. 94, pp. 7932-7934. Dec. 2003.
- [17] T. Baba and Y. Kokubun, "High efficiency light coupling from antiresonant reflecting optical waveguide to integrated photodetector using an antireflecting layer," Appl. Opt., vol. 29, pp. 2781-2792, Jun. 1990.
- [18] R. Yan, G. Yuan, R. Pownall, and K. L. Lear, "A novel low-loss y-type splitter with adjustable branching ratio," Proceedings of IEEE LEOS 20th Annual Meeting, pp. 543-544, Oct. 2007.
- [19] A. M. Raza, "A Truly CMOS Compatible Waveguide Coupled Photodiode for On-Chip Optical Interconnects," Master's, Dept. Elect. And Comput. Eng., Colorado State Univ., Fort Collins, CO, 2005.

Chapter 7

ACHIEVEMENTS AND CONCLUSIONS

This chapter summarizes and concludes the achievements in my Ph.D research work. Some thoughts on the future work are presented.

7.1 Achievements

The overall objective of this Ph.D research work is to characterize novel integrated optical waveguide devices and systems. The devices and systems we studied include structures from simple format waveguides (straight waveguides and waveguide bends) to complicated devices (LEAC waveguide biosensors and on-chip optical interconnects). In conjunction with the novel waveguide design and characterization, we analyzed leaky mode waveguide coupled and evanescent field coupled photodetectors. To achieve our objective, we have conducted both theoretical and experimental studies on prototype waveguide devices and systems. A summary of the achieved milestones is listed below for both the LEAC sensor and the on-chip interconnects system.

7.1.1 LEAC sensor concept was proposed and tested

1. LEAC sensor design and modeling

A sensor structure with and without buried detector arrays has been developed, as well as steps for its fabrication. The asymmetric waveguide sensor has a configuration which is much easier to process than the originally proposed one, while the new configuration preserves the same or better optical sensitivity. After comparison with other candidate

materials, the material of SiN_x was chosen as waveguide core and SiO_2 as lower cladding for their mechanical strength and optical properties. A sequence of steps that exploits traditional sputtering, photolithography and dry etch technologies has been modeled and developed for waveguide fabrication. We have developed a procedure for waveguide post-fabrication processing. The procedure includes a multiple step facet polishing process and end-fire light coupling. In light coupling, we developed a method for permanently bonding an optical fiber to a waveguide chip to ensure mechanical stability.

LEAC sensors have been thoroughly modeled using both commercial simulation software from Rsoft and a customized 1-D mode solver written in MATLAB. Some of the critical parameters, which are vital to ensure the LEAC sensing mechanism, were modeled and determined. For example, simulation results indicated that the optimal refractive index and thickness of the waveguide core were 1.8 and 85 to 110 nm, respectively. If the waveguide core index were smaller, a thicker adlayer would be needed to maintain the same signal modulation. On the other hand, if the waveguide core thickness were smaller, there would be no guided mode in the waveguide.

2. Initial LEAC sensor characterization

Characterizations of waveguide sensor and waveguide components have been conducted. These components include straight waveguides and waveguide bends. Specifically, observations of mode evolution in a 90-degree waveguide bend were reported for the first time. Optical waveguide bends were found effective in high order mode stripping with >15 dB/90 degree attenuation. Excessive exit loss from bent to straight waveguides was observed. In simulation, behavior of a bending waveguide mode is well modeled using the conformal mapping method.

In the initial proof-of-concept sensor experiments, NSOM was used to characterize the evanescent field response of a LEAC sensor to various adlayers. These adlayers include SiN_x (n=1.8) and photoresist (n=1.56). The thicknesses of these adlayers vary from 8 nm to 120 nm, which respond to optical field modulation observable to NSOM. The modulation depth is as large as 80% for a 17 nm SiN_x adlayer. Similar optical sensitivity was observed in multiple adlayer studies on a single waveguide. Experimental waveguide and adlayers configurations were simulated via beam propagation method. Comparisons between experimental results and numerical modeling were conducted.

Fabrication processes of a waveguide sensor with buried photodetectors were designed for both CSU cleanroom and Avago Technologies. Multiple layer photo mask sets were designed and created to generate waveguides, photodetectors, vias and metal traces.

3. Further LEAC sensor characterization

In later experiments, single and multiple immunoassay complexes on waveguides were characterized. Here, three NSOM measurements are done on immunoassay complex adlayers patterned using a microfluidic channel. The adlayer consists of biotinylated BSA, Strepta-vidin Anti-CRP and CRP layers. The total thickness of the immunoassay adalyer ranges from 12 nm without CRP to 15 nm with 95% CPR coverage. The multiple layer immunoassay complex was uniformly patterned on the waveguide surface via microfluidic channels. NSOM light intensity scans presented the light intensity modulation of the waveguide sensor is about 101% for only a 15 nm (measured) high adlayer. Another experiment was done with multiple adlayers on the waveguide. Three 50 μm long features patterned on the waveguide, each with different CPR layer coverage, 0 mg/ml, 0.6 μg/ml, and 0.6 mg/ml. As a result, the surface coverage are 0%, 1% and 90% respectively. NSOM

light intensity analysis shows that light intensity modulations are 12.8%, 15.7% and 30.2% correspondingly. As a result, a CRP adlayer of thickness 3 nm demonstrates a differential signal of 0.26 dB/nm.

Buried detector arrays for the optical waveguide biosensor were also designed, fabricated in commercial CMOS technology and tested. Photocurrent measurements of large-pitch (100 μm) array detectors with air and oil as the waveguide upper cladding demonstrated the index dependent photocurrent decay rate, 15.6 dB/mm with air and 4.3 dB/mm with oil as the upper cladding. Based on the measured absorption coefficients, the signal modulation is $\Delta_{\text{oil/air}}=72\%$. This observation validates the LEAC sensor concept that higher refractive index cladding causes less evanescent field detected by the buried detectors. In addition to bulk index changes, a film on the surface of the waveguide can also modulate the power received by the underlying detectors. A monolayer of biotinylated bovine-serum-albumin (Bio-BSA) film adsorbed onto the waveguide surface was characterized. The photocurrent decay rate using a medium pitch (10 μm) photodetector array with and without the BSA layer was 17 dB/mm and 31 dB/mm, resulting in $\Delta=45\%$ signal modulation, respectively, once again proved LEAC sensor concept. As results, a 14 dB/mm difference from the 8 nm thick film corresponds to 1.75 dB/mm/nm.

7.1.2 Two generations of on-chip optical interconnects characterized

1. First generation on-chip optical interconnects

Two important components were designed for an on-chip optical interconnect system. These components include waveguide splitters and leaky mode waveguide coupled photodiodes. The performance of the leaky mode waveguide coupled photodiodes has

been thoroughly modeled using a one-dimensional mode solver. Some of the critical parameters that impact the on-chip optical interconnects system performance were determined. For example: The waveguide's core thickness is chosen 0.35 μm and the photodiode's thickness is chosen 0.4 μm . The effective absorption coefficient of the metal-semiconductor-metal photodiodes were later measured as 20 times higher than the largest value previously reported.

NSOM was used to characterize the photodiodes and splitters. The NSOM results revealed a quick absorption of light in the photodiodes. Interference between a guided mode and a leaky mode in waveguide structure was observed for the first time. The effective absorption rate of the photodetector was $\alpha_{\text{eff}} = 0.67 \text{ dB}/\mu\text{m}$ which is the largest value published to date for a silicon detector and corresponds to 79% power transfer from the leaky mode to a 10 μm long detector. Including the effect of overlap projection and the modes bound to the p-Si indicates that 83% of the incident power is absorbed by the 10 μm long poly-Si detector.

NSOM was also used to characterize waveguide splitters. These splitters consist of three waveguide bends with 25 μm bending radius. The waveguide widths vary from 8 μm to 0.5 μm . The light loss at each splitter was quantified. These splitters were redesigned for the next generation on-chip optical interconnects system. Relatively large split losses for the three splitters were determined, 3.6dB, 2.7dB and 1.9 dB. The split loss is believed due to minimal feature size at the splitter that makes an abrupt waveguide change instead of a smooth splitting.

Photocurrents and dark-currents of these photodiodes were measured. The photocurrent to dark-current ratio was observed above 500:1 at a 3.3 V bias voltage. The 0.6 μA

photocurrent at 10 V bias voltages corresponds to a responsivity of 0.35 A/W and quantum efficiency of 67%.

2. Second generation on-chip optical interconnects

The second-generation chips are fabricated and currently being characterized. The optical parts of the first generation on-chip interconnects system has been redesigned. The upper cladding for the second-generation chip will be thicker than that of the first generation, which makes the NSOM examination of evanescent field impossible. Therefore, a second chip without deposition of upper cladding was measured. The effective absorption rate is measured $\alpha_{\text{eff}} = 0.32 \text{ dB}/\mu\text{m}$, decreased almost 50% from previous $\alpha_{\text{eff}} = 0.67 \text{ dB}/\mu\text{m}$. In opposite, waveguide splitters with no upper cladding are analyzed still with 25 μm bending radius. The observed loss of the splitter is less than 0.1 dB decreased 97% from previous 3 dB.

7.2 Conclusions and suggestions

We have designed and characterized local evanescent field array coupled waveguide biosensors and on-chip optical interconnect systems. For a preliminary waveguide sensor, the sensing capability on biological adlayers was demonstrated. In initial experiments, we were using NSOM to detect optical field modulation, which provides a good alternative to the buried detectors for the preliminary demonstration. Numerical simulations provide accurate predictions of the performance of sensors. In a complete sensor structure, buried detector arrays were implemented in the waveguide lower cladding. Buried detector arrays would provide a novel sensing technique that would enable a real-time, compact and low cost biosensing platform.

The waveguide and detectors worked well enough for the first generation on-chip optical interconnects. The performance of the photodiodes was measured both electrically and optically. In the second generation on-chip optical interconnect system, a thicker upper cladding is used that may affect both photodiodes and splitters performance. We might need to design the splitters and photodetectors with different refractive index profile to optimize the performance for both. Numerical simulations, such like 1-D modal calculation and conformal index transformation, were widely adapted to understand the experimental observations.

Complete publications and presentations

[Patent]

K. Lear, D. Dandy, **G. Yuan**, and M. Stephens, "Multi-analyte Optical Sensor," full patent filed (60/670,939) in April, 2005.

[Publications]

1. **G. Yuan**, R. Pownall, P. Nikkel, M. Stephens, X. He, C. Henry, T. Chen, D. Dandy and K.L. Lear, "Characterization of integrated waveguide sensors with buried photodetectors," submitted to Applied Physics Letters
2. Robert Pownall, C. Thangaraj, **G. Yuan**, T. Chen, Kevin L. Lear, " Truly CMOS Compatible Optical H-Tree based Clock Recovery and Distribution System" to be submitted to Journal of Lightwave Technology
3. Matthew D Stephens, **G. Yuan**, Rongjin Yan, Kevin L Lear, and David S Dandy, "Optical and physical characterization of a local evanescent array coupled biosensor: Use of evanescent field perturbations for multianalyte sensing", to be submitted to

Journal of Applied Physics

4. Matthew D. Stephens, **G. Yuan**, Xinya He, Rongjin Yan, Charles S. Henry, Kevin L. Lear, and David S. Dandy. "Evanescent Field Response of a Planar Optical Waveguide to a CRP Immunoassay". To be submitted to Analytical Chemistry
5. Rongjin Yan, **G. Yuan**, Kevin L. Lear, Matthew D. Stephens, Xinya He, Robert Pownall, Charles S. Henry, and David S. Dandy. "Characterization of evanescent field response to varying immunoassay layer thickness on planar waveguides." Submitted to IEEE Photonics Technology Letters
6. K. L. Lear, **G. Yuan**, M. D. Stephens, X. He, R. Pownall, R. Yan, C. S. Henry, and D. S. Dandy, "Response of Local Evanescent Field to Varying Immunoassay Complex Coverage," Proceedings of IEEE LEOS 20th Annual Meeting, **pp. 302-303**, Oct. 2007
7. R. Yan, **G. Yuan**, R. Pownall, and K. L. Lear, "A novel low-loss y-type splitter with adjustable branching ratio," Proceedings of IEEE LEOS 20th Annual Meeting, **pp. 543-544**, Oct. 2007
8. K. L. Lear, **G. Yuan**, M. Stephens, X. He, R. Pownall, R. Yan, P. Nikeel, C. Henry, T. Chen, D. Dandy. "A Waveguide Biosensor's Local Evanescent Field Response to an Immunoassay Complex," Digest of the IEEE LEOS Summer Topical Meetings, **pp. 97-98**, July 2007
9. R. Pownall, **G. Yuan**, P. Nikkel, T. Chen and K.L. Lear, "Geometry dependence of CMOS-compatible, polysilicon, leaky-mode photodetectors," IEEE Photonics Technology Letters, vol 19, **pp.513- 515**, Apr. 2007.
10. B. Pownall, **G. Yuan**, T. Chen, P. Nikkel and K.L. Lear, "Geometry Dependence of Leaky-Mode, Waveguide-Coupled, Polysilicon Photodetectors", Proceedings of IEEE

- LEOS 19th Annual Meeting, paper ThQ4, **pp. 865–866**, October 2006
11. **G. Yuan**, M. Stephens, D. S. Dandy, A. N. Al-Omari, and K. L. Lear, “Implementation of Buried Detector Arrays for Waveguide Sensors”, Proceedings of IEEE LEOS 19th Annual Meeting, paper TuW5, **pp. 358–359**, October 2006
 12. **G. Yuan**, M. Stephens, D. S. Dandy, J. Gerding, A. Van Orden, and K. L. Lear, “Evanescent Field Response to Small Features on a Planar Waveguide Biosensor”, Proceedings of LEOS 19th Annual Meeting, paper TuQ3, **pp. 304–305**, Oct. 2006
 13. **G. Yuan** and K.L. Lear, “Metrology of integrated waveguide devices and systems using near-field scanning optical microscopy”, Technical Digest 2006, A NIST Symposium for Photonic and Fiber Measurements (SOFM), **pp. 24-27**, Sept. 2006
 14. **G. Yuan**, R. Pownall, P. Nikkel, C. Thangaraj, T. Chen and K.L. Lear, “Characterization of CMOS compatible waveguide coupled leaky-mode photodetectors,” IEEE Photon. Tech. Letters, vol. 18, **pp.1657-1659**, August 2006.
 15. **G. Yuan**, M. Stephens, D. Dandy, and K.L. Lear, “Characterization of a 90° Waveguide Bend Using Near-Field Scanning Optical Microscopy”, Proceedings of Conference on Lasers and Electro-Optics, CLEO 2006, **paper CThBB6**, May 2006
 16. **G. Yuan**, M. Stephens, D. Dandy, J. Gerding, A. Van Orden, and K.L. Lear, “Local Evanescent, Array Coupled (LEAC) Biosensor Response to Low Index Adlayers”, Proceedings of Conference on Lasers and Electro-Optics, 2006, **CThL7**, May 2006
 17. **G. Yuan**, P. Nikkel, C. Thangaraj, T. Chen, R. Pownall, A. Iguchi, and K. Lear, “Optical Characterization of a Leaky-Mode Polysilicon Photodetector Using Near-Field Scanning Optical Microscopy”, Proceedings of Conference on Lasers and Electro-Optics, CLEO 2006, **paper CThD4**, May 2006

18. **G. Yuan**, M. Stephens, D. Dandy, and K.L. Lear, "Direct imaging of transient modal interference in a single mode optical waveguide," *IEEE Photonics Technology Letters*, vol. 17, **pp. 2382 - 2384**, Nov. 2005
19. **G. Yuan**, M. Stephens, D. Dandy, and K.L. Lear, "Characterization of a 90° waveguide bend using near-field scanning optical microscopy," *Applied Physics Letters*, vol. 87, **Article # 191107**, Oct. 2005
20. **G. Yuan**, M. Stephens, D. Dandy, and K.L. Lear, "Initial demonstration of a local, evanescent, array coupled biosensor", *Proceedings of 4th IEEE International Conference on Sensors 2005*, **paper B4P-G, pp. 908-911**, October 2005
21. A. Raza, **G. Yuan**, C. Thangaraj, T. Chen, and K.L. Lear, "Waveguide coupled CMOS photodetector for on-chip optical interconnects", *Proceedings of IEEE LEOS 17th Annual Meeting*, **pp. 152 – 153**, November, 2004
22. **G. Yuan**, M. Stephens, D. Dandy, and K.L. Lear, "Novel local evanescent field detection waveguide multianalyte biosensor", *Optical Information Systems II in series Proceedings of SPIE*, vol. 5557, **pp. 140-146**, October 2004
23. A. Raza, **G. Yuan**, C. Thangaraj, T. Chen, and K.L. Lear, "Waveguide coupled CMOS photodetector for on-chip optical interconnects", *Photonic Devices and Algorithms for Computing VI in series Proceedings of SPIE*, vol. 5556, **pp. 27-33**, October 2004

[International Conference Presentations]

1. M. Stephens, **G. Yuan**, A. Al-Omari, K.L. Lear, and D. Dandy, "Evanescent field response to patterned features on a planar waveguide measured with a buried detector array," *American Physical Society March Meeting 2007*, Denver, March 5-9, 2007
2. **G. Yuan**, R. Yan, M. Stephens, D. Dandy, and K.L. Lear, "Evanescent field response

- to small patterned features on a planar waveguide biosensor,” American Physical Society March Meeting 2007, Denver, March 5-9, 2007
3. **G. Yuan**, R. Pownall, M. Stephens, D. Dandy, T. Chen, P. Nikkel, and K.L. Lear, “Further demonstration of a local evanescent field array coupled (LEAC) biosensor concept,” American Physical Society March Meeting 2007, Denver, March 5-9, 2007
 4. R. Pownall, **G. Yuan**, and K.L. Lear, “Temperature Dependence of Polysilicon Photodetectors for Integrated Optical Sensors and Electronics Applications,” American Physical Society March Meeting 2007, Denver, March 5-9, 2007
 5. R. Yan, **G. Yuan**, R. Pownall, and K.L. Lear, “Waveguide Characterization Using Shear Force Scanning Optical Microscopy,” American Physical Society March Meeting 2007, Denver, March 5-9, 2007
 6. M. Stephens, **G. Yuan**, D. Dandy, and K.L. Lear, “Evanescent field response to affinity binding on a planar optical waveguide,” American Physical Society March Meeting 2007, Denver, March 5-9, 2007
 7. **G. Yuan**, M. Stephens, D. Dandy, and K.L. Lear, “Direct detecting thin polymer and organic adlayers using a local evanescent-field array coupled waveguide sensor,” Devices, Materials, and Technologies XI in Photonics West 2007 (SPIE), San Jose, CA, January 20-25, 2007
 8. M. Stephens, K.L. Lear, D. Dandy, **G. Yuan**, J. Gerding, A. Van Orden, and C. Henry, “Evanescent Field Response to Patterned Features on a Planar Waveguide Biosensor”, AIChE Annual Meeting, San Francisco, CA, November 12-17, 2006
 9. M. Stephens, K.L. Lear, D. Dandy, **G. Yuan**, J. Gerding, A. Van Orden, and C. Henry, “Use of a Silicon Photo-Detector to Probe the Evanescent Field Surrounding a Planar

- Waveguide Sensor”, AIChE Annual Meeting, San Francisco, CA, Nov. 12-17, 2006
10. D.S. Dandy, M.D. Stephens, K.L. Lear, **G. Yuan**, D. Grainger, and P. Wu, “A local evanescent array coupled biosensor”, Pacificchem 2005, Honolulu, Dec. 16-21, 2005
 11. M. Stephens, D. Dandy, **G. Yuan**, and K.L. Lear, “Optical and physical characterization of a Local Evanescent Array Coupled biosensor”, AIChE Annual Meeting, Cincinnati, Ohio, October 30-November 4, 2005
 12. **G. Yuan**, M. Stephens, D. Dandy, and K.L. Lear, “Characterization of Transient Interference in a Single Mode Waveguide”, OSA Annual Meeting/2005 Frontiers in Optics/ Laser Science Conference, Tucson, AZ, October 16-20, 2005
 13. M. Stephens, **G. Yuan**, K.L. Lear, and D. Dandy, “Sub-micron thickness planar optical waveguide deposition and characterization for application to evanescent wave sensing of analytes in an immunoassay biosensor”, AIChE Annual Meeting, Austin, TX, November 7-12, 2004

[Local Presentations]

1. R Yan, **G. Yuan**, K.L. Lear, M.D. Stephens, D.S. Dandy, B. Murphy, XY. He, and C.S Henry, “Local Evanescent Array Coupled (LEAC) Biosensor”, poster presented at CSU Ventures conference, at Colorado State University, Fort Collins, Feb. 05, 2008
2. R. Pownall, **G. Yuan**, C. Thangaraj, P. Nikkel, T. W. Chen and K. L. Lear, “CMOS-Compatible On-Chip Optical Interconnects,” poster presented at Colorado Photonics Industry Association (CPIA) at University of Colorado, Nov. 14 2007
3. **G. Yuan**, M. Stephens, R. Pownall, R. Yan, P. Nikkel, X. He, C. Henry, T. Chen, D. Dandy and K.L. Lear, “Further demonstration of a local, evanescent, array coupled biosensor,” poster presented at Information Science and Technology Colloquium at

Colorado State University, Fort Collins, CO, November 29, 2006

4. R. Yan, **G. Yuan**, R. Pownall, and K.L. Lear, "Implementation of shear force scanning optical microscopy (SOM) for waveguide detecting," poster presented at Information Science and Technology Colloquium at Colorado State University, Nov. 29, 2006
5. R. Pownall, **G. Yuan**, C. Thangaraj, P. Nikkel, T. Chen and K.L. Lear, "CMOS-Compatible On-Chip Optical Interconnects," poster presented at Information Science and Technology Colloquium at Colorado State University, Nov. 29, 2006
6. **G. Yuan**, M. Stephens, D. Dandy, and K.L. Lear, "Initial demonstration of a local, evanescent, array coupled (LEAC) biosensor concept", poster presented at Colorado Photonics Industry Association Annual Meeting, Boulder, CO, November 15, 2005. **(Awarded 3rd best poster out of 26.)**
7. **G. Yuan**, M. Stephens, D. Dandy, and K.L. Lear, "Local Evanescent Array Coupled (LEAC) Biosensor", poster presented at Information Science and Technology Colloquium at Colorado State University, Fort Collins, CO, April 13-14, 2005. **(Awarded 3rd best overall poster out of 147.)**
8. A. M. Raza, **G. Yuan**, C. Thangaraj, T. Chen, B. Pownall, and K. L. Lear, "Truly CMOS Compatible On-Chip Optical Interconnect for Clock Distribution", poster presented at Information Science and Technology Colloquium at Colorado State University, Fort Collins, CO, April 13-14, 2005
9. **G. Yuan** and K.L. Lear, "Multianalyte Physiological Optical Waveguide Sensor", poster presented at Colorado Photonics Industry Association Annual Meeting, Boulder, CO, November 20, 2003

Appendix A: 1-D mode solver for optical waveguide

In this appendix, the finite difference code is presented that was used to calculate waveguide mode profiles and propagation constants. The code is programmed in MATLAB. The main solver for the waveguide mode was first derived by Guangwei Yuan and then further developed and supplemented with supporting m-files by Dr. Kevin L. Lear at Colorado State University.

Wg_edit.m, this file is used to edit the waveguide structure and index profile.

```
% used for creating or editing files with the following
columns:
% column 1 is thickness; if <0 then end of data
field{1}='thickness /nm';
% column 2 is grid spacing; if 0 then auto grid
field{2}='grid spacing /nm';
% column 3 is real part of refractive index
field{3}='real index, n';
% column 4 is imaginary part of refractive index
field{4}='imag index, k';
% column 5 is grading: 0=const, 1=grade linearly between
adjacent layers field{5}='grade type, 0=constant,
1=linear';

max_field = 5;           % number of columns in wgdata
matrix and

% wgfile
% construct column header line for later use
header=sprintf('layer\t');
for f=1:max_field
    header = [header sprintf('%s\t',field{f})];
end    % for f=...

wgfile = input('Enter existing WG file name or blank for
new one: ', 's');
if length(wgfile)==0
    wgfile = input('Enter new WG file name: ', 's');
    num_layers = 0;
    wgdata(1,max_field) = 0;    % write zero here just to
set size
```

```

        wgdata(1,1) = -1;                % write negative here to
flag last line
else
    wgdata = load(wgfile);
    num_layers = 0;
    while wgdata(num_layers+1,1)>=0    % may need to fix
code to not overrun array
        num_layers = num_layers + 1;
    end
end    % if wgfile=='

%Loop for editing layers until operator exits
layer = 1;
while layer ~= 0
    % Display wgdata
    %     first show header for columns
    disp(header);
    disp(' ');

    %     then show each layer
    for l=1:num_layers
        disp(sprintf('
%d:\t%f\t%f\t%f\t%f\t%f',l,wgdata(l,:)));
    end    % for l=1:num_layers
    disp(' ');

    % Loop for editing until operator exits
    layer = input('Enter layer to edit or 0 to exit: ');
    if not(layer~=0)
        continue;    % jump to end of loop which will exit
next time
    end
    if layer > num_layers
        num_layers = num_layers+1;
        for l=num_layers:layer
            wgdata(l,1)=0;
        end
        num_layer = layer;
        wgdata(layer,:)=zeros(1,max_field);
        wgdata(num_layers+1,1) = -1;
    end    % if layer > num_layers
    for f=1:max_field
        disp(sprintf('%s = %g
',field{f},wgdata(layer,f)));
        new_val = input('Enter new value or return for no
change: ');
        if length(new_val)~=0

```

```

                wgdata(layer,f) = new_val;
            end
        end % for f=...
    end % while layer <> 0

save(wgfile, '-ascii', '-tabs', 'wgdata');

```

Wg_grid.m: This program reads a waveguide file created by wg_edit.m and creates a grid file that can be used in the finite difference model simulation. Here the waveguide grid contains a matrix that at each grid point gives the refractive index real part (n) and imaginary part (k) values. There are 5 columns in the waveguide file that describe the grid. Column 1 defines the thickness of the dielectric layer. The input of this column must be a non-zero value; otherwise the data entry ends. Column 2 defines the grid spacing while automatic grid is used when the entry is 0. Column 3 is the real part of refractive index of a dielectric layer. Column 4 is the imaginary part of refractive index of a dielectric layer. Column 5 has two entries: 0 for constant, 1 for grade linearly between adjacent layers. The latest change of the code was to put grid points close to layer boundaries.

```
Clear
```

```

% define constants
near_end = 0.1; % fraction of dx to position points near
ends

max_field = 5; % number of columns in wgdata
matrix and wgfile
% construct column header line for later use

wgfile = input('Enter WG layer file name to create grid
for: ','s');
wggridfile = input(['Enter WG grid file name or return for
' wgfile '_grid : ','s']);

```

```

if length(wggridfile)==0
    wggridfile = [wgfile '_grid'];
end

wgdata = load(wgfile);
num_layers = 0;
while wgdata(num_layers+1,1)>=0    % may need to fix code to
not overrun array
    num_layers = num_layers + 1;
end

% Display wgdata ...
disp('WG layer file to be gridded is ...');
%    first show header for columns
disp(' ');
disp('layer      d/nm    dx/nm    n        k        grade');
%    then show each layer
for l=1:num_layers
    disp(sprintf('
%d:\t%f\t%f\t%f\t%f\t%f',l,wgdata(l,:)));
end    % for l=1:num_layers
disp(' ');

disp('Grid point options:');
disp(' 0) Put grid point in center of each dx');
disp(' 1) Put grid point at ends of each dx');
disp(' 2) Put grid point in center of each dx and near
ends of each layer');
ctr_grid = input('Enter grid point option: ');
if ctr_grid==0
    disp('Warning: non-center gridding is not debugged
yet. ');
end
gd = input('Enter grid density (1=normal, 2=2x as many
points, ...): ');

% Add three extra, equally spaced grid points before layers
to make
% transparent boundary condition coefficients work
dx = wgdata(1,2)/gd;
grid_data(1,:) = [-dx 0 wgdata(1,3:5)]; % assign x=0,
layer=0, layer 1 index
grid_data(2,:) = [-dx/2 0 wgdata(1,3:5)]; % assign x=0,
layer=0, layer 1 index
grid_data(3,:) = [0 0 wgdata(1,3:5)]; % assign x=0,
layer=0, layer 1 index
i_start=3; % index to grid points

```

```

%i_start=0
x_start=0;          % cumulative position across waveguide
structure

%Loop through each layer
for layer=1:num_layers          % loop through each layer
    disp(sprintf('Processing layer %d',layer));
    thick = wgdata(layer,1);
    dx = wgdata(layer,2)/gd;
    n = wgdata(layer,3);
    k = wgdata(layer,4);
    grade = wgdata(layer,5);
    if thick <= 0
        disp('Warning: zero thickness layers not debugged
yet. ');
    end
    if grade ~= 0
        n_start = wgdata(layer-1,3); k_start =
wgdata(layer-1,4);
        n_stop = wgdata(layer+1,3); k_stop =
wgdata(layer+1,4);
        disp(sprintf('Grading from %.3f + i * %g to %.3f +
i * %g',n_start,k_start,n_stop,k_stop));
    end
    if dx > 0
        num_pts=round(thick/dx)+ctr_grid;
        for i=1:num_pts          % loop through each grid
point in layer
            x = x_start+(i-0.5-0.5*ctr_grid)*dx;
            if (x < x_start)
                x = x_start+near_end*dx;
            end
            if (x > x_start+thick)
                x = x_start+thick - near_end*dx;
            end
            if (grade ~= 0)
                if (grade > 0)
                    f = ((x-x_start)/thick)^abs(grade);
                else
                    f = 1 - ((x_start+thick-
x)/thick)^abs(grade);
                end
                n = n_start*(1-f)+n_stop*f; k = k_start*(1-
f)+k_stop*f;
            end % if (grade ~= 0)

            grid_data(i_start+i,:) = [x layer n k grade];

```

```

        % include thickness as second column for doing
integrated powers
    end % for i
    else
        disp(sprintf('Error in layer %d: autogridding not
implemented yet.',layer));
    end % if dx > 0
    % now prepare for next layer
    i_start = i_start + num_pts;
    x_start = x_start + thick;
end % for layer loop

% Now add three extra, equally spaced grid points after
layers to make
% transparent boundary condition coefficients work
dx = wgdata(layer,2)/gd;
grid_data(i_start+1,:) = [x_start num_layers+1
wgdata(num_layers,3:5)];
grid_data(i_start+2,:) = [x_start+dx/2 num_layers+1
wgdata(num_layers,3:5)];
grid_data(i_start+3,:) = [x_start+dx num_layers+1
wgdata(num_layers,3:5)];

save(wggridfile,'-ascii','-tabs','-double','grid_data');

```

wg_solve.m: This program reads a grid file with n & k values and solves for the eigenmodes of a corresponding matrix. The added user settings are used to determine which modes to keep depending on real and imaginary parts of the effective index for the mode. Modes with $n_{\text{eff}} < 1$ and radiation modes with $n_{\text{eff}} < 1$ are discarded.

```

clear

wgfile = input('Enter WG layer file name (used to create
other file names): ','s');
wggridfile = input(['Enter WG grid input file or return for
' wgfile '_grid : ','s']);
if length(wggridfile)==0
    wggridfile = [wgfile '_grid'];
end
grid_data = load(wggridfile);
wgsolnfile = input(['Enter name for WG intensity output
file or return for ' wgfile '_fld : ','s']);

```

```

if length(wgsolnfile)==0
    wgsolnfile = [wgfile '_fld'];
end
wgphifile = input(['Enter name for WG phase output file or
return for ' wgfile '_phi :  '], 's');
if length(wgphifile)==0
    wgphifile = [wgfile '_phi'];
end
wgnefffile = input(['Enter name for WG n_eff output file or
return for ' wgfile '_neff :  '], 's');
if length(wgnefffile)==0
    wgnefffile = [wgfile '_neff'];
end
lambda = input('Enter wavelength /nm: ');
k0 = 2*pi/lambda;

n_z_est = input('Enter an estimated eff. index for setting
BC transparency or return to skip: ');
if length(n_z_est)==0
    n_z_est=0;
end
% will use n_z_est as flag below; if zero then use
conventional BCs

nreal_min = input('Enter min. real(n_eff) for modes to show
or return for real(n_eff)>0.9: ');
if length(nreal_min)==0
    nreal_min=0.9;
end
nimag_max = input('Enter max. imag(n_eff) for modes to show
or return for imag(n_eff)<1.5: ');
if length(nimag_max)==0
    nimag_max=1.5;
end

BCladjust = 0.99;           % later should compute these
based on n_z_est
BCladjust = 0.99;           % later should compute these
based on n_z_est

x = grid_data(:,1);         % grid point positions
layer = grid_data(:,2);     % which layer grid point occurs
in
n = grid_data(:,3)+sqrt(-1)*grid_data(:,4);

% complex refractive index at grid point

```

```

L = length(x);      % number of grid points

M = zeros(L,L);
for s=2:L-1;
    M(s,s-1) = (2/(x(s)-x(s-1)))/(x(s+1)-x(s-1));
    M(s,s)   = -2*(1/(x(s)-x(s-1))+1/(x(s+1)-
x(s)))/(x(s+1)-x(s-1)) + (n(s)*k0)^2;
    M(s,s+1) = (2/(x(s+1)-x(s)))/(x(s+1)-x(s-1));
    % note could play games with precalculating the dx in
the demoninator,
    % but the computational effort involved in loading
the matrix is small
    % compared to that in calculating the eigenvalues.
end

% begin BOUNDARY CONDITION
if (n_z_est == 0)

    dx=x(2)-x(1);
    if dx~=(x(3)-x(2))
        disp('Error:  x=0 boundary grid points are not
equally spaced');
    end
    M(1,1)=((k0*n(1))^2)+1/((dx)^2)*BCLadjust;
    M(1,2)=-2/((dx)^2)*BCLadjust;
    M(1,3)=1/((dx)^2)*BCLadjust;

    % s=L boundary condition
    dx=x(L)-x(L-1);
    if dx~=(x(L-1)-x(L-2))
        disp('Error:  x=x_max boundary grid points are not
equally spaced');
    end
    M(L,L)=((k0*n(L))^2)+1/((dx)^2)*BCLadjust;
    M(L,L-1)=-2/((dx)^2)*BCLadjust;
    M(L,L-2)=1/((dx)^2)*BCLadjust;

else % if (n_z_est == 0)

    M(1,1)=(((k0*n(1))^2) - 1/((dx)^2) - (n_a-
0.5*n_z_est/n_a)*k0/(dx^2))/(1+1/(2*n_a*k0*dx));
    M(1,2)=1/((dx)^2)/(1+1/(2*n_a*k0*dx));

    % s=L transparent boundary
    dx=x(L)-x(L-1);

```

```

    % Calculate n_a from estimated n_z value. See 21-
    April-2006 derivation
    % notes above.
    n_a = sqrt(n_z_est^2-n(1)^2) % take postive square
    root at x=x_L boundary
    % n_a should be a complex number if there is
    radiation to boundary
    M(L,L)=(((k0*n(L))^2) - 1/((dx)^2) - (n_a-
    0.5*n_z_est/n_a)*k0/(dx^2))/(1+1/(2*n_a*k0*dx));
    M(L,L-1)=1/((dx)^2)/(1+1/(2*n_a*k0*dx));
end % if (n_z_est == 0) ... else
% end BOUNDARY CONDITION

% Find eigenvectors and eigenvalues (elements of diagonal
of diagM)
[V,diagM]=eig(M);
for s=1:L
    n_z_all(s) = sqrt(diagM(s,s))/k0;
end
% MATLAB naturally provides eigenvalues in decreasing order
of real part
% want to remove elements that have less than unity real
part
n_z = n_z_all(find((real(n_z_all)>=nreal_min) &
(imag(n_z_all)<=nimag_max)))'
n_z_ri = [real(n_z) imag(n_z)];
save(wgnefffile,'-ascii','-tabs','-
double','lambda','n_z_ri');
figure(1);
plot(n_z,'x'); % plot on the complex plane, may not
work if all real
if max(abs(imag(n_z)))==0 % if all the effective indices
are real
    xlabel('mode index'); % they will plot without x-data
    ylabel('n_{eff,z}');
else % otherwise they will plot on
the complex plane
    xlabel('Real(n_{eff,z})');
    ylabel('Imag(n_{eff,z})');
end
title(['{' wgnefffile '}']);

fld_data = [grid_data
(abs(V(:,find((real(n_z_all)>=nreal_min) &
(abs(imag(n_z_all))<=nimag_max))))).^2];

```

```

phi_data = [grid_data
(angle(V(:,find((real(n_z_all)>=nreal_min) &
(abs(imag(n_z_all))<=nimag_max)))))]];
% for some reason, matlab won't write complex numbes to
files, so save intensity and save phase of field in
separate file
save(wgsolnfile, '-ascii', '-tabs', '-double', 'fld_data');
save(wgphifile, '-ascii', '-tabs', '-double', 'phi_data');

```

wg_plot.m: This program reads a grid file created by wg_grid.m and displays the n & k values at grid points. Furthermore, it can be extended to also plot the fields

```

wggridfile = input('Enter WG grid or field data file name :
','s');
grid_data = load(wggridfile);
x = grid_data(:,1);
n = grid_data(:,3);
k = grid_data(:,4);
grid_cols = 5; % number of grid data columns in file
before mode fields

num_modes = size(grid_data,2)-5
disp(sprintf('There are %d field eigenmodes in this
file.',num_modes));
modes = input('Enter the columns of fields to plot, e.g
3:2:9: ','s');

figure();
hold on;
plot(x,n,'go--');
plot(x,k*100,'rx:');
for m=eval(modes)

plot(x,grid_data(:,m+grid_cols)/max(grid_data(:,m+grid_cols
)), 'b');
end
xlabel('position /nm');
ylabel('n, k x 100, H fields');
title(wggridfile);
hold off;

```

Appendix B: Tutorials on LASI and Waveguide Photomask Design CSU_12_2004

This tutorial material is prepared for the beginners who are in the optical waveguide design tasks. Herewith, the contents are based on the design procedures for Waveguide Photomask CSU_12_2004 using LASI layout editor 7.0. As usual, the mask design task was straightforward rather than difficult task but very time consuming that needs a lot of thinking ahead for building allocations and elements modifications.

The purpose of using LASI layout editor 7.0 to prepare the artwork is to create a high resolution (to 1 μm) Chrome photomask. Other Optoe group members at CSU used Freehand MX to create photomask on transparency photomasks for much coarser feature resolution (to 10 μm). In this case, the Chrome photomasks have incomparable features with that of transparency masks. Also, one can enjoy other advantages of the Chrome photomasks, such as, high uniformity, long durability, high reliability, as well as high density.

To begin the mask design, one needs to use standard resolution and alignment marks that allow an easy access different mask layers. In order to do that, one should plan deliberately before you begin the computer aid design (CAD) and carefully plan the valuable photomask real estate. On the other hand, cost effectiveness is a vital factor in the photomask design. In practice, we aim to put as many as possible test structures on the photomask. For example, I needed a great number of waveguide light propagation loss and bending loss tests. Not all the designed structures are expected to turn in good results after fabrication. So, I designed waveguides that not only meets my target design and modeling, but also has certain variances for extreme tests. In this case, pre-layout

simulations will save the work in later tests. One other example might be easily omitted at the first place; our waveguide samples often need to be cleaved and polished from the edge. Therefore, the sample needs a buffer length for the material loss in the mechanic polishing process.

In CSU_12_2004, the waveguide blocks were drafted to be 1 inch x 1 inch blocks which was later proven very useful for waveguide cleaving and polishing. A total 4 inch x 4 inch area was used as shown in Figure 1.

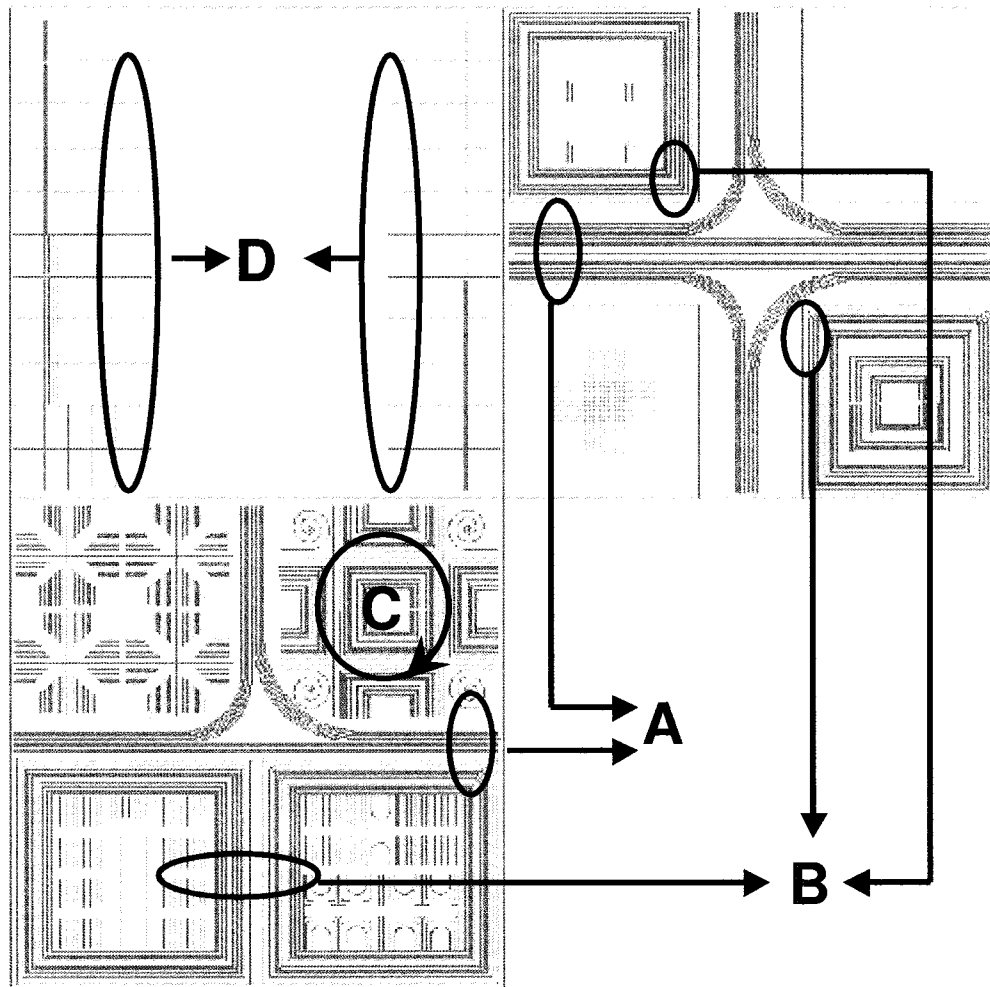


Figure 1 Layout of Photomask CSU_12_2004

There are four groups of components designed for test. Group A are straight waveguides shown in Figure 2.

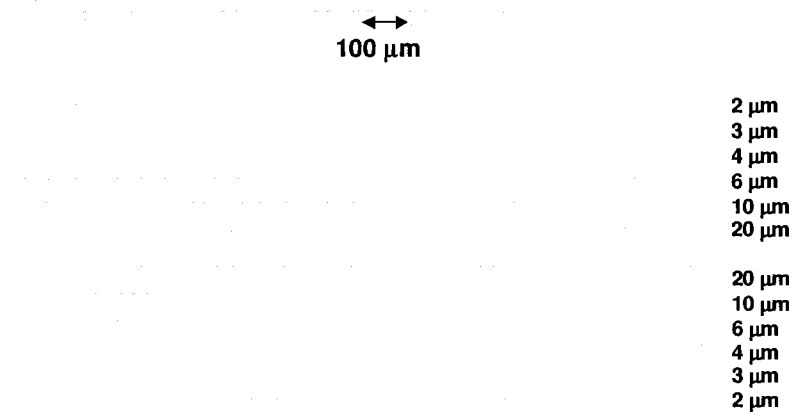


Figure 2 Group A, straight waveguides

Group B are waveguide bends shown in Figure 3.

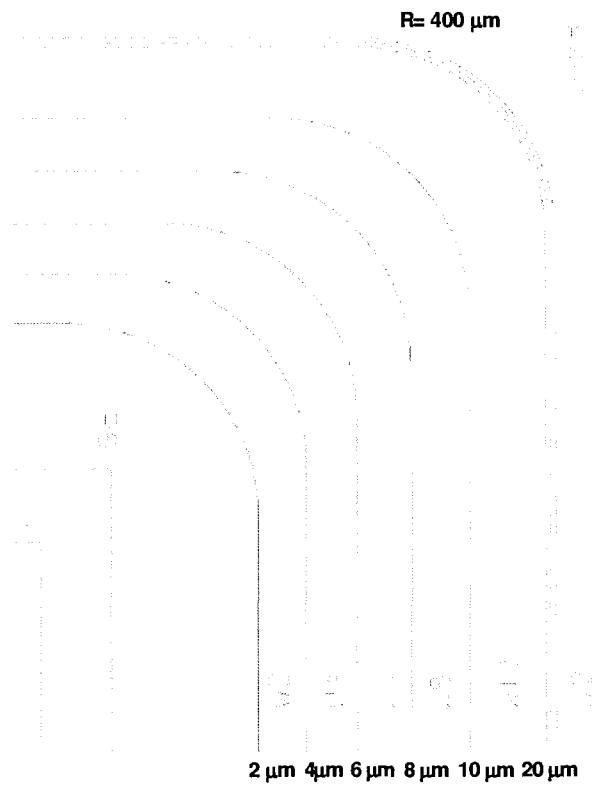


Figure 3 Group B, waveguide bends

Group C are waveguide splitters shown in Figure 4.

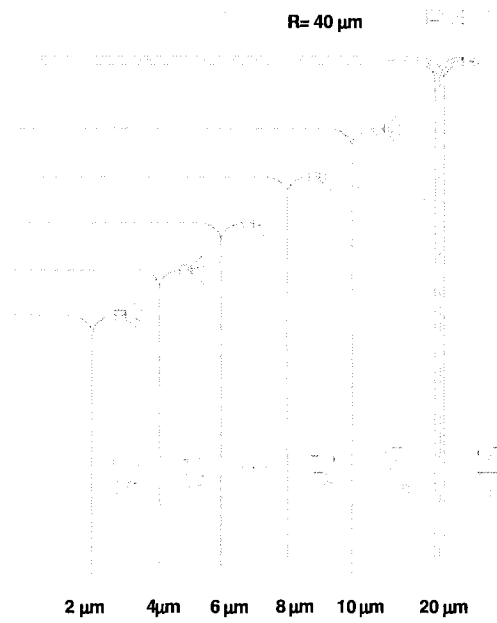


Figure 4 Group C, waveguide splitters

Group D are bar adlayers shown in Figure 5.

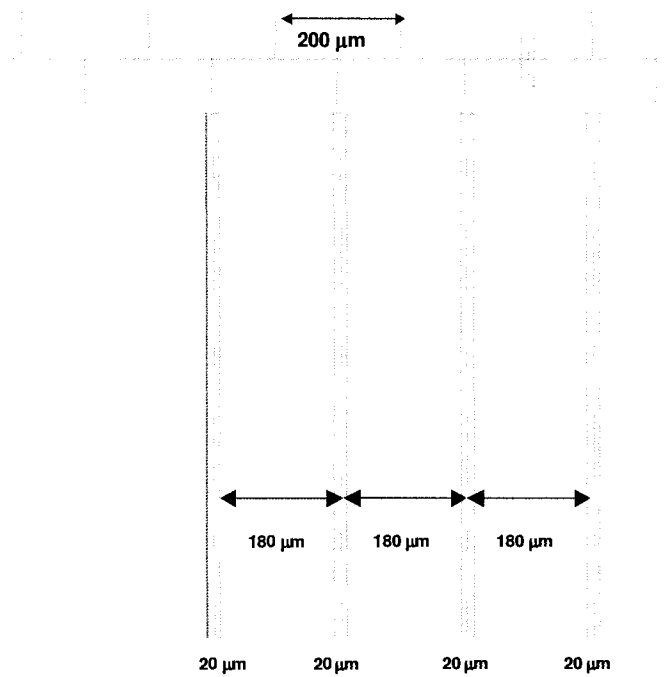


Figure 5 Group D, bar adlayers

Appendix C: Suggestions of using Rsoft

This tutorial material is prepared for the beginners who are in the optical waveguide simulation tasks using Rsoft BPM and FDTD. Rsoft is a GUI that is built to integrate Helmholtz and Maxwell function solver with field strength viewer. To begin to program, we have a global option window that allows to choose from 1) simulators (BPM or FDTD), 2) 2D or 3D, 3) Vector mode or scalar mode, 4) index profile type, and entering simulation parameters such as incident light wavelength, background index, substrate-to-background index difference, and waveguide width. Initial viewing settings are optional.

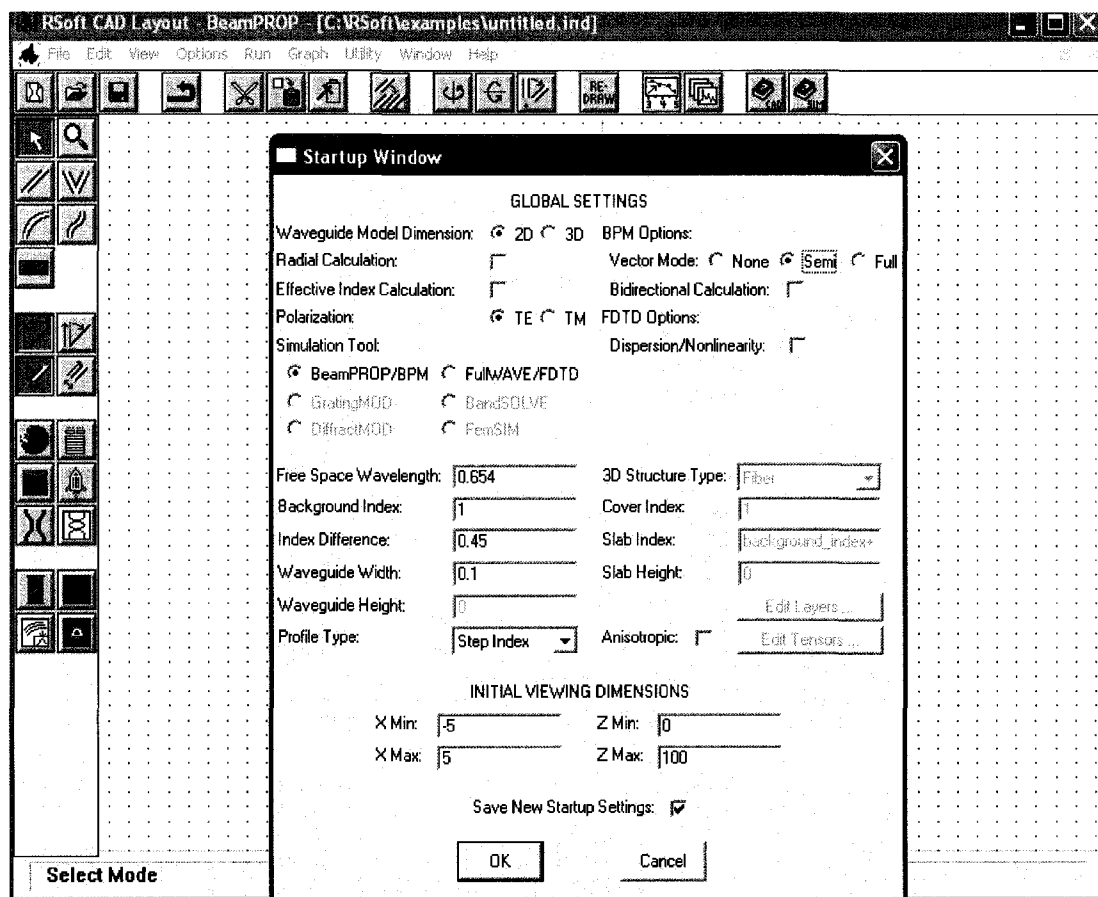


Figure 1: Global setting options

Next step is layout of the waveguide schematics. As a convention, the waveguide core is laid at the center of the layout window. Colors are chosen to distinguish substrate and core layers. Drawing tools can be found in the palate at the left hand side of the window.

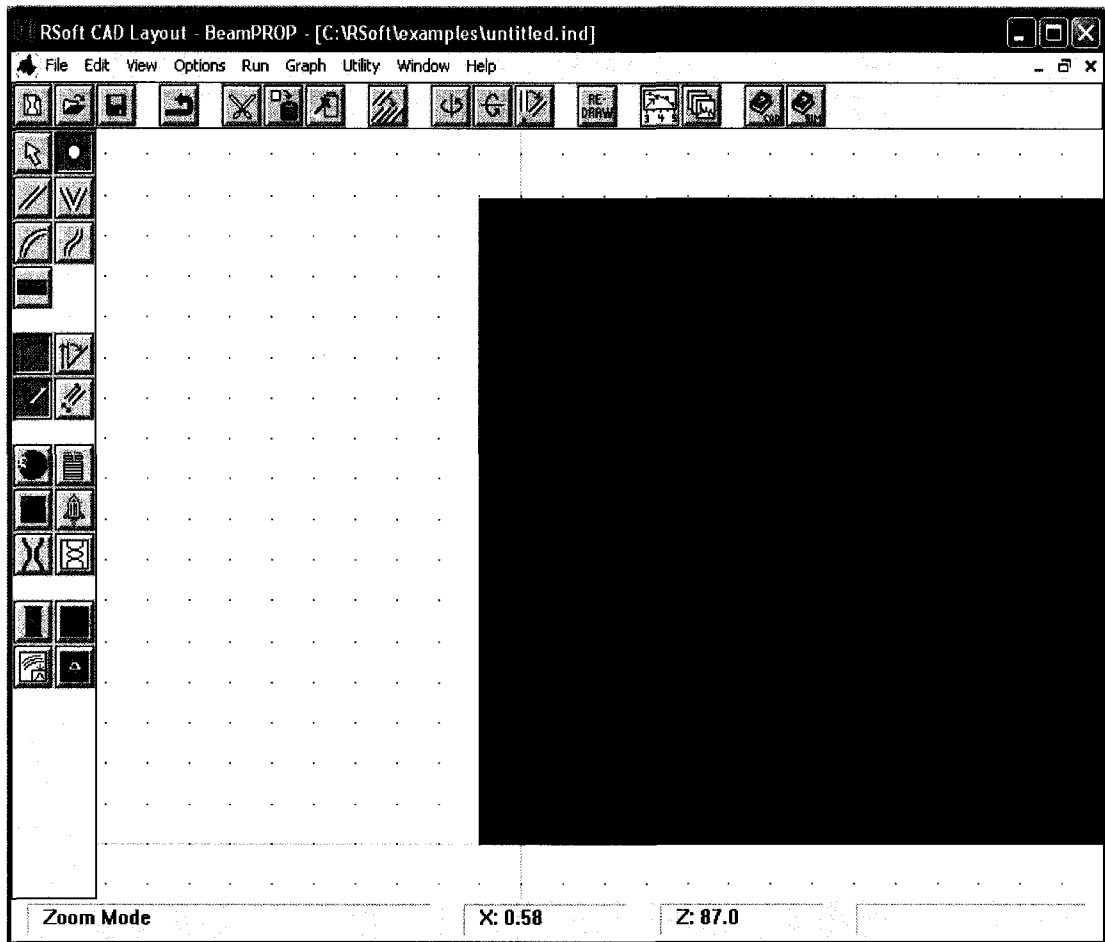


Figure 2: Layout editing window

Then we need to set parameters of the waveguide core that allow us to calculate the fundamental mode of the straight waveguide. For example as seen in the Figure 3, the refractive index step between the core and substrate is set to 0.8. The parameters, index (imaginary part), width and height are all set as default values, which we defined in the global settings. The waveguide length is set to 79.5 μm . Note that the geometry unit is micron. All settings at the beginning are default values.

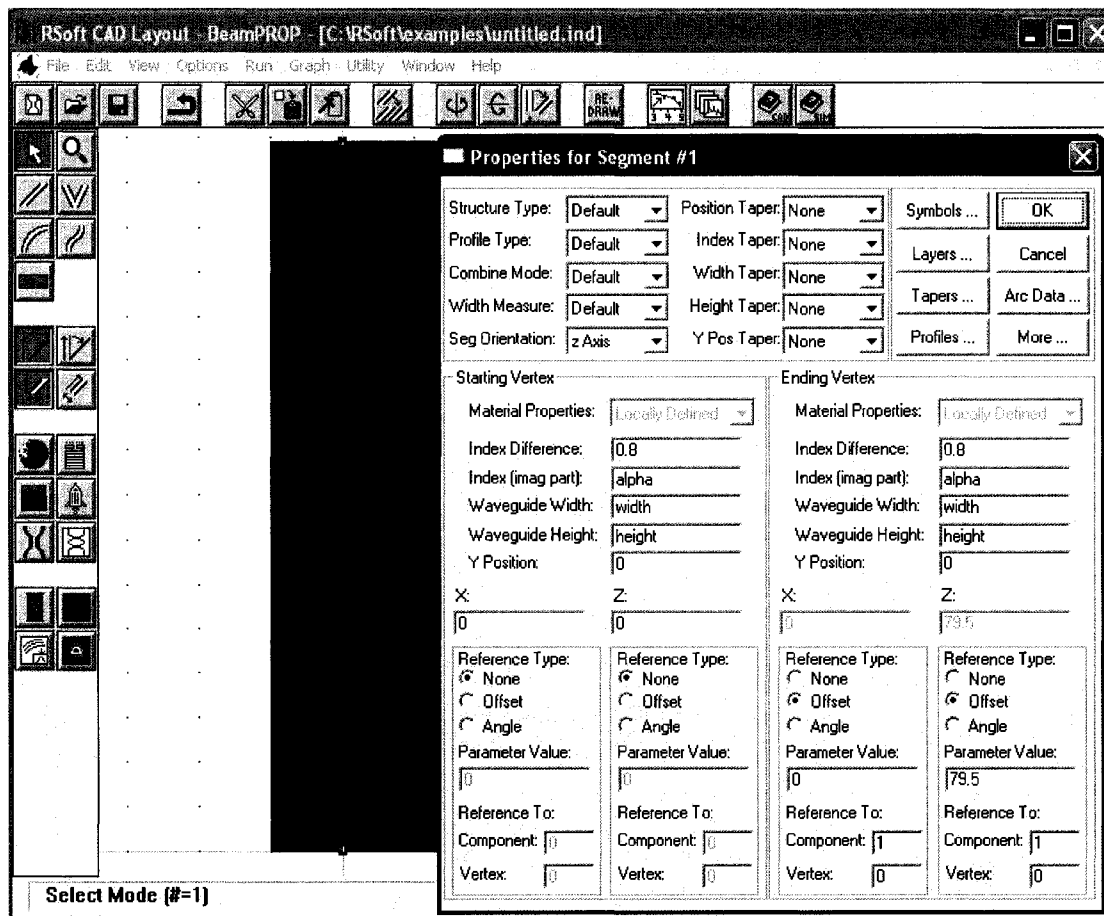


Figure 3: Schematic parameter options

Then we check the refractive index profile. As seen in Figure 4, we have a slab waveguide structure, a thin layer of waveguide core of refractive index 1.8 and width 100nm, and a bulk substrate of refractive index 1.45.

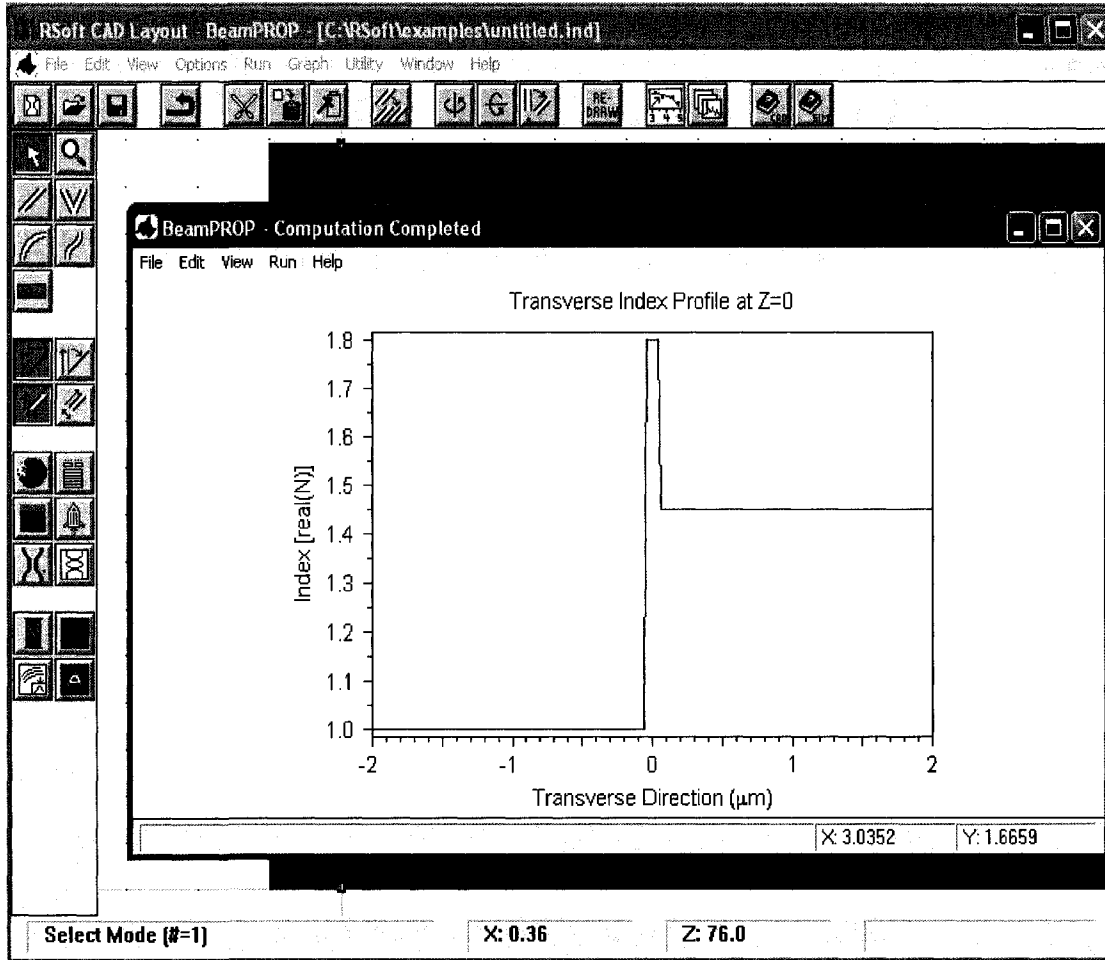


Figure 4: Plot of refractive index profile

To calculate the fundamental mode of above waveguide, we launch a Gaussian like input field and mode width set to $1\mu\text{m}$.

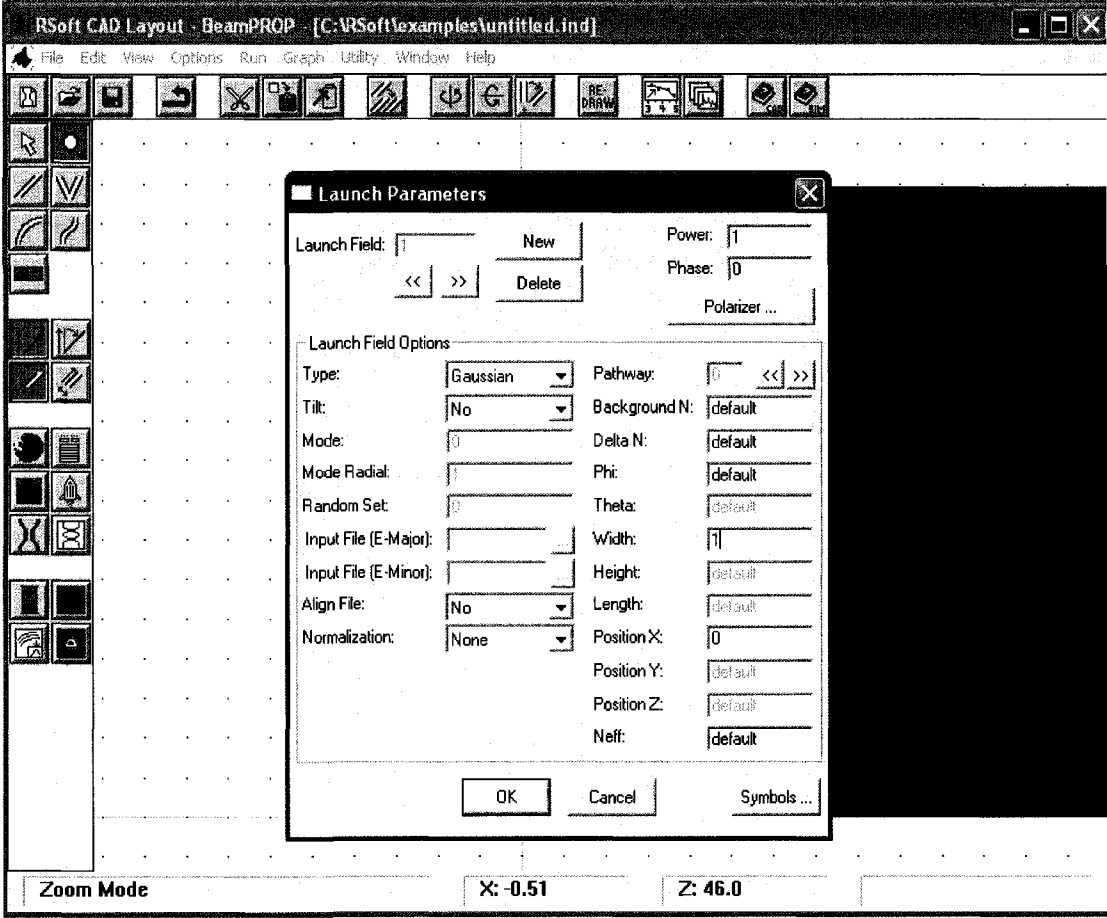


Figure 5: Launching parameters

Launching the Gaussian like mode profile into the waveguide, we are able to calculate the fundamental mode with the following steps. Save this mode profile to a file gwyuan0501.m00 (for example) that would be used in BPM and FDTD simulations.

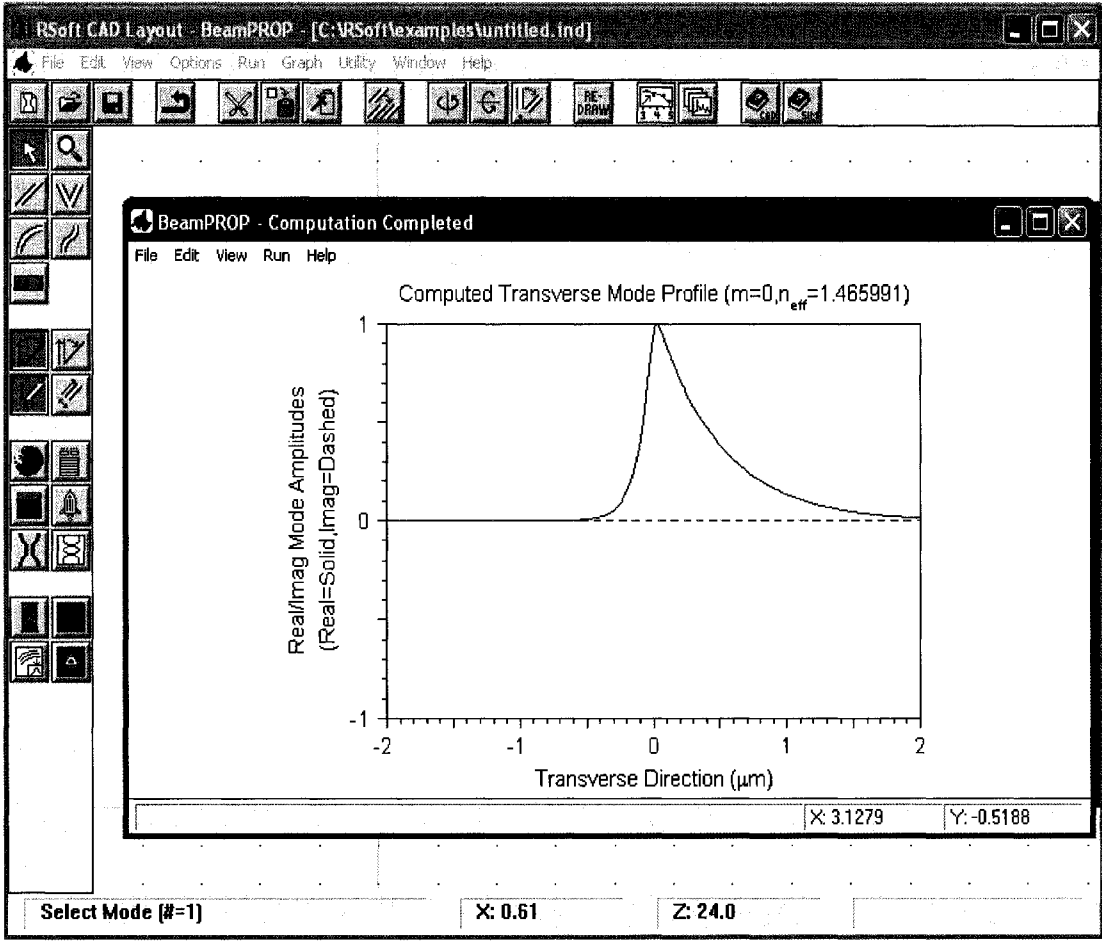


Figure 6: Mode profile plot

To mimic a sensor region on the waveguide, we draw a third block on the waveguide core. This block is about 10 μm long, 100nm tall and has a refractive index of 1.45.

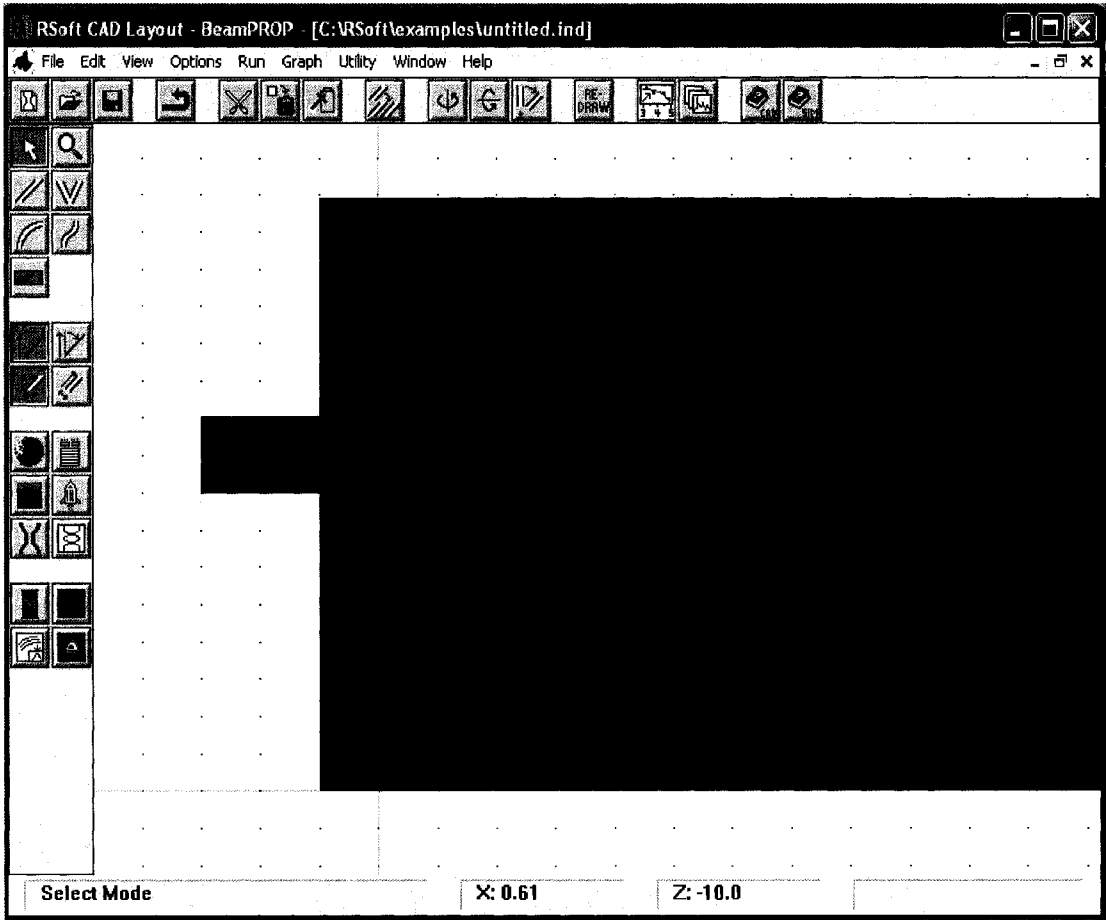


Figure 7: Pseudo-sensor sample for BPM simulation

To simulate the field response to the sensor region, the fundamental mode, which has been saved, is to be launched into the waveguide structure.

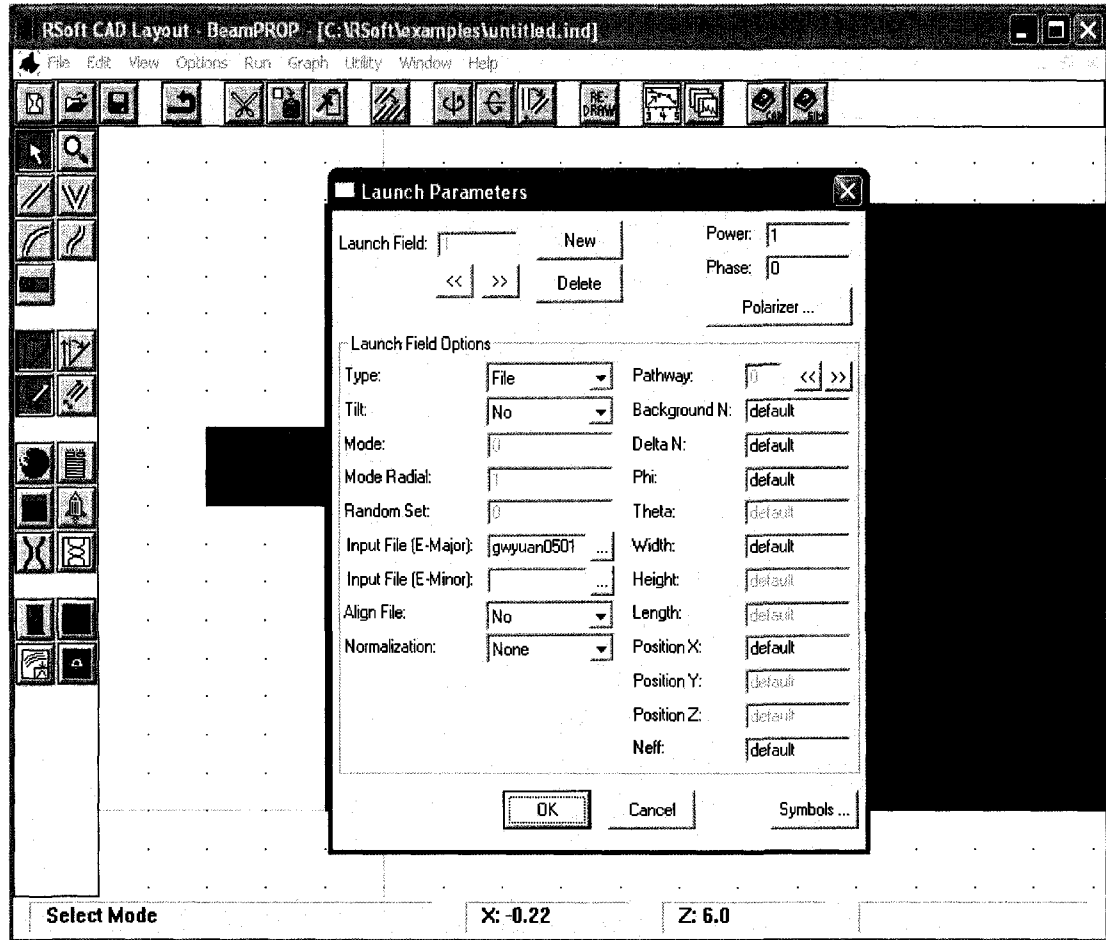


Figure 8: Revisit of launching parameters

Here is the simulation parameter setting for BPM. The total simulation region is from -2 mm to 2 mm. Computation step is 10nm in X and 100 nm in Z. Save the field profile every 1.6 mm. Plot option is ContourMap and the output is directed to the file Fld_resps_to_adlayer.

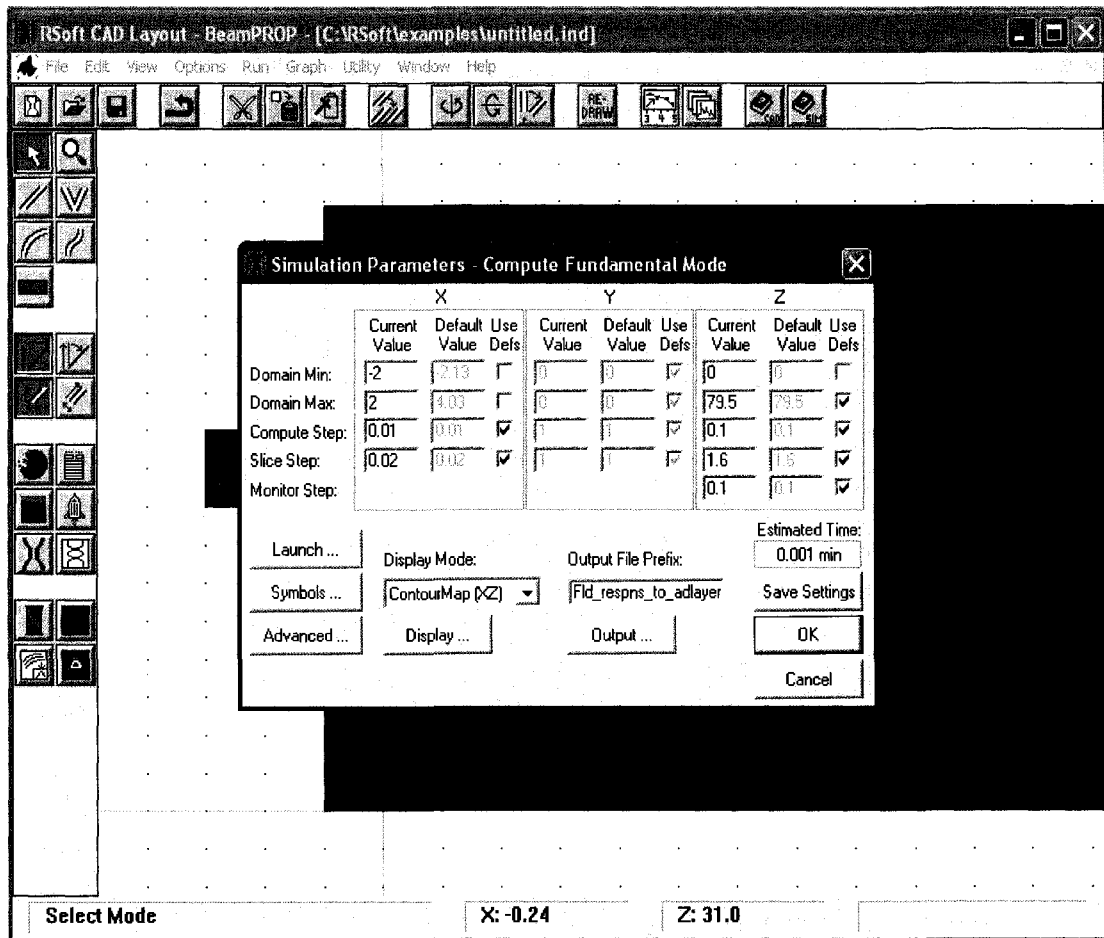


Figure 9: BPM simulation parameters

Use the plot function on the main panel to plot false color field strength. Save the output file for advance analysis. This is the end for a BPM simulation.

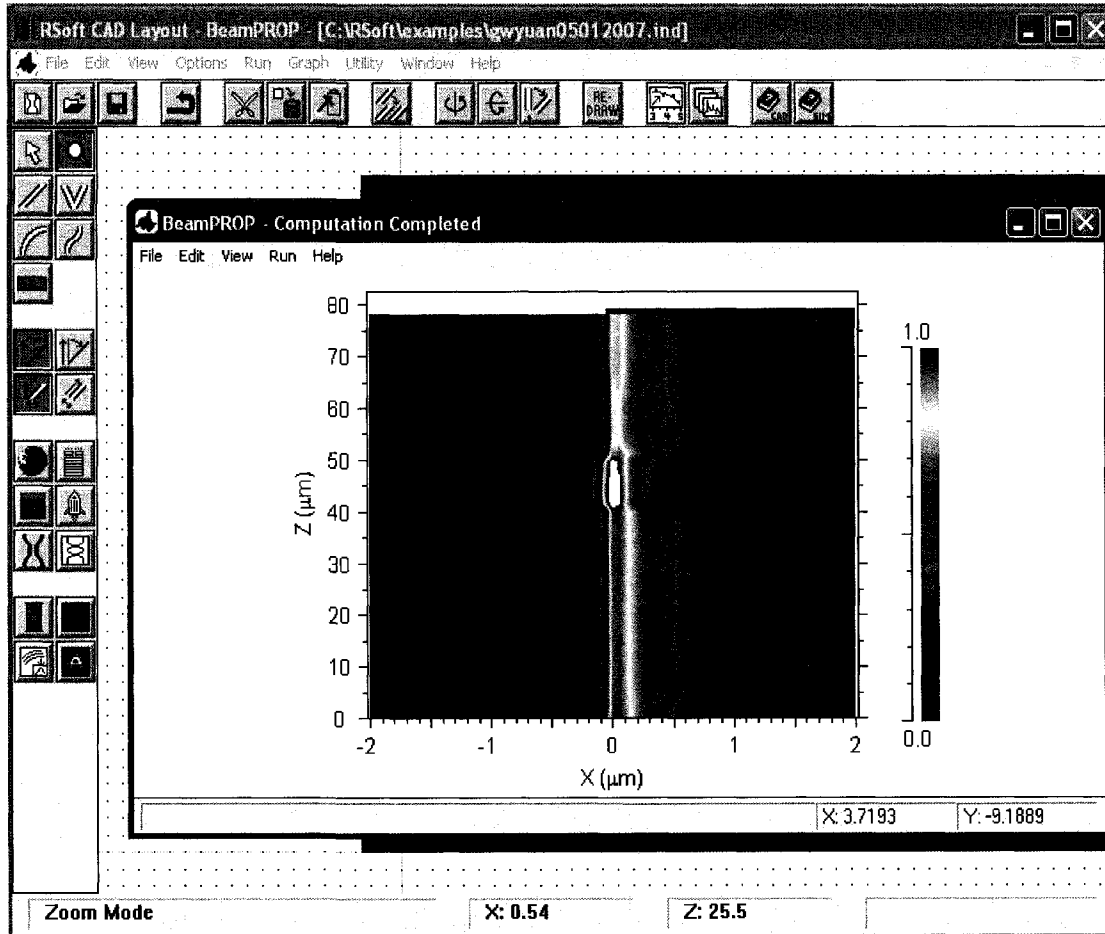


Figure 10: 2-D field strength false-color plot

To simulate a waveguide using FDTD, choose the Fullwave/FDTD option in the global settings window.

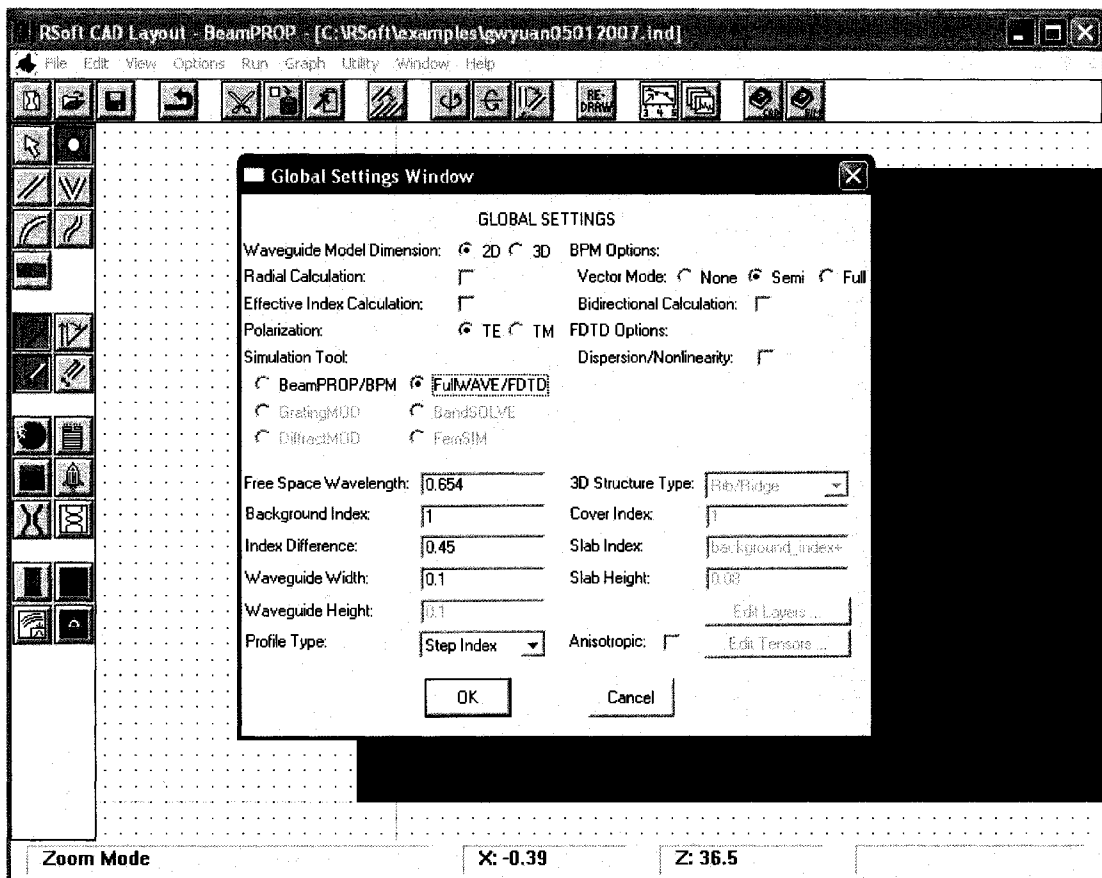


Figure 11: FDTD option

To continue, we need to set the time step in the simulation parameter setting window for FDTD. The time step needs to be smaller than the suggested stability limit. Total simulation time is suggested to be a few hundred steps. Other options can be default. Output is directed to Fld_resps_to_adlayer.

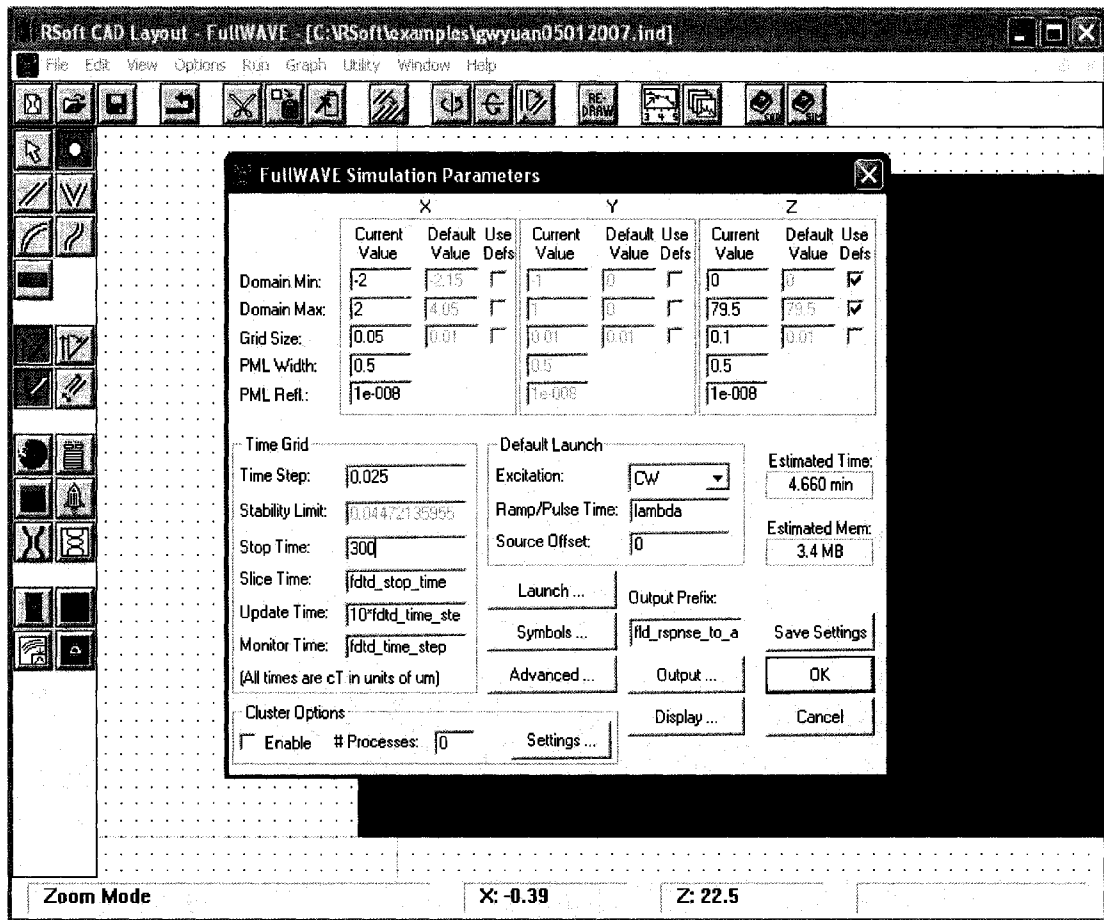


Figure 12: FDTD simulation option

Use the plot function on the main panel to plot false color field strength. Save the output file for advance analysis. This is the end for a FDTD simulation.

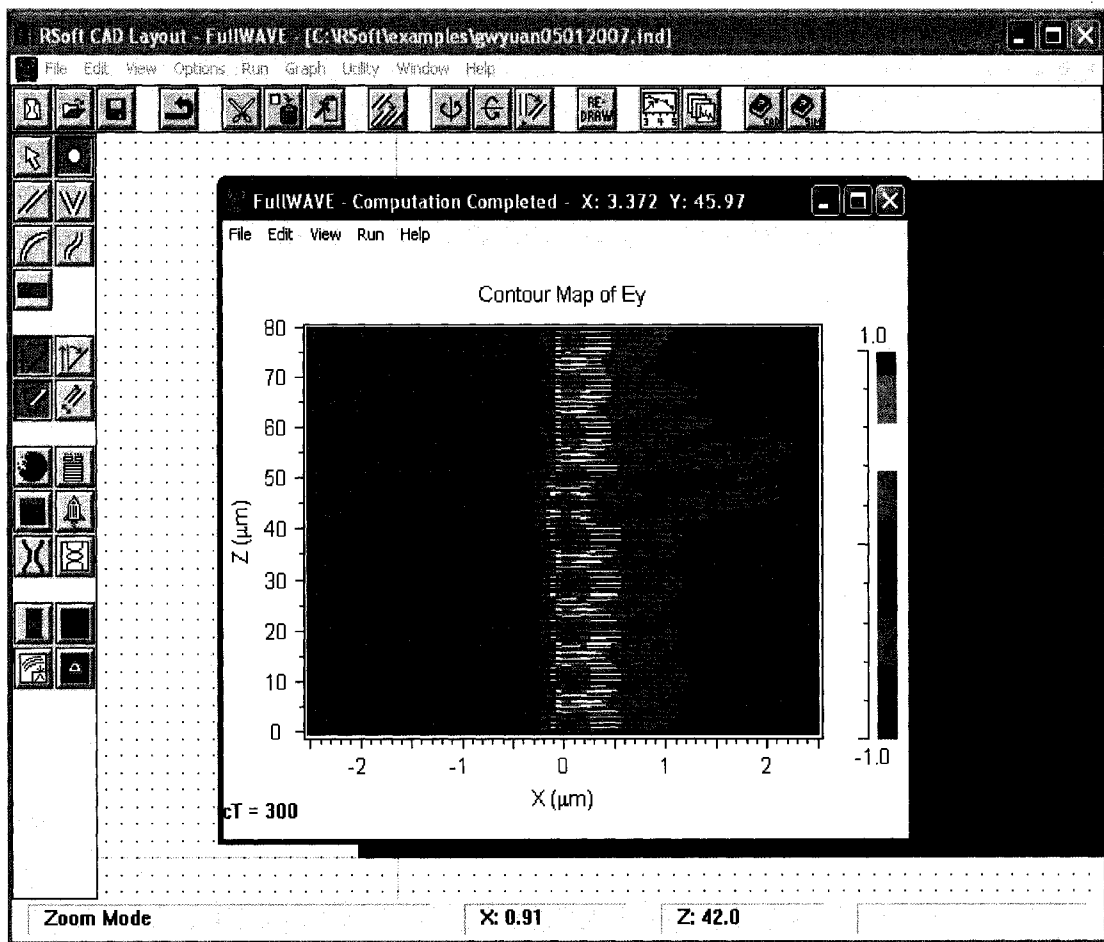


Figure 13: 2-D field strength simulation results

The field strength profile can be exported into an EXCEL file for analysis. But 2-D or 3-D simulation results are more complex and would need to be processed using higher level language such as MATLAB.

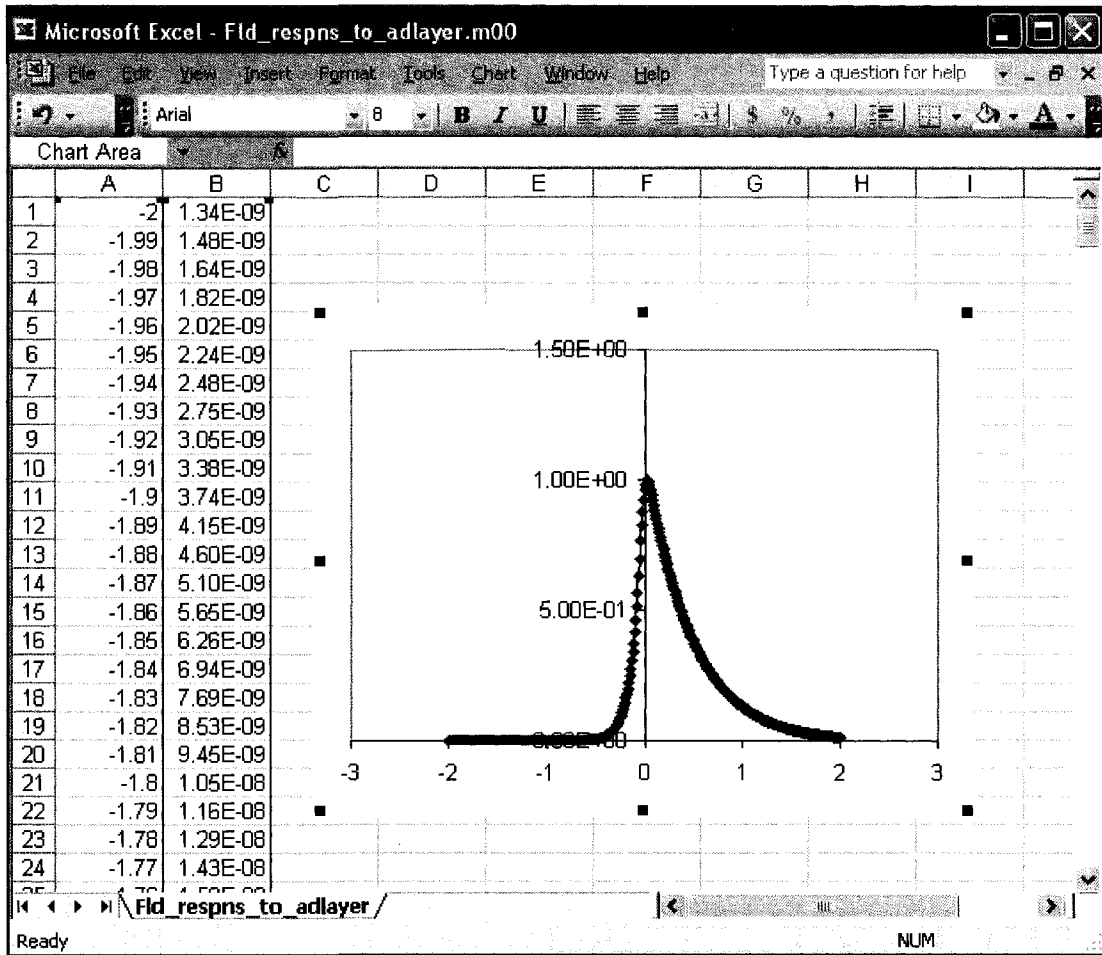


Figure 14: Sample of data retrieving